Observation of Critical Spin Dressing

by

Reza Tavakoli Dinani

M.Sc., Isfahan University of Technology, 2009
B.Sc., Isfahan University of Technology, 2006

Thesis Submitted in Partial Fulfillment of the
Requirements for the Degree of
Doctor of Philosophy

in the
Department of Physics
Faculty of Science

© Reza Tavakoli Dinani 2018
SIMON FRASER UNIVERSITY
Spring 2018

Approval

Name: **Reza Tavakoli Dinani**

Degree: **Doctor of Philosophy (Physics)**
Title: **Observation of Critical Spin Dressing**

Examining Committee: **Chair:** Dr. John Bechhoefer
Professor

Dr. Michael Hayden
Senior Supervisor
Professor

Dr. Jenifer Thewalt
Supervisor
Professor

Dr. Jeffrey McGuirk
Supervisor
Associate Professor

Dr. Levon Pogosian
Internal Examiner
Professor

Dr. Robert Golub
External Examiner
Professor
Department of Physics
North Carolina State University

Date Defended/Approved: March 26, 2018

Abstract

It has long been proposed that spin dressing could be employed to realize a highly effective helium-3 nuclear precession co-magnetometer for a neutron electric dipole moment (nEDM) search. The proposal is to apply an intense, continuous, and far off-resonant oscillating magnetic field, called a dressing field, in such a way that the apparent Larmor precession frequencies of the helium-3 and the neutron are modified. Under appropriate conditions a desirable situation known as critical spin dressing (CSD) is anticipated: the neutron and the helium-3 nucleus (or more generally, any two spin species) are expected to behave as if they had the same gyromagnetic ratio and hence should precess at the same rate in a static magnetic field.

Spin dressing has been studied in the context of the neutron, helium-3, and a variety of other systems. Critical spin dressing, however, has not previously been demonstrated. In this thesis I report the first experimental demonstration of pulsed CSD in which simultaneous spin dressing of ^{1}H and ^{19}F nuclei is achieved and studied. I also demonstrate that CSD can be performed using variety of different dressing field waveforms, a consideration that until now has received little or no attention. Examples of parameters studied include the role of phase and amplitude modulation on spin dressing. Of particular note is a significant improvement in reproducibility achieved by alternating the phase of successive cycles of the dressing field waveform by π radians. Such innovations may prove useful in an eventual nEDM search where demands on precession stability are anticipated to be extreme.

To enable my study of CSD I developed a simple and robust apparatus. The central innovation was the first use of Magneto-Impedance (MI) sensors to detect weak magnetic fields associated with the precession of nuclear magnetic moments. The thesis thus begins with summaries of experiments to characterise and validate the use of MI sensors for ultra-low field (ULF) nuclear magnetic resonance. I then describe a refined version of the ULF NMR apparatus, and the manner in which it is used to investigate CSD.

Keywords: Critical spin dressing; Spin dressing; Nuclear magnetic resonance (NMR); Ultra-low field NMR; Neutron electric dipole moment; ^{1}H NMR; ^{19}F NMR; Magneto-Impedance sensor; Remote NMR.

Dedication

To my beloved parents Abdolali and Ziba,
my wonderful wife Mina,
and
my curious son Borna.

Acknowledgements

I would like to express my sincere gratitude to my advisor Prof. Mike Hayden for the continuous support of my Ph.D studies, for his patience, motivation, and tremendous knowledge. His guidance helped me throughout the researching and writing of this thesis. I have always been motivated by his endless energy in doing research. He has had a valuable impact on my academic and research style. I wish to thank the members of my dissertation committee, Prof. Jenifer Thewalt and Assoc. Prof. Jeffrey McGuirk for their support, guidance and review of this document. I also appreciate the assistance provided by the Physics Department's research technicians Bryan Gormann, Kenneth Myrtle and David Lee in setting up my experiments.

Last but not least, I would like to thank my family: my parents, brothers and sister for their support and encouragement and my wife, Mina Khazaei, without whose patience and sacrifice I could not have completed this thesis.

Table of Contents

List of Tables

List of Figures

Chapter 1

Introduction

The history of searches for a non-zero neutron electric dipole moment (nEDM) is long [1]. It dates to the work of N. F. Ramsey and E. M. Purcell [2, 3] in the 1950s. Since then, the sensitivity of experiments to this quantity has been improved by 6 orders of magnitude [4]. Despite this enormous progress, all experiments to date are consistent with a value of zero. They simply provide an experimental upper limit on the neutron electric dipole moment. And, the sensitivity of current nEDM experiments are still far too low to be able to resolve effects at the level at which the Standard Model (SM) predicts a non-zero value for the nEDM. It seems quite likely that the search for a non-zero nEDM will continue for some time. A starting point for this thesis might be to ask the questions "Why has the possibility of a non-zero nEDM attracted so much attention?" and "How might a non-zero nEDM change our understanding of the universe?".

The universe that we live in exhibits a vast discrepancy between the amount of matter and anti-matter it contains. It is thought that this "Baryon asymmetry" [5] happened in the evolution of the early universe. In 1967, Sakharov proposed three criteria that any baryon-generating interaction must satisfy to produce matter and anti-matter at different rates. These criteria are Baryon number violation, *Charge-Parity* (CP) symmetry and *Charge* (C) symmetry violations, and the need for interactions to occur out of thermal equilibrium. A CP transformation translates matter into anti-matter and vice versa. Although there is some experimental evidence for CP violation [6, 7, 8], there is not enough to explain the observed Baryon asymmetry [9]. So, new sources of CP violation are required to explaine the observed Baryon asymmetry. Permanent EDMs of particles or nuclei, if they exist could provide the missing link [10].

P and T (*Time Reversal*) violations can happen for a particle with electric dipole moment $\boldsymbol{d}$ and magnetic moment $\boldsymbol{\mu}$ provided its ground state is not degenerate under P and T transformation. Under a P transformation (inversion of coordinates) the direction of $\boldsymbol{\mu}$ does not change but the charge distribution of the particle, and consequently the orientation of $\boldsymbol{d}$, does. This results in different energy levels for the particle in the presence of magnetic

Physical system	Laboratories location	Experimental limit (e·cm)	Predicted value (e·cm)
Neutron	ILL-Sussex-RAL	$|d_n| < 2.9 \times 10^{-26}$ [14]	10^{-31} [22]
Electron	ACME Collaboration	$|d_e| < 8.7 \times 10^{-29}$ [12]	10^{-40} [23]
Heavy Atom ^{199}Hg	Univ. of Washington	$|d_{Hg}| < 7.4 \times 10^{-30}$ [17]	10^{-33} [24]

Table 1.1: A few experimental limits for EDMs. The predicted values are based on the SM and are much smaller than the predictions of theories beyond the SM. For example left-right symmetric, multi-Higgs or supersymmetry models predict nEDMs at the level 10^{-26} - 10^{-28} e·cm [25, 26, 27].

and electric fields and thus implies P violation. Additionally, under a T transformation, the direction of $\boldsymbol{\mu}$ changes while that of $\boldsymbol{d}$ does not. This implies violation of T symmetry [11, 10]. Particle physicists are especially interested in T violations because if the laws of physics are invariant under combined symmetry operations of C, P and T (CPT transformation) then T violation is equivalent to CP violation and could shed light on the Baryon asymmetry in the universe.

1.1 Electric Dipole Moment of the Neutron

EDM experiments in laboratories around the world use different techniques and physical systems in an effort to search for direct evidence of T violation. Examples of physical systems that are studied include charged particles (such as the electron [12]), neutral particles (such as the neutron [13, 14, 4]), atoms with unpaired electrons (such as cesium [15] and thallium [16]), heavy atoms (such as ^{199}Hg [17]; ^{223}Rn; ^{225}Ra [18, 19]; ^{129}Xe [20]) and heavy molecules with unpaired electrons (such as YbF [21]). The current sensitivity of a few of these experiments to an EDM are listed in Table (1.1).

The EDM experiment that is most directly relevant to this thesis is that of the neutron.[1] A proposed nEDM experiment [28] using ultra-cold neutrons and ^{3}He is planned to run at Oak Ridge National Laboratory in 2023. It is supposed to reduce the current experimental limit for the nEDM by two orders of magnitude [29]. The use of ^{3}He in this experiment is fundamental to the anticipated improvement. It will be used as a spin analyser to detect and measure the phase of precessing neutrons. And it will be used as a reference or co-magnetometer to keep track of or monitor fluctuations in the static magnetic field.

The Hamiltonian for a polarized neutron with magnetic moment $\boldsymbol{\mu}_n = \gamma_n \boldsymbol{S}$, where

---

[1]Currently four main research groups are working on searches for the neutron EDM. They are located at TRIUMF in Canada, Oak Ridge National Laboratory in the USA, the Paul Scherrer Institute in Switzerland and a collaboration between the Institut Laue-Langevin in France and Sussex University and Rutherford Appleton Laboratory in the UK.

γ_n is its gyromagnetic ratio and $\boldsymbol{S}$ is the spin vector, and electric dipole moment $\boldsymbol{d}_\mathrm{n}$ in an external magnetic field $\mathbf{B}_0$ and electric field $\mathbf{E}$ is

$$H = -\boldsymbol{\mu}_\mathrm{n} \cdot \mathbf{B}_0 - \boldsymbol{d}_\mathrm{n} \cdot \mathbf{E}. \tag{1.1}$$

The only quantum number associated with the neutron to describe the neutron energy states is its spin. So, it is anticipated that $\boldsymbol{d}_n$ must be aligned with the spin direction (parallel or anti-parallel). The angular Larmor precession frequencies of the neutron $(\omega_\pm)$ in the combined fields, when $\mathbf{E}$ is parallel $(+)$ or anti-parallel $(-)$ to $\mathbf{B}$, are

$$\omega_\pm = \gamma_\mathrm{n} \mathrm{B}_0 \pm \frac{2\,d_\mathrm{n}\mathrm{E}}{\hbar}. \tag{1.2}$$

The experimental quantity that will be measured in the proposed nEDM experiment is the angular precession frequency of the neutron relative to that of the ^{3}He. This quantity is given by:

$$
\begin{aligned}
\omega_{rel\pm} &= \omega_\pm - \omega_3 \tag{1.3}\\
&= (\gamma_n - \gamma_3)\mathrm{B}_0 \pm \frac{2d_\mathrm{n}\mathrm{E}}{\hbar} \tag{1.4}
\end{aligned}
$$

where ω_3 is the angular Larmor frequency of the ^{3}He nucleus. Importantly, the ^{3}He nucleus is very well shielded by the closed s-shell configuration of the atoms' electrons, and so it is insensitive to changes in the electric field. The gyromagnetic ratios of the neutron [30] and the ^{3}He nucleus [31] are:

$$
\begin{aligned}
\gamma_\mathrm{n} &= -1.83247172 \times 10^8 \ (\mathrm{rad \cdot s^{-1} \cdot T^{-1}}) \tag{1.5}\\
\gamma_3 &= -2.03789410 \times 10^8 \ (\mathrm{rad \cdot s^{-1} \cdot T^{-1}}) \tag{1.6}
\end{aligned}
$$

from which it can be seen that the gyromagnetic ratio of ^{3}He is 11% larger in magnitude than that of the neutron:

$$\gamma_3 \simeq 1.11\gamma_n. \tag{1.7}$$

If ω_{rel} is measured in two configurations ($\mathbf{E}$ parallel/anti-parallel to $\mathbf{B}$), d_n can be inferred from the difference in measured precession frequencies $\omega_{rel\pm}$,

$$|\omega_{rel+} - \omega_{rel-}| = \frac{4d_\mathrm{n}\mathrm{E}}{\hbar}. \tag{1.8}$$

However, if B_0 changes in Eq. 1.4, it would give rise to an apparent EDM. For example, if B_0 changed by 1 pT between measurements of $\omega_{rel\pm}$ then the relative precession frequency of the neutron and the ^{3}He nucleus changes by 10 nHz. This seemingly small change is much larger than 0.7 nHz, the change in relative preccesion frequency one would expect if $d_\mathrm{n} \sim 10^{-30}$ e·cm and an electric field of 74 kV/cm [32, 33] was applied to the neutron-

[3]He mixture. In an ideal world one could eliminate sensitivity to static magnetic field fluctuations by measuring the precession frequency of the neutron relative to a particle with precisely the same gyromagnetic ratio. But, no such particle exists. Another solution is to modify the gyromagnetic ratios of the neutron and the [3]He nucleus so that they precess about the static field at effective precession frequencies, and arrange to make these two effective frequencies equal to one another. The process of modifying the effective or apparent gyromagnetic ratios of these systems is known as spin dressing. And the process of making the two gyromagnetic ratios equal is known as critical spin dressing (CSD).

1.2 Spin Dressing

The idea of modifying the gyromagnetic ratio of a spin system by applying time-dependant magnetic fields might seem strange but the idea is well-established and dates to work done in the 1960s by C. Cohen-Tannoudji and S. Haroche [34]. When a spin-1/2 particle simultaneously interacts with a weak static magnetic field and a strong but off-resonant oscillating magnetic field, which is called the dressing field, then it precesses about the static field at a time-averaged rate that is different than the Larmor precession frequency. It is this time-averaged precession frequency that is meant when one talks about a modified, apparent, or dressed precession frequency. This situation can be viewed as if the particle has a modified or apparent gyromagnetic ratio. It is thus common to refer to the particle as a dressed particle. One can certainly apply a dressing field to two spin species simultaneously, and in principle it should be possible to tune the modified gyromagnetic ratios of the two to be equal. This special condition is referred to as a CSD condition.

A number of spin dressing experiments directly relevant to the proposed search for an electric dipole of the neutron have been performed. These include observations of dressed neutron [35] and dressed [3]He [36, 37, 38] precession. Moreover, a number of theoretical studies examining the possibility and potential of CSD have been undertaken [28, 39]. However, to date there has never been a direct experimental test of CSD. Motivated by this, I have developed an apparatus and techniques that can be used to observe and explore CSD. Rather than using ultra-cold neutrons and [3]He as required for an nEDM search I have chosen to work with liquid mixtures containing hydrogen (^{1}H) and fluorine (^{19}F) nuclei. The advantage is that the necessary samples are commercially available, inexpensive and easy to incorporate into the CSD experiment. The gyromagnetic ratios of these nuclei [40, 41, 42] are

$$\gamma_{\mathrm{H}} = 2.67513 \times 10^8 \ (\mathrm{rad \cdot s^{-1} \cdot T^{-1}}) \tag{1.9}$$

$$\gamma_{\mathrm{F}} = 2.51662 \times 10^8 \ (\mathrm{rad \cdot s^{-1} \cdot T^{-1}}) \tag{1.10}$$

and the ratio of the two is not all that different from the ratio γ_3/γ_n; that is

$$\gamma_H \simeq 1.063\gamma_F. \tag{1.11}$$

1.3 Thesis Overview

This thesis is organized as follows. The theory of spin dressing and the CSD phenomenon are introduced and described in Chapter 2. The perspective I take is that of a classical model of spin precession to describe the evolution of a macroscopic nuclear magnetization subjected to a weak static magnetic field and strong off-resonant oscillating magnetic field. This model yields the average precession rate for an ensemble of dressed particles. I also review the quantum model for the energy levels of a dressed particle which yields a modified gyromagnetic ratio. The predictions of the two models are compared in different dressing regimes.

In Chapter 3, I discuss some of the practical aspects and challenges of performing nuclear magnetic resonance (NMR) experiments in μT-scale magnetic fields. I will refer to these as ultra-low magnetic fields (ULF). In this chapter, I describe a relatively new solid state magnetometer known as a magneto-impedance (MI) sensor. I have used MI sensors extensively in my work and report their first-ever application to NMR. Details of the apparatus and data used to validate the use of MI sensors in ULF NMR experiments are presented.

In Chapter 4, I describe simple spin dressing experiments performed on hydrogen nuclei in water. These experiments were performed using a slightly modified version of the apparatus described in Chapter 3. One of the interesting features of this work is that I am able to explore spin dressing phenomena over a much wider range of parameter space than any previous experiment. Another is that during the course of my investigations I observed the unexpected generation of spin echoes in response to far off-resonant oscillating magnetic fields. Chapter 4 also describes a classical model of spin precession that is used to assess this echo formation phenomenon.

In Chapter 5, I describe a more versatile apparatus that enabled me to perform ULF NMR on a broader range of spin species, rather than being forced to work solely with ^{1}H nuclei in water. The capability of this apparatus for detecting ULF NMR signals from one and two spin species under different experimental conditions is discussed. The remainder of the chapter is devoted to a description of the development of a composite tipping pulse for two spin species. This composite pulse nominally produces a perfect $\pi/2$ rotation for ^{1}H and ^{19}F nuclear spins. Its purpose is to prepare a clean initial condition for a CSD experiment, in which the ^{1}H and ^{19}F nuclear magnetizations are both in the transverse

plane of the Bloch sphere (perpendicular to the static magnetic field).

In Chapter 6, I describe a series of CSD experiments performed on ^{1}H and ^{19}F. These experiments include what I describe as conventional dressing field waveforms (in the sense that their application has been anticipated) and unconventional waveforms. The latter may offer certain advantages in potential applications to a nEDM search. To the best of my knowledge the work described in Chapter 6 represents the first-ever observation of critical spin dressing.

Finally, in Chapter 7, I conclude with a short summary highlighting and assessing the major accomplishments of my work.

Chapter 2

Spin Dressing

The idea and principles of Spin Dressing were developed by C. Cohen-Tannoudji and S. Haroche [34] during the 1960s and 1970s. They showed that the effective gyromagnetic ratio of a particle in a weak static magnetic field can be modified when it is subjected to a strong off-resonant oscillating magnetic field. In some experiments this interacting (atom-photon) system is referred to as a "strongly driven" system [43]. Spin dressing has been employed for a variety of applications including tuning interactions in ultra-cold gases [44], quantum information processing [45] and protecting spin states from decoherence [46]. Moreover, it has been proposed as a valuable tool for facilitating a new search for the permanent electric dipole moment of neutron [28].

In the first part of this chapter I summarize the theory of spin dressing (SD) using semi-classical and quantum models of nuclear spin precession. These models are then used throughout the thesis to simulate the average precession rates for ensembles of nuclear spins that interact with two magnetic fields simultaneously: a weak static field and an intense off-resonant oscillating field called a dressing field. I will show how time-average precession rates are modified by applying the dressing field. I will also show that the predictions of simple simulations based on the two models are consistent when Larmor precession frequencies are lower than the frequency of the applied dressing field. This is no longer true when Larmor precession frequencies are higher than the frequency of the dressing field and the amplitude of the static and the dressing fields are approximately equal. Under these conditions the simple data analysis method that I used to extract time-average precession rates from the semi-classical model of spin precession fails. One must either improve the data analysis method I employed or rely on the predictions of the quantum model.

In the second part of the chapter I describe the phenomenon of critical spin dressing (CSD), which plays a central role in my thesis. I describe the parameters that influence CSD using both the semi-classical and quantum models. The various simulation results presented here are then experimentally evaluated in the 4th and 6th chapters.

2.1 Semi-Classical Model

A particle with spin angular momentum $\mathbf{S}$ has a magnetic moment

$$\boldsymbol{\mu} = \gamma \mathbf{S} \tag{2.1}$$

where γ is its gyromagnetic ratio. According to the classical theory of electromagnetism, in the presence of an arbitrary magnetic field $\mathbf{B}$ the particle experiences a torque $\boldsymbol{\mu} \times \mathbf{B}(t)$, and so the equation of motion for the angular momentum is given by:

$$\frac{d\mathbf{S}}{dt} = \boldsymbol{\mu} \times \mathbf{B}(t). \tag{2.2}$$

This expression describes the equation of motion for a fundamentally quantum mechanical entity, but by summing over all magnetic moments in an ensemble of spins we can derive the equation of motion for a macroscopic system. For an ensemble of N particles with magnetic moment $\boldsymbol{\mu}$, the net magnetic moment per unit volume V is

$$\mathbf{M} = \frac{1}{V} \sum_{i=1}^{N} \boldsymbol{\mu}_i \tag{2.3}$$

where $\mathbf{M}$ is called the magnetization. The equation of motion for $\mathbf{M}$ is given by:

$$\frac{d\mathbf{M}}{dt} = \gamma \mathbf{M} \times \mathbf{B}(t). \tag{2.4}$$

For a static magnetic field $\mathbf{B}_0 = B_0\,\hat{z}$ and a linearly-polarized oscillating field $\mathbf{B}_d = B_d\cos(\omega_d t)\hat{x}$ (i.e. a dressing field) the classical equation of motion for the components of $\mathbf{M}$ are

$$
\begin{aligned}
\frac{dM_x}{dt} &= \gamma M_y B_0 \\
\frac{dM_y}{dt} &= \gamma M_z B_d \cos(\omega_d t) - \gamma M_x B_0 \\
\frac{dM_z}{dt} &= -\gamma M_y B_d \cos(\omega_d t)
\end{aligned}
\tag{2.5}
$$

where $\omega_d = 2\pi f_d$ is the angular dressing frequency, which can be smaller or larger than the angular Larmor frequency $\omega_L = \gamma B_0$. Note that these are simply the Bloch equations in the absence of relaxation processes [47]. These differential equations can be integrated numerically given initial conditions for $\mathbf{M}$. I have performed such calculations throughout this thesis using code written in the Python programming language. At the core of this calculation I use the *integrate.odeint* module from the *Scipy* library (an open source library of scientific tools) to obtain $M_x(t)$, $M_y(t)$ and $M_z(t)$. This module in turn uses LSODA from the FORTRAN library *odepack*.

Equations 2.5 show that the dynamics or time-evolution of $\mathbf{M}$ depends on the values
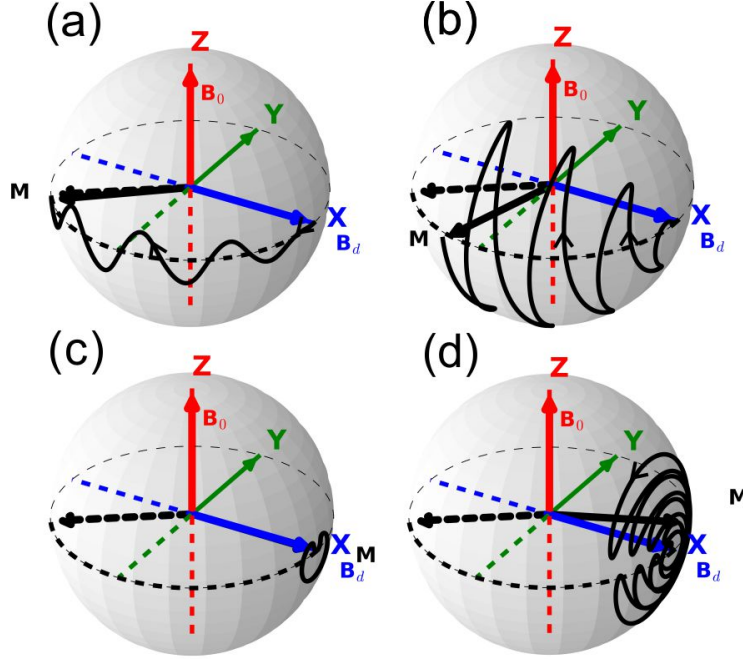
Figure 2.1: Simulated semi-classical trajectories of dressed (solid line) and undressed (dashed line) macroscopic magnetizations $\mathbf{M}$, for an ensemble of hydrogen nuclei on the surface of the Bloch sphere. The parameter y is fixed at 0.1 while the parameter x is set to (a) 0.2; (b) 1.0; (c) 2.4 and (d) 3.0 in the various panels. The average precession rate of the dressed spin system can be positive (a-b), zero (c) and even negative (d) but it is always smaller than the precession rate of the undressed spins. Simulation results were obtained using $f_{\mathrm{L}} = 100$ Hz and $f_{\mathrm{d}} = 1$ kHz, and the trajectories are shown for a 4 ms evolution period. $\mathbf{M}$ was initially directed along the positive x-axis.

of three experimental parameters: B_0, B_{d} and ω_{d}. A useful way of parameterizing different regimes of behaviour is to introduce dimensionless parameters x and y defined such that

$$x = \frac{\gamma B_{\mathrm{d}}}{\omega_{\mathrm{d}}}, \; y = \frac{\gamma B_0}{\omega_{\mathrm{d}}}. \tag{2.6}$$

In other words, these dressing parameters characterize the intensity of the dressing field (x) and the static field (y) in angular frequency units normalized to the applied dressing field frequency. Wherever in this chapter I talk about calculations performed using specific values of these dressing parameters, or any other parameter that involves the gyromagnetic ratio γ, I obtained those results using the gyromagnetic ratio of ^{1}H.

The numerical solution of Eq. 2.5 shows that for non-zero values of x, the time-average rate at which $\mathbf{M}$ precesses about $\mathbf{B}_0$ implies an effective gyromagnetic ratio that is different than that of the undressed spins. The dressed precession frequency $\bar{f}_{\mathrm{L}}$ can be lower or higher than $|f_{\mathrm{L}}|$ depending on the value of y. When $y < 1$, $|\bar{f}_{\mathrm{L}}|$ is always less than $|f_{\mathrm{L}}|$ but when $y > 1$, $|\bar{f}_{\mathrm{L}}|$ is usually higher than $|f_{\mathrm{L}}|$. Examples of classical trajectories for $\mathbf{M}$ in the regimes $y < 1$ and $y > 1$ are shown in Figs. 2.1 and 2.2, respectively. These trajectories
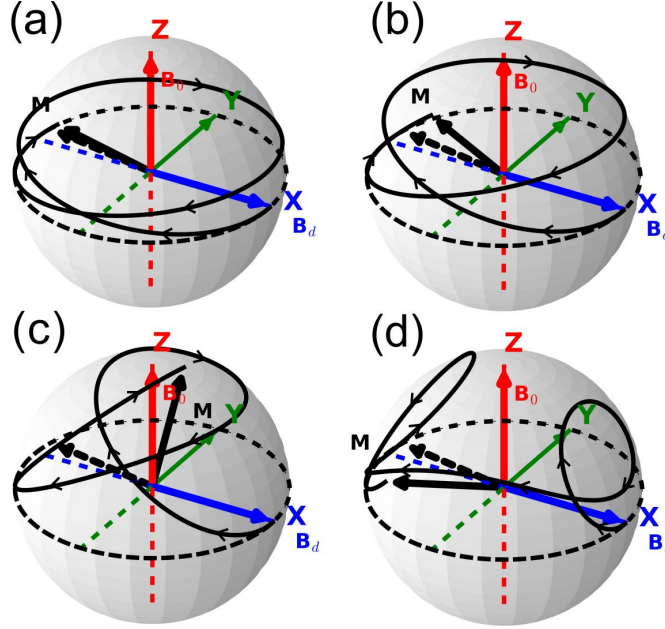
Figure 2.2: Simulated semi-classical trajectories of dressed (solid line) and undressed (dashed line) macroscopic magnetizations $\mathbf{M}$, for an ensemble of hydrogen nuclei, on the surface of the Bloch sphere. The parameter y is fixed at 3.0 while the parameter x is set to (a) 0.5; (b) 1.0; (c) 2.4 and (d) 6.0 in the various panels. In most cases (a, b, c) the average precession rate $\bar{f}_{\mathrm{L}}$ of the dressed spins is positive and larger than that of the undressed spins. The exception is case (d) for which $\bar{f}_{\mathrm{L}} < f_{\mathrm{L}}$. Simulation results were obtained using $f_{\mathrm{L}} = 3$ kHz and $f_{\mathrm{d}} = 1$ kHz, and trajectories are shown for a 0.5 ms evolution period. $\mathbf{M}$ was initially directed along the positive x-axis.

are plotted as curves on the surface of the Bloch sphere, and represent the path followed by the tip of the vector $\mathbf{M}(t)$ starting from the initial condition $\mathbf{M}|_{t=0} = \mathrm{M}\,\hat{x}$.

When $y < 1$ the dressing field periodically drives $\mathbf{M}$ away from the equatorial plane. This results in $|\bar{f}_{\mathrm{L}}| < |f_{\mathrm{L}}|$ as shown in Fig. 2.1. At some specific values of x (for example at $x = 2.4$), $\bar{f}_{\mathrm{L}}$ is identically zero and $\mathbf{M}$ follows a closed quasi-circular path about a fixed axis in the transverse plane. This situation can be viewed as a case in which the modified gyromagnetic ratio is zero. At other values of x (for example at $x = 3.0$), the dressed spins precess in the opposite sense relative to the undressed spins. This situation can be viewed as one in which the modified gyromagnetic ratio is negative.

2.1.1   Calculation of the Average Precession Rate when $y < 1$

To calculate the average precession rate of the dressed spin system about $\mathrm{B}_0\,\hat{z}$ in the presence of a dressing field $\mathrm{B}_{\mathrm{d}}(\mathrm{t})\,\hat{x}$, I plotted the Cartesian components of $\mathbf{M}(\mathrm{t})$ as a function of time then fit a sinusoidal function to the x-component (parallel to the dressing field). I will explain why the x-component of $\mathbf{M}$ is chosen. Three fit parameters, amplitude, fre-
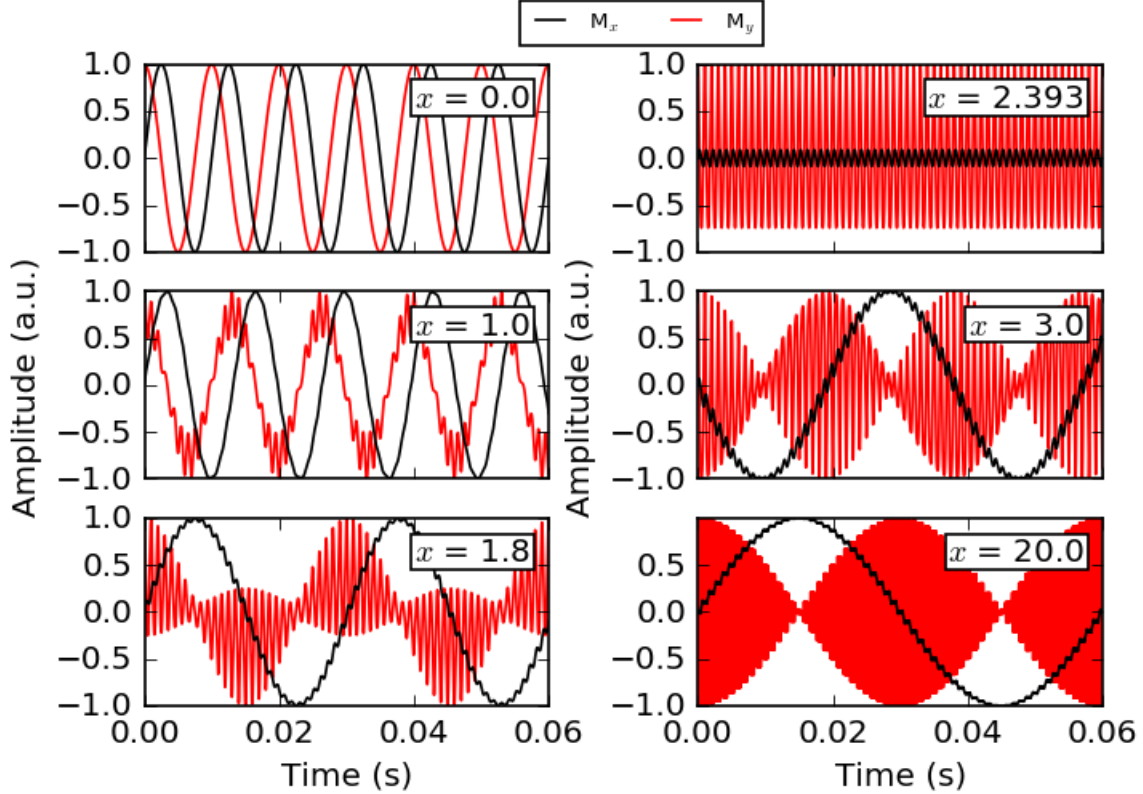
Figure 2.3: Simulation of $M_x(t)$ and $M_y(t)$ in the presence of a static field B_0 $\hat{z}$ and a dressing field $B_d \cos(\omega_d t)$ $\hat{x}$ for $y = 0.1$ ($f_L = 100$ Hz, $f_d = 1$ kHz). $\mathbf{M}$ was initially directed along the positive y-axis. In each case results are shown for 60 ms. The sign of the modified gyromagnetic ratio can be inferred from the phase of $M_x(t)$: $\gamma' > 0$ at $x = 0.0, 1.0, 1.8$, and 20; $\gamma' < 0$ at $x = 3.0$; $\gamma' = 0$ at $x = 2.393$.

quency and phase, were employed. However, an upper (1.1 M) and a lower limit (0.8 M) were applied to the amplitude of the fit function. The fit window was fixed for all of the calculations except when the period of the oscillation became very long. For this case the fit window is increased so that a single period of the oscillation appears in the fit window.

Figure 2.3 shows simulation results obtained by integrating Eq. 2.5 to obtain $M_x(t)$ and $M_y(t)$ with a Larmor frequency of $f_L = 100$ Hz and $f_d = 1$ kHz. Also, the boundary condition $\mathbf{M}|_{t=0} = \mathrm{M}\,\hat{y}$ was applied. This specific boundary condition let me extract the sign of the modified gyromagnetic ratio from the initial phase of M_x. Both M_x and M_y oscillate at an average precession rate $\bar{f}_L$ combined with the dressing frequency f_d. The x and y components exhibit small and large amplitude oscillations at the dressing frequency f_d, respectively. These oscillations have little effect on the dynamics of the x component and hence I chose $M_x(t)$ to fit because it shows a simple waveform. As the value of x is increased, the value of $\bar{f}_L$ inferred from these simulations also changes, mirroring the anticipated modification of the gyromagnetic ratio. In Fig. 2.3, at $x = 2.393$, $\mathbf{M}$ does not
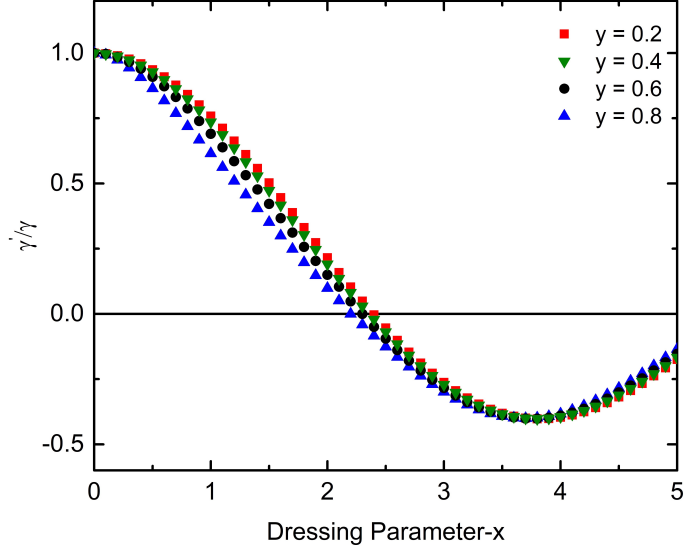
Figure 2.4: Summary of modified or apparent gyromagnetic ratio γ' extracted from simulations such as those shown in Fig. 2.3. The results have been normalized to γ, and are shown for $y = 0.2$ (■); $y = 0.4$ (▼); $y = 0.6$ (●); $y = 0.8$ (▲). Calculations were performed using the semi-classical model of spin precession for ^{1}H nuclei with $f_L = 100$ Hz and $f_d = 1$ kHz.

show a clear low frequency oscillation. This means $\mathbf{M}$ does not precess about the static field implying that the modified gyromagnetic ratio $\gamma' = 0$. A situation similar to this case is illustrated in Fig. 2.1-c.[1] At $x = 3.0$ the initial phase of $M_x(t)$ is changed from 0 to π as one would expect for counter-clockwise rather than clockwise precession implying γ' is negative rather than positive. The situation similar to this case is pictured in Fig. 2.1-d. Except for the case where $x = 0$, which corresponds to no dressing field, the full trajectory of $\mathbf{M}$ clearly involves motions at higher frequencies. This structure has only a very minor influence on the inferred time-average precession behaviour of $\mathbf{M}$ except for at $y \simeq 1$ where the amplitude of the ripples is larger and the simple sinusoidal approximation is not reasonable. After extracting $\bar{f}_L$ from fits to $M_x(t)$ I obtained the modified or apparent gyromagnetic ratio γ' by assuming $\gamma'/\gamma = \bar{f}_L/f_L$, being careful to account for the sense of the precession in order to obtain the correct sign.

Figure 2.4 summarizes the apparent gyromagnetic ratio γ' extracted from these simulations as a function of x. These results reveal $|\gamma'| < \gamma$ for $y < 1$. The various curves shown in Fig. 2.4 (corresponding to different values of y), are distinct when x is small but become hard to distinguish from one another when x is large. In Chapter 4, I will show that my spin dressing experiment can resolve differences between curves for γ' at small x when y is varied, in the regime $y < 1$.

---

[1]Note that in Figs. 2.1 and 2.2 $\mathbf{M}$ is initially directed along the x-axis instead of the y-axis. This is simply for better graphical clarity.

2.1.2 Calculation of the Average Precession Rate when $y > 1$
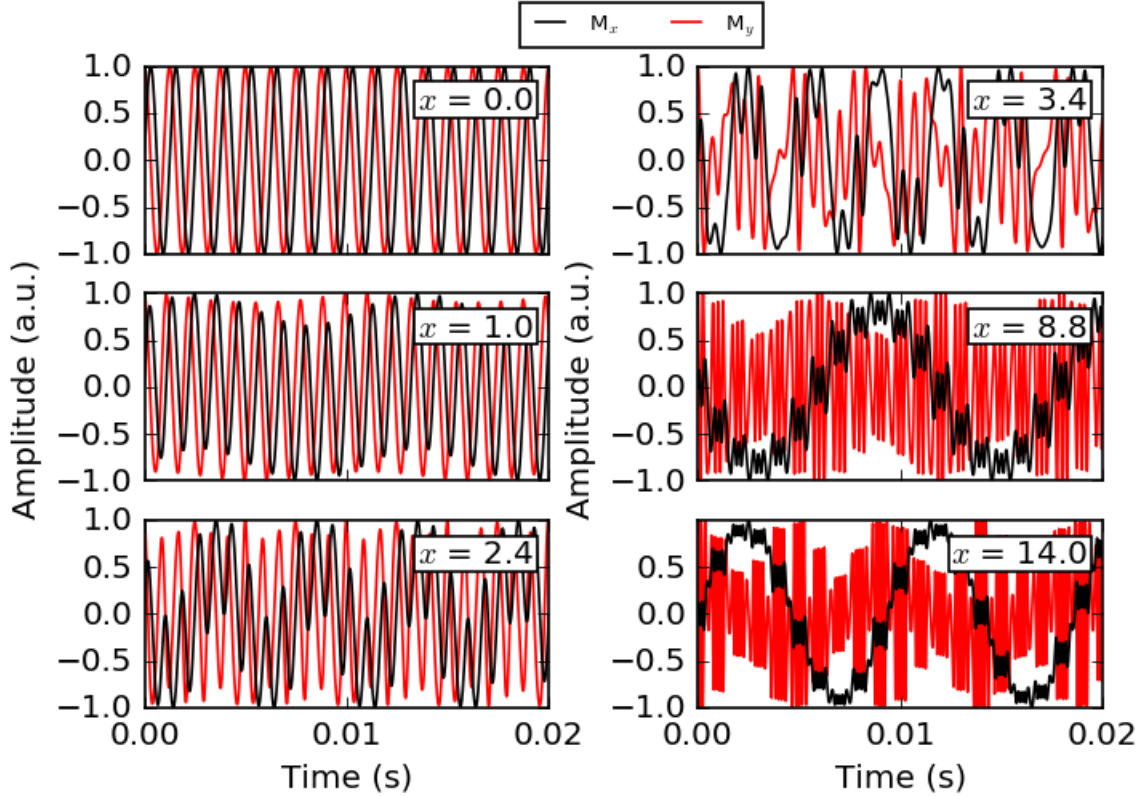
Figure 2.5: Simulation of $M_x(t)$ and $M_y(t)$ in the presence of a static field $B_0 \ \hat{z}$ and dressing field $B_d \cos(\omega_d t) \ \hat{x}$, for $y = 1.60$. $\mathbf{M}$ was initially directed along the positive y-axis.

Figure 2.5 shows numerical solutions of Eq. 2.5 for $M_x(t)$ and $M_y(t)$ based on the semi-classical model of spin precession. These results were obtained for a dressing parameter $y = 1.6$ corresponding to $f_d = 800$ Hz and $f_L = 500$ Hz for ^{1}H nuclei. At $x = 1.0$, 8.8 and 14.0, $M_x(t)$ appears to oscillate at a single frequency, but at $x = 2.4$ and 3.4 the dynamics of $\mathbf{M}$ are complex and it is not immediately obvious what the time-average precession looks like. This illustrates that in the regime $y > 1$ the simple method that I have used to extract $\bar{f}_L$, from the semi-classical results for $\mathbf{M}(t)$, does not work perfectly for all values of x.

Figure 2.6 shows results for normalized values of γ' extracted from simulations with $y > 1$. As above, γ' is obtained simply by fitting a sinusoidal function to $M_x(t)$ and thereby extracting $\bar{f}_L$. Also shown in this plot, as a simple measure of the quality of these fits, is the adjusted coefficient of determination (adjusted R-squared), which is equal to 1 for a perfect fit. At high values of y the simple parameter extraction process works for a broad range of x, while for $y < 2$ it is limited to small values of x. For example, at $y = 8$ it is possible to continuously track γ' up to $x \simeq 7$ while for $y = 1.28$ this is only possible up to $x \simeq 1$. As a crude figure of merit, when $x \simeq y$ the simplistic parameter extraction

13
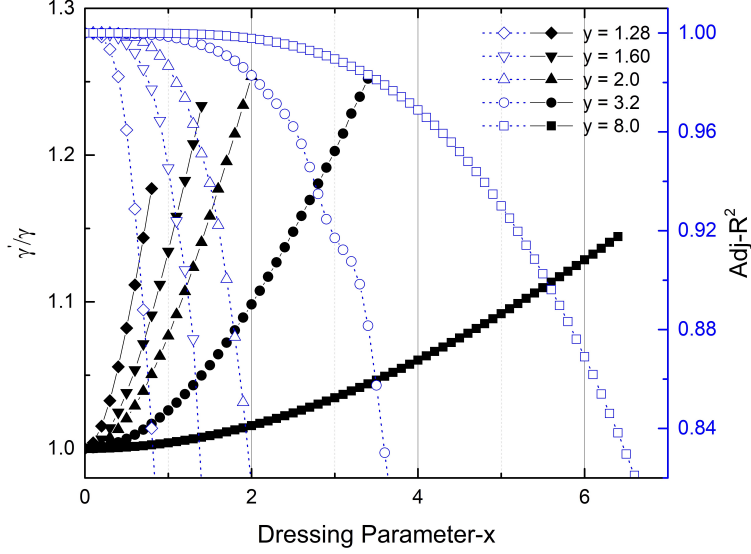
Figure 2.6: Summary of modified or apparent gyromagnetic ratio γ' extracted from simulations such as those shown in Fig. 2.5. The results (filled markers) have been normalized to γ, as indicated by the scale displayed on the left vertical axis, and are shown for $y > 1$, $f_{\mathrm{d}} = 500$ Hz and $f_{\mathrm{L}} = y f_{\mathrm{d}}$. Also shown is the adjusted coefficient of determination Adj-R^2 (unfilled markers), with the corresponding scale displayed on the right vertical axis, obtained when a simple sinusoidal function $A \sin(2\pi \bar{f}_{\mathrm{L}} t + \phi)$ is fit to $M_{\mathrm{x}}(t)$ to extract an estimate of $\bar{f}_{\mathrm{L}}$, where the amplitude of A is bounded to the range $0.8M < A < 1.2M$.

process fails because the magnitude of the static and time-dependent magnetic fields are equal and make similar contributions to the dynamics of **M**.

2.2 Quantum Model

I next briefly review the quantum approach to this problem, following the work of Cohen-Tannoudji [48] to describe the interaction of a spin-1/2 system with a weak static magnetic field and a dressing field. The energy levels of a quantum spin-1/2 system in the presence of a static magnetic field B_0 are split by:

$$\Delta E = 2\mu B_0 = \hbar \gamma B_0. \tag{2.7}$$

Let us consider a situation where a dressing field is applied to this system at angular frequency ω_{d} resulting in a modified gyromagnetic ratio γ'. In this case the separation of the levels can be written $\hbar \gamma' B_0$; or in terms of the dressing parameter $y = \gamma B_0/\omega_{\mathrm{d}}$, it is

$$\Delta E/\hbar \omega_{\mathrm{d}} = y \frac{\gamma'}{\gamma}. \tag{2.8}$$

So, if we know the energy levels we can determine the splitting and infer the modified gyromagnetic ratio.

The energy levels of a particle with magnetic moment $\boldsymbol{\mu}$ interacting with a static field $\mathbf{B}_0$ and an intense off-resonant radio-frequency (RF) field $\mathbf{B}_d$, can be obtained from the appropriate Hamiltonian [48]:

$$H = H_0 + H_{rf}. \tag{2.9}$$

Here H_0 represents the Hamiltonian for the particle in the static magnetic field and the photons with angular frequency ω_d associated with the dressing field. It is given by:

$$H_0 = -\boldsymbol{\mu} \cdot \mathbf{B}_0 + \hbar \omega_d a^\dagger a \tag{2.10}$$

where a and $a^\dagger$ are the photon creation and annihilation operators. The second term in Eq. 2.9, H_{rf}, represents the interaction between the particle and the RF field. If we consider an atom with spin angular momentum $\mathbf{S}$ in the presence of a static field B_0 aligned in the z-direction, the first term of Eq. 2.10 becomes $\gamma B_0 S_z$ or $\omega_L S_z$. The second term in Eq. 2.10 represents the number of photons with angular frequency ω_d and energy $\hbar \omega_d$. In terms of the Pauli matrix σ_z, Eq. 2.10 can be written

$$H_0 = -\frac{\hbar}{2} \omega_L \sigma_z + n \hbar \omega_d \tag{2.11}$$

where for reference the Pauli matrices are:

$$\sigma_x = \begin{pmatrix} 0 & 1 \\ 1 & 0 \end{pmatrix}, \ \sigma_y = \begin{pmatrix} 0 & -i \\ i & 0 \end{pmatrix}, \ \sigma_z = \begin{pmatrix} 1 & 0 \\ 0 & -1 \end{pmatrix}. \tag{2.12}$$

Note also for later reference that

$$\sigma_x = \frac{\sigma_+ + \sigma_-}{2} \tag{2.13}$$

where

$$\sigma_+ = \begin{pmatrix} 0 & 2 \\ 0 & 0 \end{pmatrix}, \ \sigma_- = \begin{pmatrix} 0 & 0 \\ 2 & 0 \end{pmatrix}. \tag{2.14}$$

The interaction term in Eq. 2.9 is given by $H_{rf} = \boldsymbol{\mu} \cdot \mathbf{B}_d$ where $\mathbf{B}_d = B_d \cos(\omega_d t) \hat{x}$. In the quantized theory of fields this becomes [49]:

$$\mathbf{B}_d = \frac{\beta}{\sqrt{k}} (a e^{ikx} + a^\dagger e^{-ikx}) \hat{x} \tag{2.15}$$

where β is a constant and k is the wave number. If the wavelength of the RF field is very much larger than the size of the particle, use of the dipole approximation ($kx \ll 1$) is justified and H_{rf} becomes

$$H_{rf} = -\lambda J_x (a + a^\dagger) \tag{2.16}$$

where λ is another constant that represents as the intensity of the dressing field and J_x is the angular momentum, which in the case of a spin-1/2 system would be $S_x = \hbar\sigma_x/2$. Using the fact that the quantum state describing the RF field is a coherent state [50], λ can be determined. A coherent state $|\alpha\rangle$ is the eigenstate of the annihilation operator a:

$$a|\alpha\rangle = \alpha|\alpha\rangle \tag{2.17}$$

where α satisfies

$$\langle\alpha|a^\dagger a|\alpha\rangle = n = \alpha^2 \tag{2.18}$$

and n is the average number of photons in the field. Thus $\alpha = 1/\sqrt{n}$. The expectation value for H_{rf} should be equal to its classical value $-\gamma J_x B_\mathrm{d}$ which results in

$$\langle\alpha|\lambda(a + a^\dagger)|\alpha\rangle = \gamma B_\mathrm{d} = \omega \tag{2.19}$$
$$2\lambda\alpha = \omega. \tag{2.20}$$

Thus the parameter λ can be determined: $\lambda = \omega/2\sqrt{n}$.

With these observations, the full Hamiltonian for the interacting atom-photon system is:

$$H = -\frac{\hbar}{2}\omega_\mathrm{L}\sigma_z + n\hbar\omega_\mathrm{d} - \frac{\hbar\omega}{4\sqrt{n}}\sigma_x(a + a^\dagger). \tag{2.21}$$

Alternatively, in terms of the dressing parameters $x = \frac{\omega}{\omega_\mathrm{d}}$ and $y = \frac{\omega_\mathrm{L}}{\omega_\mathrm{d}}$, it is

$$\frac{H}{\hbar\omega_\mathrm{d}} = -\frac{y\sigma_z}{2} + a^\dagger a - \frac{x}{4\sqrt{n}}\sigma_x(a + a^\dagger). \tag{2.22}$$

In the absence of the static field ($y = 0$), or for a very weak static field ($y \ll 1$), we can solve for the eigenstates of this Hamiltonian in the basis states $|n, \xi_\pm\rangle = |n\rangle|\xi_\pm\rangle$ where $|\xi_\pm\rangle$ represents the eigenstates of the Pauli matrix σ_x. This leads to:

$$\frac{H}{\hbar\omega_\mathrm{d}}|n, \xi_\pm\rangle = \left[\left(a^\dagger + \frac{\epsilon x}{4\sqrt{n}}\right)\left(a + \frac{\epsilon x}{4\sqrt{n}}\right) - \frac{x^2}{16n}\right]|n, \xi_\pm\rangle \tag{2.23}$$

where ϵ is the eigenvalue of σ_x. We can rewrite H in terms of the displacement operator D which is unitary and thus satisfies $DD^\dagger = D^\dagger D = 1$. A further property of D is that

$$D\left(\frac{\epsilon x}{4\sqrt{n}}\right) \; a \; D^\dagger\left(\frac{\epsilon x}{4\sqrt{n}}\right) = \left(a + \frac{\epsilon x}{2\sqrt{n}}\right) \tag{2.24}$$
$$D\left(\frac{\epsilon x}{4\sqrt{n}}\right) \; a^\dagger \; D^\dagger\left(\frac{\epsilon x}{4\sqrt{n}}\right) = \left(a^\dagger + \frac{\epsilon x}{2\sqrt{n}}\right). \tag{2.25}$$

The eigenstates of H can then be defined as

$$|n_\epsilon\rangle = D\left(\frac{\epsilon x}{4\sqrt{n}}\right)|n\rangle. \tag{2.26}$$

In the case where the static magnetic field is zero the eigenvalues of H are

$$\frac{H}{\hbar\omega_{\mathrm{d}}}|n_\epsilon,\xi_\pm\rangle = D\left(a^\dagger a - \frac{x^2}{16n}\right)D^\dagger |n_\epsilon,\xi_\pm\rangle \tag{2.27}$$

$$= D\left(a^\dagger a - \frac{x^2}{16n}\right)D^\dagger D |n,\xi_\pm\rangle \tag{2.28}$$

$$= D\left(n - \frac{x^2}{16n}\right)|n,\xi_\pm\rangle \tag{2.29}$$

$$= \left(n - \frac{x^2}{16n}\right)|n_\epsilon,\xi_\pm\rangle \tag{2.30}$$

$$\frac{E}{\hbar\omega_{\mathrm{d}}} = n - \frac{x^2}{16n}. \tag{2.31}$$

Eq. 2.31 represents the diagonal matrix elements of the Hamiltonian H. It also shows that irrespective of ϵ there is always two-fold degeneracy associated with states $|n_+,\xi_+\rangle$ and $|n_-,\xi_-\rangle$.[2] At this point if we add a weak static magnetic field to H as a perturbation, off diagonal elements that couple $|n_\pm\rangle$ together are generated and the degeneracy is removed,

$$H |n_\epsilon,\xi_\pm\rangle = \begin{pmatrix} n - \frac{x^2}{4n} & -\frac{y}{2}\langle n_+|n_-\rangle \\ -\frac{y}{2}\langle n_-|n_+\rangle & n - \frac{x^2}{4n} \end{pmatrix}\begin{pmatrix} |n_+,\xi_+\rangle \\ |n_-,\xi_-\rangle \end{pmatrix}. \tag{2.32}$$

The effect of this coupling on the energy levels, provided $n \gg 1$, is proportional to the zeroth-order Bessel function $J_0(x)$ [51].[3] That is, the energy levels of the system consisting of a spin in a weak magnetic field interacting with n photons becomes,

$$\frac{E}{\hbar\omega_{\mathrm{d}}} = n - \frac{x^2}{4n} \pm \frac{y}{2}J_0(x). \tag{2.33}$$

The influence of the static field appears in Eq. 2.33 as a perturbation that splits degenerate levels. The term responsible for this splitting can be rewritten in terms of a modified or apparent gyromagnetic ratio

$$\gamma' = \gamma J_0(x). \tag{2.34}$$

This equation reveals that the sign and the magnitude of γ' are influenced by the dressing parameter x, through the Bessel function $J_0(x)$. Figure 2.7 shows this function which is quasi-periodic and clearly changes sign as x varied. The zeroes of $J_0(x)$ represent conditions

---

[2]Note that $|n_\pm,\xi_\pm\rangle = D\left(\frac{\pm x}{4\sqrt{n}}\right)|n,\xi_\pm\rangle$.

[3]For $n \gg 1$: $\langle n_+|(n-q)_-\rangle = J_q(x)$.
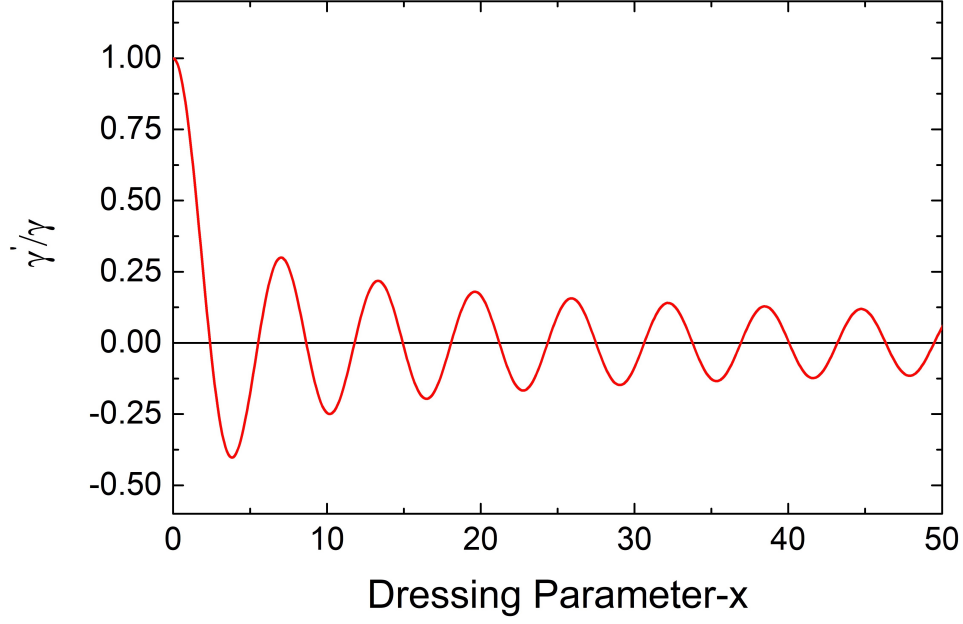
Figure 2.7: Zeroth-order Bessel function $J_0(x)$. In the limit $y \ll 1$ (weak static field), the normalized modified gyromagnetic ratio γ'/γ is equal to $J_0(x)$.

under which the modified gyromagnetic ratio is zero. The first 5 zeros of $J_0(x)$ occur at $x \simeq 2.40, 5.52, 8.65, 11.79$ and 14.93.

Equation 2.33 and the solution presented above are valid for weak static magnetic fields $(y \ll 1)$. In general we can calculate the energy levels of this system for any values of y if we know the matrix form of the Hamiltonian in terms of x and y. If we start from Eq. 2.22, the matrix form of the Hamiltonian in the basis $|n, \pm\rangle$ is

$$
\begin{pmatrix}
\vdots \\
|n-1, -\rangle \\
|n-1, +\rangle \\
|n, -\rangle \\
|n, +\rangle \\
|n+1, -\rangle \\
|n+1, +\rangle \\
\vdots
\end{pmatrix}
\tag{2.35}
$$

18

where $|\pm\rangle$ represents the eigenstates of σ_z. The diagonal elements of the Hamiltonian, associated with the non-interacting terms, are given by $n \mp \frac{y}{2}$ or

$$
\begin{pmatrix}
\ddots & & & & & & \\
 & n-1+\frac{y}{2} & 0 & 0 & 0 & 0 & 0 \\
 & 0 & n-1-\frac{y}{2} & 0 & 0 & 0 & 0 \\
 & 0 & 0 & n+\frac{y}{2} & 0 & 0 & 0 \\
 & 0 & 0 & 0 & n-\frac{y}{2} & 0 & 0 \\
 & 0 & 0 & 0 & 0 & n+1+\frac{y}{2} & 0 \\
 & 0 & 0 & 0 & 0 & 0 & n+1-\frac{y}{2} \\
 & & & & & & \ddots
\end{pmatrix}.
\tag{2.36}
$$

As before, the coupling terms in Eq. 2.22 produce off-diagonal elements in the Hamiltonian. These terms include the operators a, $a^\dagger$, σ_- and σ_+. The eigenvalue equations for these operators acting on the eigenstates $|n, \pm\rangle$ are given by:

$$
a\,|n,\pm\rangle = \sqrt{n}\,|n-1,\pm\rangle \tag{2.37}
$$
$$
a^\dagger\,|n,\pm\rangle = \sqrt{n+1}\,|n+1,\pm\rangle \tag{2.38}
$$
$$
\sigma_\pm\,|n,\pm\rangle = 2\,|n,\mp\rangle \tag{2.39}
$$

and so:

$$
\sigma_\pm a\,|n,\mp\rangle = 2\sqrt{n}\,|n-1,\pm\rangle \tag{2.40}
$$
$$
\sigma_\pm a^\dagger\,|n,\mp\rangle = 2\sqrt{n+1}\,|n+1,\pm\rangle. \tag{2.41}
$$

When the coupling term in Eq. 2.22 is included, the matrix 2.36, becomes

$$
H =
\begin{pmatrix}
\ddots & & & & & & \\
 & n-1+\frac{y}{2} & 0 & 0 & -\frac{x}{4} & 0 & 0 \\
 & 0 & n-1-\frac{y}{2} & -\frac{x}{4} & 0 & 0 & 0 \\
 & 0 & -\frac{x}{4} & n+\frac{y}{2} & 0 & 0 & -\frac{x}{4} \\
 & -\frac{x}{4} & 0 & 0 & n-\frac{y}{2} & -\frac{x}{4} & 0 \\
 & 0 & 0 & 0 & -\frac{x}{4} & n+1+\frac{y}{2} & 0 \\
 & 0 & 0 & -\frac{x}{4} & 0 & 0 & n+1-\frac{y}{2} \\
 & & & & & & \ddots
\end{pmatrix}.
\tag{2.42}
$$

From the eigenvalues of this matrix, the energy levels of the full quantum system can be calculated for arbitrary fields. In the discussion that follows I show how numerical solutions for these eigenvalues are obtained for different dressing parameters x and y.

My solution for the eigenvalues of the infinite Hamiltonian matrix 2.42 were gener-
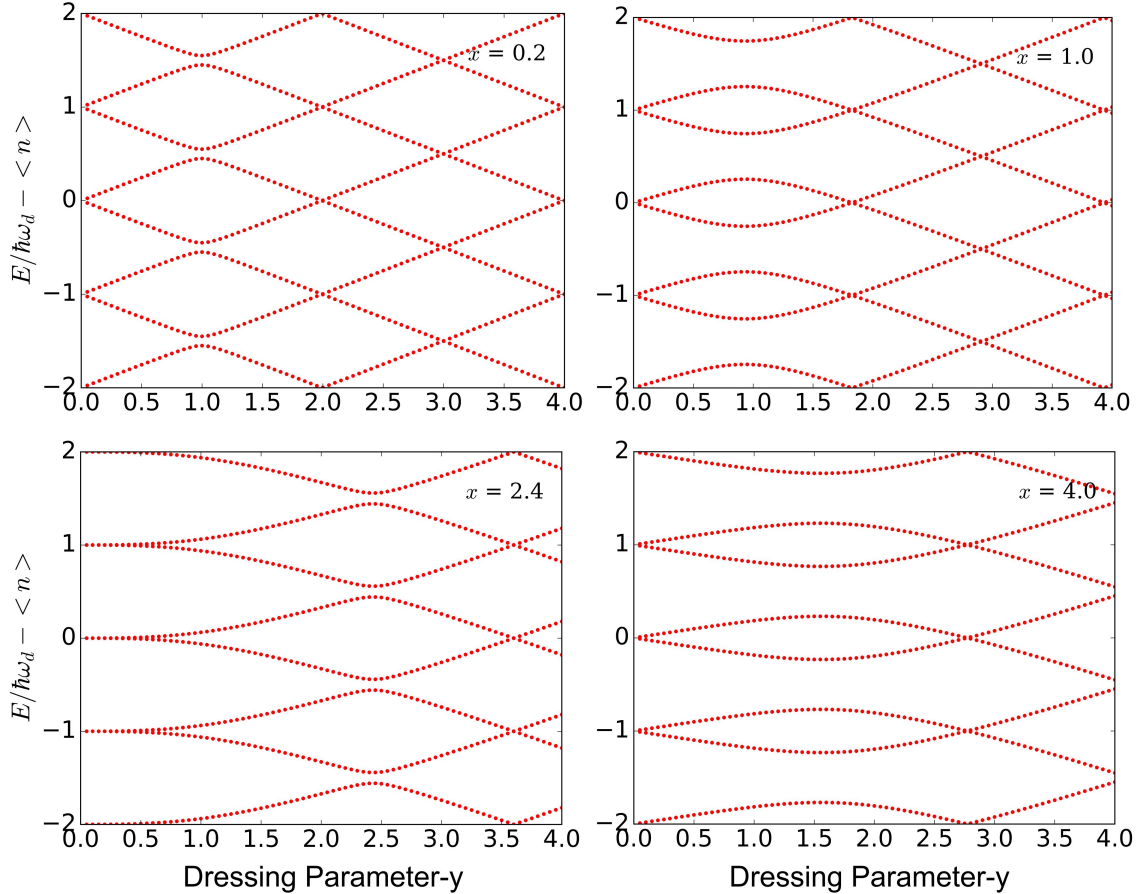
Figure 2.8: Energy levels for the interacting atom-photon system. The static field is B_0 $\hat{z}$ and the dressing field is $B_d \cos(\omega_d t)$ $\hat{x}$. In each plot the parameter x is fixed and y is varied. Avoided crossings are introduced as the amplitude B_d (and hence x) is increased. At $x = 2.4$, corresponding to the first zero of the Bessel function $J_0(x)$, and for $y \ll 1$ the energies of spin up/down states are degenerate. This situation corresponds to the case where the modified gyromagnetic ratio γ' is zero.

ated by first truncating the size of the problem to 300 basis vectors. I then used the *linalg.eigvals* module of the open source *Scipy* library to calculate the eigenvalues of the resulting 300×300 Hamiltonian matrix.

Figure 2.8 shows examples of the energy levels calculated in this manner, for a range of dressing parameters x and y. In each plot, x is fixed and y is varied. When both of the dressing parameters are zero, corresponding to the absence of any magnetic fields, the system has two-fold degeneracy as one would expect for spin up and down states. This degeneracy is split by applying the static field ($y > 0$). When the dressing field is also turned on (i.e. $x > 0$), avoided crossings of the energy levels are introduced. For fixed values of x these avoided-crossings only occur at small values of y. When the static field is increased the levels start to cross again. Under very specific conditions, such as in the vicin-
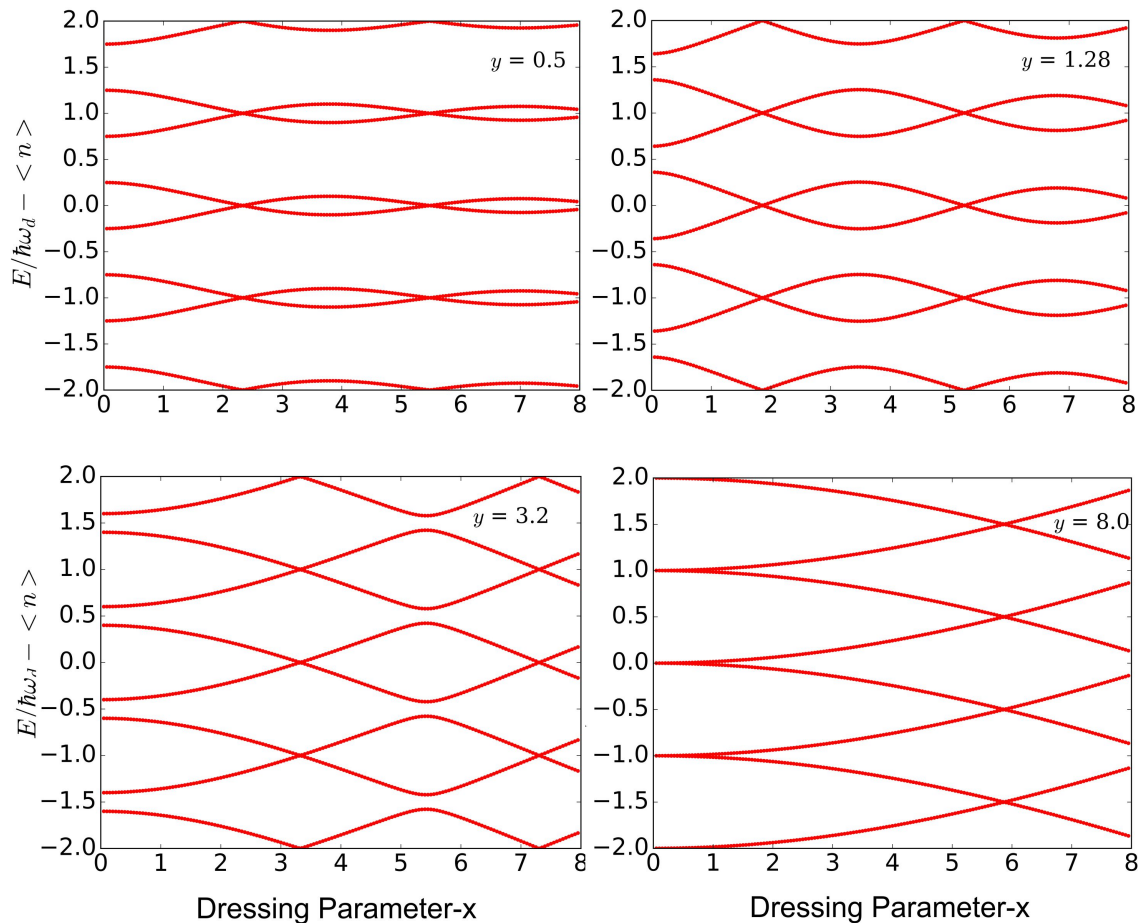
Figure 2.9: Simulated energy levels of the atom-photon system interacting with the static field $B_0\hat{z}$ and the dressing field $B_d\cos(\omega_d t)\ \hat{x}$. In each plot y is fixed and x is varied.

ity of $x = 2.4$ (corresponding to the first zero of $J_0(x)$, the system again shows evidence for degeneracy for small values of y (eventually, as y is increased, this degeneracy disappears). This begs the question why should degeneracy occur when neither the static nor the dynamic magnetic fields are zero? This phenomenon can be explained by introducing a modified or apparent gyromagnetic ratio that depends on the dressing parameter x, as was done in Eq. 2.2. In the semi-classical analogy to this situation, illustrated in Fig. 2.1-c, the nuclear magnetization follows a closed trajectory about the axis defined by the direction of $\mathbf{B}_d$. Even though the static field is finite, the nuclear magnetization does not precess around $\mathbf{B}_0$.

Figure 2.9 shows the calculated energy levels for various fixed values of y (rather than x). That is, in each plot y is fixed and x is varied. When the dressing field is zero and hence $x = 0$, the energy levels are split by the static field ($y \neq 0$), with the magnitude of the splitting being equal to y. When the dressing field is turned on the separation becomes

$y\gamma^{'}/\gamma$ rather than y. And as long as $y \ll 1$ it is equal to $yJ_0(x)$. Values for the modified or apparent gyromagnetic ratio $\gamma^{'}/\gamma$ can be extracted from the separation of energy levels at different values of x. In the following section the values extracted from this analogy are compared to the equivalent results obtained from the semi-classical model.

2.3   Comparison of the Semi-Classical and Quantum Models
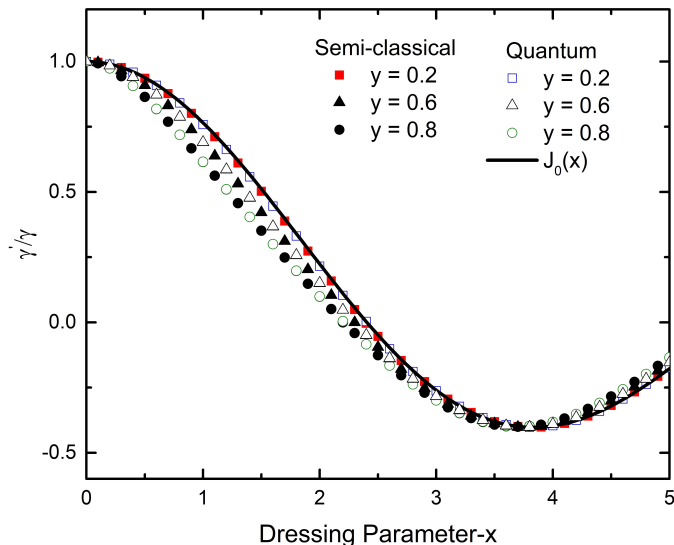
Figure 2.10: Comparison of normalized modified gyromagnetic ratios $\gamma^{'}/\gamma$ for $y < 1$, as calculated from the semi-classical and quantum models.

The previous two sections outlined two different methods for calculating the modified or apparent gyromagnetic ratio $\gamma^{'}$ as a function of dressing parameters x and y. The first approach, based on a semi-classical model of spin precession, involved tracking the average precession rate of the transverse components of **M** about $\mathbf{B}_0$. The second approach, based on a quantum model of energy levels, involved tracking the separation between adjacent energy levels.

In the regime $y < 1$, both models yield identical results for $\gamma^{'}/\gamma$. This equivalence is shown in Fig. 2.10. I observed a maximum deviation of 0.001% between the results of the two models for $y = 0.2$ and 0.4. This deviation increases to 0.02% for $y = 0.6$ and 0.8. However in the regime $y > 1$, agreement is only observed over a small range of x, as is evident in Fig. 2.11. The issue is that the very simplistic analysis method used to extract the time average precession frequency from the semi-classical trajectories fails at approximately the point where $x = y$. One could perhaps improve on the analysis of the semi-classical results by using Fourier Transforms to reveal all frequencies associated with
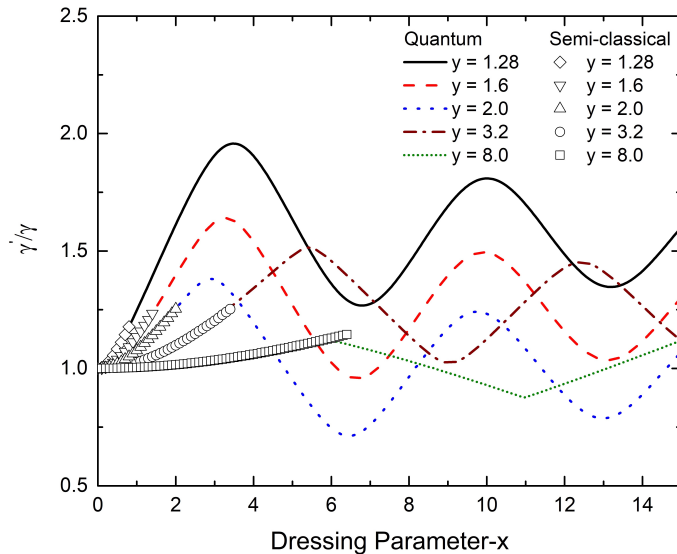
Figure 2.11: Comparison of normalized modified gyromagnetic ratios γ'/γ for $y > 1$, as calculated from the classical and quantum models.

the precession of $\mathbf{M}$ about $\mathbf{B}_0$.

2.4   Critical Spin Dressing

The discussion of spin dressing above focused on a single spin species, but this is not a requirement. If a dressing field is applied to a mixture of two spin species, with different gyromagnetic ratios, it is possible to generate conditions where both species end up precessing about the static field at the same average precession rate. This phenomenon is called critical spin dressing (CSD) and is anticipated as an important mode of operation for a proposed experiment to search for the electric dipole moment of the neutron (nEDM) [28]. The goal of this proposed experiment is to study neutron spin precession in combined magnetic and electric fields. Rather than studying neutrons alone, ^{3}He is added and is used as a comagnetometer against which the neutron spin precession is referenced. The gyromagnetic ratios of these two spin species differ by $\sim 11\%$. It is anticipated that important gains in sensitivity can be realized by applying CSD to force the neutron and ^{3}He nuclear spins to precess at the same rate, in a given static magnetic field. In this thesis I use hydrogen and fluorine nuclear spins (as proxies for neutrons and ^{3}He) to investigate the phenomenon of CSD.

The gyromagnetic ratios of ^{1}H and ^{19}F nuclear spins differ by 6% [40, 41]:

23

$$\gamma_{\text{H}} = 267.513 \times 10^6 (\text{rad} \cdot \text{s}^{-1} \cdot \text{T}^{-1}) \tag{2.43}$$

$$\gamma_{\text{F}} = 251.662 \times 10^6 (\text{rad} \cdot \text{s}^{-1} \cdot \text{T}^{-1}) \tag{2.44}$$

$$\alpha = \frac{\gamma_{\text{F}}}{\gamma_{\text{H}}} = 0.94074. \tag{2.45}$$

Under CSD conditions the modified gyromagnetic ratios of both are equal. That is $\gamma_{\text{H}}' = \gamma_{\text{F}}'$. This occurs at critical values of x (i.e. x_c) that can be calculated in the regime $y \ll 1$ as follows. In this regime $\gamma' = \gamma J_0(x)$. So, x_c for a mixture of ^{1}H and ^{19}F can be inferred from

$$\gamma_{\text{H}} \ J_0(\frac{\gamma_{\text{H}} \text{B}_0}{\omega_{\text{d}}}) = \gamma_{\text{F}} \ J_0(\frac{\gamma_{\text{F}} \text{B}_0}{\omega_{\text{d}}}) \tag{2.46}$$

or

$$J_0(x_c) = \alpha J_0(\alpha x_c) \tag{2.47}$$

where x_c is $\frac{\gamma_{\text{H}} \text{B}_0}{\omega_{\text{d}}}$.

Graphically, the solution for Eq. 2.47 corresponds to the crossing points of γ_{F}' and γ_{H}' as a function of the dressing parameter x. Figure 2.12-a shows the locations of these crossing points for ^{1}H and ^{19}F nuclei in the limit $y \ll 1$. In terms of the normalized relative difference between γ_{H}' and γ_{F}' which I define as

$$\eta'(x) = \frac{\gamma_{\text{H}}' - \gamma_{\text{F}}'}{\gamma_{\text{H}}}. \tag{2.48}$$
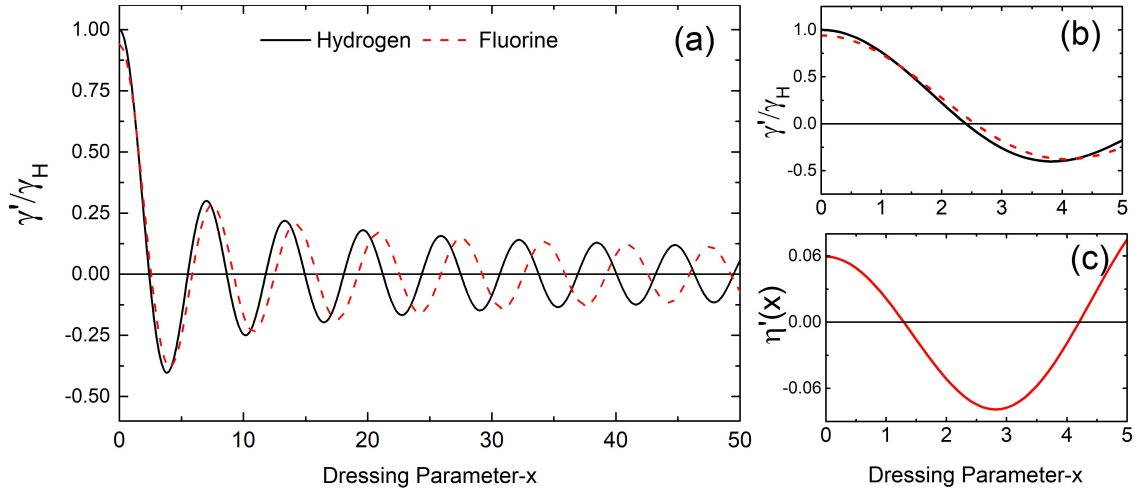
Figure 2.12: The modified gyromagnetic ratio of ^{1}H and ^{19}F nuclei, normalized to the ^{1}H gyromagnetic ratio γ_{H}, predicted by perturbation theory in the regime $y \ll 1$, over (a) a broad and (b) a narrow range of x. (c) Plot of $\eta'(x) = \frac{\gamma_{\text{H}}' - \gamma_{\text{F}}'}{\gamma_{\text{H}}}$; zeros of $\eta'(x)$ characterize critical spin dressing conditions.
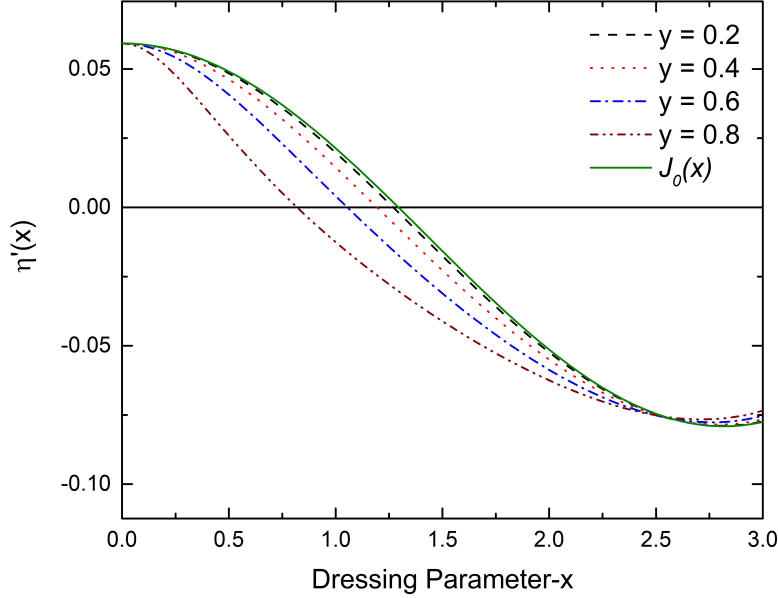
Figure 2.13: Simulation of $\eta'(x)$ for ^{1}H and ^{19}F in the regime $0 < y < 1$.

CSD occurs when η' is zero. Figure 2.12-c shows $\eta'(x)$ for small values of x. Zero crossings of this function represent CSD conditions. There are many such zero crossings but the first one is the most practical as it requires the least intense dressing field and also because it is less sensitive to variations in x than its neighbours. Table 2.1 summarizes the location of the first few critical spin dressing points for ^{1}H and ^{19}F as well as the derivative $d\eta'(x)/dx|_{x=x_c}$ at these points.

Over the range $0 < y < 1$, $\eta'(x)$ behaves more or less the same as it does for $y \ll 1$. However, there are small differences in x_c and $d\eta'/dx|_{x=x_c}$ as y is varied. Figure 2.13 shows the calculated behaviour of η' for $y = 0.2, 0.4, 0.6$ and 0.8. As y increases, x_c decreases. For example, $x_c = 1.27$ at $y = 0.2$ while $x_c = 0.82$ at $y = 0.8$. Also as y approaches one, $\eta'(x)$ becomes more sensitive to variations in y (that is, to variations in the static field). Table 2.2 shows relative changes in η' at x_c when the static field or y is changed by 1%, for a system of ^{1}H and ^{19}F nuclei.

x_c	$|d\eta'/dx|_{x=x_c}$
1.29	0.075
4.20	0.096
7.37	0.123
10.58	0.145

Table 2.1: Locations of critical spin dressing points ($x_c = \gamma_\mathrm{H} B_0/\omega_\mathrm{d}$) and corresponding sensitivities of η' to variations in x (i.e., $d\eta'/dx$) at these points, for a mixture of ^{1}H and ^{19}F nuclei. It is assumed $y \ll 1$.

25

y	0.2	0.4	0.6	0.8
x_c	1.27	1.19	1.05	0.82
$\Delta\eta'/\eta'_{x_c}$	0.07%	0.25%	0.62%	1.5%

Table 2.2: Location of the first zero of η' and the relative change in η' when y is changed by $\pm 1\%$, for several values of y.

2.4.1 Effect of The Background Static Field on CSD

An important factor that influences γ' and consequently η' is the alignment of the static field with the dressing field. This effect is observed in the experimental data for CSD. I will refer to this effect in Ch. 6 where I demonstrate CSD. Nominally the two fields are orthogonal. A misalignment between the static field and the dressing field introduces a small projection of $\mathbf{B}_0$ onto the $\mathbf{B}_\mathrm{d}$ axis. This effect can be ignored for most values of x, but not when $\gamma' \simeq 0$. To obtain some insight into issues that arise when $\gamma' \simeq 0$ let us use the quantum model, described in Sec. 2.2. Then I add the contribution of a weak static field $\Delta\mathrm{B}\,\hat{x}$, parallel to an existing dressing field, to the Hamiltonian. The resulting Hamiltonian is similar to Eq. 2.22 but involves a new term $\gamma\,\Delta B\,\sigma_\mathrm{x}/2\omega_\mathrm{d}$. The Hamiltonian can now be written:

$$\frac{H}{\hbar\omega_\mathrm{d}} - n = -\frac{y}{2}\sigma_z - \frac{y}{2}\kappa\sigma_x - \frac{x}{4\sqrt{n}}\sigma_x(a^\dagger + a) \tag{2.49}$$
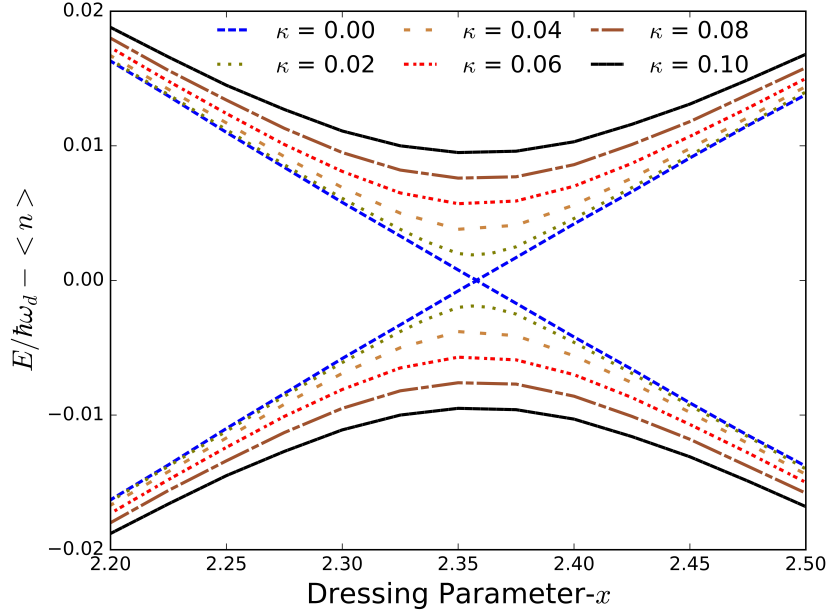
Figure 2.14: Energy levels at $y = 0.4$. The energies of the two states cross when $\kappa = 0$ (static and dressing fields orthogonal) but an avoided crossing emerges when a misalignment is introduced ($\kappa \neq 0$).
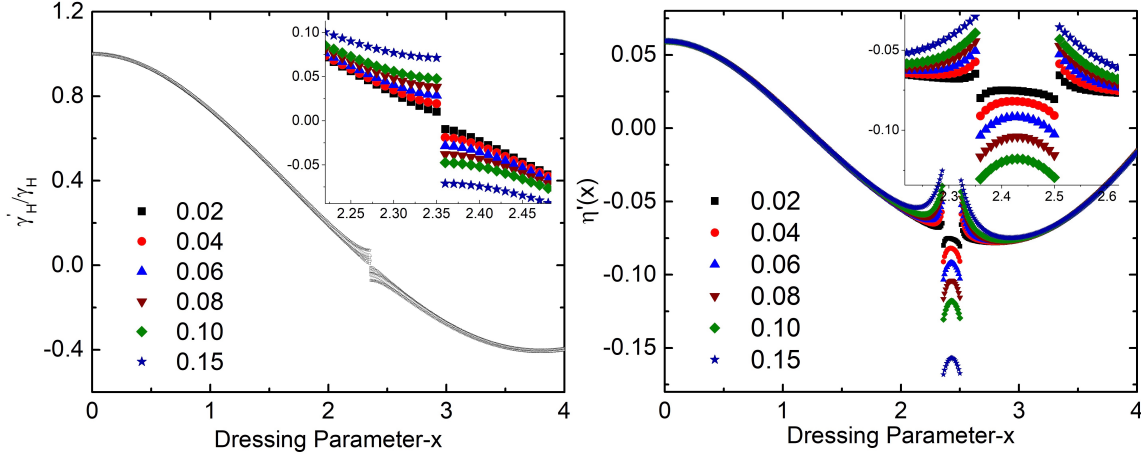
Figure 2.15: Influence of field alignment in the vicinity of the first zero crossing of γ_{H}' at $y = 0.4$ on (left) the normalized apparent gyromagnetic ratio of ^{1}H nuclei and on (right) the difference of the normalized apparent gyromagnetic ratios of ^{1}H and ^{19}F nuclei. As in Fig. 2.14, the various curves correspond to different degrees of field misalignment as characterized by the parameter κ.

where $\kappa = \frac{\Delta B}{B_0}$. The same method described in Sec. 2.2 can be used to numerically calculate the energy levels of Eq. 2.49. Figure 2.14 shows part of the energy level diagram at $y = 0.4$ for different values of κ. Level crossing occurs at $\kappa = 0$ as it should but, as κ is increased an avoided crossing emerges. This influences the time-average precession rate of nuclear spins and consequently the value of γ'. So, inferred values of γ' under this condition deviate from the prediction of the quantum model. The effect of this anti-crossing on γ_{H}' and on $\eta'(x)$ is further demonstrated in Fig. 2.15.

2.4.2 Effect of an Imperfect $\pi/2$ Rotation on CSD

An experimental investigation of CSD is potentially sensitive to the initial condition for $\mathbf{M}$. The analysis earlier in this chapter assumed $\mathbf{M}$ was subjected to a $\pi/2$ rotation (placing it in the equatorial plane of the Bloch sphere) immediately before the dressing field is applied. However, a simple simultaneous $\pi/2$ rotation for two spin species with different gyromagnetic ratios is not possible. A $\pi/2$ rotation for one of the two might leave the magnetization for one species in the equatorial plane, but the magnetization of the other will be left with a component along the static field. To investigate the effect of an imperfect $\pi/2$ rotation on CSD, I used the semi-classical model of spin precession. The semi-classical model is a time-dependent problem and the initial condition of $\mathbf{M}(\mathrm{t})$ can be varied, while the quantum model is a time-independent problem. I chose ^{1}H and ^{19}F Larmor frequencies of 200 and 188 Hz, respectively and set the dressing field frequency f_{d} to 500 Hz (corresponding to $y = 0.4$). To start the simulation I assumed $\mathbf{M}_{\mathrm{H}}$ and $\mathbf{M}_{\mathrm{F}}$ were both initially aligned
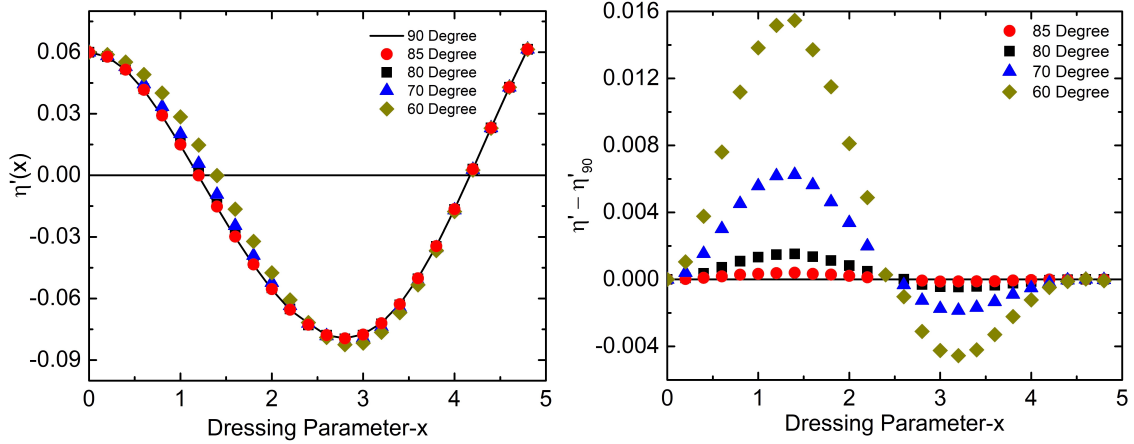
Figure 2.16: (Left)Demonstration of the effect of perfect and imperfect $\pi/2$ rotation pulses on $\eta^{'}(x)$. (Right) The deviation of $\eta^{'}$ from $\eta^{'}_{90}$, where the former is calculated for an imperfect $\pi/2$ rotation and latter for a perfect $\pi/2$ rotation.

with $\mathbf{B}_0$, and that a perfect $\pi/2$ rotation was then applied to the ^{1}H nuclei. This results in a rotation angle θ less than $\pi/2$ for the ^{19}F. Figure 2.16 shows calculated results for $\eta^{'}$ at different ^{19}F rotation angles (in practice, the ^{19}F rotation angle is set by its gyromagnetic ratio; the goal here was to examine sensitivity to this rotation angle.). Also shown in this figure is the deviation of $\eta^{'}$ from the case in which both spin species experience a perfect $\pi/2$ rotation. For example consider a tipping pulse that rotates ^{1}H by 90° and ^{19}F by 85°. This pulse leaves 8.7% of the initial $\mathbf{M}_F$ aligned with $\mathbf{B}_0$. The value of $\eta^{'}$ that one then obtains deviates by up to 0.6% from the ideal case in which $\mathbf{M}_H$ and $\mathbf{M}_F$ are both initially in the transverse plane. This deviation increases as the fraction of $\mathbf{M}_F$ aligned with $\mathbf{B}_0$, increases. Irrespective of the ^{19}F rotation angle, $\eta^{'}$ always crosses zero, indicating the point at which CSD occurs.

Chapter 3

Ultra-Low Field NMR of ^{1}H Nuclei

In order to perform a critical spin dressing experiment in which two spin species are forced to precess at the same average precession rate about a static field $\mathbf{B}_0$, an intense far off-resonant oscillating magnetic field $\mathbf{B}_\mathrm{d}(t)$ is required. This field, which is applied perpendicular to $\mathbf{B}_0$, is referred to as a dressing field. The frequency f_d and the amplitude B_d of the dressing field are conveniently described in terms of the dimensionless dressing parameters $x = \gamma \mathrm{B}_\mathrm{d}/2\pi f_\mathrm{d}$ and $y = \gamma \mathrm{B}_0/2\pi f_\mathrm{d}$, where B_0 is the magnitude of the static field. If the dressing parameter y is assumed to be very small ($y \ll 1$), as it is anticipated to be for a proposed search for the electric dipole moment of the neutron [28], and if one is interested in exploring a wide range of the dressing parameter x, such as from 0 to 40, then the desired limits on the parameters f_d, B_d and B_0 are:

$$f_\mathrm{L} \quad \ll \quad f_\mathrm{d} \tag{3.1}$$

$$\mathrm{B}_\mathrm{d} \quad \leq \quad \frac{40\mathrm{B}_0}{y} \tag{3.2}$$

where $f_\mathrm{L} = \gamma \mathrm{B}_0/2\pi$ is the Larmor precession frequency. The motivation for choosing a wide operating range for x is that it opens the door to studying spin dressing (and critical spin dressing) over a range of parameter space that to the best of my knowledge has not previously been examined. Equations 3.1 and 3.2 result from choosing $y \ll 1$ and $x \leq 40$ respectively. Once a decision about the magnitude of the static field B_0 is made, the range of dressing field parameters f_d and B_d are defined by Eqs. 3.1 and 3.2.

In principle the value of B_0 is arbitrary, but in practice it is strongly constrained by the extreme values of x and y that one wants to explore. In general it is much easier from a technical point of view to work at the smallest values of B_0 possible. This statement is reinforced by Table 3.1 which shows the nominal values of f_d and B_d required to perform a spin dressing experiment on an ensemble of hydrogen nuclei in a sample of water for a given static field B_0, a dressing parameter y of 0.1, and a dressing parameter x in the range 0 to 40.

Static field B_0	Larmor frequency	Dressing frequency	Maximum dressing field B_d	Current required to produce B_d
1 - 100 nT	0.04 - 4 Hz	0.4 - 40 Hz	0.4 - 40 μT	0.3 - 30 mA
1 - 100 μT	0.04 - 4 kHz	0.4 - 40 kHz	0.4 - 40 mT	0.3 - 30 A
1 - 100 mT	0.04 - 4 MHz	0.4 - 40 MHz	0.4 - 40 T	0.3 - 30 kA

Table 3.1: Nominal values of the static field (B_0), ^{1}H Larmor frequency (f_L), dressing field frequency (f_d) and RMS dressing field amplitude (B_d) to achieve a dressing parameter $x = 40$. The AC current required to drive a solenoidal coil with a winding density of 10 turns per cm to generate B_d is shown in the last column on the right. The dressing parameter y is assumed to be 0.1.

A competing concern is that the signal to noise ratio (SNR) in a conventional nuclear magnetic resonance (NMR) experiment degrades as the static field is decreased. Two factors cause this reduction: the thermal equilibrium nuclear spin magnetization produced by a static field in the μT range is much smaller than it is in the mT or T ranges, as is the time rate of change of the nuclear magnetization as it precesses.

In the high temperature limit the thermal equilibrium nuclear magnetization M is given by:

$$\mathrm{M} \;=\; \rho\, \frac{\gamma^2 \hbar^2 \mathrm{B}_0}{4 k_B T} \tag{3.3}$$

where ρ is the nuclear spin density, γ is the gyromagnetic ratio, k_B is the Boltzmann constant and T is the absolute temperature. The magnetization M in Eq. 3.3 scales linearly with the static magnetic field, so by reducing the static field B_0 the nuclear magnetization M decreases as does the magnetic field B_M associated with M. Ultimately it is B_M (or the time rate of change of B_M) that is monitored in NMR experiments and so it is desirable to make M as large as possible. To compensate for the fact that a weak static field is desired in a dressing experiment, we can thermally pre-polarize the nuclear spin ensemble in a high field region and then transfer the sample into an ultra-low-field region [52].

Conventional inductive detection coils are based on Faraday's law. The emf that is induced is equal to the time rate of change of the magnetic flux Φ. That is,

$$\mathrm{V_{emf}} \;=\; -\,\frac{d\Phi}{dt} \tag{3.4}$$

which in turn is proportional to the time rate of change of the transverse component of the precessing nuclear magnetization $\mathrm{M_{xy}}(t)$. Since that precession occurs at the angular Larmor frequency $\omega_L = \gamma B_0$, $\mathrm{V_{emf}}$ is proportional to the static field B_0 for a fixed value of $\mathrm{M_{xy}}$. Again, operating in very weak magnetic fields implies that inductively detected signals will be very weak. To address this issue we can use detectors that are sensitive to the magnitude of the magnetic field B_M associated with the precessing nuclear magnetization $\mathbf{M}$ rather than the rate at which $\mathbf{B}_M$ changes. One example of such a detector is a

Magneto-Impedance sensor [53, 54], which is sensitive to the magnitude and polarity of the magnetic field to which it is exposed.

In this chapter I will discuss how I have incorporated Magneto-Impedance sensors into an apparatus for performing ultra-low-field NMR experiments. This represents the first time that these solid state magnetometers have been used for NMR. Three examples of NMR experiments are described, and are used to develop and evaluate methods that are then used for spin dressing experiments later in the thesis. In this sense this chapter describes the experimental foundations upon which my spin dressing and critical spin dressing experiments are based.

To begin I describe the characteristics of Magneto-Impedance sensors and the experiments we designed and performed to detect alternating magnetic fields associated with longitudinal and transverse nuclear magnetizations. These experiments include Adiabatic Fast Passage (AFP), ULF NMR of spatially-modulated longitudinal nuclear magnetization and pulsed ULF NMR on stationary samples. The same apparatus was used for all of these experiments, with minor differences in detection circuits and applied magnetic fields. Technical details specific to individual experiment are described separately.

The experiments described here and in subsequent chapters are classified as remote detection NMR experiments [55]. The sample is first polarized in a high field region (1.5 T) and then transferred quickly into a ULF region ($\sim$4 μT) where some form of signal is detected. In between, the sample magnetization $\mathbf{M}$ can be intentionally manipulated. For example, in the AFP experiment described later in this chapter we encode a spatially-varying nuclear magnetization pattern that is subsequently detected. Or, RF fields can be applied to the sample once it arrives in the ULF region in order to manipulate $\mathbf{M}$ before detection. The latter approach is also demonstrated in this chapter, and is then used in the spin dressing experiment described in Chapter 4.

3.1   Magnetometer

Examples of magnetometers that have been used previously to detect ULF NMR signals include atomic magnetometers and Superconducting Quantum Interference Devices (SQUIDs) [56, 57]. A good review article on using ^{87}Rb atomic magnetometer for ULF NMR can be found here [58]. SQUIDs must be operated at cryogenic temperatures[1] and atomic magnetometers tend to be complex devices that are difficult to incorporate into other experiments. In contrast, there are some solid-state magnetometers that are easy to use and which do not require special operating conditions. A few that might be suitable for a spin dressing experiment include Anisotropic-Magneto-Resistance (AMR) sensors [59], Flux-Gate magnetometers [60] and Magneto-Impedance sensors [54].

---

[1]High-T$_\mathrm{C}$ SQUIDs are typically operated at 77 K and low-T$_\mathrm{C}$ SQUIDs at $\lesssim$ 4 K.

Anisotropic Magneto Resistance (AMR) sensors are small[2], inexpensive and have a dynamic range of about ± 5 G. They can measure the magnitude and the polarity of DC and AC magnetic fields and their response is proportional to the magnitude of the field (B) rather than the time rate of change of the field ($\frac{dB}{dt}$). They saturate at fields larger than about 5 G, but can be reinitialized by applying a suitable set/reset recovery pulse. But ultimately AMR sensors are quite insensitive. As an example, a popular AMR sensor made by Honeywell (HMC1001) has a magnetic noise density of 18 pT/$\sqrt{\text{Hz}}$ at 1 kHz and 30 pT/$\sqrt{\text{Hz}}$ at 100 Hz and, provided it operates in feedback mode, it exhibits noise densities of 12 pT/$\sqrt{\text{Hz}}$ at 1 kHz and $\sim$20 pT/$\sqrt{\text{Hz}}$ at 100 Hz [61].

Flux-Gate magnetometers [60] were first developed in the 1930s. They are inexpensive and relatively sensitive. They are sensitive to the polarity and the magnitude of the field and their response is proportional to the magnitude of the field. The magnetic noise density they exhibit is very low ($\sim$5 pT/$\sqrt{\text{Hz}}$ at 1 Hz), but they are bulky [62] and their sensitive area tends to be quite large (usually 5 $\times$2 cm^2). Recently, miniature flux-gates have been developed, but as their size shrinks they lose sensitivity. For example, micro-flux-gate sensors with areas of a few mm^2 have magnetic field noise densities of 5 nT/$\sqrt{\text{Hz}}$ [63] at 10 Hz and 70 nT/$\sqrt{\text{Hz}}$ at 1 Hz [64].

Magneto-Impedance (MI) sensors were first developed in the 1990s. They have the advantage of being compact and relatively sensitive. They exhibit magnetic noise densities of order $\sim$5 pT/$\sqrt{\text{Hz}}$ at 10 Hz, which is comparable to flux-gate magnetometers and unshielded high-T_c SQUIDs [65]. And, it is predicted that their ultimate performance could yet be significantly better [66]. MI sensors can measure both the polarity and the magnitude of the field and their response is proportional to the magnitude of the field. The sensitive area of MI sensors is typically 1×6 mm^2, which is quite small.

After conducting a number of preliminary experiments with AMR sensors, I decided to investigate MI sensors. In 2014 we obtained a prototype MI sensor that exhibited a factor of ten lower noise density compared to AMR sensors. A decision was made to perform a series of test experiments using these MI sensors, to evaluate their performance for an eventual spin dressing experiment. These test experiments are the primary focus of this chapter.

3.1.1 Anisotropic-Magneto Resistance Sensor

AMR sensors are inexpensive and commercially available[3] in one-, two- and three-axis versions. They are functionally similar to a 4-element Wheatstone bridge in which the resistance of all 4 branches depends on the orientation of magnetic domains within the resistive material [67]. These resistive elements are made of nickel-iron deposited on a silicon

---

[2]A variety of AMR sensors have been developed. The most sensitive sensors have dimensions of order 1 $\times$ 4 $\times$ 9 mm^3 but additional space is required for signal processing circuitry.

[3]A typical sensor, without signal processing circuitry currently costs about $\sim$ \$25 CAD.
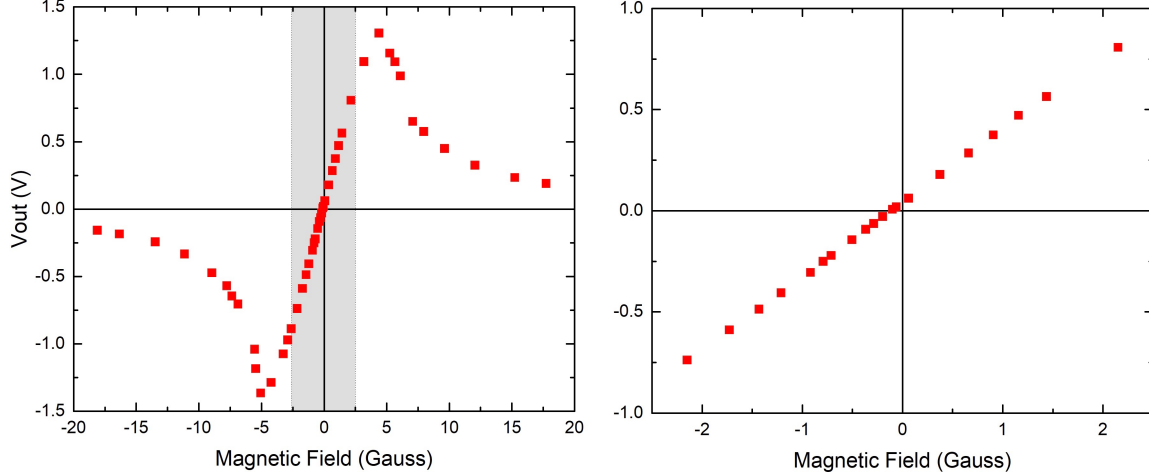
Figure 3.1: DC response of an HMC1001 AMR sensor over a broad (left) and narrow (right) range of applied magnetic field, when biased at 10 V with a gain of 12. The grey band which is enlarged on the right shows the linear response region for the sensor. Beyond this regime sensor sensitivity degrades.

wafer. Their operating range is $\pm$ 5 G. The most sensitive readily available AMR sensor is the HMC1001 [61] manufactured by Honeywell. This is a single axis device and employs a surface mount sensor with a nominal sensitivity of 3.2 (mV/G $\cdot$ V$_b$) where V$_b$ is the DC voltage applied across the bridge. Figure 3.1 shows an example of an AMR sensor response to a DC magnetic field.

3.1.2 Magneto-Impedance Sensor

Magneto-Impedance (MI) sensors are based on the MI effect in amorphous wires [53, 68, 69]. This effect involves changes in the electrical impedance of a magnetic wire that carries an AC current, when the wire is subjected to an external magnetic field aligned with its axis, as shown in Fig. 3.2. The AC current through the wire is typically low (in the range of few mA) [70] and typically at frequencies in the range 1 - 100 MHz, although recently the effect has been observed at much lower frequencies [71]. The wires that are employed are usually very thin with diameters in the range 10 - 1000 μm. They are made of magnetic materials such as FeSiB [72], CoSiB [73] and FeCoSiB [74] and are usually magnetized in the circumferential direction to achieve the highest sensitivity. Based on the frequency at which the AC current is driven through the wires, the sensors are classified as Magneto-Impedance (MI) or Giant-Magneto-Impedance (GMI) sensors. In MI sensors the skin depth δ is large relative to the diameter of the wire but in GMI sensors it is much smaller and the AC currents flow near the surface of the wire [75, 76]. Recall that the skin depth δ for a
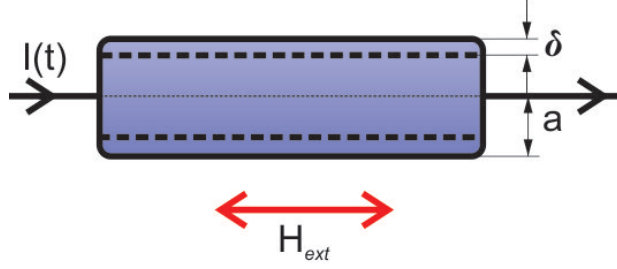
Figure 3.2: The alternating flow of current I(t) through (or near the surface of) an amorphous magnetic wire generates a circumferential magnetization. The impedance Z of the wire is strongly dependent on the component of the applied external magnetic field H_{ext} aligned with the direction of the current.

good conductor is given by:

$$\delta = \sqrt{\frac{2\rho}{\omega\mu(H_{ext})}} \tag{3.5}$$

where ρ is the resistivity, ω is the angular frequency of the AC current, H_{ext} is the applied magnetic field, and μ is the magnetic permeability (which can depend on H_{ext}). Maxwell's equations can be solved with the appropriate boundary conditions to relate the impedance of the wire to δ [77, 78]. Since δ depends on μ, and μ in turn depends on the applied magnetic field, the impedance of the wire ultimately depends on the external magnetic field. For a cylindrical magnetic conductor of radius a the impedance Z is given by:

$$Z = \frac{1}{2}R_{dc}ka\frac{J_0(ka)}{J_1(ka)} \tag{3.6}$$

where $k = (1-j)/\delta$, R_{dc} is the DC resistance of the wire, $j = \sqrt{-1}$, J_0 and J_1 are the zeroth and first order Bessel functions, respectively.

MI and GMI sensors have many potential uses including detection of biomolecules [79], non-destructive crack detection [80], target detection and process control [81], space and aerospace research [81], electronic compasses and many other applications [82]. The work described in this chapter adds a new application: NMR.

My work is conducted using a prototype MI sensor made by Aichi Micro Intelligent Corp. (model MI-CB-1DJM-A). This device exhibits a noise density of 5 pT/$\sqrt{Hz}$ at 10 Hz, has a sensitivity of 5 V/μT, a sensitive area of 0.8×6 mm^2, a dynamic range of ±30 μT and a frequency response spanning 0.1 Hz - 10 kHz (set by high-and-low-pass filters). It is encapsulated in a chip mounted to a board with ancillary electronics. The specific model I used requires an external 1 MHz oscillator to produce the necessary AC current.

For the experiments described in this chapter I used two MI sensors arranged in a gradiometer configuration to minimize the influence of environmental magnetic field fluctuations, and to add the NMR signals detected by each sensor. Figure 3.3 shows the location
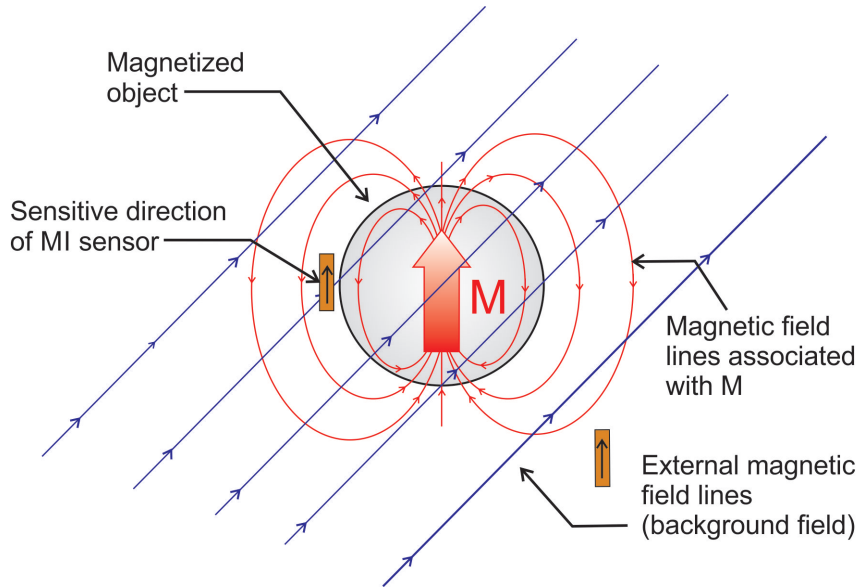
Figure 3.3: A simple gradiometer arrangement involving two Magneto-Impedance sensors. The difference between the outputs of the two sensors is fed into a phase sensitive detector, to reject the common mode signal associated with magnetic fields from distance sources. At the same time, the signal associated with the nearby magnetized source is enhanced.
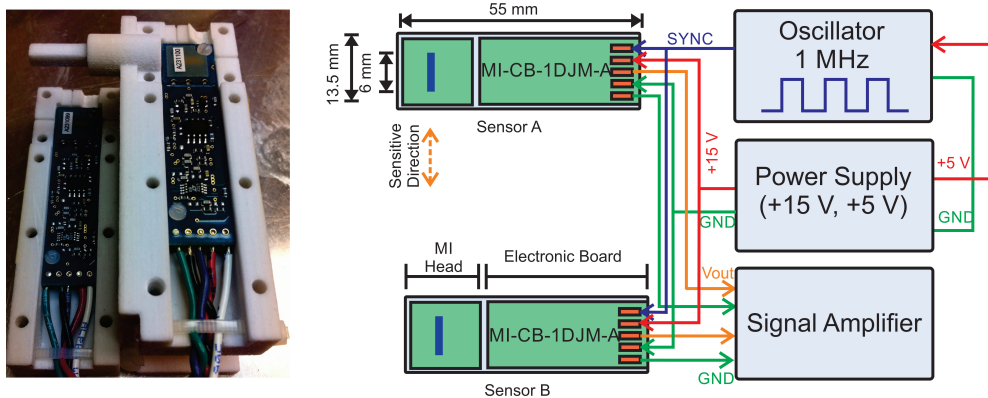
Figure 3.4: (Left) Two MI sensors arranged in a gradiometer configuration (described in the text) and mounted on a 3D printed sensor holder. (Right) MI sensor connection diagram. The oscillator operates at 1 MHz and produces a square waveform with 50% duty cycle and 0 - 5 V amplitude. The signal amplifier consists of a transformer and phase sensitive detector.

of the sensitive part of the sensors relative to a magnetized object (NMR sample). This configuration requires careful alignment of the sensors with one another. To accomplish this I designed a 3D model of a support structure using AutoCAD drawing software, and then generated the structure using a 3D printer. The final product and wiring configuration I employed are shown in Fig. 3.4.

I measured the sensitivity of the MI sensors by placing them in a very uniform alternat-
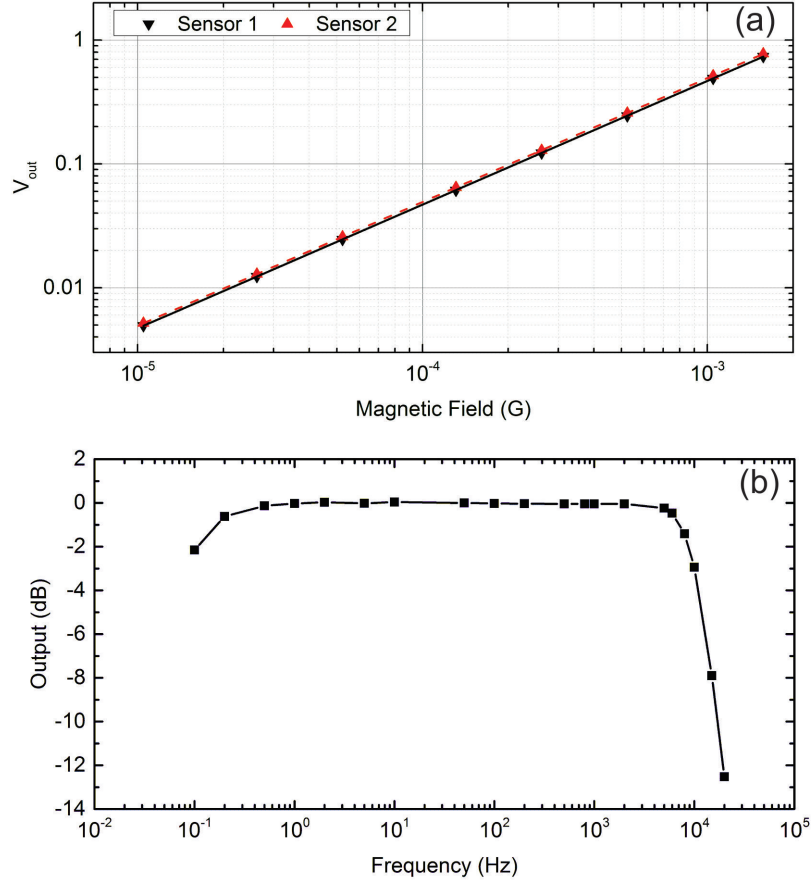
Figure 3.5: The response of the MI sensors to an alternating magnetic field B. (a) Shows the response of two MI sensors to a 1 kHz alternating magnetic field. The equation of the best fit lines are $y = 2.666(2) + 0.9987(4)\,x$ for sensor 1 ((—)) and $y = 2.691(1) + 0.9996(3)\,x$ for sensor 2 (- -) where y is $log_{10}V_{out}$ and x is $log_{10}B$. (b) Shows the relative frequency response of the MI sensors.

ing magnetic field which was designed for Magnetic Resonance Imaging in very low magnetic fields [83] and monitored their output with a Phase Sensitive Detector (PSD).[4] The alternating field was generated by a sine-ϕ-like current distribution involving five saddle-shaped current elements mounted on a 98 cm long cylinder with a radius of 27 cm. The sensitivities that I measured were 4.68 ± 0.03 V/μT and 4.93 ± 0.03 V/μT, both of which were constant over the frequency range 0.5 Hz - 5 kHz. Figure 3.5-a shows the linear response of the sensors to an AC magnetic field at 1 kHz and Fig. 3.5-b shows the response at constant drive amplitude as the frequency is varied. The influence of the high pass filter at 0.1 Hz and the low pass filter at 10 kHz are evident.

To amplify the output of the sensors I used a low noise transformer-coupled preamplifier[5] with an input noise density of 0.1 nV/$\sqrt{\text{Hz}}$. This transformer has a nominal gain of

---

[4]Stanford Research Systems model SR830 DSP
[5]Stanford Research Systems model SR554
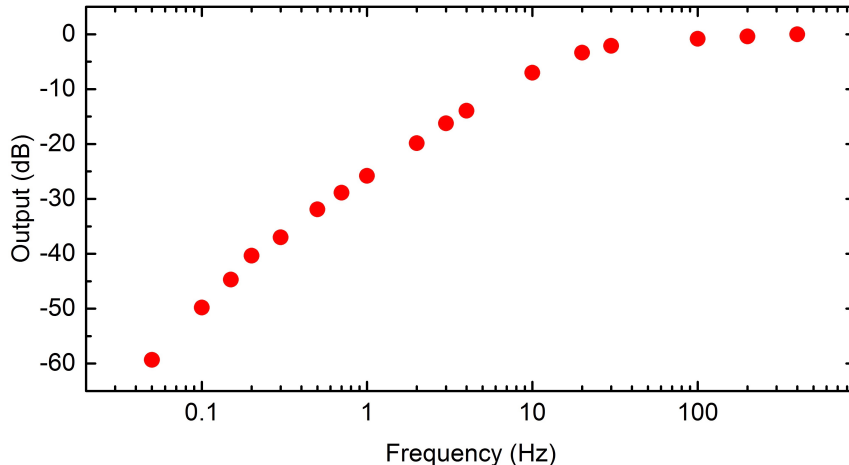
Figure 3.6: Response of the the two MI sensors to a localized oscillating magnetic source measured relative to the output at 400 Hz where a maximum is observed. The sensor outputs are amplified by a SRS 554 transformer, which contributes to the observed frequency dependence.

500 between ~100 Hz and ~1 kHz. The gain falls off outside of this band. The maximum gain I measured when the sensor outputs were connected to the differential mode of the transformer was 480 at 400 Hz. Figure 3.6 shows the manner in which the transformer-coupled response of the MI sensors to an AC magnetic field falls off at frequencies below 400 Hz. This response is measured relative to that observed at 400 Hz. A small 4-turn coil with radius 5 mm was used to produce the AC magnetic field for this test. The coil was placed at a distance of 25 mm from the sensors. Below approximately 0.2 Hz both the sensor electronics and the transformer contribute to the frequency dependence of the response. Between 0.2 and 100 Hz only the transformer contributes to the observed frequency dependence. Over the range 100 - 400 Hz the response changes very little.

3.2   Adiabatic Fast Passage Experiment

As a test of the viability of using MI sensors to monitor nuclear magnetic resonance phenomena, it was decided to use Adiabatic Fast Passage (AFP) methods [84] to imprint an alternating longitudinal nuclear magnetization pattern on a stream of flowing water. The MI sensors were then used to directly monitor the resulting magnetic field variations in the vicinity of the stream. The situation we consider is one in which nuclear spins are initially aligned with the local static magnetic field $\mathbf{B}_0$. However, because of motion (caused by the flow of the water) and an intentionally applied linear magnetic field gradient, the local magnetic field experienced by nuclear spins is time dependent, that is, $dB_0/dt \neq 0$. In particular we choose $dB_0/dt < 0$. If the spins are simultaneously exposed to an oscillating magnetic

37
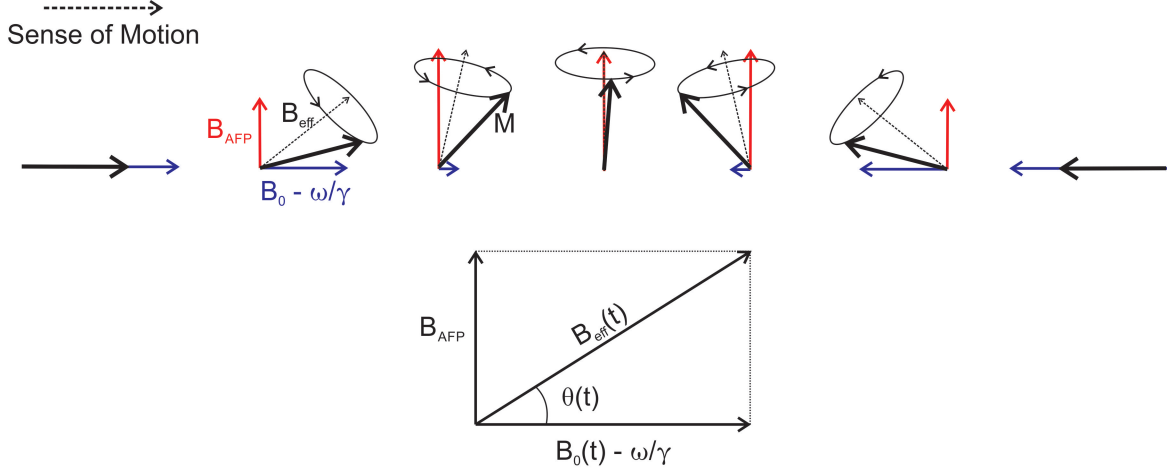
Figure 3.7: Classical picture of Adiabatic Fast Passage in a frame rotating at resonant angular frequency ω. (Top) Schematic view of the orientation of the nuclear magnetization $\mathbf{M}$ relative to the effective magnetic field $\mathbf{B}_{\text{eff}}$, (Bottom) components of $\mathbf{B}_{\text{eff}}$ in the rotating frame.

field $\mathbf{B}_{\text{AFP}}$ perpendicular to the magnetic field, and resonant with the nuclear spins at some particular location along the trajectory where $\mathbf{B} = \mathbf{B}_{\text{res}}$, an inversion can occur. That is, the spins end up anti-aligned with $\mathbf{B}_0$. In a classical picture of spin dynamics, this inversion occurs because the direction of the effective field $\mathbf{B}_{\text{eff}}$ they experience (in a reference frame rotating at angular frequency ω) rotates by 180° as the water passes through resonance. This situation is shown in Fig. 3.7. In this picture the effective field is defined as:

$$\mathbf{B}_{\text{eff}} \;=\; (\mathbf{B}_0 \;-\; \frac{\boldsymbol{\omega}}{\gamma}) \;+\; \mathbf{B}_{\text{AFP}} \tag{3.7}$$

where $\boldsymbol{\omega} = \gamma \mathbf{B}_{\text{res}}$ and $\mathbf{B}_0$ is a function of position. In two extreme cases, far above and below resonance, we can ignore $\mathbf{B}_{\text{AFP}}$. Then the effective field is parallel (for far above resonance) or anti-parallel (for far below resonance) with $\mathbf{B}_0$. And its magnitude is $|\mathbf{B}_0 - \omega/\gamma|$. As $\mathbf{B}_0$ changes between these two extreme values the direction of $\mathbf{B}_{\text{eff}}$ begins to rotate. If the rate of this rotation is slow enough the nuclear magnetization $\mathbf{M}$, that precesses about $\mathbf{B}_{\text{eff}}$, can rotate simultaneously with $\mathbf{B}_{\text{eff}}$. Consequently a magnetization $\mathbf{M}$ that was initially parallel to $\mathbf{B}_0$ ends up anti-parallel to $\mathbf{B}_0$.

For AFP to invert the nuclear magnetization $\mathbf{M}$ effectively, two conditions must be satisfied. First, during precession of $\mathbf{M}$ about $\mathbf{B}_{\text{eff}}$ the transverse component of $\mathbf{M}$ should not decay quickly. So the first condition is given by:

$$\frac{1}{T_2} \;\ll\; \gamma B_{\text{eff}}. \tag{3.8}$$

The second condition involves the precession rate of the magnetization about $\mathbf{B}_{\text{eff}}$, which needs to be much faster than the rotation rate of $\mathbf{B}_{\text{eff}}$. This condition is defined as:

$$\frac{d\theta}{dt} \ll \omega_{\text{eff}} \tag{3.9}$$

where $\tan\theta = \frac{\text{B}_{\text{AFP}}}{\text{B}_0(t) - \omega/\gamma}$ and $\omega_{\text{eff}} = \gamma\text{B}_{\text{eff}}$. So $\frac{d\theta}{dt}$ is given by:

$$\frac{d\theta}{dt} = \frac{\text{B}_{\text{AFP}}}{\text{B}_{\text{eff}}^2} \frac{d\text{B}_0(t)}{dt} \tag{3.10}$$

and the second AFP condition is

$$\frac{\text{B}_{\text{AFP}}}{\text{B}_{\text{eff}}^2} \frac{d\text{B}_0(t)}{dt} \ll \gamma\text{B}_{\text{eff}}. \tag{3.11}$$

Equations 3.8 and 3.11 must be valid for all values of B_{eff}. For example the minimum value of B_{eff}, in the vicinity of the resonance, is $\text{B}_{\text{eff}} = \text{B}_{\text{AFP}}$. Under these conditions Eqs. 3.8 and 3.11 are

$$\frac{1}{\text{T}_2} \ll \gamma\text{B}_{\text{AFP}} \tag{3.12}$$

$$\frac{d\text{B}_0(t)}{dt} \ll \gamma\text{B}_{\text{AFP}}^2. \tag{3.13}$$

Note that the rate at which B_0 changes must be faster than T_2. Together, Eqs. (3.12) and (3.13) provide an upper and a lower limit on the time variation of B_0

$$\frac{\text{B}_{\text{AFP}}}{\text{T}_2} \ll \frac{d\text{B}_0}{dt} \ll \gamma\text{B}_{\text{AFP}}^2. \tag{3.14}$$

It is also useful to note that the time variation of B_0 can be written

$$\frac{d\text{B}_0}{dt} = \bar{v} \frac{d\text{B}_0}{dx} \tag{3.15}$$

where $\bar{v}$ is the average speed at which the magnetization $\mathbf{M}$ moves and $d\text{B}_0/dx$ is the local gradient of B_0.

3.2.1 Apparatus

In our apparatus, which is shown schematically in Fig. 3.8, a continuous flow of tap water first passes through a 600 ml reservoir in which ^{1}H nuclei are polarized to thermal equilibrium in a 1.5 T magnetic field produced by a superconducting magnet. Thereafter, the local static magnetic field $\mathbf{B}_0$ to which the water is exposed along its flow path decreases monotonically, eventually reaching the μT regime. The water exits the polarizing magnet
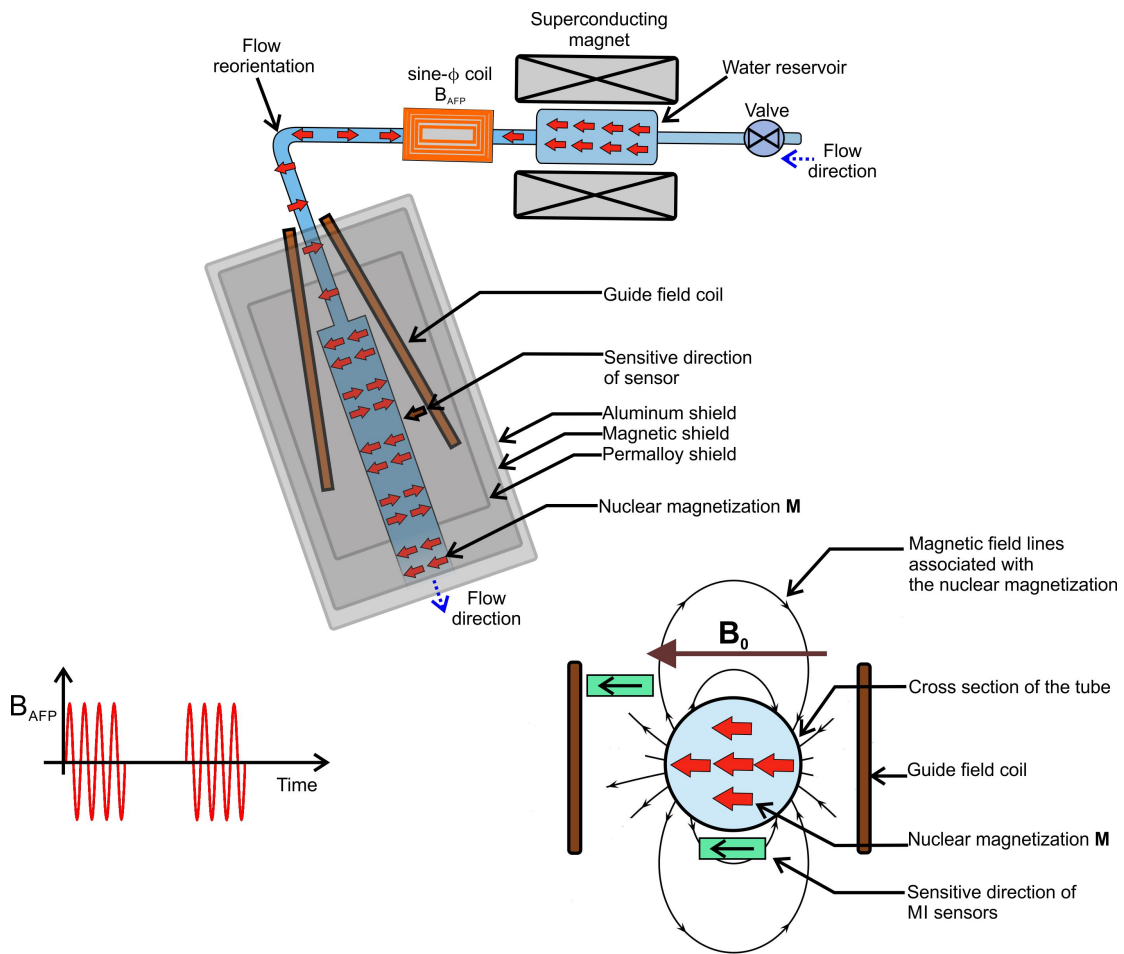
Figure 3.8: Overview of the AFP experiment (not to scale). The approximate position of the sensors relative to the cross section of the 3/8" PVC tube is shown in the inset at the bottom right. The time dependence of the AFP modulation pattern is shown in the bottom left.

through a $\frac{1}{8}$ inch inner-diameter PVC tube aligned with a field line. Flow rates at average linear speeds $\bar{v}$ of up to 6 m/s are employed, giving rise to turbulent conditions. En route, we modulate the nuclear magnetization $\mathbf{M}$ using AFP. As the local static field $\mathbf{B}_0$ decreases a 78 kHz resonant oscillating magnetic field $\mathbf{B}_{\mathrm{AFP}}$ can be applied perpendicular to the tube axis. If $\mathbf{B}_{\mathrm{AFP}}$ is applied, the ^{1}H nuclear magnetization $\mathbf{M}$ undergoes an AFP inversion that leaves it anti-parallel (rather than parallel) to $\mathbf{B}_0$. However if $\mathbf{B}_{\mathrm{AFP}}$ is not applied, then $\mathbf{M}$ exits the AFP region in its initial orientation. Next, as $\mathbf{B}_0$ continues to decrease (and facilitated by coils that produce a guide field), the flow is gradually reoriented so that it ends up perpendicular to the orientation of $\mathbf{B}_0$ (which is produced by the fringe field of the polarizing magnet, and thus varies as a function of position); Thereafter $\mathbf{M}$ is maintained perpendicular (rather than parallel) to the tube axis. At the same time the flow enters a region that is well-shielded from magnetic noise.

Finally, the tube diameter is abruptly increased to $\frac{3}{8}$ of an inch, reducing $\bar{v}$ by a factor of 9. The water then flows past two MI sensors arranged in a gradiometer configuration. The sensitive axes of these sensors are aligned to respond to the magnetic field $\mathbf{B}_{\mathrm{M}}$ associated with the component of $\mathbf{M}$ that is parallel (or anti-parallel) to $\mathbf{B}_0$. Further details regarding each component of this apparatus are described in the following four subsections.

3.2.1.1 Flow Characteristics

The maximum water pressure available at the source is 56 psi which yields an outlet flow rate of $\sim$45 ml/s and average linear speed of $\bar{v} = 6$ m/s. A solenoid valve was installed at the inlet of the flow path to control the flow. The flow rate was measured by activating the solenoid valve for a certain amount of time and then measuring the volume of water exhausted. At the maximum flow rate the water spends $\sim$13 s inside the pre-polarization reservoir in the superconducting magnet. This is considerably longer than the longitudinal nuclear relaxation time T_1, and so the ^{1}H nuclei effectively reach thermal equilibrium (i.e. they polarize). The total length of the flow path between the magnet and the sensors is $\sim$4.2 m. The minimum travel time obtained with the maximum tap water pressure is 0.7 s. Under these conditions the water flow pattern is expected to be turbulent. Reynold's number [85] characterizes the strength of inertial forces to viscous forces. It is defined as,

$$Re = \frac{\bar{v} D_H}{\mathsf{v}} \qquad (3.16)$$

where $\bar{v}$ is the average speed of the fluid, D_H is the hydraulic diameter of the tube and v is the kinematic viscosity of the fluid. For the parameters of our experiment $\mathsf{v} = 1.004 \times 10^{-6}$ m^2/s, $\bar{v} = 5.8$ m/s and $D_H = 3.17$ mm ($\frac{1}{8}$ inch ID tube) the maximum Reynolds number we would expect is 18.8×10^3. The critical Reynolds number for this geometry is of order $\sim$2100,

and hence we expect the flow in our apparatus to be turbulent.

3.2.1.2 AFP and Guide Fields

The oscillating AFP field $\mathbf{B}_{\mathrm{AFP}}$ is produced by an 8 turn sine-ϕ coil [86] that is 25 cm long and has a radius of 6.8 cm. It produces a field of 0.79 G per Ampere of applied current. This field is alternately turned on and off at a modulation frequency $f_{\mathrm{m}} \lesssim 50$ Hz to periodically change the direction of the nuclear magnetization. The spatial distribution of the amplitude of $\mathbf{B}_{\mathrm{AFP}}$ and the local static magnetic field are shown in Fig. 3.9. For an AFP frequency $f_{\mathrm{AFP}} = 78$ kHz, amplitude $\mathrm{B}_{\mathrm{AFP}} = 5~\mu\mathrm{T}$, local magnetic field gradient $d\mathrm{B}_0/dt = 24~\mu\mathrm{T/cm}$ and $\mathrm{T}_2 \sim 0.7$ s[6] the AFP conditions given by Eq. 3.14 are satisfied.

A pair of 76 cm long trapezoidal coils were used to generate a guide field to maintain the orientation of $\mathbf{M}$ perpendicular to the tube axis. The separation between these coils varies from 5 to 9 cm as the tube, and hence the flow of water, enters the low field region inside the magnetic shields (see Fig. 3.8). The strength of the magnetic field produced by these coils correspondingly decreases.
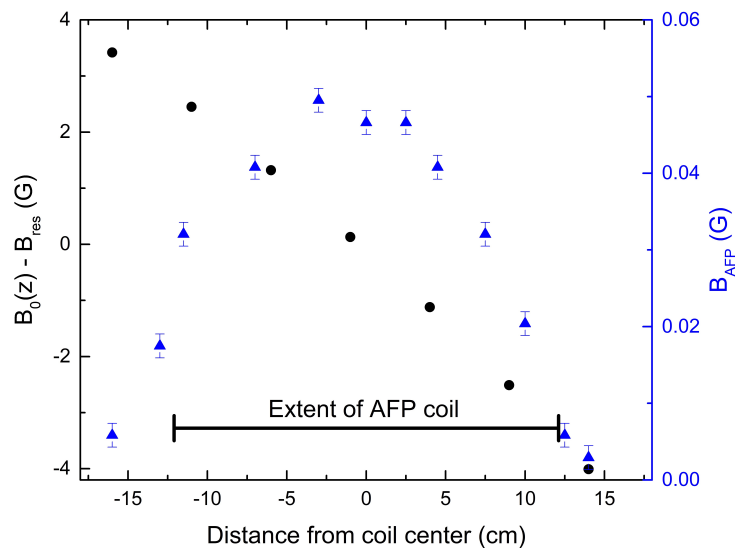
Figure 3.9: Measured static (B_0 ; ●) and oscillating ($\mathrm{B}_{\mathrm{AFP}}$; ▲) magnetic field profiles relative to the center of the sine-ϕ coil. Note that an offset $\mathrm{B}_{\mathrm{res}}$ corresponding to the magnetic field required to produce a $^1\mathrm{H}$ Larmor frequency $f_{\mathrm{L}} = 78$ kHz has been subtracted from B_0. The average local magnetic field gradient inside the sine-ϕ coil is $d\mathrm{B}_0/dx = 0.24(1)$ G/cm.
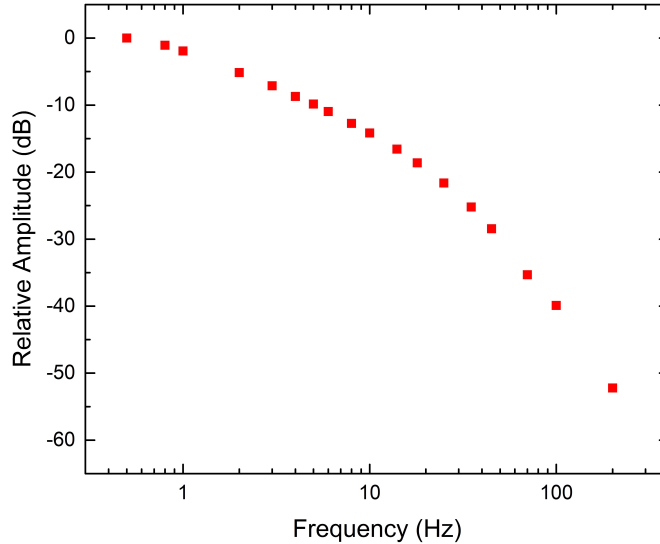
Figure 3.10: Screening of AC magnetic fields provided by the aluminum and the high-permeability shields. See text for details.

3.2.1.3 Passive Shielding

Three concentric cylindrical metal shields were used to isolate the sample and sensors from external electromagnetic interference. The largest of these a 1.8 m long aluminium shield, with a diameter of 76 cm and a wall thickness of 7 mm which provides effective Faraday screening. The second shield is made of a high permeability metal. It is also 1.8 m long; it has diameter of 70 cm and a wall thickness of 3 mm. In addition to enhancing Faraday screening it also shunts static magnetic field lines (primarily from the polarizing magnetic field) away from the low field region of the experiment. The smallest and innermost shield is made of permalloy.[7] It is 83 cm long, with a diameter of 26 cm and a wall thickness of ∼1 mm. It reduces the static magnetic field in the vicinity of the sensors by one order of magnitude, and improves the field homogeneity.

The efficiency of the Faraday and magnetic screening provided by the shields are demonstrated in Figs. 3.10 and 3.11. Figure 3.10 shows the attenuation of the rms amplitude of an external alternating magnetic field at the center of the shields as the frequency is increased. The external magnetic field was generated by 4 loops of copper wire wrapped around the circumference of the aluminium shield. These loops were then driven by a function generator to create an alternating magnetic field parallel to the axis of the shields. The amplitude of this field was then monitored using a MI sensor with its sensitive axis aligned with the axis of the shields. I measured ∼50 dB attenuation at 200 Hz relative to 0.5 Hz. This corresponds to the frequency at which most of the measurements reported in this chapter and in the following chapters are performed. Also, Fig. 3.11 illustrates the suppression of the static

---

[6]This corresponds to the measured high field value of T_1; see Fig. 3.17.

[7]Co-Netic AA stress annealed shield.
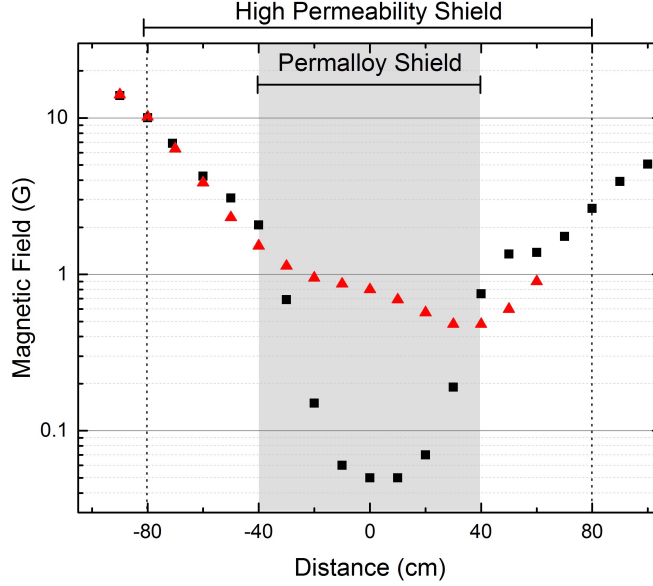
Figure 3.11: Measured axial component of magnetic field along the axis of the metal shield, relative to the center of the shields where the MI sensors are located (μT region). (▲): with high permeability shield only, (■): with high permeability and permalloy shields. Adding the permalloy shield reduces the central field by one order of magnitude and makes it more uniform. The spatial extent of the permalloy shield is shown in grey. The shields were located 4 m away from a 1.5 T superconducting magnet with a 30 cm bore.

magnetic field by the shields. A gaussmeter[8] was used to measure the axial component of the longitudinal component of the static magnetic field inside the shield, revealing a 20 dB attenuation of the static field at the location where the MI sensors reside.

3.2.2 Signal Detection Circuit

The outputs of the two sensors are fed into a differential input transformer[9] coupled to a Phase Sensitive Detector (PSD) as previously described.[10] The physical orientation of the two sensors (indicated by arrows aligned with their sensitive directions in Figs. 3.3 and 3.8) is the same but their outputs are monitored in a differential mode. This provides common mode rejection of magnetic field changes associated with distant sources (interference). At the same time, signals associated with variations in the dipolar magnetic field associated with the nuclear magnetization **M** reinforce one another. The output of the PSD can be displayed, recorded and analysed by an oscilloscope[11] or a digital multimeter.[12] Typically the latter was operated at 1 reading every 0.8 s. Ideally the data that are recorded corre-

---

[8]Group 3 gaussmeter model DTM-151 with a model MPT-231-7s hall probe.
[9]Stanford Research System model SR554
[10]Stanford Research Systems model SR830 DSP
[11]Tektronix model TDS 7054 Digital Phosphor Oscilloscope
[12]Hewlett Packard model 3457A
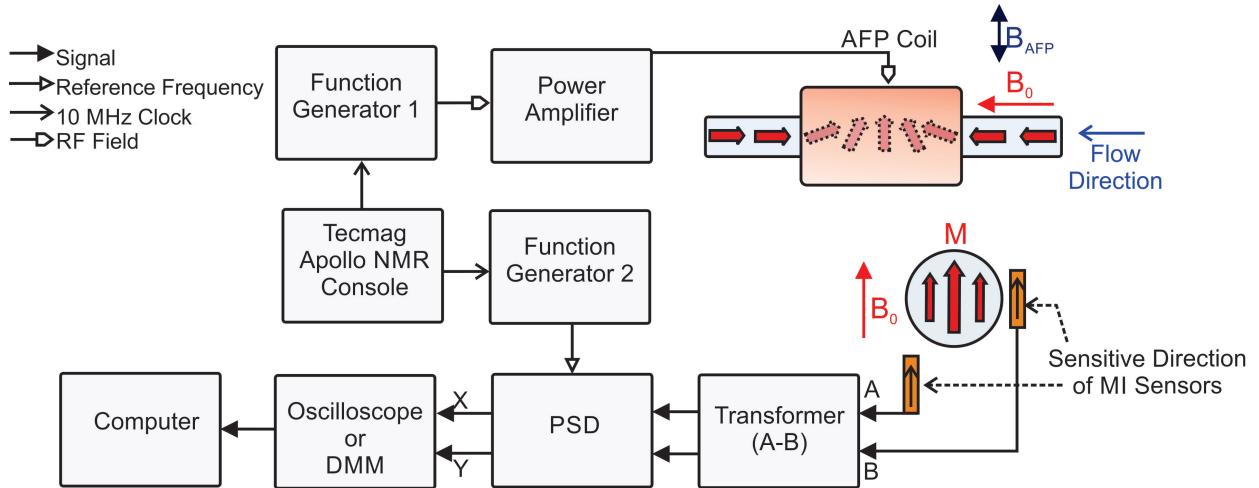
Figure 3.12: Overview of AFP signal detection circuit. The nominal gain of the transformer is 500 but it falls off below 100 Hz (see Fig. 3.6). This effect influences the overall gain in the vicinity of the AFP modulation frequency. A Tecmag Apollo NMR Console is used as the reference clock.

spond to a continuous alternation between the two magnetization states. That is, a square wave at the AFP modulation frequency. The digital multimeter (DMM) output can be sent to a computer using a GPIB connection and a Labview interface. The AFP field B_{AFP} was turned on and off using a function generator[13] that produced a 100% amplitude-modulated signal. The signal was then fed to a power amplifier[14] that in turn drove the sine-ϕ coil. A second function generator,[15] phase-locked to the first, was used to produce the reference for the PSD. Overall synchronization was accomplished using a Tecmag Apollo NMR console. Figure 3.12 shows a block diagram of the AFP signal detection circuit.

3.2.3 AFP Experiments

AFP-modulated nuclear magnetization signals were generated and observed under a variety of different conditions, and for a variety of purposes. A number of these experiments are summarized in the following subsections. In general, the purpose of these experiments is to explore and demonstrate the viability of using MI sensors for ULF NMR.

---

[13] Agilent 33250A 80 MHz
[14] Hewlett-Packard model 467A
[15] Standard Research Systems model DS345

3.2.3.1 Signal-to-Noise Ratio

In the first version of this experiment I did not use magnetic shields or the low noise transformer. Instead I employed three orthogonal Helmholtz pairs to suppress the local magnetic field (approximately 1 mT, associated with the polarizing magnet). This suppression is needed to keep the MI sensors from saturating. In this configuration I observed modulated sensor outputs at the AFP frequency that were resolved with a signal to noise ratio (SNR) of 14 for an equivalent noise bandwidth (ENBW) of 1.25 mHz; see Figs. 3.13 and 3.14. I also used a gradient coil aligned with the water tube axis to improve the homogeneity of the static field. These coils were driven by HP 6002A power supplies operated in constant current mode.

I improved the SNR of this experiment by one order of magnitude by introducing the magnetic shields and the low noise transformer. Figure 3.13 shows the signal levels observed when magnetized water flowed through the system, and when it was stationary (and hence only noise was recorded). Figure 3.14 shows the corresponding signal-to-noise ratio. In both cases data are plotted as a function of the equivalent noise bandwidth set by the PSD time constant and the low pass filter roll off. In Fig. 3.14 the signal amplitude is independent of bandwidth, as it should be. But the noise level is suppressed as the time constant is increased. One undesirable consequence of using the magnetic shields is that the ^{1}H nuclei
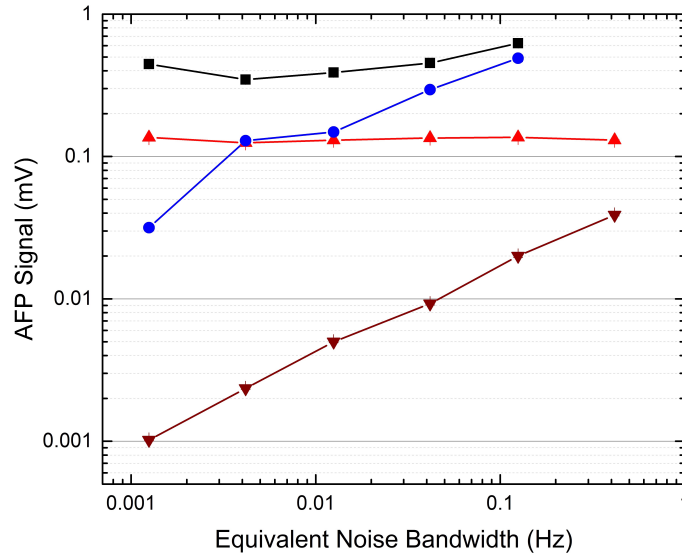
Figure 3.13: Effect of magnetic shields and transformer on AFP signal and noise level in terms of PSD equivalent noise bandwidth. (■): AFP signal without shields or transformer, (●): background noise without shields or transformer, observed when the water flow is stopped, (▲): AFP signal with shields and transformer, (▼): background noise with shields and transformer observed when the water flow is stopped. Data recorded with $f_\mathrm{m} = 4$ Hz, $f_\mathrm{AFP} = 78$ kHz, PSD output low pass filtered with a 12 dB/octave roll off. Lines are meant as guides for the eye.
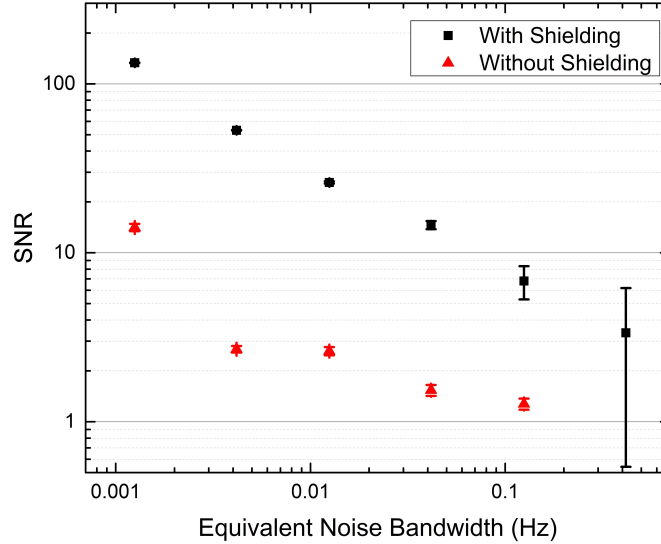
Figure 3.14: Signal-to-noise ratio observed in AFP experiments as a function of equivalent noise bandwidth. Here $f_{\mathrm{m}} = 4$ Hz, $f_{\mathrm{AFP}} = 78$ kHz, and the PSD output was low pass filtered with a 12 dB/octave roll off. ($\blacktriangle$): without magnetic shields, ($\blacksquare$): with magnetic shields.

must travel a distance ~ 1.5 m longer to reach the MI sensors. This in turn reduces the signal magnitude as is evident in Fig. 3.14.

3.2.3.2 AFP-modulated Signals

Figure 3.15 shows recordings of the magnetic field $\mathbf{B}_{\mathrm{M}}$ associated with the longitudinal component of the AFP-modulated nuclear magnetization $\mathbf{M}$. The modulation pattern is a square waveform with a frequency f_{m} of 4 Hz. Averaging improves the quality of the data but is ultimately limited by fluctuations in the pressure of the water supply. The signals exhibit a sinusoidal rather than square waveform for two reasons. First, whenever we turn the AFP field on/off those nuclei that are already inside the AFP coil experience a rotation somewhere between 0 and 180 degrees. This yields a smooth transition between the parallel and anti-parallel states of the nuclear magnetization. Second, the boundaries between regions with different magnetizations are mixed somewhat by the turbulent flow. The same type of effects were observed in an earlier experiment [55] in which AMR sensors were employed instead of MI sensors.

3.2.3.3 Frequency Response

Figure 3.16 shows the dependence of the detected signal on the AFP modulation frequency. These data were recorded with an equivalent noise bandwidth of 41.7 mHz. The maximum
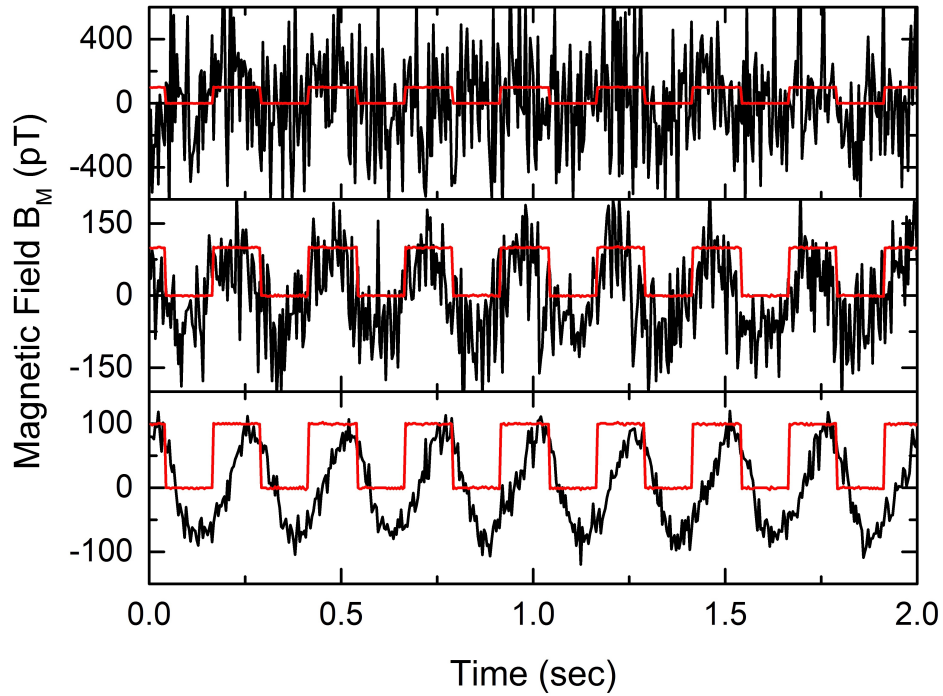
Figure 3.15: AFP signals acquired at $f_{\mathrm{m}} = 4$ Hz when a ~ 33 ml/s flow rate was employed. Three examples are shown. The top panel shows a single shot acquisition. The middle panel shows the effect of averaging over 10 repetitions of this experiment, and the bottom panel shows the effect of averaging over 600 repetitions. The square modulation pattern used to turn the AFP field on and off is also shown.
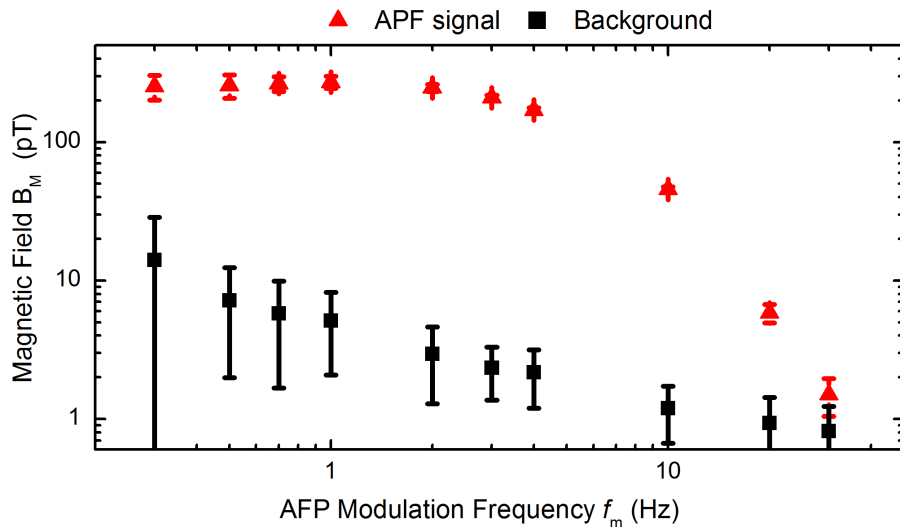
Figure 3.16: RMS field B_{M} measured when AFP is used to periodically flip the orientation of $\mathbf{M}$ relative to $\mathbf{B}_0$ ($\blacktriangle$; $\bar{v} = 5.8$ m/s), The noise observed when the water is stationary ($\blacksquare$; $\bar{v} = 0$ m/s) reflects the intrinsic noise density of the sensors.

48

SNR ~ 80 was obtained[16] at a modulation frequency $f_m = 4$ Hz. At low modulation rates the magnitude of B_M is independent of f_m and is consistent with the field expected from water polarized in a 0.3 T field. At higher rates it is attenuated because of (a) mixing of water downstream of the abrupt flow expansion and (b) the spatial extent of the fields produced by the AFP coil. We can define a threshold frequency f_t associated with this attenuation:

$$f_t = \bar{v}/4l \tag{3.17}$$

where $\bar{v}$ is the average speed of $\mathbf{M}$ and l is the spatial extent of the $\mathbf{B}_{AFP}$ field. Equation 3.17 suggests that the shortest time for $\mathbf{M}$ to transit the entire profile of $\mathbf{B}_{AFP}$, should be equal to one quarter of the modulation period. This ensures that over a distance l the magnetization $\mathbf{M}$ is either fully parallel or anti-parallel to the static field. Modulation at higher frequencies will lead to signal attenuation. Using parameters appropriate to my experiment ($l = 30$ cm and $\bar{v} = 5.8$ m/s) yields $f_t = 5.6$ Hz which compares favourably to the value $f_t \sim 4$ Hz inferred from Fig. 3.16.

3.2.3.4 Longitudinal Nuclear Relaxation Time T_1

The longitudinal nuclear relaxation time T_1 is an important parameter in most NMR experiments. One of the first things we did was to characterize an effective relaxation time in connection with the fraction of nuclear magnetization that arrives in the ultra-low-field region of the apparatus where NMR detection takes place. The AFP signal amplitude was measured at different flow rates, corresponding to different transport times. An exponential
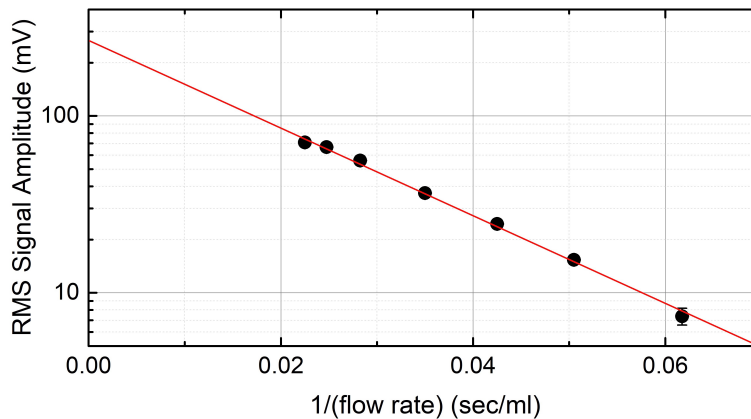
Figure 3.17: RMS AFP signal amplitude as a function of inverse flow rate. Approximately 25% of the initial nuclear magnetization arrives in the μT region where NMR detection takes place. The slope of a straight line fit to these data implies an effective $T_1 = 0.70(6)$ s.

---

[16] A flow rate (~ 46 ml/s) was employed in this measurement yielding a higher SNR compared to data in Fig. 3.14 where the flow rate ~ 33 ml/s was employed.

decay was observed. At the maximum flow rate (46 ml/s), up to one-quarter of the nuclear magnetization leaving the 1.5 T polarization magnet, reaches the ultra-low-field portion of the apparatus after travelling a distance of 4.2 m. Figure 3.17 shows the RMS AFP signal amplitude as a function of the inverse flow rate. By extrapolating the data to infinite flow rate (or zero transport time) we can extract the amplitude of the AFP signal that would be produced in a 1.5 T field. The slope of a straight line fit to these data yields an effective nuclear relaxation time $T_1 = 0.70(6)$ s. Note that this experiment does not determine the location(s) where, or mechanism by which, relaxation occurs.

3.2.3.5 Estimation of Anticipated AFP Signal Magnitude

A simple model of a magnetized cylindrical object can be used to estimate the order of magnitude of the AFP signal. The field produced by this object is sensed by the two MI sensors and corresponds to the magnetic field B_M associated with the modulated nuclear magnetization M. In this model an infinitely long cylinder aligned in the x direction is filled with polarized water with a magnetic moment per unit volume M. Imagine that the cylinder is sliced into many small disks with thickness dx. For each of these disks we assign a point-like magnetic dipole moment $d\mathbf{m}$ at its center which in turn produces the magnetic field $d\mathbf{B}_{\text{dip}}$ at two points of interest (where the sensitive parts of the two MI sensors are located). Ultimately, we can integrate over the volume of the cylinder to find B_M.

The magnetic field produced by a small magnetic dipole moment $d\mathbf{m}$ is given by:

$$d\mathbf{B}_{\text{dip}} = \frac{\mu_0}{4\pi r^3}\left(3(d\mathbf{m}\cdot\hat{\mathbf{r}})\hat{\mathbf{r}} - d\mathbf{m}\right) \tag{3.18}$$

where $dm = M\pi R^2 dx$, R is the radius of the cylinder, r is the distance between the dipole moment $d\mathbf{m}$ and the sensor and $\hat{\mathbf{r}}$ is the unit vector associated with r. For the orientations of $d\mathbf{m}$ and $\hat{\mathbf{r}}$ shown in Fig. 3.18, the total magnetic field B_M at a sensor is:

$$\mathbf{B}_M = \int d\mathbf{B}_{\text{dip}} = \frac{\mu_0 R^2 \mathbf{M}}{4}\int_{-\infty}^{+\infty}\frac{dx}{(y^2 + x^2)^{3/2}} = -\frac{\mu_0 R^2}{2y^2}\mathbf{M} \tag{3.19}$$

where y is the shortest distance between the axis of the cylinder and the sensitive part of the MI sensor. For an ensemble of nuclear spins with $n_{\pm}$ denoting the density of spins parallel or anti-parallel to the polarizing field B_p the total nuclear magnetic moment per unit volume M is given by:

$$M = (n_+ - n_-)\mu_p \tag{3.20}$$

where μ_p is the nuclear magnetic moment of a single ^{1}H nucleus. The difference in the number density of spins parallel and anti-parallel to the polarizing field is related to the
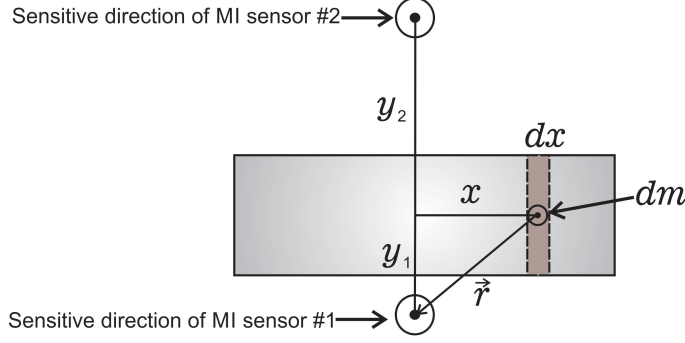
Figure 3.18: Schematic showing relative positions and orientations of a small magnetic dipole moment dm and two MI sensors (Not to scale).

polarization P of the nuclear spin ensemble which is:

$$P \; = \; \frac{n_+ - n_-}{n_+ + n_-} \; = \; \tanh(\mu_p B_p / k_B T) \tag{3.21}$$

where T is the absolute temperature and $n \; = \; n_+ + n_-$ is the total spin density of the sample. At room temperature and $B_p = 1.5$ T the polarization is approximately $\mu_p B_p / k_B T$. Thus inside the polarizing magnet $M \; = \; n\mu_p^2 B_p / k_B T$. Outside of the polarizing magnet M decays exponentially with a time constant T_1, as discussed in the previous subsection. Combining these results the anticipated magnitude of the magnetic field B_{dip} associated with M at the location of the MI sensors (B_{M1} and B_{M2}) is given by:

$$B_M \; = \; B_{M1} \; + \; B_{M2} \; = \; n\mu_0\mu_p^2 \, \frac{R^2 B_p}{2k_B T} \, \left(\frac{1}{y_1^2} + \frac{1}{y_2^2} \right) \, e^{-t/T_1} \tag{3.22}$$

where $y_1 \; = \; 10$ mm and $y_2 \; = \; 29$ mm correspond to the shortest distances between the two MI sensors and the tube axis, and t is the transport time from the polarizing magnet to the vicinity of the MI sensors. For $T_1 = 0.7$ s, $t = 0.72$ s and $R \; \sim \; 5$ mm one expects the sum of the fields detected by the sensors to be of order $B_M \; \sim \; 300$ pT, which is close to the measured peak amplitude $B_M \; \sim \; 350$ pT observed in my AFP experiment.

3.3   Ultra-Low-Field NMR Experiments

In addition to the AFP experiment described above I performed two further ultra-low-field (ULF) NMR experiments to test the viability of using MI sensors to monitor nuclear magnetic resonance phenomena. These experiments are performed in static fields between 5 - 20 μT and involve the application of steady or pulsed oscillating magnetic fields to manipulate the nuclear magnetization.

3.3.1 Steady Flow of AFP-Modulated Water

In the first and simpler version of the two ULF NMR experiments I apply a continuous $\mathbf{B}_1$ field to the AFP-modulated flow of water. The amplitude of the resonant $\mathbf{B}_1$ field is adjusted to produce a $\pi/2$ rotation of the nuclear magnetization $\mathbf{M}$ as the water flows through the $\mathbf{B}_1$ coil. Following this manipulation, $\mathbf{M}$ is perpendicular to the static field $\mathbf{B}_0$ and the sensitive axis of the sensors, so the AFP signal amplitude drops to zero.

3.3.1.1 Apparatus

The same apparatus was used as described in section 3.2.1 and shown in Fig. 3.8. The only new feature was that I placed a small RF coil in the ULF region of the apparatus, 10 cm upstream from the MI sensors. This coil enabled me to apply a continuous $\mathbf{B}_1$ field perpendicular to the tube axis and to $\mathbf{B}_0$. It is driven by a synchronized function generator.

Figure 3.19 shows the ULF region of the apparatus, including the MI sensors, the B_1 coil, the flow expansion and the coils that produce the guide field. The AFP-modulated nuclear magnetization $\mathbf{M}$ that enters the $\mu\mathrm{T}$ region, where the RF $\mathbf{B}_1$ coil and the MI sensors reside, is aligned perpendicular to the flow direction (rather than parallel or anti-parallel). The frequency of $\mathbf{B}_1$ is tuned to values in the range 200 - 800 Hz, and its amplitude is set to rotate the nuclear magnetization $\mathbf{M}$ by 90 degrees as $^1\mathrm{H}$ nuclei pass through resonance at the Larmor frequency f_L. The B_1 coil can nominally be placed at any point along the flow path but must be kept far enough away from the MI sensors to avoid obscuring NMR signals. Note that the stray field produced by the B_1 coil is orthogonal to the sensors. In detail, the B_1 coil is actively-screened to further suppress stray fields. The $\mathbf{B}_1$ field is generated by two pairs of coils in a rectangular Helmholtz configuration. I call these the
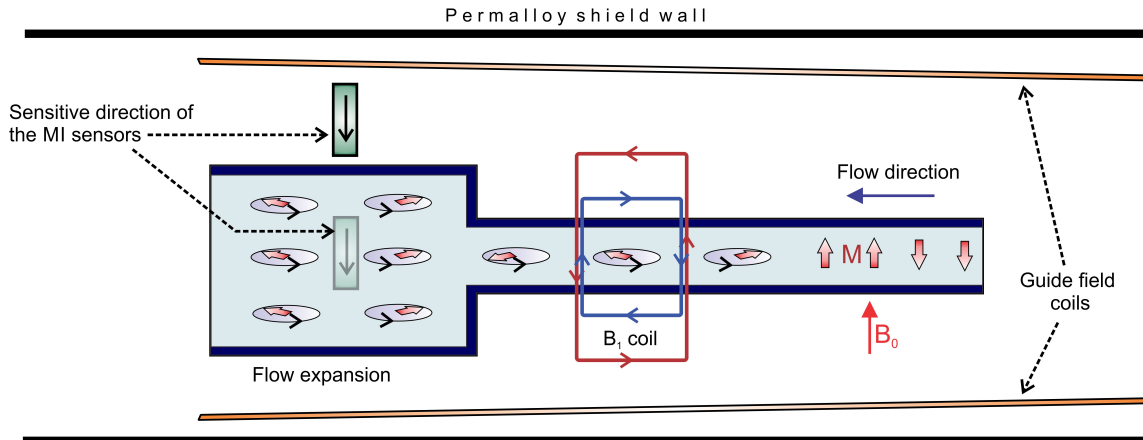
Figure 3.19: Overview of the $\mu\mathrm{T}$ region of the ULF NMR apparatus as configured to study the steady flow of AFP-modulated nuclear magnetization $\mathbf{M}$. The B_1 field is resonant with the nuclear spins as they pass through the B_1 coil. (Not to scale).
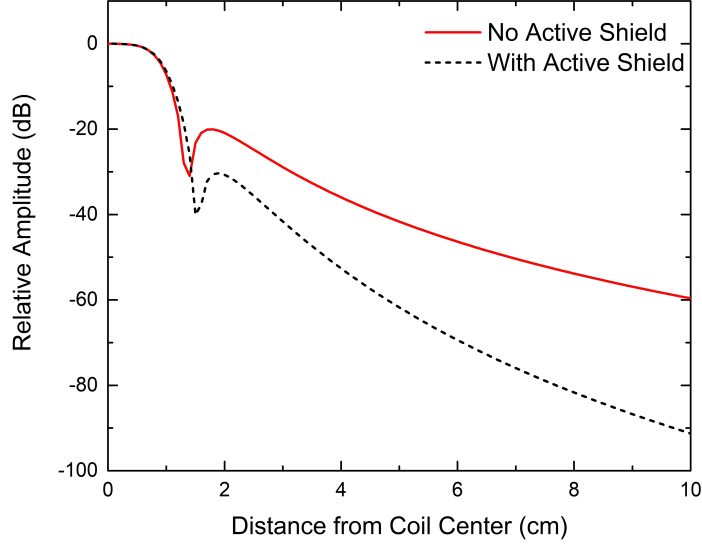
Figure 3.20: Amplitude of the B_1 field relative to its maximum value at the center of the coils. The field outside the coils is strongly suppressed by active shielding and enables us to generate B_1 fields continuously without influencing the functionality of the MI sensors.

main and the active shielding coils. The main Helmholtz pair has 8 turns, each with an area of 2×2 cm^2, and a separation distance of 2 cm. The active shielding coil has 4 turns, each with an area of 2×4 cm^2, and a separation distance of 2 cm. Both pairs of coils carry the same current but in opposite senses. The dimensions and the number of turns are chosen so that the total magnetic dipole moment of the combination is zero and consequently the stray magnetic field is suppressed at a distance far from the coils (e.g. where the MI sensors reside). This minimizes cross talk between the B_1 field and the MI sensors and restricts the B_1 field profile to a well defined region so that it does not influence the nuclear magnetizations when it is in the vicinity of the sensors.

Figure. 3.20 shows the results of a calculation of the relative magnitude of B_1 with and without active shielding. This calculation was performed using the BiotSavart magnetic field modelling software package [87], and shows that active shielding attenuates the magnitude of B_1 at the location of the MI sensors by a factor of 30.

3.3.1.2 Signal Detection Circuit

Figure 3.21 shows the signal detection circuit used for studying AFP-modulated nuclear magnetization. As before, the two MI sensors have the same orientation and their outputs are fed into the transformer and phase sensitive detector (PSD) in a differential mode. This rejects the common mode magnetic fields associated with distant sources while adding those associated with the nuclear magnetization in the nearby tube. I monitor the in-phase (X) and out-of-phase (Y) components of the PSD output relative to a reference oscillator, which
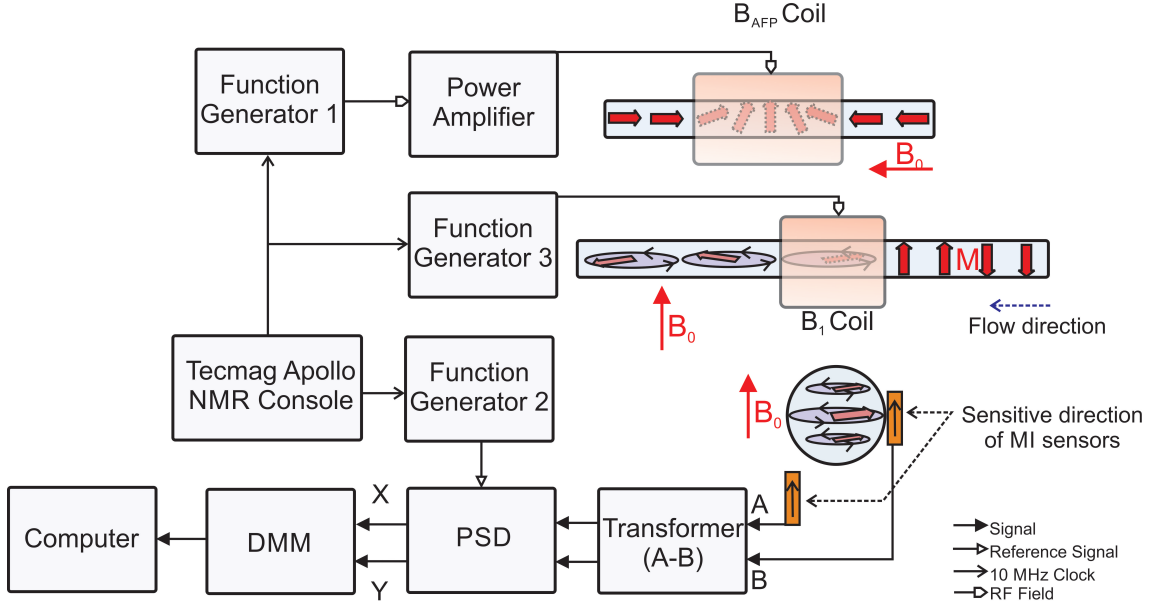
Figure 3.21: Magnetization encoding and signal detection circuit for studying a steady flow of AFP-modulated nuclear magnetization. B_{AFP} is modulated at f_m =4 Hz and the B_1 field is a continuous sine wave at a frequency in the range 200 - 800 Hz.

is set at the nominal Larmor frequency of ^1H nuclei, through the DMM. To simplify signal analysis I tune the phase of the PSD reference signal so that the signal associated with the detected AFP modulated magnetization signal is in-phase with the reference.

Three function generators are shown in Fig. 3.21. They are used, (a) to produce a 78 kHz AFP field modulated at 4 Hz, (b) to generate the reference oscilator signal for the PSD at the Larmor frequency and (c) to generate a B_1 field at frequencies in the range 200 - 800 Hz. All three are synchronized to a 10 MHz clock signal from a Tecmag Apollo NMR console.

3.3.1.3 Results

Figure 3.22 shows data from a ULF NMR experiment in which signals generated by AFP-modulated nuclear magnetization are monitored at different flow rates while a continuous B_1 field at frequency f is applied. This was accomplished by subjecting the MI sensor output to synchronous detection at the AFP modulation rate $f_m = 4$ Hz. The amplitude of the B_1 field was adjusted to produce $\pi/2$ rotations on resonance, as water flowed through the B_1 coil. The frequency f was then varied to reveal the resonance profile. The duration of the tipping pulse in this experiment, and hence the Full Width at Half Maximum (FWHM) of the resonance, is set by two factors: (a) the average velocity $\bar{v}$ or time-of-flight for ^1H nuclei through the B_1 field region and (b) turbulent mixing of the flowing water. The FWHM of
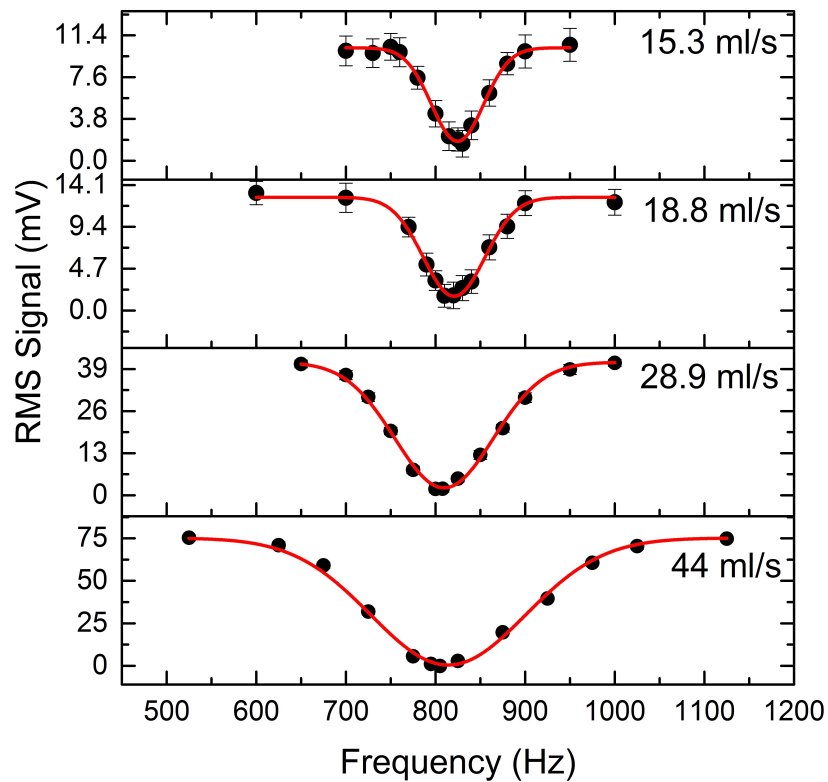
Figure 3.22: ^{1}H NMR resonance profiles at 20 μT revealed by applying a B$_1$ field at frequency f (in the vicinity of the Larmor frequency f_L = 0.8 kHz) to the AFP-modulated flow of water: f_m = 4 Hz with ENBW = 41.6 mHz; the flow rates (average velocity $\bar{v}$) from top to bottom are 15.3 ml/s (1.9 m/s), 18.8 ml/s (2.4 m/s), 28.9 ml/s (3.7 m/s) and 46.0 ml/s (5.9 m/s).
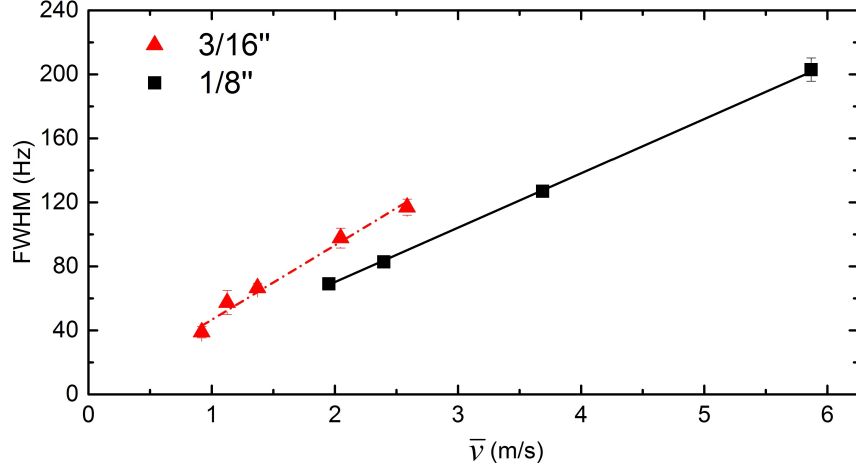
Figure 3.23: Measured Full Width at Half Maximum (FWHM) of ULF NMR profiles obtained from flowing AFP-modulated water, as a function of flow speed $\bar{v}$. Measurements were performed in two tubes with different diameters: 1/8" (■) and 3/16" (▲). Straight lines have been fit to the data yielding (—): $46.5(3.0)\ \bar{v} + 2.3(1.4)$; (—): $33.9(0.5)\ \bar{v} + 0.1(5.4)$.

the resonance profiles shown in Fig. 3.22 are obtained by fitting a Gaussian model function to the data. The relationship between FWHM and the average water velocity as it passes through the B_1 coil is shown in Fig. 3.23. Data are presented for different flow rates and for two different tube diameters (1/8" and 3/16" ID). Both of these parameters influence the Reynolds number of the flow. Clearly the FWHM increases as $\bar{v}$ increases, while at any given average velocity the FWHM is larger, by a factor of 1.5 associated with the ratio in diameters, in the bigger tube.

It would be interesting to follow this behaviour to lower Reynolds numbers, but in the current implementation of this experiment we are limited by T_1 relaxation and the stability of the flow rate. The former effect is evident in Fig. 3.22; the signal to noise ratio of data acquired at low flow rates (corresponding to long transport times) is lower than at high flow rates. Recall that the longitudinal magnetization decays with a time constant $T_1 \simeq 0.7\ s$.

3.3.2 Pulsed NMR

In the second version of the two ULF NMR experiments I used to test the viability of using MI sensors to monitor nuclear magnetic resonance phenomena, the AFP field is eliminated and instead we work with stationary samples. Water is allowed to flow through the system long enough (typically a few seconds) to transport polarized ^{1}H nuclei from the polarizing magnet to the ULF region. The water flow is then stopped by activating two solenoid valves. This brings the sample to rest, at which point a $\pi/2$ tipping pulse is applied to nuclear magnetization **M**. Finally a free induction decay (FID) signal produced by the precession of ^{1}H nuclei spins in the static magnetic field is detected and recorded. This experiment represents
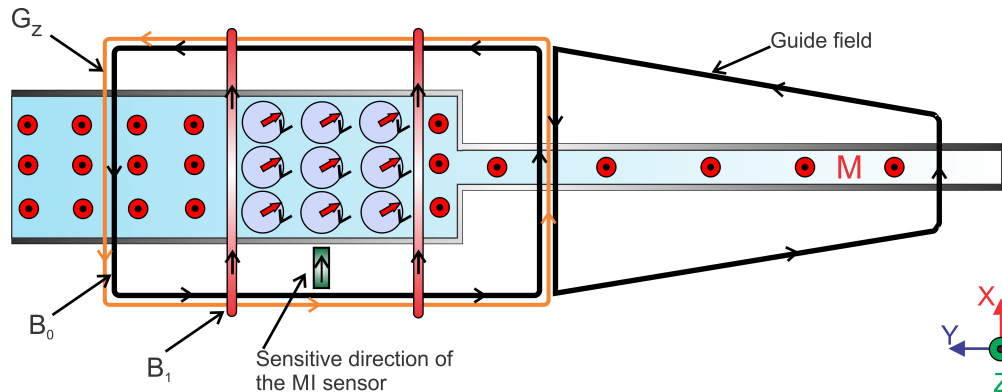
Figure 3.24: Side view of coils and the water-filled tube in the ULF region of the apparatus. The water is stationary (not moving) and the nuclear magnetization is initially aligned with the static field $\mathbf{B}_0$. When a tipping pulse is applied $\mathbf{M}$ is rotated into the transverse plane and precesses about $\mathbf{B}_0$. This is shown schematically in the diagram (Not to scale).

a critical step towards the spin dressing experiments described later in the thesis. The most important distinction between this experiment and those described previously, is that we now directly monitor the Larmor precession of the transverse nuclear magnetization rather than simply looking at modulated longitudinal magnetization patterns.

3.3.2.1 Apparatus

Figure 3.24 shows the ULF region of the apparatus, as configured for direct detection of the magnetic fields associated with Larmor precession. Unlike the case in Sec. 3.3.1 the AFP field was not used. The static field $\mathbf{B}_0$ was reconfigured to be more uniform, to obtain longer spin coherence times. Additionally, a coil intended to generate a linear gradient $\mathbf{G}_z$[17] in $\mathbf{B}_0$ along the z-axis to further improve field homogeneity was added. Finally a coil was added to generate $\mathbf{B}_1$ fields along the y-axis in order to be able to perform pulsed NMR.

The B_1 field is generated by a pair of circular Helmholtz coils. Each coil has two turns, with a diameter of 17 cm. They are separated by 8 cm. A function generator[18] was used to drive the $\mathbf{B}_1$ coils and create tipping pulses. The current amplitude was set to generate a $\pi/2$ rotation in 10 ms; hence the duration of a $\pi/2$ rotation corresponds to two periods of Larmor precession (or two cycles of the B_1 waveform). A pair of rectangular Helmholtz coils was used to generate the static field $\mathbf{B}_0$. Each coil has 9 turns and was wrapped on a former with dimensions 40 cm$\times$12 cm. The two coils were separated by 8 cm. A DC power supply[19] was used to control the currents used to produce $\mathbf{B}_0$ and $\mathbf{G}_z$. The coils that produce the linear field gradient $\mathbf{G}_z$ in the direction of the static field were generated by

---

[17]$d\mathrm{B}_z/dz$

[18]Stanford Research Systems model DS345.

[19]Agilent model E3631A
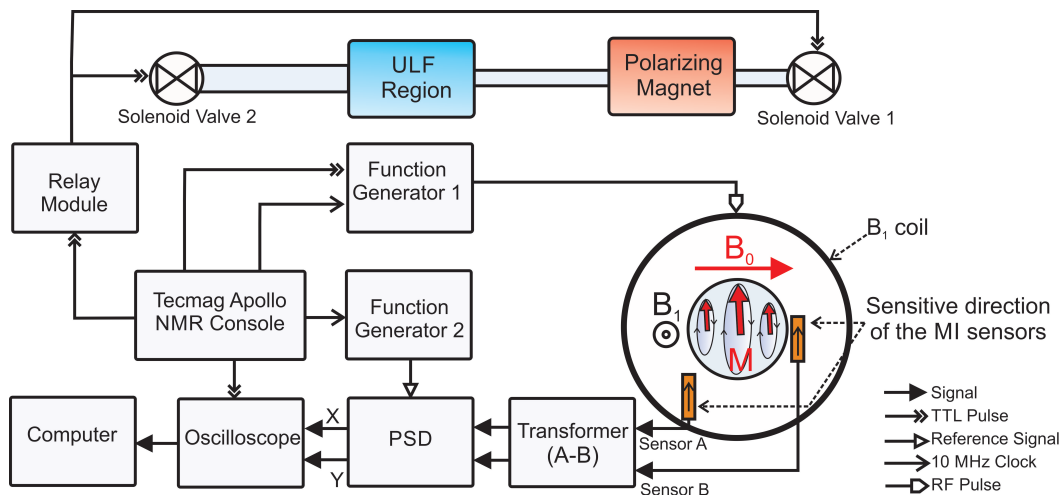
Figure 3.25: Overview of pulsed ULF NMR signal detection circuit. A Tecmag Apollo NMR console is used to control the sequence of events. A cross section of the tube containing the nuclear magnetization **M**, and indicating the position and orientation of the MI sensors, is shown.

two rectangular loops of wire that were wrapped on the static field coil former.

To start and stop water flow at appropriate times, two solenoid valves were employed. These were ASCO "normally-closed" solenoid valves. One valve was inserted at the water source (before the polarizing magnet) and the other was inserted at the outlet, downstream from the MI sensors. Both valves were controlled via relays driven by TTL pulses from a Tecmag Apollo NMR Console.

3.3.2.2 Signal Detection Circuit

The signal detection circuit employed for this experiment is shown in Fig. 3.25. A Tecmag Apollo NMR console is used to synchronize devices, and to initiate and control events. A key difference with respect to the previously described experiments is that data aquisition is now controlled by a sequence of pulses, rather than being run continuously. The function generator used to drive the B_1 coil (an Agilent 33250A 80 MHz arbitrary waveform generator) is programed to apply a synchronized train of pulses. I accomplished this using the Agilent Waveform Editor to produce Carr-Purcell-Meiboom-Gill (CPMG) tipping pulse trains [88, 89].

3.3.2.3 Results

Figure 3.26 summarizes the pulse sequences used for CPMG spin echo and FID experiments. These experiments are initiated by opening the two solenoid valves. Un-polarized ^{1}H nuclei
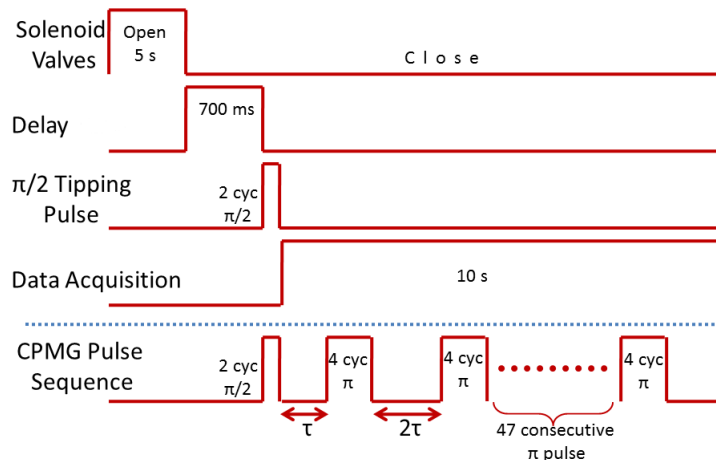
Figure 3.26: The sequence of events for a pulsed ULF NMR experiment in which the free induction decay of ^{1}H nuclei is observed. For the CPMG variant of this experiment, the $\pi/2$ tipping pulse is followed by a series of π pulses as shown at the bottom of the figure.
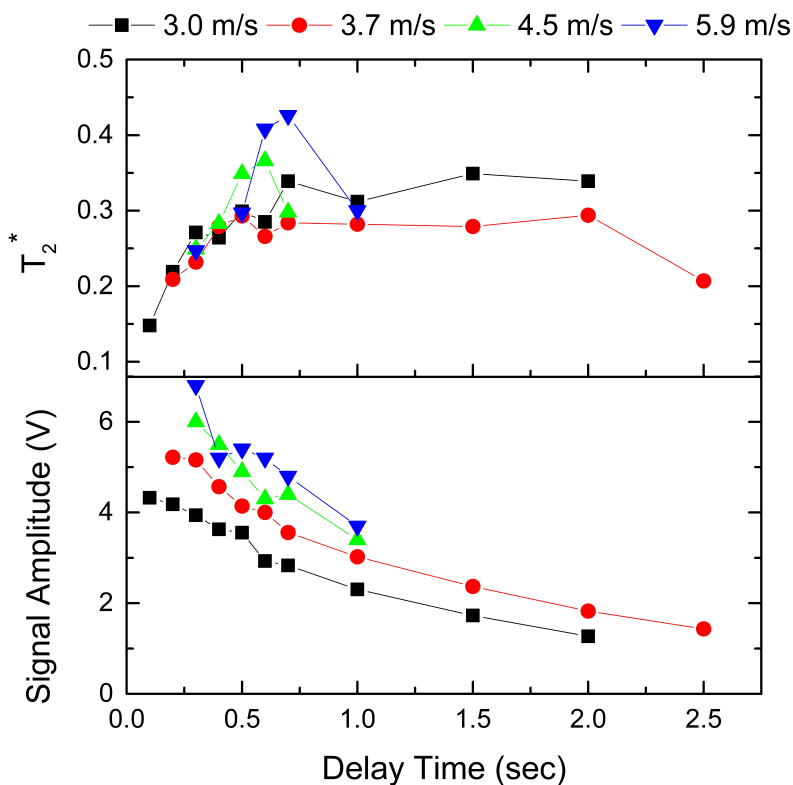
Figure 3.27: Signal amplitude and T_2^* relaxation time for stationary samples, having arrived at average speeds of 3.0 m/s (■), 3.7 m/s (●), 4.5 m/s (▲) and 5.9 m/s (▼), and after delay times as indicated. Lines are drawn as guides for the eye.

are flushed from the system and are replaced by polarized ^{1}H nuclei. The valves remain
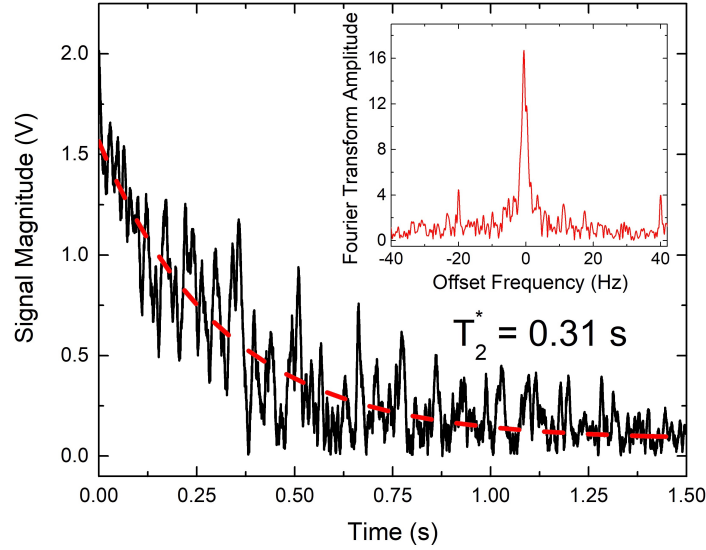
Figure 3.28: Single shot ^{1}H free induction decay signal and corresponding Fourier transform (inset). The Larmor frequency $f_L = 200$ Hz, the transverse relaxation time inferred from the FID is $T_2^* = 0.31$ s and the Full Width at Half Maximum of the resonance is ~ 2 Hz. Small spikes in the Fourier transform are associated with the 3rd and 4th harmonics of 60 Hz noise.
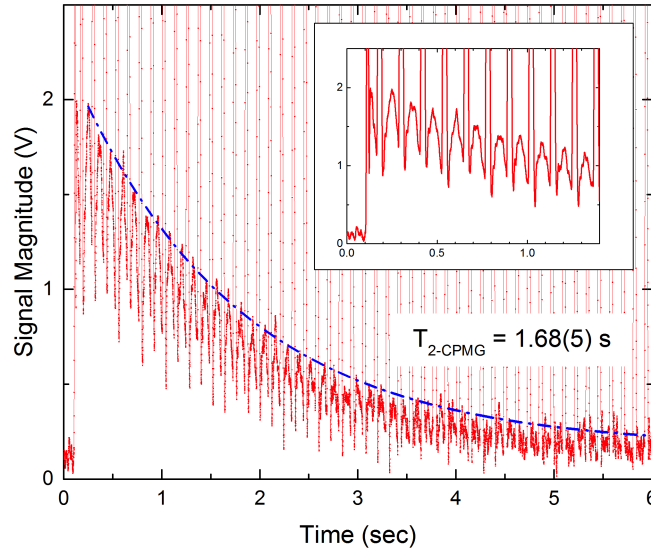
Figure 3.29: ^{1}H CPMG spin echo train at 4.7 μT. The vertical spikes separated by 100 ms are caused by the response of the MI sensors to the π pulses. The revivals between the π pulses are the echoes. Inset: Expanded view of the first 10 spin echoes.

open for a time ≥ 3 s and are then closed.[20] A delay is then imposed to allow eddies in

---

[20]After closing the valves the $\frac{3}{8}$" PVC tube becomes inflated slightly. This elastic deformation can influence eddies in the water. To minimize this effect I replaced the $\frac{3}{8}$" PVC tube with the same size copper tube. The only region in which the $\frac{3}{8}$" PVC tube is used after the flow expansion point is the first 25 cm length.

the water to decay. Next a $\pi/2$ tipping pulse is applied to rotate the nuclear magnetization **M** into the transverse plane, at which point the free induction decay of **M** is monitored by two MI sensors arranged in a gradiometer configuration. If desired, a coherent series of π pulses is applied to generate a CPMG spin echo train. A linear field gradient is typically applied during CPMG sequences, to shorten the spin-dephasing time. I employed a 10 ms $\pi/2$ pulse followed by 50 consecutive π pulses with duration 20 ms and zero initial phase for each pulse. Echoes thus form at $\tau = 50$ ms after each π pulse.

The average speed $\bar{v}$ of **M** and the delay after stopping the water flow need to be chosen appropriately because they influence the transverse relaxation time and the signal-to-noise (SNR) of the FID signals. To find optimum values I conducted a search, varying the water source pressure and delay time. Then I measured the transverse relaxation time and the magnitude of FID signals. Figure 3.27 shows the time constant T_2^* for the FID decay as a function of water speed and delay. Higher speeds yield higher signal amplitudes because depolarization is less of an issue, but the trade off is that the FIDs die off faster because of mixing that occurs as eddy currents in the water persist.

I chose to operate with a water source pressure of 30 psi yielding an average flow speed of $\bar{v} = 3.8$ m/s, and a 0.7 s delay time. Under these conditions, up to 6% of the nuclear magnetization leaving the 1.5 T polarization magnet reaches the ULF portion of the apparatus. Figure 3.28 shows an example of a single shot ^{1}H FID at 4.7 μT (recorded with an equivalent noise bandwidth of 41.6 Hz) exhibiting an SNR ~ 4. Because of the inhomogeneity in **B**$_0$, the FID signal decays on a time-scale of $T_2^* = 0.31$ s. For an exponential FID signal the corresponding Fourier transform is a Lorentzian function. And the Lorentzian Full Width at Half Maximum (FWHM) of the resonance is $1/\pi T_2$. This implies a FWHM ~ 1 Hz in my experiment.

Figure 3.29 shows data from a CPMG experiment. The MI sensors recover very quickly after the π pulses are applied enabling us to see the spin echo pattern. Since the nuclear magnetization is periodically refocused the influence of field inhomogeneity on T_2^* is eliminated and a much longer decay time $T_{2\text{CPMG}} = 1.68 \pm 0.05$ s is observed. This value is less than that observed in pure water (typically 3-4 s) because of impurities [90].[21]

3.4 Conclusion

The work discussed in this chapter shows that MI sensors can be used for ULF NMR, and thus represent a new experimental tool. The remainder of this thesis will focus on a specific application, but the potential of these sensors is much broader. For example, one could combine MI sensors with hyper-polarization methods as a powerful tool for j-coupling

---

[21]As an example, the clear PVC tubes used in the apparatus turn green over time, indicating copper oxidation.

spectroscopy [91], relaxometry [92, 93] and diffusometry [94]. MI sensors could also be integrated with microfluidic techniques to study flow patterns and average velocities, or to monitor the time evolution of the concentration of molecules in reactions without having tracers [95] such as fluorescent dyes that may influence the physical and chemical properties of the solvent [96].

In the next chapter I will describe a series of spin dressing experiments performed using MI sensors. The apparatus and techniques are a simple extension of the experiments described above.

Chapter 4

Spin Dressing Experiments

In this chapter I describe a simple, practical and robust method to explore ^{1}H nuclear spin dressing phenomena over a wide range of parameters. The use of Magneto-Impedance (MI) sensors for direct detection of the magnetic fields of precessing nuclei is a key element of the experiment. I will also report the observation of spin echo formation in response to the application of finite-duration dressing field pulses. A simple classical model of spin precession is used to explain and model this unanticipated effect.

The apparatus and the method of analysis that I describe in this chapter to observe spin dressing phenomena, only works for one spin species (^{1}H nuclei of water). In subsequent chapters (5 and 6) I will describe a refined version of the apparatus and introduce an improved method of analysis to explore spin dressing phenomena for other spin species.

4.1   Apparatus

The apparatus used to perform spin dressing experiments is the same as that described in Chapter 3 (Sec. 3.3.2) except it also includes a new coil to generate the dressing field $\mathbf{B}_\mathrm{d}$. A diagram showing the ULF portion of the apparatus is shown in Fig. 4.1.

As before, two solenoid valves are used to control the flow of polarized ^{1}H nuclei from the 1.5 T region to the μT region. These valves are installed at the inlet and outlet of the flow path. When the valves are open, tap water flows through the system at a steady rate of $\sim$40 ml/s and pushes the polarized nuclei from a 600 ml reservoir towards a well-shielded area where a pair of MI sensors reside. The water exits the polarizing magnet through a $\frac{1}{8}$ inch inner-diameter PVC tube aligned with the local static field $\mathbf{B}_0$, which decreases monotonically. As B_0 decreases the flow is gradually reoriented so that it ends up perpendicular to $\mathbf{B}_0$ (which is produced by the fringe field of the polarizing magnet and thus varies as a function of position). Thereafter the ^{1}H nuclear magnetization $\mathbf{M}$ is perpendicular to the tube axis (rather than parallel to it). Finally the tube's inner diam-
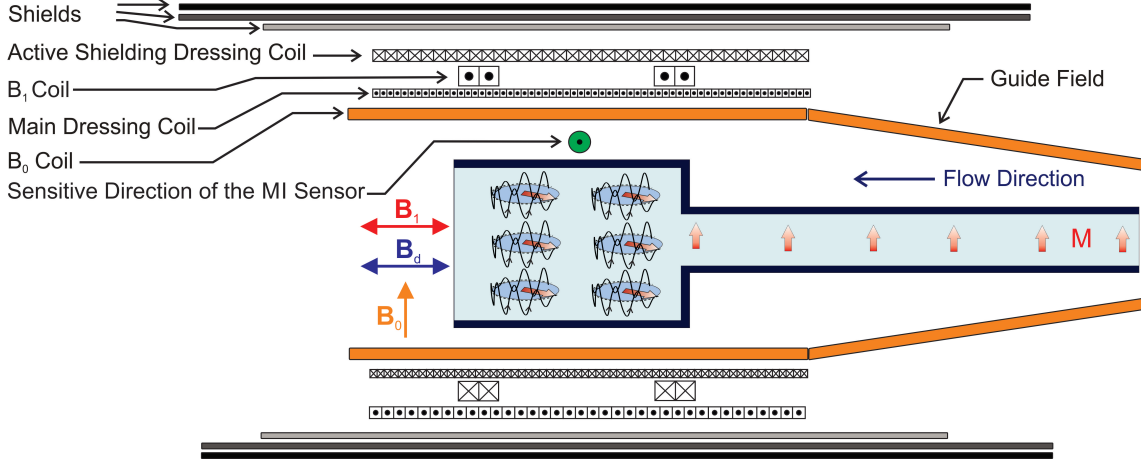
Figure 4.1: Overview of ultra-low-field region of the spin dressing apparatus. Nuclear spins in the centre of the apparatus are rotated into the transverse plane and then subjected to a dressing field that causes **M** to oscillate about the equatorial plane. This behaviour is shown schematically in the figure. Active shielding is employed to minimize screening currents in the magnetic shields.

eter is abruptly increased to $\frac{3}{8}$ inch just before it flows past two MI sensors arranged in a gradiometer configuration. This expansion is employed to increase the magnitude of the magnetic field $\mathbf{B}_M$ sensed by MI sensors. Recall that $\mathbf{B}_M$ is the field associated with the precessing nuclear magnetization **M**. Theoretically, the field B_M, due to an infinitely long cylinder with magnetization **M** perpendicular to its axis varies as the square of R/r [97], where r is the distance from the axis of the cylinder and R is the diameter of the cylinder. Thus the expansion (in tube diameter) from $\frac{1}{8}$ to $\frac{3}{8}$ inch results in a one order of magnitude increase in B_M at a given distance r.

Once polarized ^{1}H nuclear spins arrive at the sensors the solenoid valves are simultaneously closed to stop the flow. After a short time delay, to allow eddy currents in the water to subside, the resonant oscillating magnetic field $\mathbf{B}_1$, which is aligned with the axis of the tube, is applied to rotate **M** into the transverse plane, and nuclear spin precession is observed at the Larmor frequency f_L using the MI sensors. Next, during the FID and after a time period τ has elapsed, a strong off-resonant oscillating magnetic field $\mathbf{B}_d$ (the dressing field) is applied along the axis of the tube for a time period Δt. During Δt, the ^{1}H nuclei acquire a modified gyromagnetic ratio $|\gamma'| < \gamma$ that can be measured by monitoring the phase of **M** that is accumulated while the dressing field is applied. The time period between the application of $\mathbf{B}_1$ and $\mathbf{B}_d$ is chosen so that $\mathbf{B}_d$ always starts with a well-defined phase relationship with respect to $\mathbf{B}_1$. This phase relationship is established coherency is employed for all spin dressing and critical spin dressing experiments reported in this chap-
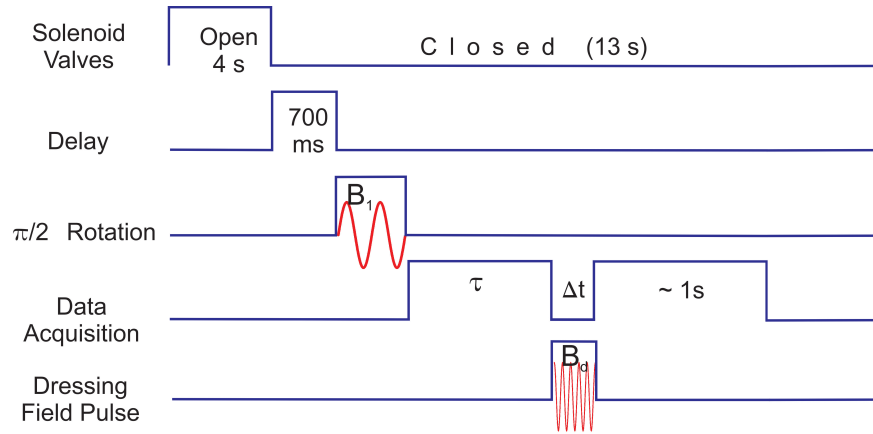
Figure 4.2: Sequence of events in a spin dressing experiment (Not to scale). TNMR software running on a TecMag Apollo NMR console was used to set the time and duration of each event.

ter and Ch. 6. Furthermore, a cosine waveform is employed for the applied dressing field.[1] Figure 4.2 shows the sequence of events in this measurement. The sequence is initiated by closing the solenoid valves.

4.1.1 Signal Detection Circuit

Figure 4.3 summarizes the various electronic components used to observe and record spin dressing phenomena. The sensor outputs are amplified by a low noise transformer and then fed into a phase sensitive detector (PSD). The output of the PSD can then be displayed on an oscilloscope or recorded as a computer data file using a Labview program. Three function generators were used to act as an oscillator for the PSD, to drive the $\mathbf{B}_1$ coil and to drive the $\mathbf{B}_d$ coil. The latter devices must be arbitrary waveform generators. I used a Stanford Research Systems model DS345 and Agilent model 33250A, which can be programmed using Arbitrary Waveform Composer (AWC) and Agilent Waveform Editor software, respectively. All of the function generators are synchronized to a 10 MHz reference clock generated by a Tecmag Apollo NMR Console. The entire experimental sequence is fixed to an integer number of periods of the reference oscillator, to simplify coherent superposition of FID responses when data are averaged. The duration and time of each event is set by TNMR software, running on the NMR console.

The output of the function generator that drives the $\mathbf{B}_d$ coil is fed to an audio power

---

[1] In preliminary experiments a sine waveform was employed and a discrepancy between observations and simulated data (based on the quantum model that was described in Ch. 2) was observed. No discrepancy was observed when a cosine waveform was employed.

Figure 4.3: Block diagram of circuit used to observe and record spin dressing phenomena. Event sequences are coordinated by TTL logic pulses generated by a Tecmag Apollo NMR console running TNMR Software.

amplifier[2] in order to generate an oscillating magnetic field that is much stronger than $\mathbf{B}_0$. Several precautions related to the use of this audio amplifier are noted below:

- Any small DC current offset associated with the amplifier must be avoided, to avoid introducing a static magnetic field in the wrong direction. I used a summing amplifier to add an adjustable DC offset to the input of the audio amplifier, to ensure that the DC component of the output could be set to zero. I also inserted high power noise gates[3] on the output of the amplifier to keep noise from being fed to the experiment when the amplifier was in a quiescent state.

- Direct monitoring of the audio amplifier output current tends to influence $\mathbf{B}_d$ and adds 60-cycle noise. An optically-isolated current monitor circuit, as shown in Fig. 4.5, was used to measure the current delivered to the dressing field coil with good success.

- Maximum power transfer for this amplifier ($\sim$1.5 kW at 1 kHz) occurs for a load impedance of 3 - 4 Ω. I inserted a 10 Ω (20 watt) load in series with the $\mathbf{B}_d$ coil to bring down the maximum available power to $\sim$ 700 W at 1 kHz. Since the load was only rated for a fraction of the amplifier power, it was important to avoid driving a continuous high-amplitude current with the amplifier. Otherwise the load and coils would be damaged.

---

[2]Crown M-600 amplifier with a frequency response spanning DC - 20 kHz.

[3]Two back-to-back pairs of Diodes Incorporated model 10A05 diodes, which can handle 10 A of continuous current.

4.1.2 Dressing Field Design

The dressing field $B_d(t)$ is generated by running currents through two coaxial solenoids. I refer to the inner coil as the main coil and the outer coil as an active shield [86]. The coils have different diameters and numbers of turns but carry the same current (in opposite senses). The active shield coil minimizes eddy currents in the permalloy shield during and after generation of the dressing field $\mathbf{B}_d$. It is designed such that the total magnetic moment of the pair of current-carrying coils is zero. To achieve this, for coaxial coils labelled by indices 1 and 2 we have

$$N_1 R_1^2 = N_2 R_2^2 \tag{4.1}$$

where N is the number of turns and R is the radius of each coil. For a finite length solenoid the field produced at the center of the coil is

$$\mathrm{B}_{in} \; = \; \frac{\mu_0 N \mathrm{I}}{\sqrt{l^2 + 4R^2}} \tag{4.2}$$

where l is the length of coil. The field produced at the center of the two concentric solenoids is thus given by

$$\mathrm{B}_{in} = \mu_0 \mathrm{I} \left(\frac{N_1}{\sqrt{l^2 + 4R_1^2}} - \frac{N_2}{\sqrt{l^2 + 4R_2^2}} \right). \tag{4.3}$$

I used Eq. 4.1 to choose the appropriate dimensions for the dressing field coils. I chose $R_1 = 8.5$ cm, $N_1 = 75$ turns and $R_2 = 10.6$ cm, $N_2 = 48$ turns for the main and the active shielding coils, respectively. Both of the coils are $l = 20$ cm long. The winding density of the main coil is uniform but the winding density of the active shielding coil is only semi-uniform. It consists of 45 turns which are distributed uniformly and 9 extra turns. I refer to these as compensation loops. The current through 6 of these loops is in the same sense as in the active shielding coil while the current through the other 3 loops is in the opposite sense. Physically the combination of the active shielding and compensation loops amounts to 54 turns. But, the combination is equivalent to a net 48 turns carrying current in the same direction. The positions and senses of the current through the compensation loops are chosen by trial and error so that: the magnetic moment of the active shielding coil is the same as that of the main coil and the total magnetic field outside of the coils is as small as possible for a given current. Table 4.1 summarizes the location of compensation loops relative to the center of the dressing coils as well as the sense of the current they carry. Also Table 4.2 lists characteristics of the dressing coils.

I also used the BiotSavart software package [87] to model the field produced by both coils, both inside and outside. Figure 4.4 shows the calculated relative amplitude profile of the dressing field along various transverse and longitudinal axes. The active shield and compensation loops reduce the axial component of $\mathbf{B}_d$ on the permalloy shield (radius 13 cm)

Position (cm)	0	±1.2	±9.0	±11.0	±12.6
Current Direction	+	-	+	-	-

Table 4.1: Relative location and current through compensation loops. Current through the main coil is assumed to be positive (+) while that through the active shielding coil is negative (-). Positions are measured relative to the center of the coils.

	R (cm)	N	l (cm)	L (μH)	R (Ω)
Main coil	8.5	75	20	577.8(1)	1.452(1)
Active shield coil	10.5	45	20	325.1(1)	1.173(1)

Table 4.2: Dressing coil characteristics. Radius (R), number of turns (N), length (l), inductance (L) and DC resistance (R) of the dressing coils. The resistance and inductance were measured using a Stanford Research Systems model SR720 LCR meter.
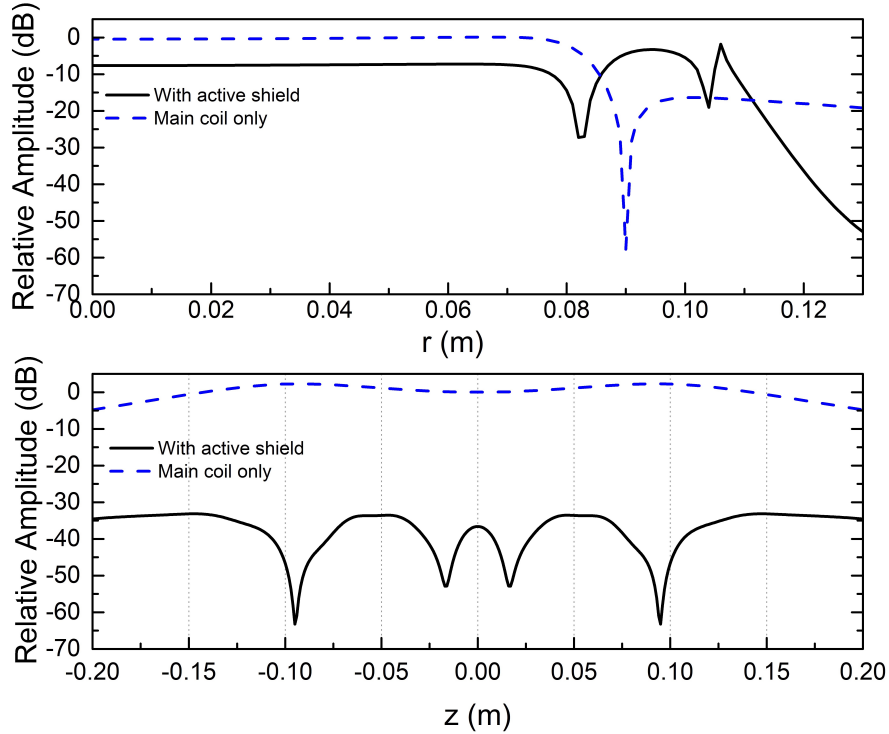
Figure 4.4: Calculated relative dressing field amplitude along various axes illustrating the influence of active shielding. Transverse and longitudinal profiles for the axial component (z direction) of dressing field are plotted on the top and bottom respectively. The former is calculated at $z = 0$ and the latter at $r = 13$ cm where the wall of the permalloy shield is located. All curves are referenced to the field at the midpoint of the main coil.

by a factor 40 and at the centre of the dressing coil by a factor of 2.5.
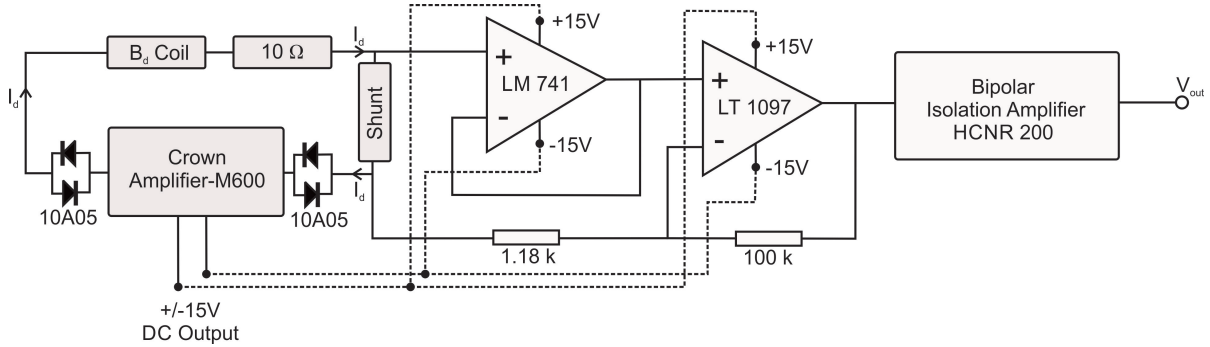
Figure 4.5: Optically-isolated current monitor circuit. Current flow through the shunt resistor is buffered amplified and then passed through a bipolar optical-isolation stage. The back-to-back diodes act as noise gates.

B_d vs. I_d (Experiment)	$B_d^* = -0.14(1) + 1.590(6)\ I_d^{**}$
B_d vs. I_d (Simulation[†])	$B_d = 1.57\ I_d$
B_d vs. I_d (Simple theory[‡])	$B_d = 1.52\ I_d$

Table 4.3: Calibration of dressing field B_d against current flow I_d through the dressing field coil. * Measured in Gauss; ** Measured for $I_d > 0.5$ A; [†] Using the BiotSavart software package; [‡] Using Eq. 4.3.

4.1.3 Dressing Field Calibration

I used a Group 3 gaussmeter[4] to measure B_d and thus calibrate the dressing parameter x in terms of the current used to generate the dressing field. Recall that $x = \gamma B_d / \omega_d$. In detail, there are three steps to the calibration procedure. First, the AC gain of the gaussmeter (which responds to fields over the range 8 Hz - 3 kHz) is calibrated against very high accuracy DC mode readings acquired using the same device. This was accomplished using magnetic fields generated by a reference coil, employing identical measured AC and DC currents. Next, the response of the optically-isolated current monitoring circuit to current flow through a shunt resistor in the audio amplifier was characterized; see Fig. 4.5. Finally, the optocoupler output was calibrated against measured AC dressing field amplitudes. Once these calibrations are combined and accounted for the AC magnetic (dressing) fields inferred from the current monitor output agree with expectations based on geometry at the 1% level. Table 4.3 summarizes the relationship between B_d and I_d obtained from the calibration, from the Biotsavart field modelling software, and from Eq. 4.3. Figure 4.6 shows B_d at low currents. The non-linearity in this regime comes from the optocoupler and the noise gate diodes.

---

[4]Digital Teslameter model DTM-151 with miniature high sensitivity Hall probe model MPT-231. Teslameter zero drift: $\pm(1\ \mu T + 0.0003\%$ of full-scale$)/^\circ$C max.

$B_d = -0.122(8) + 1.43(6)\, I_d + 0.3(1)\, I_d^2 - 0.24(7)\, I_d^3 + 0.05(1)\, I_d^4$

$B_d = -0.14(1) + 1.590(6)\, I_d$
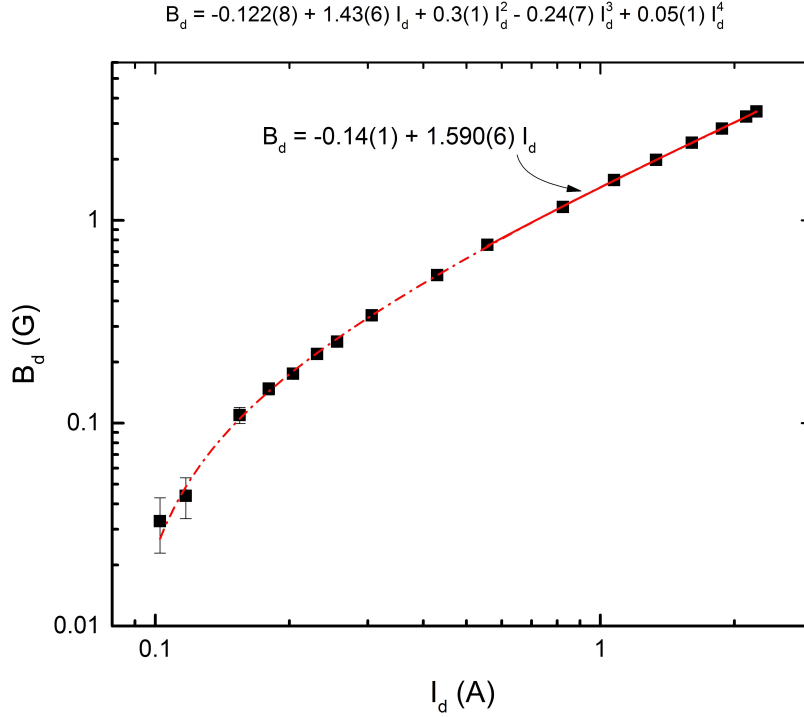
Figure 4.6: Measured RMS dressing field B_d in terms of the current passing through the dressing field coil I_d. The data are fit by a 4th order polynomial function (- . -) over the entire current range, and by a linear function (—) for $I_d > 0.5$ A.

4.2 Data Analysis Method

In the spin dressing experiment I monitor the average precession rate $\bar{f}_L$ of the dressed nuclear spins to infer their modified gyromagnetic ratio γ'. The experimental data that I use is the free-induction-decay (FID) signal of a precessing nuclear magnetization $\mathbf{M}$ whose precession rate changes whenever the dressing field is applied. In my experiment these signals are sensed by the MI sensors. But, upon application of the dressing field pulse the sensors saturate.[5] Thus a direct measurement of the average precession rate from FID data during the dressing field pulse is not feasible. However, the phase of the FID signal before and after application of the dressing field pulse can be used to reveal $\bar{f}_L$. When the dressing field pulse is applied, the precession rate of $\mathbf{M}$ changes. In turn this influences the phase of the FID signal. This results in a phase lag or lead in the FID signal depending on whether $\bar{f}_L$ is less than or greater than the normal precession rate. In my experiment I measure these phase variations in the FID signals.

I recorded FID signals before and after applying a finite-duration dressing field $\mathbf{B}_d = B_d \cos(\omega_d t)\ \hat{x}$ and determined the change in phase that occurred because of the modified

---

[5]The sensitive axes of the MI sensors are supposed to be perpendicular to $\mathbf{B}_d$. However, if they are not then any small projection of $\mathbf{B}_d$ on the sensitive axis of a sensor can potentially cause it to saturate.
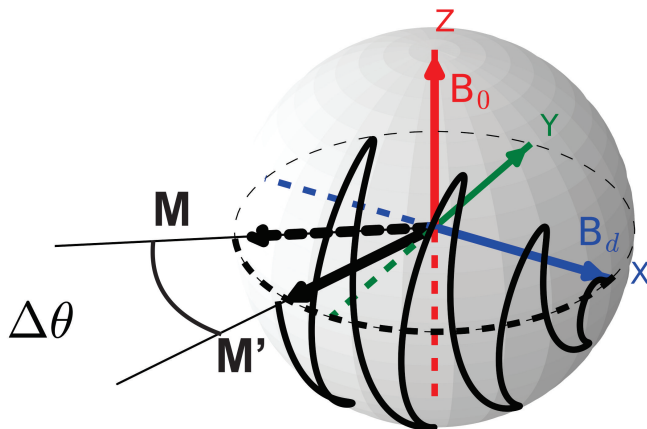
Figure 4.7: Semi-classical trajectories of dressed (–) and undressed spins (- -), on the surface of the Bloch sphere, under conditions where the spin dressing parameters $y = 0.1$ and $x = 1.0$. The incremental phase $\Delta\theta$ corresponds to the angle between $\mathbf{M}$ and $\mathbf{M}'$, the time averaged magnetization vectors for undressed and dressed spins, respectively. The difference arises from the application of the dressing field.

gyromagnetic ratio γ' that was temporarily acquired by the ^{1}H nuclei. If ω and ω' denote the angular Larmor frequencies of undressed and dressed spins in a static field $B_0 \, \hat{z}$, then the incremental phase change incurred as a result of applying $\mathbf{B}_d$ for a time Δt is

$$
\begin{aligned}
\Delta\theta &= (\omega' - \omega)\Delta t \\
&= B_0(\gamma' - \gamma)\Delta t.
\end{aligned}
\tag{4.4}
$$

Figure 4.7 illustrates a phase lag graphically, on the Bloch sphere, for spin dressing conditions where $y < 1$. In terms of the frequency f_L, N cycles of a dressing field $\mathbf{B}_d$ applied at frequency f_d yields

$$
\Delta\theta = 2\pi N \frac{f_L}{f_d}(\frac{\gamma'}{\gamma} - 1),
\tag{4.5}
$$

or in terms of the dressing parameters x and y

$$
\Delta\theta = 2\pi N y \left[J_0(x) - 1 \right],
\tag{4.6}
$$

as long as $y \ll 1$. Otherwise a numerical solution for γ'/γ (instead of the zeroth-order Bessel function) must be employed as described in Ch. 2. The maximum absolute value of the right hand side of Eq. 4.6 is $2.8\pi N y$ which occurs when $J_0(x)$ assumes its lowest value, which is -0.40. As long as N is small, $\Delta\theta$ is less than 2π and a measurement of $\Delta\theta$ is direct and unambiguous for any values of x. If the maximum value of $\Delta\theta$ exceeds 2π then a series of measurements of $\Delta\theta$ for values of x less than the value in which we are interested is needed. In this way we can count the number of complete rotations in phase and get the
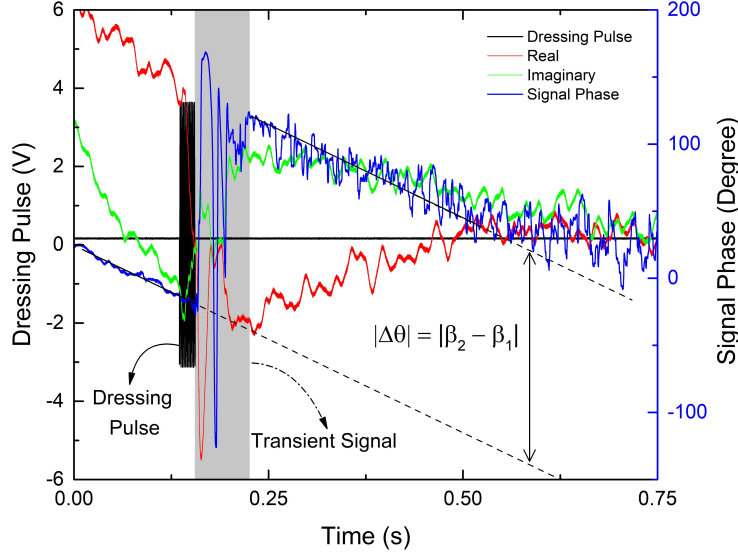
Figure 4.8: Example of FID data from a ^{1}H spin dressing experiment at $y = 0.4$ and $x = 12.17$ with $f_L = 200$ Hz and $f_d = 500$ Hz. A 20 ms dressing field pulse was applied. The various traces correspond to the (—) real part of the signal, the (—) imaginary part of the signal, the (—) phase of the signal and the (—) dressing pulse waveform. The phase of the signal is plotted in degrees as indicated on the right axis. The phase of the signal, before and after the dressing field pulse, is fit with two linear functions with the same slope. The difference between intercepts of the fit lines (θ_1 and θ_2) represents the phase lag $\Delta\theta$. The transient signals due to application of the dressing field pulse are shown in the grey area.

correct value of γ'.

Figure 4.8 shows complex FID data referenced to a 200 Hz local oscillator. The phase of the signal clearly changes after a 20 ms dressing field pulse is applied at 500 Hz, corresponding to a 10 cycle-long B_d waveform. Provided the Larmor frequency is very close to the local oscillator, then the phase lag $\Delta\theta$ can be calculated by fitting the FID phase data with two linear functions[6]

$$\theta_{\text{before}} = \alpha t + \beta_1 \tag{4.7}$$

$$\theta_{\text{after}} = \alpha t + \beta_2 \tag{4.8}$$

where θ_{before} and θ_{after} are the FID phase before and after the dressing field pulse, respectively. The fit functions must have the same slope but can acquire different intercepts. The difference between the intercepts,

$$\Delta\theta = \beta_2 - \beta_1 \tag{4.9}$$

---

[6]Note that the linear phase drift evident in Fig. 4.8 simply reflects a 0.48 Hz frequency offset between the Larmor frequency and the local oscillator.

which is in units of Volts, represents $\Delta\theta$. I map this value for $\Delta\theta$ into units of degrees and use Eq. 4.5 to calculate γ'/γ. For all of the data presented in this chapter I used this data analysis protocol. The method is simple, quick and practical. However, it only works for one spin species.

A more sophisticated approach is to offset the local oscillator from the Larmor frequency. Then the real and imaginary FID signals behave like damped sinusoids. These signals can be fit with model damped sinusoidal functions. The phase of the signals can then be extracted from the fitting parameters. And consequently one can calculate the phase lag $\Delta\theta$. This approach to data analysis is more complex than the linear fit function method described above. However, it works for two or any number of spin species that are simultaneously dressed. I will demonstrate this method of analysis in Chapter 6 when I discuss critical spin dressing of ^{1}H and ^{19}F.

4.3   Results

In the following subsections, I demonstrate first the results of spin dressing experiments on ^{1}H nuclei in two different regimes: $y < 1$ and $y > 1$. Recall that $y = \gamma B_0/\omega_d$. These results are compared with simulated values obtained from the quantum model that I described in Ch. 2. Second, the observation of spin echo formation in response to an off-resonant dressing field is investigated. Note that all data presented in this chapter are obtained for ^{1}H nuclei of water. So all references to γ, γ' or Larmor frequency f_L correspond to values for ^{1}H nuclei.

4.3.1   Spin Dressing Experiment: $y < 1$

In the regime $y < 1$, and therefore $|\gamma'/\gamma| < 1$, the phase shift $\Delta\theta$ is always negative (i.e. it is a phase lag). This is consistent with the experimental data for γ'/γ at $y = 0.4$ shown in Fig. 4.9. These data were acquired at $B_0 = 4.69$ μT (corresponding to $f_L = 200$ Hz) with a dressing frequency $f_d = 500$ Hz and variable dressing field amplitudes up to $B_d = 470$ μT. They were acquired with an equivalent noise bandwidth of 27 Hz. They prompt two observations. First, they are generally consistent with expectations based on perturbation theory, as outlined in Ch. 2 section 2. That is $\gamma'/\gamma = J_0(x)$. Second, this measurement probes a much broader range of the dressing parameter x than has been explored previously [37, 38, 36].

If the dressing parameter y is increased, so that it approaches $y = 1$, measured values of γ'/γ deviate from $J_0(x)$. This deviation is only significant for small values of x. Figure 4.10 shows two additional measurements of γ'/γ as a function of x, for $y = 0.2$ and $y = 0.8$. These measurements were performed with $f_d = 1$ kHz, at $f_L = 200$ Hz (for $y = 0.2$) and $f_L = 800$ Hz (for $y = 0.8$). The dressing field pulse was 10 ms long for $y = 0.2$
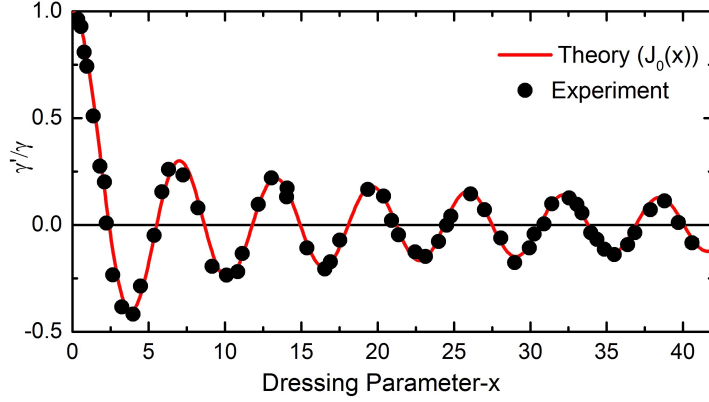
Figure 4.9: Measured modified ^{1}H Gyromagnetic ratio ($\bullet$) for dressing parameters $y = f_{\mathrm{L}}/f_{\mathrm{d}} = 0.4$ and $0 < x < 40$. Note that γ'/γ is expected to be equal to the zeroth-order Bessel function $J_0(x)$ in the limit $y \ll 1$ (—).
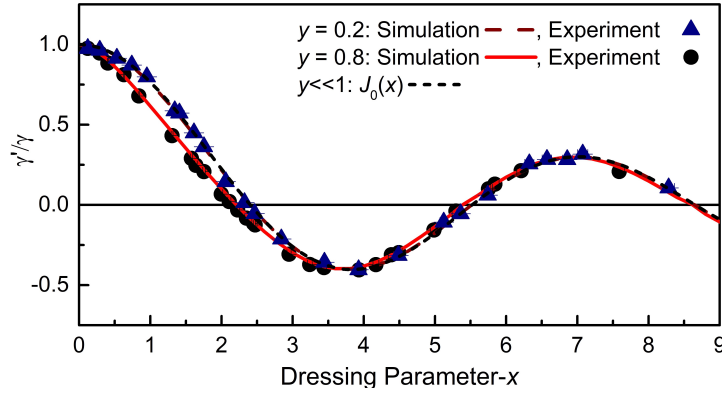
Figure 4.10: Modified ^{1}H Gyromagnetic ratio as measured with $f_{\mathrm{d}} = 1$ kHz and $f_{\mathrm{L}} = 200$ Hz ($\blacktriangle$) and $f_{\mathrm{L}} = 800$ Hz ($\bullet$); also shown are semi-classical simulations for $y = 0.2$ (dashed line) and $y = 0.8$ (solid line). As expected, no significant difference was observed between results at $y = 0.2$ and the zeroth-order Bessel function $J_0(x)$ expected for $y \ll 1$ (short dashed line).

and 3 ms long for $y = 0.8$. The ability of this experiment to resolve variations in γ'/γ for different values of y is indicative of its potential, and plays an important role in our later exploration of critical spin dressing at small values of x.

4.3.2 Spin Dressing Experiment: $y > 1$

I performed a series of measurements in the regime $y > 1$ to explore γ', and in many situations I observed discrepancies between experiment and simulations[7] particularly at large values of x. However, at small values of x the experiment and simulation are consistent. Figure 4.11 shows data for γ'/γ at $y = 1.28$ and $y = 2.0$ (corresponding to $f_{\mathrm{d}} = 500$ Hz

---

[7]Obtained from the quantum model described in Ch. 2 Sec. 2.
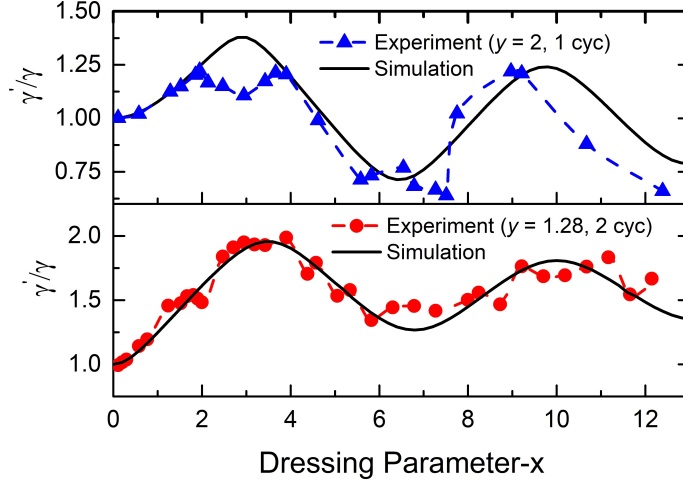
Figure 4.11: Modified gyromagnetic ratio as measured with $f_d = 500$ Hz and $f_L = 640$ Hz ($-\bullet-$, y = 1.28, 2-cycle pulse duration) and $f_L = 1$ kHz ($-\blacktriangle-$, y = 2.0, 1-cycle pulse duration). In both cases the experimental data are compared with simulations that are obtained from the quantum model as described in chapter 2. Dashed lines are merely a guide for the eye.

and $f_L = 640$ Hz and $f_L = 1$ kHz). The dressing field pulse durations for these experiments were 2-cycles long (for $y = 1.28$) and 1-cycle long (for $y = 2.0$). Surprisingly, in most of these experiments I observed the formation of echoes in FID signals. This unanticipated observation complicates determination of the phase shift and hence the modified gyromagnetic ratio. But, it is an intriguing observation in of itself, and is explored in the next section.

It is interesting to note that in previous studies of spin dressing [38], data for γ'/γ were only reported up to $x = 0.5, 1.0, 1.5, 2.75$ and 4.5 for $y = 1.10, 1.5, 2.5, 4.5$ and 7.5, respectively. One might ask why in Ref. [38] no experimental data are reported at high values of x? Was the discrepancy that I observed in my experiments at $y > 1$ also observed there?

4.3.3 Off-Resonant Spin Echo

Spin echoes were discovered by Erwin Hahn [98] in 1950 and later developed by Herman Carr and Edward Purcell [88]. In a conventional spin echo a dephased transverse component of the nuclear magnetization is inverted by a single π pulse (or a train of π pulses) following an initial on-resonant $\pi/2$ pulse. This results in a revival of the transverse nuclear magnetization that is called a spin echo. There are numerous versions of spin echo pulse sequences [99, 100], all of which involve applying on-resonant π pulses. In this subsection, I demonstrate spin echo formation in response to far off-resonant dressing field pulses.

4.3.3.1 Observation
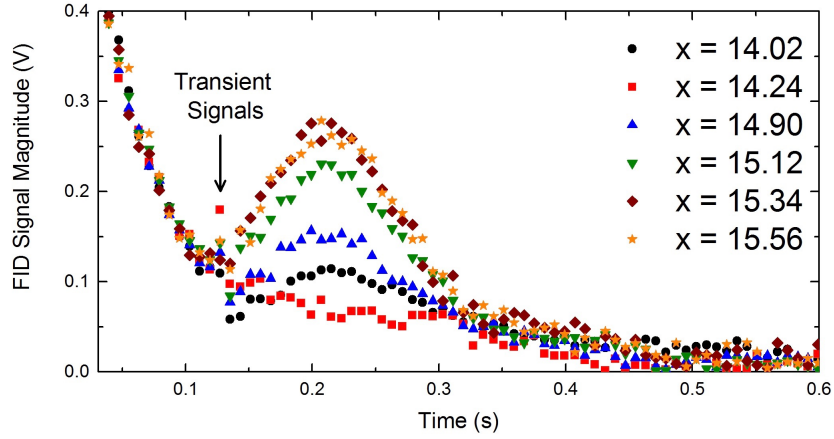
Figure 4.12: Magnitude of FID signals at $y = 7.14$ for different dressing parameters x. The FID signals are recorded following a $\pi/2$ tipping pulse applied at time $t = 0$. A single cycle dressing pulse duration is applied at $t = 120$ ms after the tipping pulse and a strong revival of the transverse magnetization (an echo) is observed at $t \sim 215$ ms in the vicinity of $x \sim 15$. The transient signals associated with application of the dressing pulse is indicated by an arrow.

During investigations of γ'/γ for $y > 1$, I observed FID signals that did not decay at anticipated rates, and which showed evidence of echo formation. The observation of echoes, or a revival of the transverse nuclear magnetization, during spin dressing experiments seems counter-intuitive because the pulsed dressing fields are applied at frequencies far away from resonance. At first I thought that the effect might be caused by imperfect or misaligned dressing fields or even by eddy currents in the water. But, as I acquired more data I started to see that they formed in a quasi periodic pattern in terms of the dressing parameter x. Moreover, I performed two measurements that convinced me the off-resonant echo formations are due to a real and systematic effect. First, I observed that the echo peaks were not suppressed by signal averaging. Second, echo trains, analogous to those generated in CPMG experiments, can be generated when a train of off-resonant dressing pulses are applied. Data associated with these two observations are discussed below.

Figure 4.12 shows the magnitude of FID signals at $y = 7.14$ for different values of x, revealing very clear revivals of the transverse nuclear magnetization. Each trace represents the average of four acquisitions. In this particular set of experiments, the Larmor frequency was $f_L = 4$ kHz, and the dressing field frequency was $f_d = 560$ Hz. Figure 4.13 shows data illustrating the formation of an echo train in response to repeated applications of a far off-resonant dressing field pulse that was selected to produce large revivals. The 2.0 s decay time inferred from these data is similar to that observed when a conventional pulse train composed of on-resonant π pulses is employed.
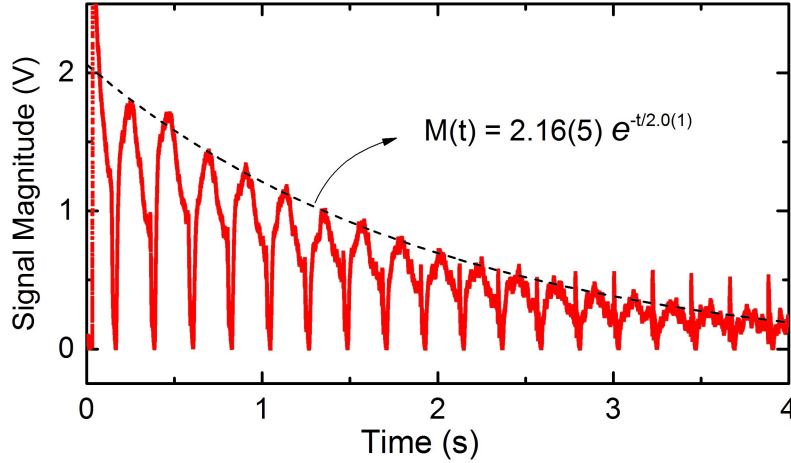
Figure 4.13: Echo train generated by applying 5 cycle-long dressing field pulses with $x = 1.93$ and $y = 2.0$ ($f_L = 1$ kHz; $f_d = 500$ Hz) every 200 ms. The peak echo amplitude decays with a time constant comparable to that observed when a CPMG echo train is generated.

Now let us discuss the parameters than can influence off-resonant echo formation. As I observed, the duration of the dressing field and dressing parameter y can strongly affect echo formation. To demonstrate the contribution of these two parameters we need a parameter to quantify echo formation. To quantify the revival of transverse nuclear magnetization I introduce a figure of merit χ defined such that

$$\chi = \frac{A(x)}{A_0} \tag{4.10}$$
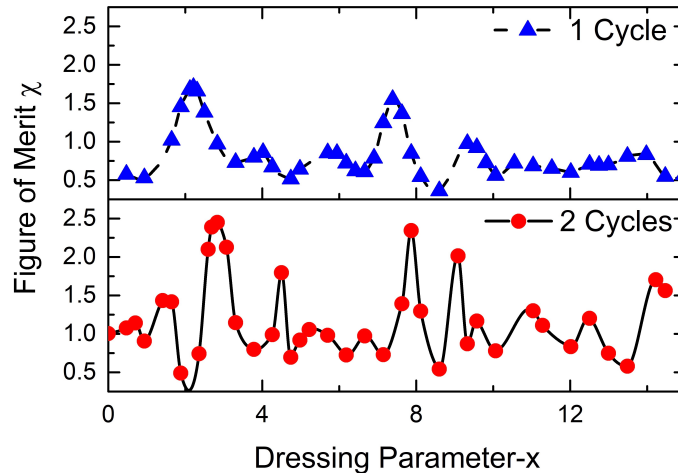
Figure 4.14: Figure of merit χ at $y = 2.0$ ($f_d = 500$ Hz and $f_L = 1$ kHz) for 2 ms (top) and 4 ms (bottom) dressing field pulses. The longer pulse results in stronger and more frequent echoes. Lines are drawn as a guide for the eye.
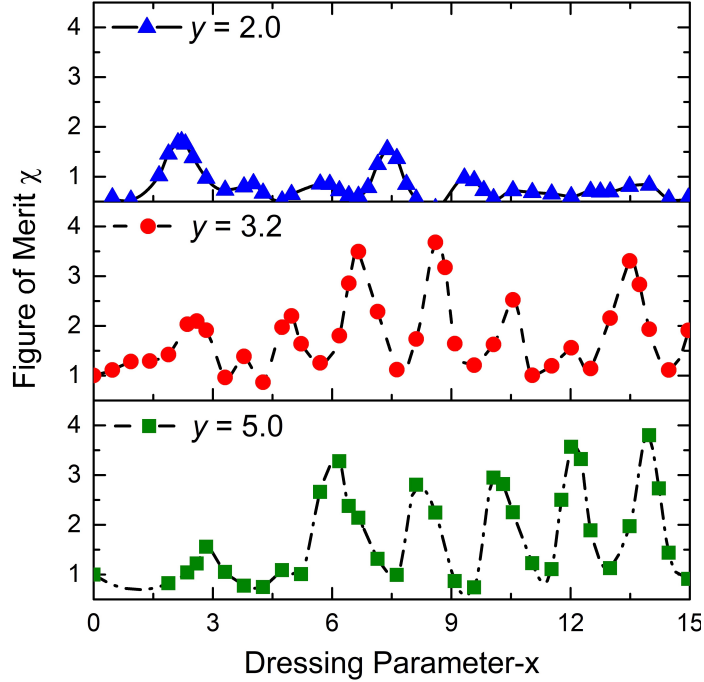
Figure 4.15: Figure of merit χ for fixed dressing field pulse duration at different values of y acquired with $f_d = 500$ Hz and $f_L = 1.0$ kHz (top); $f_L = 1.6$ kHz (middle); $f_L = 2.5$ kHz (bottom). Dashed lines are merely a guide for the eye.

where $A(x)$ is the area under the FID signal after a dressing field pulse characterized by the dressing parameter x and A_0 is the corresponding area when $x = 0$. Thus $\chi > 1$ reflects a revival of the transverse nuclear magnetization while $\chi < 1$ reflects a suppression. The latter can arise when the dressing field pulse transfers transverse nuclear magnetization to the longitudinal axis of the Bloch sphere.

Figure 4.14 shows an example of the figure of merit χ in terms of x for $y = 2$ and for two different dressing field pulse durations, acquired with $f_L = 1$ kHz and $f_d = 500$ Hz. The peaks that are evident represent conditions where echoes form. Varying the duration of the dressing field pulse influences the pattern that is observed. Figure 4.15 shows data for χ at different values of y following a single-cycle dressing field pulse at $f_d = 500$ Hz. The pattern of echoes is stronger and more clearly resolved at $y = 5$ than it is at $y = 2$.

4.3.3.2 Classical Model of Spin Precession and Off-Resonant Echo

In an attempt to gain some insight into the formation of echoes in response to pulsed dressing fields, I developed a simple classical model of spin precession in the presence of a linear field gradient. I assumed that the phases of spins precessing in the transverse plane

are initially distributed uniformly, such that

$$\phi_i = \pm 2\pi (1 - \frac{i}{N}) \tag{4.11}$$

where $2N + 1$ is the total number of spins considered. I further assumed that the Larmor precession frequencies of the spin with initial phase $\phi = 0$ is f_L. These initial conditions are intended to represent the transverse nuclear magnetization "long after" the initial $\pi/2$ pulse in my experiments. With these simple initial conditions, I then integrated the equations of motion (Bloch equations [101]):

$$
\begin{aligned}
\frac{d\text{M}_x}{dt} &= \gamma \text{M}_y \text{B}_0 - \frac{\text{M}_x}{\text{T}_2}, \\
\frac{d\text{M}_y}{dt} &= \gamma \text{M}_z \text{B}_d(t) - \gamma \text{M}_x \text{B}_0 - \frac{\text{M}_y}{\text{T}_2}, \\
\frac{d\text{M}_z}{dt} &= -\gamma \text{M}_y \text{B}_d(t) - \frac{\text{M}_z}{\text{T}_1}
\end{aligned}
\tag{4.12}
$$

where T_1 and T_2 are the usual longitudinal and transverse relaxation times, respectively. The time t runs from 0 to t_2. I assumed at $t = 0$ the nuclear spins have the phase distribution given by Eq. 4.11 because of the linear field gradient $\text{G}_z \, \hat{z}$. For times after $t = 0$, the magnetic field in which spin precession takes place is

$$
\begin{aligned}
(\text{B}_0 + \text{G}_z) \, \hat{z} + \text{B}_d \, \cos(2\pi f_d t) \, \hat{x} \qquad & 0 \leq t \leq t_1 \\
(\text{B}_0 + \text{G}_z) \, \hat{z} \qquad & t_1 \leq t \leq t_2.
\end{aligned}
\tag{4.13}
$$

Equations 4.12 were numerically integrated[8] using *integrate.odeint* module from the open source *Scipy* library of scientific tools, which uses the LSODA[9] module from the FORTRAN library *odepack*.[10] By solving the differential equations in Eq. 4.12 for $2N + 1$ discrete spins[11] and summing, the total magnetization in x-y plane is simply

$$
\begin{aligned}
\text{M}_x &= \sum_{i=1}^{2N+1} \text{M}_{ix} \\
\text{M}_y &= \sum_{i=1}^{2N+1} \text{M}_{iy} \\
\text{M}_{xy}(t) &= \sqrt{\text{M}_x^2 + \text{M}_y^2}.
\end{aligned}
\tag{4.14}
$$

---

[8] Employing $\text{T}_1 = 2$ s and $\text{T}_2 = 0.1$ s.
[9] Ordinary differential equation solver for stiff or non-stiff systems.
[10] Ordinary differential equation package.
[11] I employed $N = 10$.
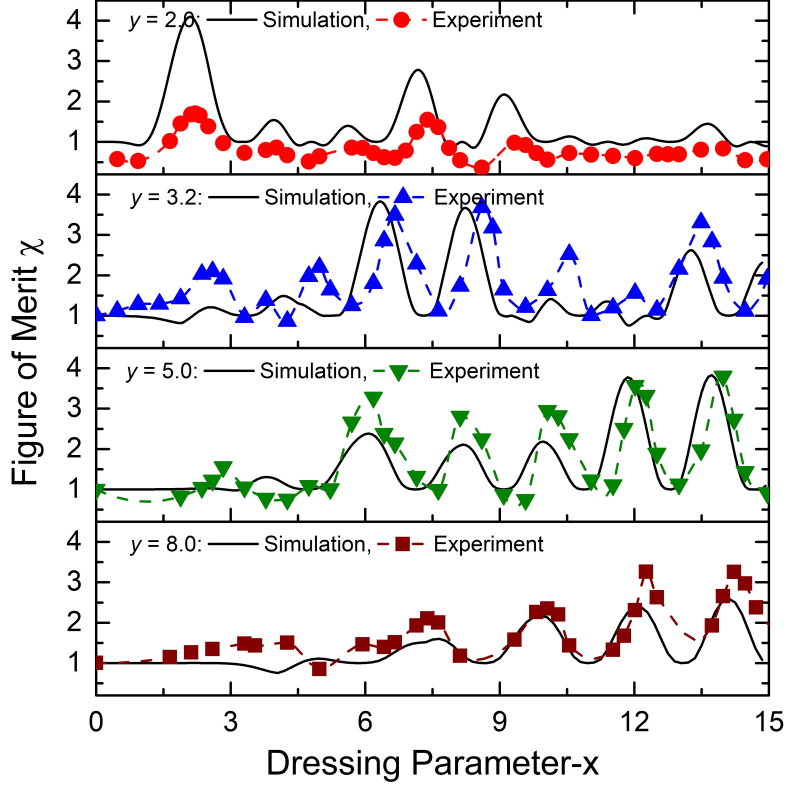
Figure 4.16: Experimental and simulated figure of merit χ observed following a single-cycle dressing field pulse at $y = 2.0$ ($f_L = 1$ kHz; $f_d = 500$ Hz; (-●-) experiment, $y = 3.2$ ($f_L = 1.6$ kHz; $f_d = 500$ Hz; (-▲-) experiment, $y = 5.0$ ($f_L = 2.5$ kHz; $f_d = 500$ Hz; (-▼-) experiment and $y = 8.0$ ($f_L = 4$ kHz; $f_d = 500$ Hz; (-■-) experiment. The simulated values are shown by a solid line. Dashed lines are drawn as a guide for the eye.

The figure of merit χ defined by Eq. 4.10 can then be calculated from this model as

$$\chi = \frac{\int_{t_1}^{t} \mathrm{M}_{xy}(t)dt \, |_{\mathrm{B_d} \neq 0}}{\int_{t_1}^{t} \mathrm{M}_{xy}(t)dt \, |_{\mathrm{B_d} = 0}}. \tag{4.15}$$

Now we can compare the simulated results for χ with experimental data. Figure 4.16 shows a comparison between the figure of merit χ obtained from experiments and from the simple model described above. The model does a remarkable job predicting the height and position of the echoes given the crude approximations upon which it is based. It is noteworthy that good correspondence between experimental and simulated echo locations is observed up to $x = 35$ as is shown in Fig. 4.17 where a single cycle-long duration pulse was applied at $y = 7.14$ ($f_L = 4$ kHz; $f_d = 560$ Hz).
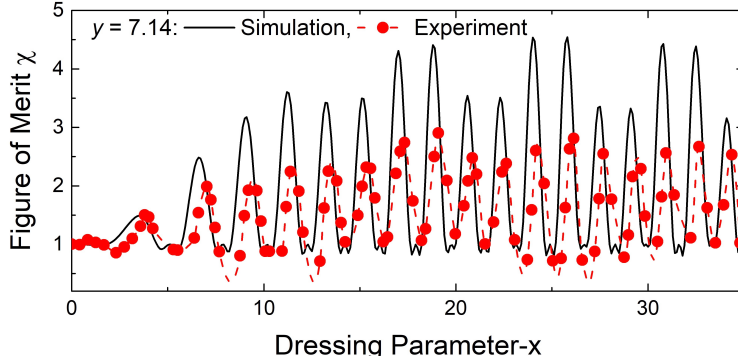
Figure 4.17: Experimental and simulated figure of merit χ following a single-cycle dressing field pulse at $y = 7.14$ ($f_L = 4$ kHz; $f_d = 560$ Hz); -●- experiment; – simulation. Dashed lines are merely a guide for the eye.

4.3.3.3 Phase Space for Echo Formation

So far we have investigated echo formation at a few discrete values of y. Further insight into the echo formation process can be obtained by generating a phase space plot, in terms of the parameters x and y. Figure 4.18 shows a contour plot of simulated figures of merit χ at $f_d = 500$ Hz for dressing field pulses of duration 1/4, 1/2, 1 and 2 cycles. Each plot is made of 2375 simulated values of χ at a resolution of 0.4 in x and y. The echo formation process clearly depends on the length of the dressing field pulse. Echoes occur at high values of y over the full range of x, while at small y they only form at small values of x. In Ch. 6, in which I report the observation of critical spin dressing, contour plots such as these will be employed to choose appropriate parameters for x and y, so as to avoid echo formation.

One can describe off-resonant spin echo formation in terms of multiphoton processes, which are also called multiphoton excitations or resonances. These proceses have been widely studied in atomic and molecular physics [102], quantum information [103, 104] and condensed matter physics [105, 106]. Furthermore, this phenomena has been examined in NMR [107, 108] and electron paramagnetic resonance (EPR) experiments [109]. Multiphoton excitations in a two-level quantum system can happen if the sum of the energies of absorbed photons is equal to the difference between energy levels. And it usually happens when the system is subjected to a sufficiently strong oscillating magnetic field (RF field) [110]. Depending on the orientation of the oscillating field relative to the static field, odd or even [111] numbers of photons can be absorbed by the system.

Echo formation due to an off-resonant RF pulse or, in my experiments, a dressing field pulse has a simple application in NMR spectroscopy. If the dressing field frequency is out of the bandwidth of a NMR receiver, then one can use off-resonant dressing pulses instead of on-resonant π pulses to bypass the dead-time of a NMR receiver [112].[12] In addition,

---

[12]The receiver dead-time is the time following a tipping pulse during which NMR signals can not be monitored by conventional inductive coils, due to RF ring-down in the detector circuit.
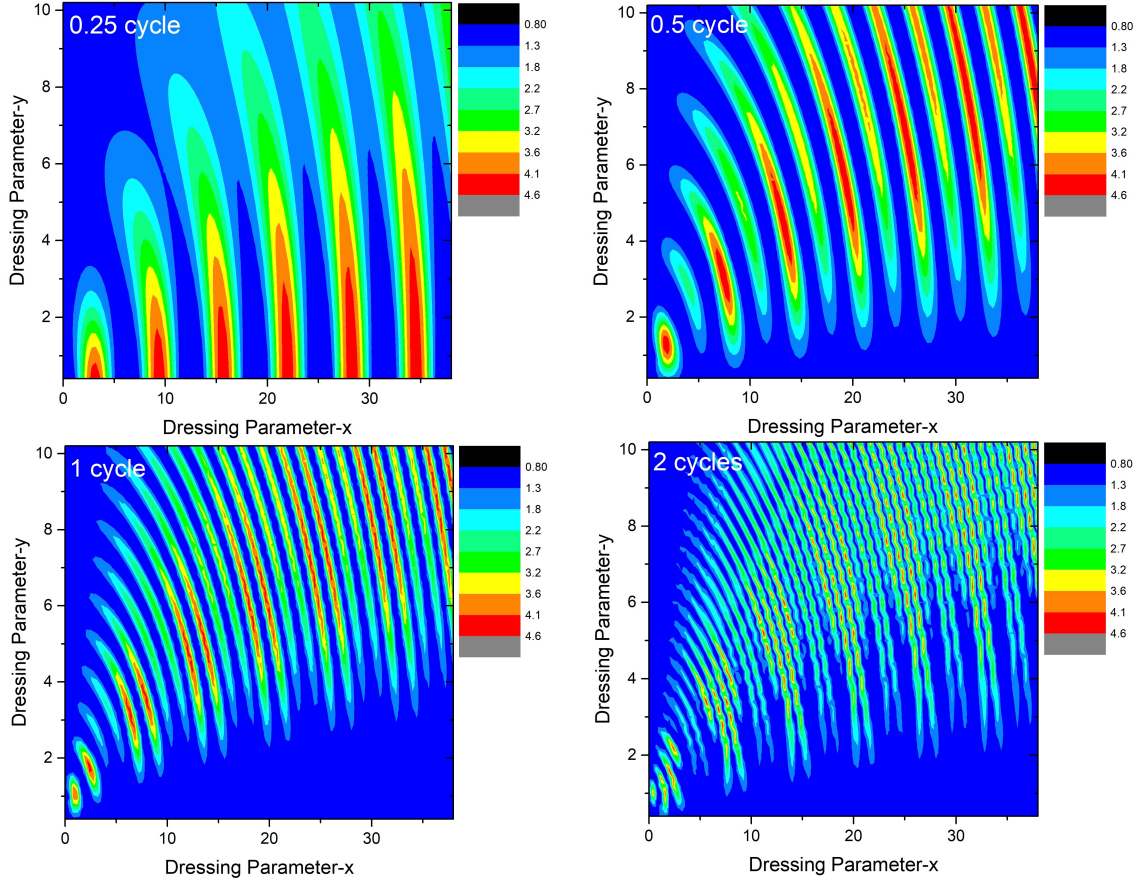
Figure 4.18: Contour plots of simulated figure of merit χ, corresponding to the echo formation, as a function of x and y following dressing field pulses of duration 1/4, 1/2, 1 and 2 cycles, applied at $f_\mathrm{d} = 500$ Hz. Echoes are more often observed in red regions, and never occur in blue areas. The quasi periodic dependence of echoes on the parameters x and y is observed in the experiments.

multiphoton excitations can be controlled through pulse shape optimization [113] which has potential applications to quantum information, where un-desirable effects of multi-photon processes must be avoided. This is analogous to the phase-modulated dressing field pulses that I employed in critical spin dressing experiments, and will discuss in more detail in Ch. 6 Sec. 3.

A full explanation of the echo formation described in this chapter is a bit off topic, as far as my primary goal is concerned. I have only explored this phenomena to know how my spin dressing experiment might be influenced by spin echo formation.

4.4 Conclusion

The experiments described in this chapter demonstrate a simple, practical and robust method for exploring spin dressing phenomena over a wide range of experimental parameters. A key innovation underpinning their success is the use of magneto-impedance sensors for direct detection of the magnetic fields of precessing nuclei. A simple data analysis method based on the phase of FID signals was developed. The method can be used to extract useful information about the average precession rate and the modified gyromagnetic ratio of dressed nuclear spins. This method only works for one spin species.

The spin dressing experiments demonstrated in this chapter yielded promising results, and pave the way toward the critical spin dressing experiments described in Ch. 6.

Chapter 5

Spin Dressing Revisited

In this chapter I introduce a new apparatus that I developed to advance the experiments described in Ch. 4. This apparatus offers several advantages, but in particular it does not rely on the flow of water (or other liquid), and is readily adapted to multi-nuclear NMR experiments. I will describe this apparatus and illustrate its operation using samples containing ^{1}H and ^{19}F nuclei. It will then be used in Ch. 6 to observe and study critical spin dressing.

The previous two chapters were focused on a ULF NMR apparatus that intrinsically relied on the flow of polarized water. An alternate approach is needed to accomodate other spin species. To this end, I develloped a pneumatic sample transfer system to transport a cell containing a sample between a polarizing magnet and the ULF region where experiments are performed. Pneumatic and mechanical sample-transfer systems have been employed previously for high and low field NMR experiments [52, 114], including relaxometry experiments [115, 116] in which polarization and measurement regions are spatially separated.

5.1 Modified ULF NMR Apparatus

The experiments described in this chapter are performed using an apparatus in which samples are first thermally polarized in a high field region (1.5 T) and then transferred to a well-shielded region with μT-scale fields. A magnetic field $\mathbf{B}_1$ is then applied on-resonance to rotate the nuclear magnetization $\mathbf{M}$ into the transverse plane, at which point spin precession about $\mathbf{B}_0$ is monitored by a pair of magneto-impedance sensors arranged in a gradiometer configuration. The sensitive axes of the MI sensors are perpendicular to both $\mathbf{B}_1$ and $\mathbf{B}_0$. The sample is confined to a 15 ml Nalgene bottle (or a cylindrical Teflon cell) which is transported pneumatically between the high and ultra-low field regions inside a 2.0 m-long PVC tube.[1] As before, pulsed dressing fields $\mathbf{B}_\mathrm{d}$ are applied to periodically drive $\mathbf{M}$ away

---

[1]Schedule 40.

from the equatorial plane of the Bloch sphere, and thereby modify the apparent gyromagnetic ratio of nuclear spins. The field $\mathbf{B}_d$ is aligned parallel to $\mathbf{B}_1$ and perpendicular to both $\mathbf{B}_0$ and the sensitive axis of the MI sensors.

5.1.1 Sample Transfer System (STS)

Figure 5.1 illustrates the sample transfer system (STS), which uses high pressure air to transport the sample cell from the high field region to the ULF region. The transport time is 0.3 s with an average speed of $\bar{v} = 6.5$ m/s, when 90 psi of air pressure is applied. The STS returns the cell back to the high field region at an average speed of 1 m/s. There are four main components of the STS that will be described in detail below: solenoid valves, transfer line, cell stopper and a monitor window.

Solenoid valves (SV) are used to control the flow of high pressure air through the STS. I used four ASCO normally-closed solenoid valves, two of which control the inlet for high pressure air and two of which control exhaust ports. The cell moves from the high field region to the ULF region when the SV 1 and 3 are open, and SV 2 and 4 are closed. When SV 1 and 3 are closed, and SV 2 and 4 are open, the cell returns to the high field region. All of the SVs are controlled by 2 sets of 2-channel relay modules which are triggered by 5 V TTL logic pulses generated by a Tecmag NMR console.

The STS transfer line is made from a schedule 40 PVC tube, and can tolerate up to 400 psi of pressure. The tube has an inner diameter of 25.7(2) mm, a wall thickness of 3.9(1) mm and a total length of 3.5 m. The distance travelled by the cell as it moves be-
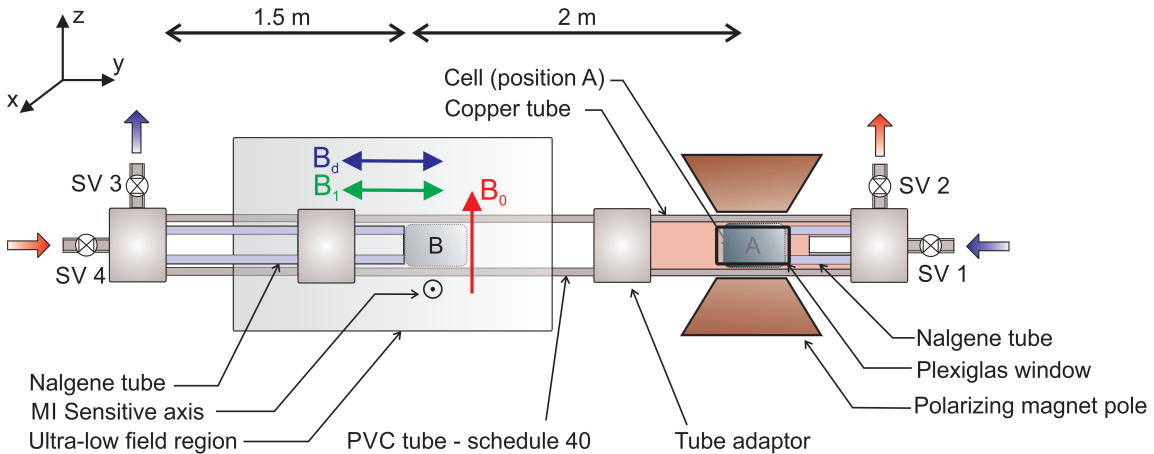
Figure 5.1: Schematic of sample transfer system (STS). Flow of high pressure air is controled by four solenoid valves (SV). When SV-1 and SV-3 are open, and SV-2 and SV-4 are closed, the cell moves from position A (high field region) to position B (ultra-low field region). To return the cell to position A, SV-1 and SV-3 are closed, and SV-2 and SV-4 are opened (Not to scale).

tween the high field region and the low field region where the MI sensors reside is 2 m. The first 20 cm of the transfer line, in the high field region, is made of a copper tube with an ID of 25.6(1) mm and a wall thickness of 1.7(1) mm. The copper tube is used for convenience, because it was easier to install a clear window through which the position and the status of the sample cell can be monitored after each manipulation.

The cell stopper is a 1.5 m-long Nalgene tube with an ID of 5/8" and an OD of 7/8" that is placed inside the transfer line between the end where SV-3 and SV-4 are installed and the location where the MI sensors reside. This long PVC tube was chosen to dampen and transfer the recoil force, generated by the high speed sample cell, to the end of the STS line. This stopper is used to bring the high speed cell to rest when it reaches the μT region. A 3 cm long length of Nalgene tubing is placed at the other end of the transfer line, in the high field region where SV-1 and SV-2 are located, to stop the cell when it returns to the polarization station.

A rectangular window (1 cm $\times$ 3 cm) made of plexiglas is embedded in the copper segment of the transfer line at the high field end to (a) check the position of the cell each time it returns to the polarization station and to (b) inspect the cell for leaks. In an earlier version of the STS, I used a plexiglas tube for this purpose but it was not strong enough to withstand the necessary stresses, and was susceptible to damage due to chemical leaks (such as exposure to acetone samples).

To measure the speed of the cell, as it moves from the high field region to the ULF region, I used the scheme summarized in Fig. 5.2 which makes use of inductive sensors. I mounted a magnetic cube (2.7 mm on a side; weight 0.2 g) on the cap of a Nalgene sample
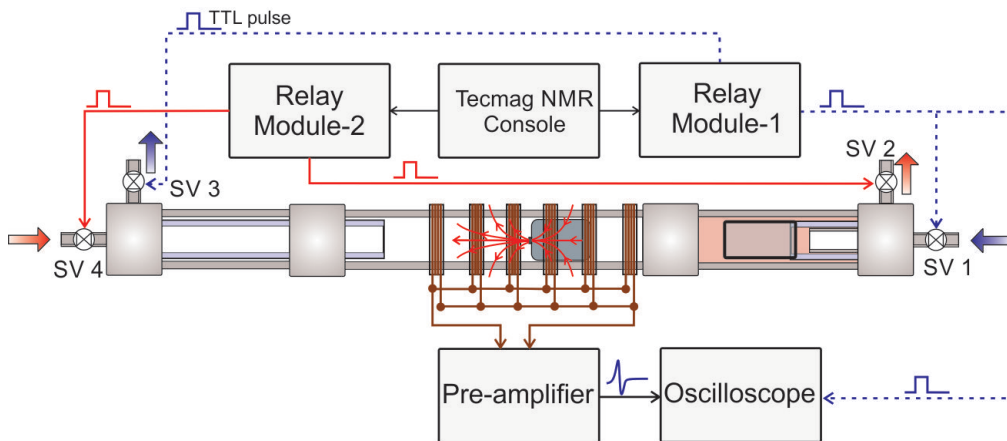
Figure 5.2: Apparatus used to measure the velocity and transport time for the cell (Not to scale). The small magnet attached to the cap of the cell induces an emf across the inductive coils as the cell passes by. These emfs appear as bipolar spikes on the oscilloscope. The dashed signal line indicates the TTL logic pulse used to trigger SV-1, SV-3, and the oscilloscope. The solid signal line indicates the TTL logic pulse used to trigger SV-2 and SV-4, and consequently to return the cell back to the high field region.
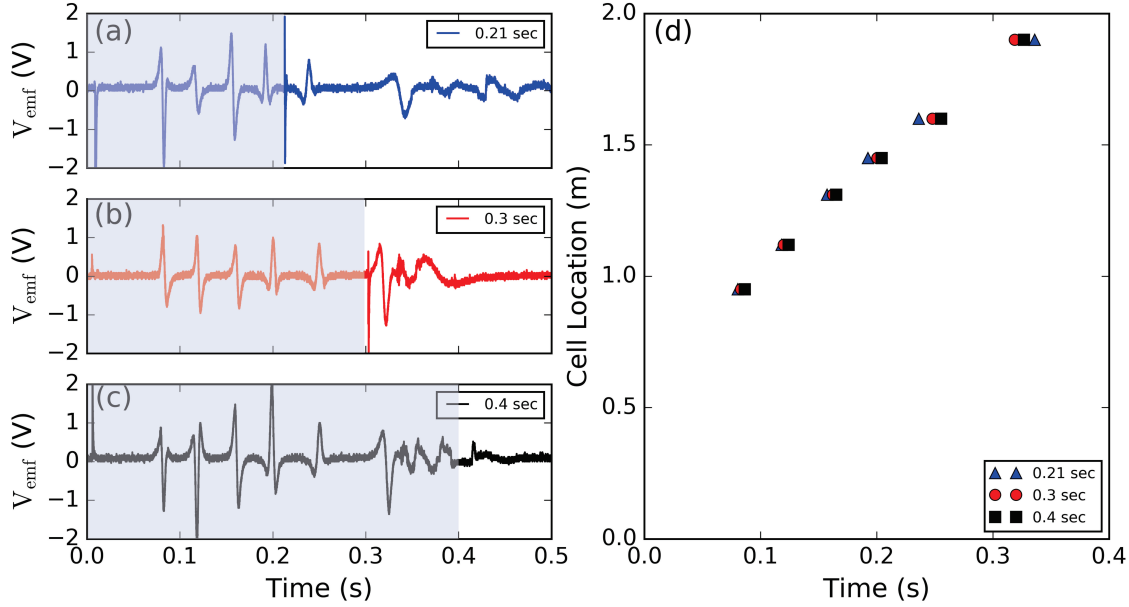
Figure 5.3: (a-c): Induced voltage V_{emf} across the six inductive pick up coils, which are connected in parallel. Spikes reveal the time at which the cell passes each coil. The high pressure air pulse is applied in the grey regions. (d): Location of the cell relative to the polarizing station as a function of time for different high pressure pulse durations 0.21 s (▲); 0.3 s (●) and 0.4 s (■); Four averages were employed.

cell. This magnet produces a field of ∼3 mT at a distance of 4 mm the surface of either pole. I then wound 6 circular coils with an OD of 6 cm, comprising 100 turns each. These 6 coils are connected in parallel, so that the emf across any one coil appears across all six. The sample transfer tube was arranged to pass through these sensor coils. The change in magnetic flux passing through the coil as the magnet passes by induces a voltage V_{emf} that is then amplified by a low noise pre-amplifier[2] and fed to an oscilloscope.[3] The oscilloscope is triggered as SV 1 and 3 are opened (and SV 2 and 4 are closed) and the high pressure air pushes the sample cell towards the μT region. Figure 5.3 shows experimental timing data acquired using this system.

As the cell passes through one of the pick up coils the magnet induces an emf V_{emf} which appears as a bipolar spike on the oscilloscope. The position of the coils and the time at which spikes appear can be used to determine the average velocity $\bar{v}$ of the cell. Over the first 80 cm of its travel the average speed $\bar{v}$ of the cell is ∼12 m/s but for the rest of its trajectory it is ∼4 m/s. The duration of the high pressure air pulses is chosen to ensure the cell reaches the stopper but does not suffer a violent collision causing it to rebound (and hence to stop far away from the MI sensors). Figure 5.3-b shows that after a 0.3 s high pressure air pulse plus a delay time of 0.1 s no further spikes appear. This means the

---

[2]Stanford Research Systems low noise pre-amplifier model SR560.
[3]Tektronix model TDS 7054 Digital Phosphor Oscilloscope

cell does not move any more. And this combination of pulse duration and delay time is sufficient to bring the cell to rest in the correct location. Note that the experimental and geometric parameters such as the pressure of the pulse, ID of the STS line, OD of the cell, tube adaptors used in STS line, weight of the cell and sample and friction between the STS line and the cell wall can influence the pulse duration and the delay time.

5.1.2 Polarizing Magnet

An electromagnet[4] driven by a Varian Model 6004 regulated current power supply, was used to thermally polarize samples. The electromagnet and the power supply are water-cooled. The two magnet coils are connected in parallel to yield a smaller total resistance and permit higher currents for a given supply voltage. The power supply is operated at a current of 80 A, corresponding to 40 A through either coil. Under these conditions the temperature on the surface of the coils reaches a steady temperature $\sim$45°C after $\sim$20 min.

The pole faces of the magnet are 18 cm in diameter and were initially 9 cm apart. Two truncated cones fabricated from mild-steel were manufactured and installed on the pole faces to concentrate flux and make the gap as small as possible. The diameters of the base and top of the truncated cone were 18 cm and 6.5 cm, respectively. After installation of these flux concentrators the gap was 3.3 cm. The geometry of the modified poles guides the magnetic field lines to a smaller volume and hence creates a stronger field in that re-
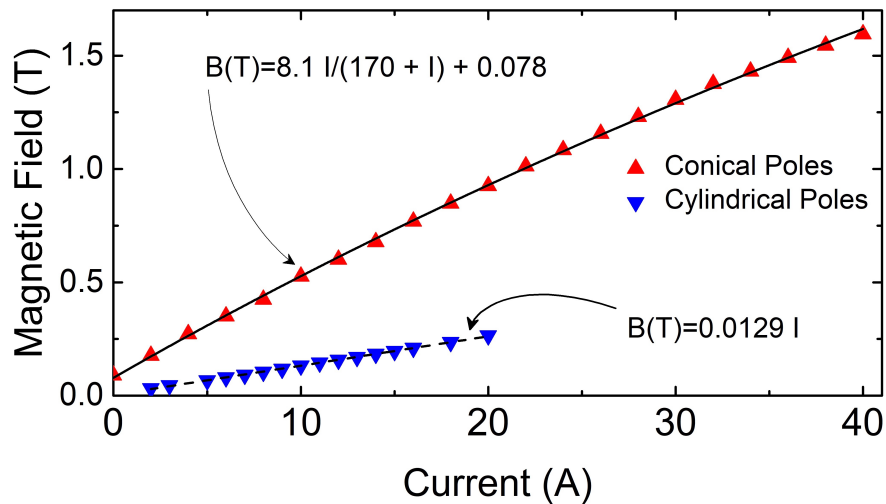
Figure 5.4: Magnetic field produced by the electromagnet between two flat cylindrical poles (▼; 9 cm separation; 18 cm diameter), and between two truncated cones (▲; 3.3 cm separation; 6.5 cm diameter). At high fields the mild steel used for the flux concentrators begins to saturate and the field is no longer a linear function of current. Empirical fit functions are shown on the plot.

---

[4]Walker Scientific Model L-75BF (50 A; 100 V DC)

gion. Figure 5.4 shows the magnetic field strength between the poles before and after this modification. The flux concentrators increased the magnetic field by a factor of 3.7. As the magnetic field increases the mild-steel from which the truncated cones are manufactured shows evidence of a non-linear response.

5.1.3 Magnetic Fields for ULF NMR

Five different sets of coils are used to generate magnetic fields for the ULF NMR apparatus. These include a conventional field $\mathbf{B}_1$, a dressing field $\mathbf{B}_d$, a static field $\mathbf{B}_0$, gradient fields $\mathbf{G}$, and a guide field. The coils used to produce $\mathbf{B}_1$ and $\mathbf{B}_d$ are the same as those described in Ch. 4 but the remaining coils were designed specifically for the ULF NMR apparatus described in this chapter.

To produce a uniform field $\mathbf{B}_0$ that is perpendicular to the transfer tube axis, I used a 60 cm long, 8 rung sine-ϕ coil [86] wound on the outer surface of a PVC tube with an OD of 5.5 inches. The conductors used for this coil were made from copper tape with a width of 5.92(1) mm and a thickness of 0.1 mm. The surface current distribution for a sine-ϕ coil is:

$$I(\phi) \sim \sum_{i=1}^{4N} \delta(\phi - \phi_i) \tag{5.1}$$

where 4N is the total number of current carrying conductors and so each quadrant of the coil has N wires. The angle ϕ_i in one quadrant of the coil satisfies

$$\phi_i = \arccos(1 - \frac{2i - 1}{2N}). \tag{5.2}$$

The currents are then distributed symmetrically at $\pm\phi_i$ and $\pm(180^o - \phi_i)$. For a sine-ϕ coil with 8 rungs, the angles ϕ_i are: 20.4°, 35.7°, 46.6°, 55.8°, 64.1°, 71.8°, 79.2° and 86.5°.

The magnitude of B_0 at the center of the coil was both calculated and measured as a function of the current with and without considering the effect of magnetic shields. Calculations were performed using the BiotSavart software package. Measurements were

	Calculated	Experiment (Hall probe)	Experiment (NMR)
B_0(G) (Without shield)	0.758 I	0.786(8) I	Not available
B_0(G) (With shield)	Not available	0.900(5) I	0.898(2) I

Table 5.1: Experimental and calculated field-current calibration factors for the sine-ϕ coil. The range of currents employed in the measurements was 0.2 - 1 A for the Hall probe and 10 - 200 mA for NMR experiments. The latter range yields [1]H Larmor precession frequencies $\lesssim$ 1 kHz. Calculations were performed using the BiotSavart software package.

performed using a gaussmeter[5] and ULF NMR spin precession techniques. Table 5.1 compares the results of these three different determinations. A relatively large discrepancy was observed between measurements performed using the gaussmeter with and without the magnetic shields. This is due to the shield surrounding the sine-ϕ coil. It can be shown, using boundary conditions for the equivalent magnetostatic problem [97], that the normal component of the magnetic field lines produced by the sine-ϕ coil, near the surface of the high permeability shield, are much stronger than the tangential component. One can remove the shield and add image currents to satisfy these boundary conditions. The direction of the image currents must be the same as the current through the sine-ϕ coil, but with different magnitude and distribution. This results in a weaker field between the coil and the shield. However, it increases the field inside the coil.

Two sets of guide field coils are used to keep the quantization axis perpendicular to the transfer tube as polarized nuclei travel from the fringe fields of the polarizing magnet to the ULF region. The first set consists of a pair of rectangular coils with 10 turns each. These coils are 96 cm × 7 cm, and are separated by 9 cm. Typically, 1 A of current passes through the coils. The second set also consists of a pair of rectangular coils with 10 turns each. They are 40 cm × 12 cm, and are separated by 8 cm. Approximately half of the length of these coils are located inside the permalloy shield. Figure 5.5 shows the arrangement of the guide field coils.

Three sets of coils producing linear magnetic field gradients $\mathbf{G}_x$, $\mathbf{G}_y$ and $\mathbf{G}_z$ are employed to improve the homogeniety of the static field $\mathbf{B}_0$. These gradient coils are wound on the same PVC tube as the B_0 coil, and are aligned with $\mathbf{B}_0$ which defines the z direction. Figure 5.6 shows the current distributions for each of the gradient coils and Table 5.2 shows calculated results for the field gradients that are generated at the center of the coils where the sample cell is stopped. In these results the effect of magnetic shields is not considered. So the results only give an order of magnitude indication of the strength of the field gradients.
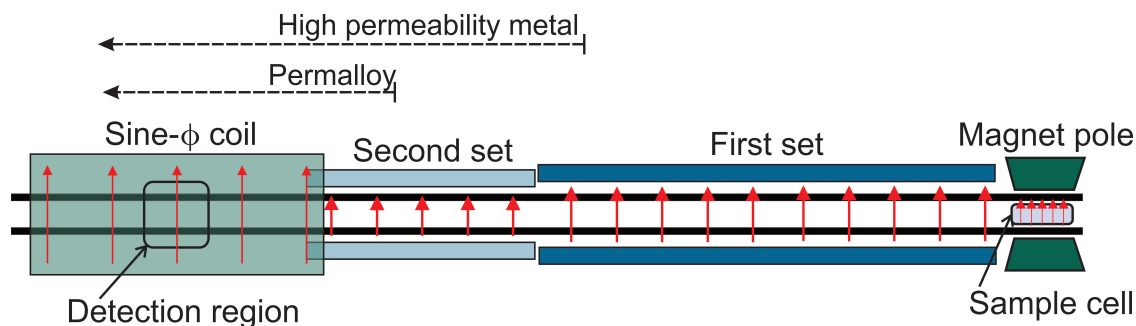
Figure 5.5: Guide field coil arrangement (Not to scale). The direction of the local static field is indicated by red arrows.

---

[5]GMW model DTM-151 Digital Teslameter with model MPT-231 miniature high sensitivity Hall probe.

Coil label	G_x	G_y	G_z
Field gradient (μT/cm)	2.4	1.82	1.51

Table 5.2: Strength of the field gradient coils, calculated using the BiotSavart software package, at their midpoint where the cell is positioned for NMR experiments when 0.1 A current flows through the coils. The effect of magnetic shields that surrounded the coils is not considered.
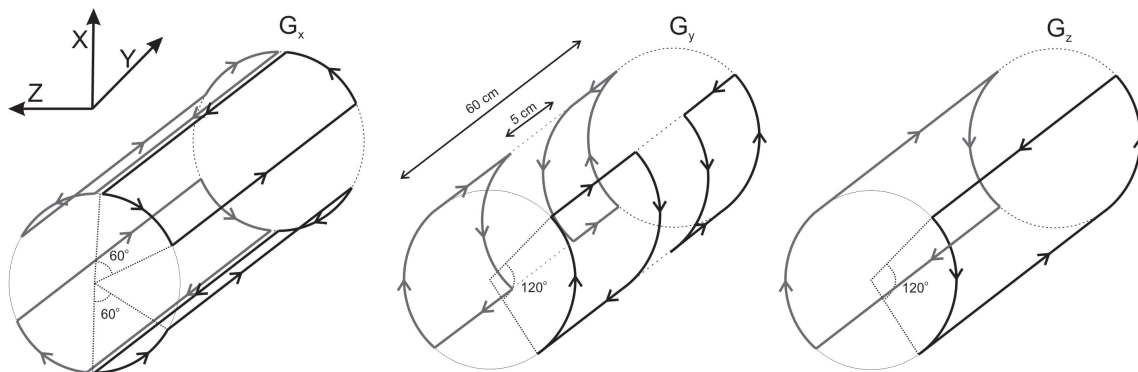
Figure 5.6: Current distributions for the coils used to generate the linear gradients G_x, G_y and G_z.

As will be seen later, it will be useful to momentarily apply magnetic field gradients to dephase the transverse component of the nuclear magnetization. An important consideration is that this "crusher gradient" will saturate the MI sensors if it has a component parallel to the sensitive axis of the detector. In the ULF NMR apparatus described here the sensitive axis of the MI sensors is along the x-axis. All three of the field gradient coil sets produce a small magnetic field B_x along the x-axis but, for a given current, the coil producing G_y generates a much smaller B_x than the other two, by 2 orders of magnitude. Hence, a crusher gradient will typically be generated using y-directed field gradients. Figure 5.7 shows calculated results for the B_x component of the fields, produced by the gradient coils, obtained using the BiotSavart software package.

5.1.4 Relative Position of the Sample and the Sensor

Two MI sensors in a gradiometer configuration were used to monitor NMR spin precession signals. This requires that the alignment of the sensors be set precisely. I designed a 3D model of a fixture to hold the sensors and then fabricated it using a 3D printer in the SFU machine shop. See Fig. 5.8 for details. The body of the sensor holder is in the form of a semi-cylinder designed to fit into the coil used to generate the static field B_0, and which has an ID of 5". When the MI sensors are installed in this holder their sensitive volumes
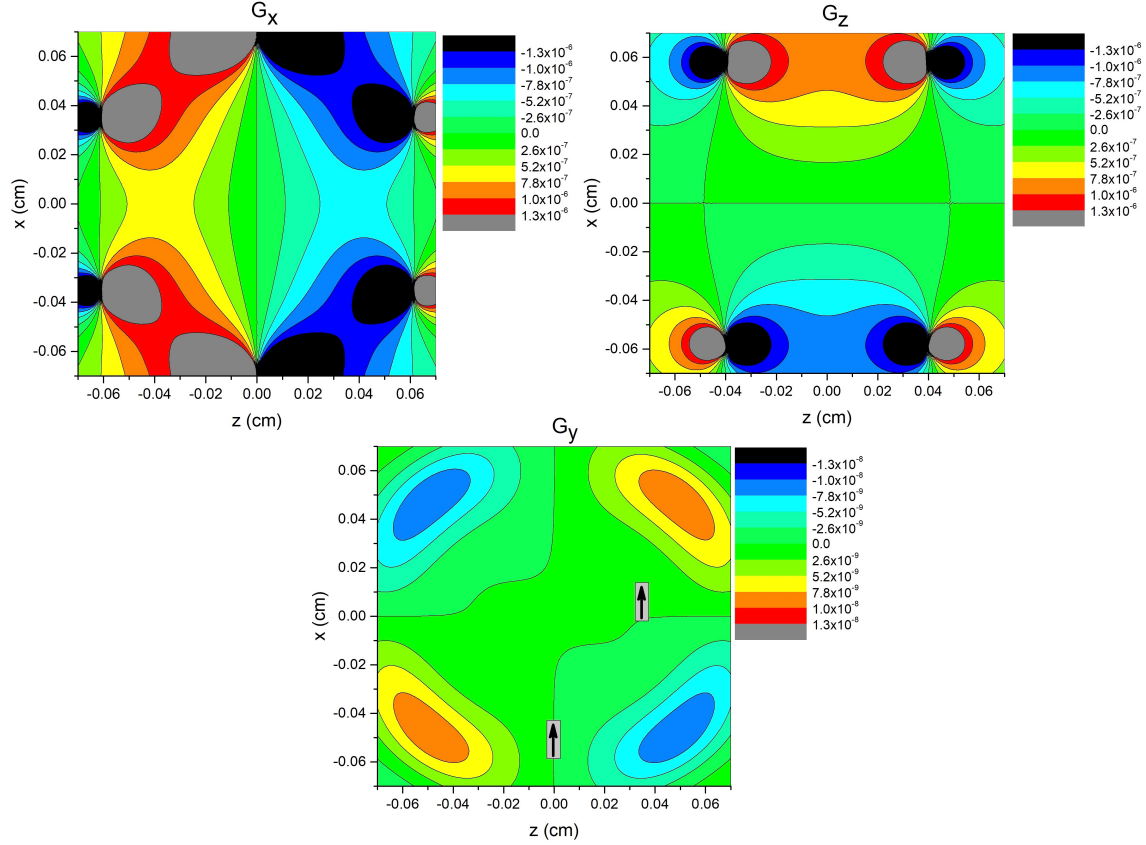
Figure 5.7: Contour plots showing calculated values of B_x produced by the three gradient coils. This is the component of the magnetic field parallel to the sensitive axis of the MI sensors. Results are shown for the case where 100 mA of current pass through the coils. The field B_x produced by the y-gradient coil is 100 times weaker than that produced by the other two. The positions and sensitive directions of the MI sensors relative to the center of the coils are identified on the contour plot for G_y, in the bottom panel.

are located at radii of 18.8 mm and 25.4 mm from the axis of the sine-ϕ coil.

Figure 5.8 illustrates the relative locations of the sensors, the sample transfer tube and the cell. A 2 mm gap exists between the outer wall of the sample transfer tube and the surface of the closest MI sensor. This gap is needed to protect against possible mechanical vibration of the STS during sample transfers. Taking into account this gap, the position of the MI sensors, the wall thickness of the PVC tube (3.9 mm) and the geometry of the cell (ID~23 mm), the distance between the closest nuclear spins in the sample and the sensitive volume of the MI sensor is approximately 7.3 mm.

A simple model can be used to estimate the anticipated magnetic field produced by polarized nuclei in the sample at the location of the MI sensors. For an infinitely long cylinder that is uniformly magnetized in the transverse direction, the magnetic field $\mathbf{B}_M$
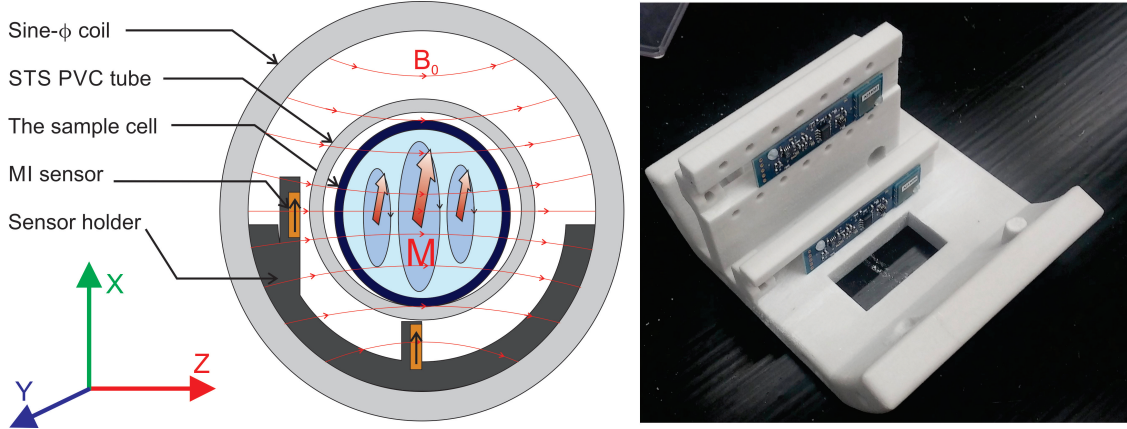
Figure 5.8: (Left): Cross section of the sample cell, STS tube, sensor holder and B_0 sine-ϕ coil (Not to scale). The sensitive axis of the MI sensors are identified by arrows. (Right): 3D printed sensor holder, the two MI sensors and their associated circuitry, after installation.

associated with $\mathbf{M}$ can be written

$$\mathbf{B}_{\mathrm{M}}(\rho, \phi) \; = \; \frac{\mu_0 \mathrm{M} R^2}{2\rho^2}(\cos\phi \; \hat{\rho} + \sin\phi \; \hat{\phi}) \tag{5.3}$$

where $\rho \; > \; R$ is the radial distance from the axis, R is the radius of the cylinder and the use of cylindrical coordinates is implied. The magnitude of this field at radius ρ is

$$\mathrm{B}_{\mathrm{M}}(\rho) = \frac{\mu_0 \mathrm{M}}{2}\left(\frac{R}{\rho}\right)^2. \tag{5.4}$$

I experimentally confirmed the dependency of B_{M}, in Eq. 5.4, on R^2. Figure 5.9 shows experimental data for B_{M} in terms of $2R$. Data were obtained from ULF NMR experiments performed on $^1\mathrm{H}$ nuclei of water.[6] The water sample was placed inside 3 cm long cylindrical cells with various IDs and a fixed OD ~ 25 mm. The cells were machined to produce different IDs. The y-axis in Fig. 5.9 shows the peak amplitude of the field B_{M} associated with a precessing $^1\mathrm{H}$ nuclear magnetization $\mathbf{M}$. B_{M} was monitored using two MI sensors, arranged in a gradiometer configuration. The locations of the sensitive axes of the sensors, relative to the axis of the sample transfer tube, were fixed at $\rho_1 = 18.8(2)$ mm and $\rho_2 = 25.5(2)$ mm. B_{M} was measured for the cells with different ID. It turned out that B_{M} is quadratic in ID (or R) for ID $\lesssim 17$ mm. For ID $\gtrsim 17$ mm B_{M} seems to be linear rather than quadratic. However, the data in this range are not sufficient to make a definitive conclusion. Let us assume B_{M} varies linearly at large IDs and extrapolate to the location of the MI sensor closest to the sample transfer tube. This yields an estimate for B_{M} corresponding to a cell with infinitely thin walls so that the MI sensor is as close as possible to the sample. This value of B_{M} is $\sim 60\%$ higher than the values that I can currently measure. One could design

---

[6]The experiments will be explained in detail in Section 5.2.
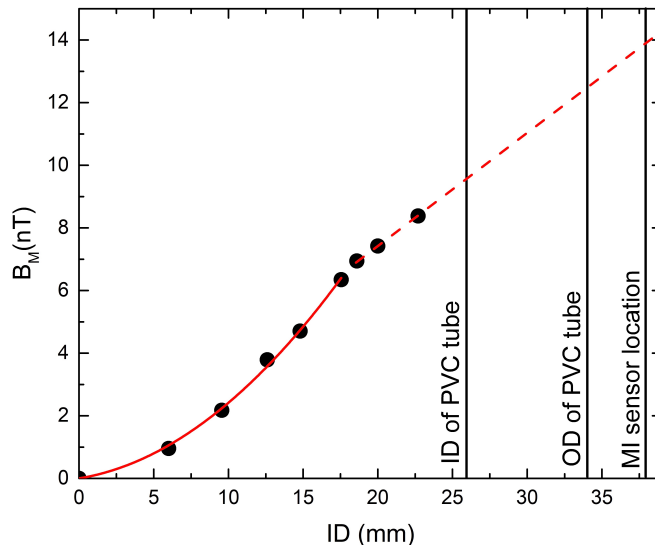
Figure 5.9: Experimental data (points) for the magnetic field B_M as inferred from the amplitude of free induction decay signals from ^{1}H nuclei in water inside a cylindrical cell with the specified inner diameters. Data were obtained from ultra-low field NMR at a ^{1}H Larmor frequency of 200 Hz. The ID (25.8 mm) and OD (33.6 mm) of the sample transfer tube and the location of the closest MI sensor (37.6 mm) are indicated by vertical lines. The solid curve is a fit function that is quadratic in the the ID of the cell. The dashed line is used to extrapolate data at large ID values.

an apparatus with optimum dimensions to detect higher signals.[7]

5.1.5   Samples and Cells

My goal is to study samples containing ^{1}H and ^{19}F nuclei, and to incorporate them into a critical spin dressing experiment. As sources of ^{1}H nuclei I used three samples: water (deionized), acetone and pentane. As the source of ^{19}F nuclei I used hexafluorobenzene (HFB) which is an organic aromatic compound. It is simply a derivative of benzene in which the hydrogen atoms have been replaced with fluorine. That is, it is a Halogenated-Hydrocarbon. Table 5.3 summarizes the general properties of these compounds.[8]

I used two types of plastic cells to carry samples between the high and ultra-low field regions. They are made from high-density Polyethylene (HDPE) and Teflon.[9] Figure 5.10 shows photographs of both types of cells as well as drawings of their cross sections.

HDPE cells are light,[10] impact resistant, inexpensive and commercially available. I em-

---

[7]Optimum dimensions imply a larger cell ID, thinner sample transfer tube wall and MI sensors placed closer to the sample transfer tube.

[8]All of the samples except the deionized water were obtained from Sigma Aldrich. The acetone and hexafluorobenzene are $\geq$99.5% NMR grade and the pentane is 98% Reagent grade.

[9]Glass-filled Polytetrafluoroethylene (PTFE).

[10]The mass of the bottle without the cap is 5.3 gr.

Name	Formula	Density (kg/m^3)	Molar mass (g/mol)	Boiling Point (^oC)	Relaxation Time T_2 (s)
Water*	H_2O	1000	18	100	1-3
Acetone	C_3H_6O	791	58.08	56	14
Pentane	C_5H_{12}	626	72.45	36.1	10.5
HFB	C_6F_6	1612	186.06	80.1	19

Table 5.3: General properties of samples used for ULF NMR. Values for T_2 (except water) are extracted from [52].

HDPE bottle   Teflon bottle
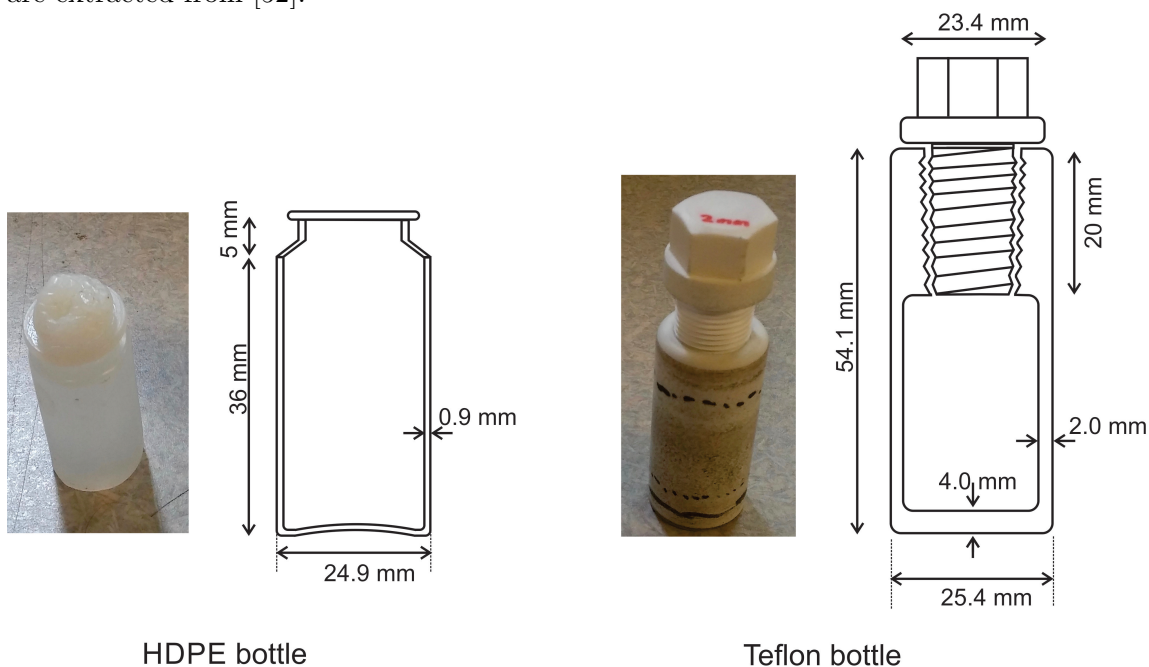
Figure 5.10: Plastic cells used in ULF NMR experiments. (Left) Flame-sealed 15 ml HDPE Nalgene bottle; (Right) custom-machined 12 ml Teflon bottle made from glass-filled Poly-tetrafluoroethylene.

ployed 15 ml Nalgene HDPE bottles manufactured by Nalge Nunc International. These bottles have an OD of 24.8 mm and a wall thickness of 1 mm. Their caps are made of Polypropylene (PP), which is not impact resistant and cracks easily. To address this issue I removed the cap and used a torch to heat and deform the top part of the cell, leaving a small hole through which the sample could be poured or injected into the cell. This hole was made as narrow as possible and was then either sealed using epoxy[11] (after injecting the sample) or it was sealed using a flame. As a note of caution HDPE bottles are not recommended for use with acetone and HFB for storage times longer than a few days.

The Teflon cell and its cap are more expensive because they were custom-machined from raw material. After machining the cell and the cap together they are ∼10 times more

---

[11]I used Devcon Epoxy Model No. 14250, intended for general use.

massive than the HDPE cell.[12] The volume of this cell is 12 ml, its OD is 25.5 mm and its wall thickness is 2 mm. It is resistant against impact and chemically resistant to acetone and Pentane. It can be also used with HFB, however HFB softens the thin walls of the cell after one day. As a result I had to remove the HFB from the cell at the end of every day. In this mode of operation I was able to use the same cell over and over again.

5.2   ULF NMR Results

The sequence of events shown in Fig. 5.11 are those used to perform a basic ULF NMR experiment. Once the sample reaches a thermally polarized state in the high field region, the cell is transferred to the experimental region by opening solenoid valves SV1 and SV3 (while SV2 and SV4 are closed) for 0.3 s. After an additional 0.1 s delay (to let the cell come to rest after hitting the cell stopper), a B_1 tipping pulse is applied to rotate the nuclear magnetization into the transverse plane. The tipping pulse usually consists of two-cycles of an oscillating magnetic field B_1 applied on-resonance (or close to resonance) at a frequency of 200 Hz. Next the free induction decay (FID) of the precessing nuclear magnetization is monitored by the MI sensors. Their output is fed into the low noise transformer and from there into a phase sensitive detector (PSD). The real and imaginary components of the FID (as measured relative to a local oscillator usually at 160 Hz) are displayed and recorded by the oscilloscope. The acquisition time is typically 1-2 sec. Afterwards the cell is transferred back to the high field region by opening SV2 and SV4 (while SV1 and SV3 are closed).
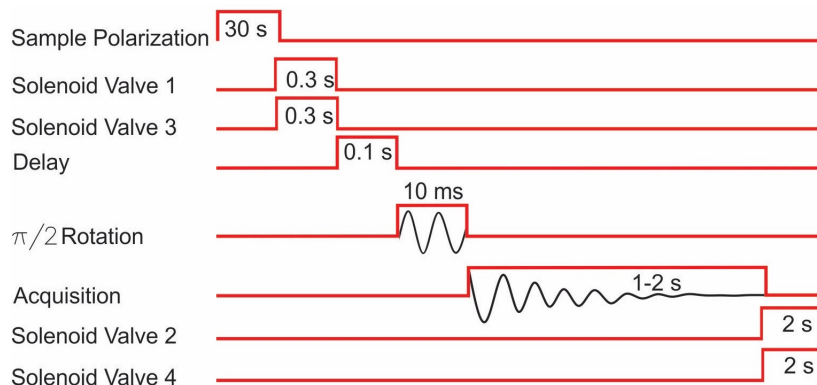
Figure 5.11: Sequence of events in a ULF NMR experiment in which the sample is shuttled between high and ultra-low field regions. Not to scale.
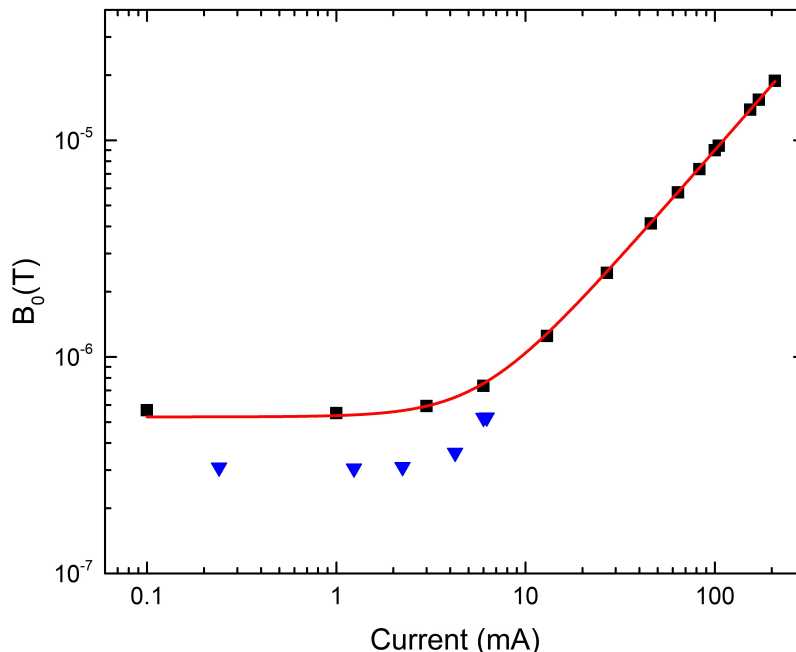
Figure 5.12: Measurements (■) of the static magnetic field B_0 inferred from proton Larmor precession frequencies as a function of current through the sine-ϕ coil. At low currents the data level off because of background fields in the transverse direction. This residual can be suppressed by applying a small DC field in the y direction (▼). (Solid line): fit function $B_0(I) = \sqrt{530(30) + (89.8(2)I)^2}$, where I is in units of mA and B_0 is in nT.

5.2.1 ULF NMR: One Spin Species

The static magnetic field B_0 can be inferred from the Larmor precession frequency f_L of ^{1}H nuclei in deionized water. Figure 5.12 shows an example of such a measurement as a function of the current passing through the sine-ϕ coil. At low currents B_0 is independent of the current. This is attributed to background fields (i.e. from other sources) that are perpendicular to $\mathbf{B}_0$.[13] The data are well fit by an exponential function combined with a linear function, from which I infer a background field of 530 nT in a transverse direction. When a DC current is applied to the $\mathbf{B}_1$ coil (generating a magnetic field in the y direction) the total background field can be reduced to 300 nT. From the linear part of the graph in Fig. 5.12 I extracted a calibration of B_0 in terms of a current of 0.898(2) G/A.

I explored the dependence of the ULF NMR signal-to-noise ratio (SNR) on experimental parameters such as the Larmor frequency and the polarizing field as well as the influence of signal averaging. These studies are briefly summarized below. A SNR of order ~4.5 was observed for a single shot FID acquisitions using ^{1}H nuclei in deionized water, at Lar-

---

[12]The cell and the cap together have a mass of 50.1 gr.

[13]These fields also have a component parallel to $\mathbf{B}_0$. This component was cancelled by reversing the current through the $\mathbf{B}_0$ coil.
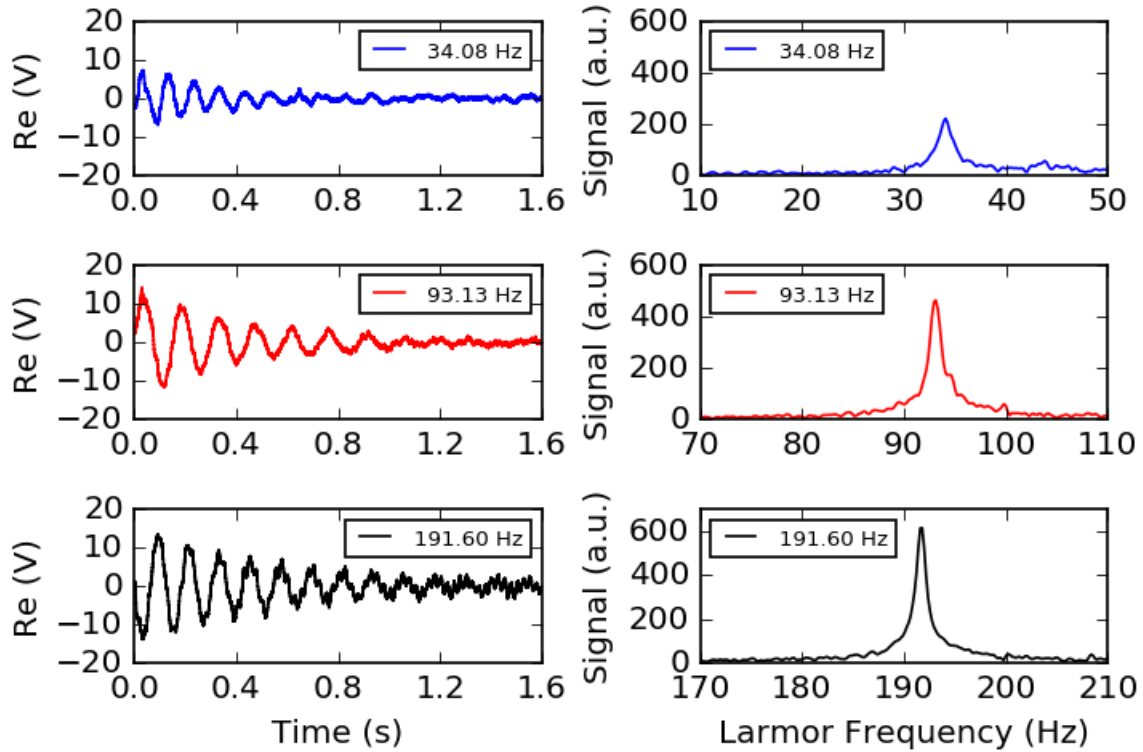
Figure 5.13: Real part of single shot FID signals (left column) and their Fourier transforms (right column) in different magnetic fields (and hence Larmor frequencies). Experiments performed using ^{1}H nuclei in deionized water, prepolarized at 1.6 T. A bandwidth of 83 Hz was used for signal acquisition. The local oscillator frequency was 44 Hz (top panels), 100 Hz (middle panels) and 200 Hz (bottom panels).

mor frequencies in the range of 100 - 200 Hz.[14] This SNR is a bit higher than the value SNR ~ 3.7 that was reported in Ch. 3 for the pulsed NMR measurement. This is a result of the shorter transfer time and the larger volume of polarized sample near the sensors. Figure 5.13 shows experimental recordings of FIDs and their Fourier transforms (FT) at different Larmor frequencies. The decrease in signal magnitude at low f_L is due in part to the frequency dependence of the transformer gain. An additional contribution to this decrease comes from the orientation of the residual background magnetic field relative to the field produced by the sine-ϕ coil. At low f_L the background field is comparable in magnitude to B_0 and thus changes the axis about which the nuclear magnetization $\mathbf{M}$ precesses. This reduces the projection of $\mathbf{B}_M$, the magnetic field associated with $\mathbf{M}$, on the sensitive axis of the MI sensors and thereby reduces the apparent FID amplitude.

Signal averaging can be used to increase SNR. I obtained a SNR in order of $\sim$18.5 when 16 sequential FIDs were averaged (employing deionized water at f_L = 191 Hz). Figure 5.14

---

[14]To measure the SNR I divided the peak amplitude of the FT (at the Larmor frequency) by the highest amplitude of the FT associated with noise. The latter is dominated by noise at the 4$^{\text{th}}$ harmonic of 60 Hz.
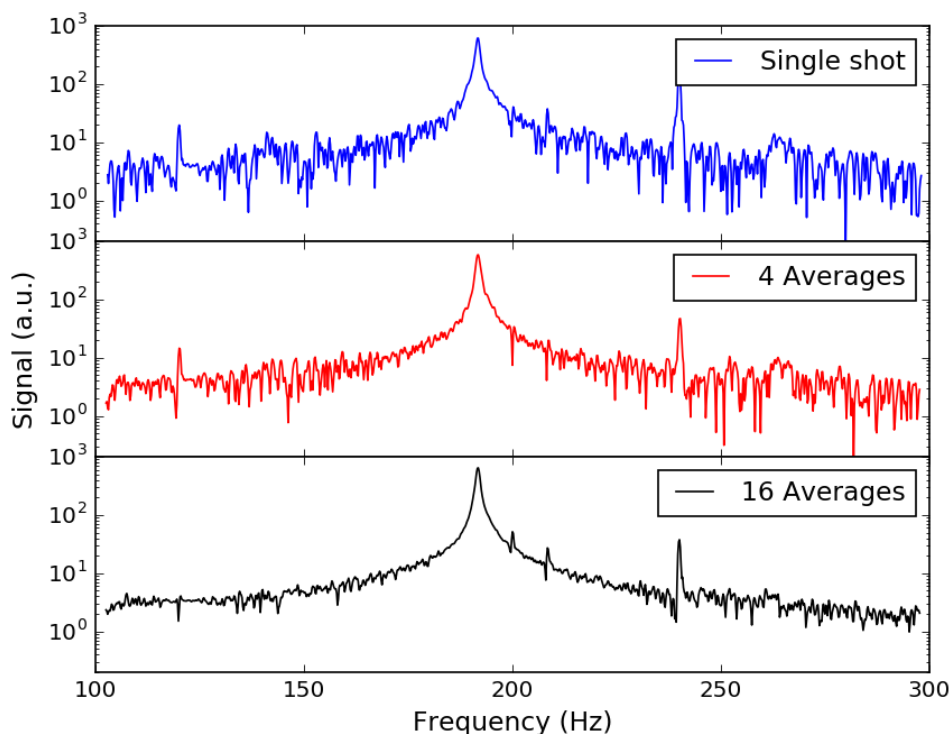
Figure 5.14: Fourier transform of ^{1}H FID signals at $f_L = 191.60$ Hz. Deionized water was used as a sample. (top panel) single shot; (middle panel): 4 averages and (bottom panel): 16 averages. A pre-polarization field of 1.6 T and a signal detection bandwidth of 83 Hz were employed.

illustrates the suppression of noise in the FT as the number of averages is increased.

Another parameter that can influence SNR is the polarization field B_p. Figure 5.15 summarizes the observed relationship between SNR and B_p using deionized water at $f_L = 191$ Hz. The FTs of FID signals at $B_p = 1.6$, 0.77 and 0.09 T are also shown. Two features are noteworthy. First, at low polarizing fields the SNR increases in proportion to B_p, but then eventually starts to saturate. Second, quite reasonable SNRs of order ~20 are observed at $B_p = 0.09$ T. This is remarkably low, but still higher than the SNR reported in Ch. 3 Sec. 3.2, and suggests that one might be able to polarize samples in situ, rather than in a separate polarization region.

Spin dephasing times T_2^* of deionized water, acetone, HFB and pentane were measured, and the results are summarized in Table 5.4. All of the observed values lie in the range 0.2 - 0.6 s. Factors that contribute to the decay time T_2^* of the FID envelope include dipolar interactions with paramagnetic Oxygen molecules dissolved in samples and spin dephasing caused by field inhomogeniety. The effect of the latter can be removed using a Carr-Purcell-Meiboom-Gill (CPMG) pulse sequence to periodically refocus the magnetization [88, 89].

99
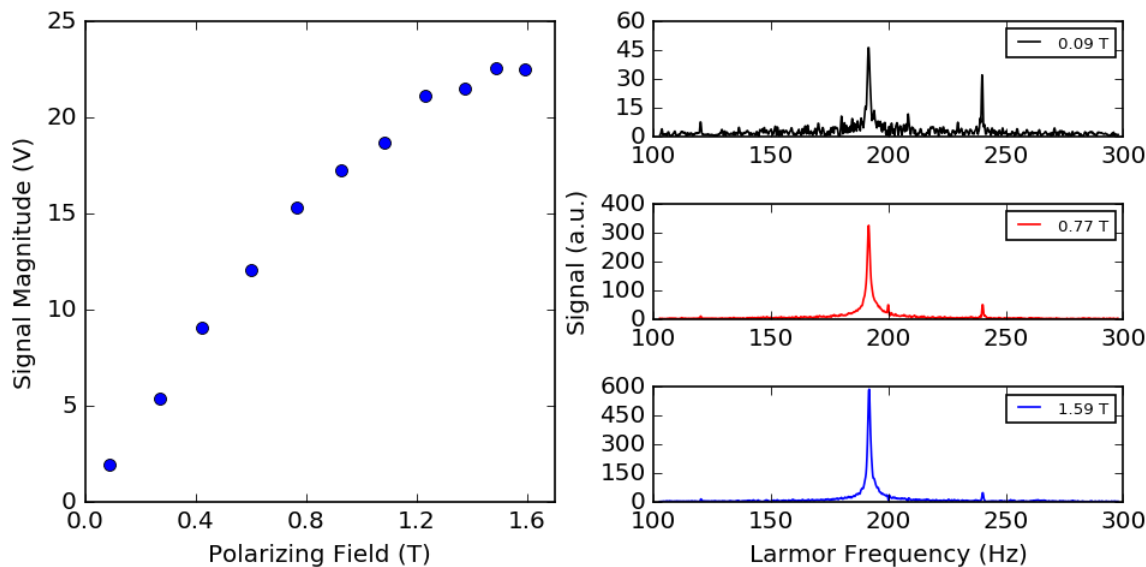
Figure 5.15: (Left): Effect of polarizing field B_p on the amplitude of FID signals, (right): Fourier transforms of FID signals at $B_p = 0.09$ T (top-right); 0.77 T (middle-right) and 1.59 T (bottom-right). Data were recorded at $f_L = 191.60$ Hz with a bandwidth of 83 Hz; Four averages were employed.

	Deionized water	Acetone	HFB	Pentane
T_2^* (s)	0.52(2)	0.56(2)	0.25(3)	0.57(1)

Table 5.4: Spin dephasing times T_2^* in seconds.

The CPMG sequence I employed started with a 1-cycle $\pi/2$ rotation (at 200 Hz) followed by a train of 2-cycle π rotations separated by 40 ms. I was able to measure $T_{2CPMG} = 3.2 \pm 0.2$ s for the deionized water. This value is higher, by a factor 2, than the value $T_{2CPMG} = 1.68$ s that I reported in Ch. 3 using tap water. It shows how the spin dephasing time can be improved by purifying the sample. I also employed the CPMG sequence on acetone, HFB and pentane, and measured values of T_{2CPMG} between 1.5 and 2 s. These are much lower than the T_2 relaxation times listed in Table 5.3, for samples that have been degassed.[15] Hence, the quality of the NMR signals in my experiment could be significantly improved if the sample materials were degassed, flamed sealed in glass cells and then placed inside an appropriate sample carrier. The carrier would be needed to protect the glass cells against mechanical impacts exerted on the cell as it is shuttled back and forth. This is part of a plan to upgrade the current apparatus, but is not reported in my thesis.

---

[15]Through 5 freeze-thaw cycles under vacuum.
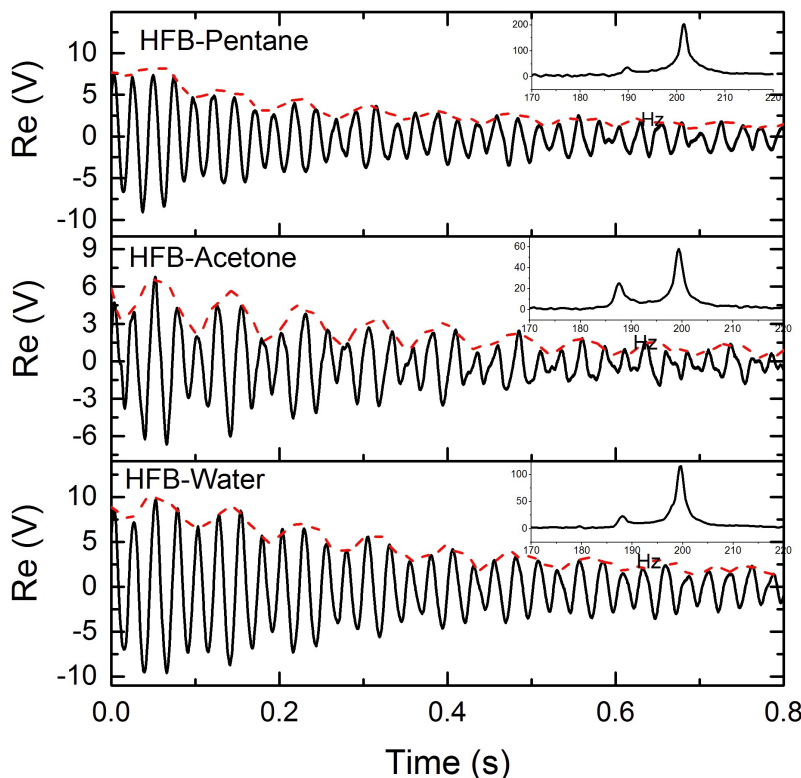
Figure 5.16: Real part (solid line) and magnitude (dashed line) of FID signals acquired from samples containing ^{19}F and ^{1}H nuclei. From top to bottom the samples consist of a) 4.0 ml of HFB and 8.0 ml of pentane (top); b) 5.6 ml of HFB and 9.6 ml of acetone (middle) and c) 6.0 ml of HFB and 9.6 ml of water (bottom). Fourier transforms are shown in the insets. Data recorded at $B_0 = 4.7$ μT and a bandwidth of 83 Hz. Each FID is averaged 4 times.

5.2.2 ULF NMR: Two Spin Species

Mixtures of HFB & acetone, HFB & pentane and HFB & water were used as sources of ^{1}H and ^{19}F nuclei, to investigate the detection of ULF NMR signals from two spin species simultaneously. Acetone and pentane are miscible in HFB but water is not. Therefore a HFB & water mixture might not be appropriate for use in a critical spin dressing experiment if the goal is to work with homogeneous samples. Figure 5.16 shows FID data acquired from all three mixtures. Double peaks, corresponding to the two different nuclear precession frequencies are evident. The higher frequency peak is from the ^{1}H nuclei.

The signals shown in Fig. 5.16 correspond to the oscillating magnetic field $\mathbf{B_M} = \mathbf{B_H} + \mathbf{B_F}$ associated with the precessing nuclear magnetization $\mathbf{M} = \mathbf{M_H} + \mathbf{M_F}$, where the subscripts H and F denote contributions from ^{1}H and ^{19}F nuclei, respectively. A 10 ms tipping pulse at 200 Hz is used to initiate these FIDs. This pulse is spectrally broad. Its FWHM is

101

Sample	Ratio of $^{19}F/^{1}H$ nuclei (Stoichiometry)	Ratio of FID amplitudes (Experiment)	Ratio of FT peak areas (Experiment)
HFB/Water	0.29	0.24	0.23
HFB/Acetone	0.37	0.43	0.43
HFB/Pentane	0.25	0.17	0.20

Table 5.5: Comparison of the relative number of ^{1}H and ^{19}F nuclei in each sample with the ratio of FID amplitudes and FT peak areas. Each peak area in the final column is calculated between frequencies $f_L \pm$ FWHM.

approximately $1.2/\tau$, where τ is the pulse duration, which is of order 120 Hz in this case.[16] As a result, both $\mathbf{M_H}$ and $\mathbf{M_F}$ are rotated by approximately the same angle. The frequency of the tipping pulse is chosen so that it is resonant with the ^{1}H in the field B_0, and its amplitude is chosen so as to produce a 90° rotation for the ^{1}H nuclei. This places $\mathbf{M_H}$ in the equatorial plane of the Bloch sphere but leaves $\mathbf{M_F}$ with a small residual component along $\mathbf{B_0}$. I will return to this later in this chapter and discuss a method to rotate both $\mathbf{M_H}$ and $\mathbf{M_F}$ into the equatorial plane.

FID data from all three mixtures are well fit by the sum of two exponentially decaying sinusoids. The ratio of the number of ^{19}F and ^{1}H nuclei in the sample can then be inferred from the relative amplitude of the two components. Alternatively this ratio can be inferred from the relative areas of the two peaks in the Fourier transform. Table 5.5 shows the relative number of ^{1}H and ^{19}F spins in the sample determined from stoichiometry, from the ratio of the two signal components extracted from fits to the FIDs, and from the areas of the FTs. The stoichiometric determination is given by:

$$\frac{N_F}{N_H} = \frac{M_H \, \rho_F \, V_F \, \zeta_F}{M_F \, \rho_H \, V_H \, \zeta_H} \tag{5.6}$$

where M_i is the molar mass, ρ_i is the density, V_i is the volume of each substance employed and ζ_i is the number of unpaired nuclear spins contributed by each molecule.

The Larmor frequencies of ^{1}H (f_{LH}) and ^{19}F (f_{LF}) nuclei, for each measurement, can be extracted from these data with typical precisions of 2 mHz and 7 mHz, respectively. The difference between these precisions is due to the relative number of nuclear spins employed. Accurate measurements of Larmor frequencies are often required in physics, as is the case for searches for the neutron electric dipole moment [118], the development of sen-

---

[16]The Fourier transform of a square pulse of duration τ

$$\Pi_\tau(t) = \begin{cases} 1, & |t| \leq \tau/2 \\ 0, & |t| > \tau/2 \end{cases} \tag{5.5}$$

is $H(f) = \tau \text{sinc}(\pi\tau f)$ with FWHM = $1.2067/\tau$ [117].
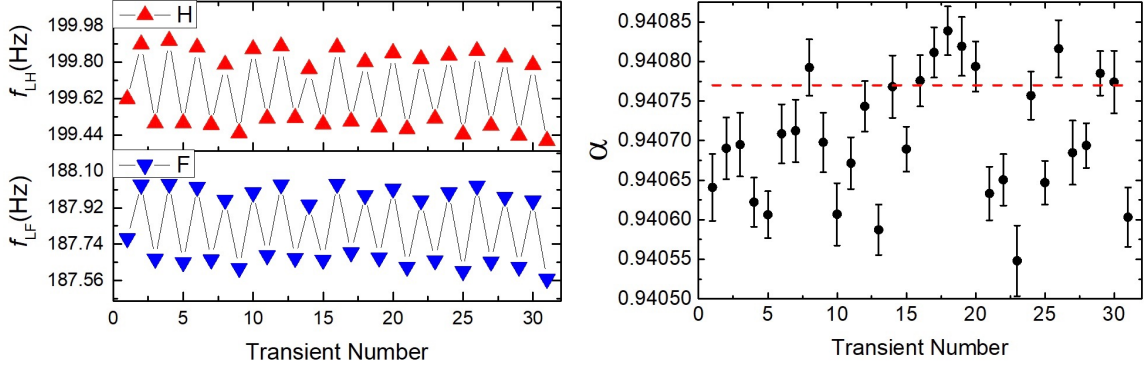
Figure 5.17: Characterization of the extent to which ^{1}H-^{19}F precession frequencies track one another as the static field is modulated between 4.731 and 4.722 μT. Also shown is the inferred ratio $\alpha = \gamma_F/\gamma_H$, which is robust against field variations, as desired for co-magnetometry. The data corresponding α is distributed about the ratio of literature values of γ_H and γ_F [42], which is identified by dashed line $\alpha = 0.94077$. Uncertainty in B_0 was 1 nT and data recorded at bandwidth of 83 Hz.

sitive gyroscopes [119], studies of spin-gravity coupling [120] and tests of Lorentz and CPT violation [121]. A limiting factor in such experiments is the inevitable fluctuation of the static magnetic field about which the nuclear spin precesses. One method to combat these fluctuations is to use a second nuclear spin species as a comagnetometer against which the precession of the first nuclear spin can be compared. For example, in a sample containing ^{1}H and ^{19}F nuclei, either one could be used to monitor the precession rate of the other. To investigate this concept I intentionally modulated the amplitude of the static magnetic field $\mathbf{B}_0$ and attempted to determine how precisely the precession of the two nuclear spins tracked one another. The left-hand side of Fig. 5.17 shows f_{LH} and f_{LF} as inferred from a series of FIDs generated as the static magnetic field is alternated between nominal values of 4.731 and 4.722 μT. This represents a 0.1% variation in B_0 and hence f_L. The right-hand side of Fig. 5.17 then shows the inferred ratio of the two gyromagnetic ratios γ_F/γ_H. Recall that this ratio is defined as α, see Eq. 2.41. There is no obvious indication that the experimentally determined ratio α is modulated. These data yield an average value of $\alpha = 0.94070(8)$ which is consistent with the value $\alpha = 0.94077(3)$ inferred from previous measurements of γ_F and γ_H [52, 42]. These data also help to inform the accuracy and reproducibility of Larmor frequency measurements obtained with our apparatus. For example, when the static field was set to $B_0 = 4.731$ μT I measured the average values $\bar{f}_{LH} = 199.840(10)$ and $\bar{f}_{LF} = 187.997(9)$ and when the field was set to $B_0 = 4.722$ μT I measured $\bar{f}_{LH} = 199.490(11)$ and $\bar{f}_{LF} = 187.656(11)$. The uncertainty associated with these measurements is approximately 10 mHz for both nuclear spins. This is higher than the uncertainty associated with a single Larmor frequency measurement as discussed at the beginning of this section. This difference is primarily due to the drift in the measured Lar-

mor frequency that is caused by drift in the static field. Over the 4 hour time period during which the data in Fig. 5.17 were obtained, I observed a 36(4) mHz/h change in f_{LH} and a 33(4) mHz/h change in f_{LF}. These drifts in frequencies are equivalent to a $\sim$0.25 nT/h drift in B_0.

As a side note, the effect of chemical shifts, associated with the chemical compounds used in my co-magnetometery experiment, can influence the determination of the ratio of the gyromagnetic ratios of two spin species. In my experiment the measured value of α in terms of the actual value of $\alpha = (\gamma_F/\gamma_H)_{\text{actual}}$ is

$$\alpha_{\text{measured}} = \left(\frac{\gamma_F}{\gamma_H}\right)_{\text{measured}} = \frac{1+\delta_F}{1+\delta_H}\left(\frac{\gamma_F}{\gamma_H}\right)_{\text{actual}} \tag{5.7}$$

$$\tag{5.8}$$

where δ_F and δ_H are the chemical shifts of the ^{19}F in HFB and ^{1}H in acetone, respectively. Chemical shifts are usually expressed in parts per million (ppm). Up to the first order of approximation one can find the relation between the measured and actual values of α,

$$\alpha_{\text{measured}} \approx (1+\delta_F - \delta_H)\,\alpha. \tag{5.9}$$

Note that these chemical shifts must be measured relative to the individual ^{19}F and ^{1}H nuclear spins rather than relative to conventional reference compounds.

5.3 Tuning $\pi/2$ Rotations

Uniform and precise tipping pulses are often desirable in NMR, particularly when trains of tipping pulses are employed and errors are allowed to accumulate. Examples include spin echo sequences [89], magnetic resonance imaging (MRI) [122] and the use of NMR in quantum computing [123, 124]. They are also potentially important in setting the initial conditions for pulsed critical spin dressing experiments, so as to ensure that all of the nuclear magnetization is initially in the equatorial plane of the Bloch sphere. An important diagnostic in these applications is to find the amplitude and waveform of the B_1 field corresponding to a $\pi/2$ rotation, for one- and multi- spin species. I used a method related to the optimum $\pi/2$ rotation pulses for experiments involving one and two spin species to investigate effects related to the use of linearly polarized B_1 fields.

As a matter of convenience, most NMR experiments are performed using linearly polarized B_1 fields. These fields can be decomposed into the sum of two circularly polarized counter-rotating fields. One of these two (e.g. the clockwise polarized field) is typically tuned close to resonance while the other (e.g. counter clockwise polarized field) is then by necessity off resonance. In high field NMR, in a reference frame rotating at the Lar-

mor frequency, the effect of the off-resonant component can be ignored in a first order approximation and the linearly polarized B_1 can be treated as a circularly polarized field of amplitude $B_1/2$. This is called the Rotating Wave Approximation (RWA) [47]. However in a system subjected to strong driving field the RWA breaks down and the off resonant component of the B_1 field can perturb spin dynamics [125]. This is known as the Bloch-Siegert effect [126, 127, 128]. In my ULF NMR experiments, and in particular when I tried to set accurate $\pi/2$ rotations, I observed effects that can be attributed to the Bloch-Siegert effect.

5.3.1 Method

A finite duration linearly-polarized oscillating magnetic field $\mathbf{B}_1 = B_1 \sin(\omega t) \, \hat{x}$ is used as the default tipping pulse in my ULF NMR experiment. The angular frequency of the tipping pulse is tuned to the angular Larmor frequency of the ^{1}H nuclei and its amplitude B_1 is chosen to produce a $\pi/2$ rotation for the ^{1}H nuclei. The amplitude that generates this rotation is determined using a sequence of two tipping pulses separated by a time τ as summarized in Fig. 5.18. The first pulse in this sequence rotates the magnetization $\mathbf{M}$, initially directed along $\mathbf{B}_0$, by an angle θ. Immediately afterward a pulsed magnetic field gradient is applied to de-phase the transverse component of $\mathbf{M}$ as quickly as possible. The second tipping pulse then rotates the remaining magnetization $\mathbf{M}$, which is parallel to $\mathbf{B}_0$, by an angle that is close to $\pi/2$. Note that in situations where this method is applied to samples that are hyperpolarized or in a non-equilibrium state the longitudinal component of $\mathbf{M}$ decays continuously with a time constant T_1. However, in conventional high field NMR, where samples are initially in thermal equilibrium, the longitudinal component of $\mathbf{M}$ relaxes toward a larger thermal equilibrium magnetization with time constant T_1.

The time interval between the two pulses should ideally be much shorter than the longitudinal spin relaxation time T_1 and must be longer than several spin dephasing time
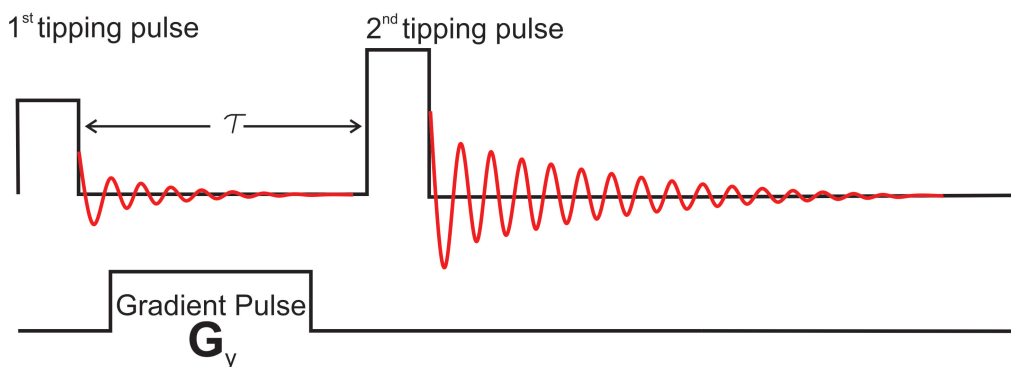
Figure 5.18: Pulse sequence used to find the amplitude of a B_1 field required to produce a $\pi/2$ rotation. The gradient de-phases the precessing magnetization before the second tipping pulse is applied.

constants T_2^* to ensure that the transverse magnetization from the first FID does not contribute to the amplitude of the second FID. This sets constraints on the strength of the pulsed magnetic field gradient between the two tipping pulses. The current used to generate this gradient is controlled by a solid state relay. The orientation $\mathbf{G}_y$ of the gradient is chosen so that it does not saturate the MI sensors as discussed in Sec. 5.1.3.[17]

I monitor the amplitude A_θ and the phase Φ_θ of the second FID while varying the amplitude of the first pulse, and hence θ. For convenience, A_θ is normalized to a reference amplitude A_0 obtained by setting the amplitude of the first pulse to zero. This normalized amplitude characterizes the fraction of the initial nuclear magnetization that is left along z by the first pulse. The condition for a $\pi/2$ rotation is obtained when $A_\theta = 0$ and simultaneously Φ_θ changes by π.

5.3.2   Deviation From Rotating Wave Approximation

Figure 5.19 shows data from the experiment described above. The normalized FID amplitude A_θ/A_0 is interpreted as the normalized fraction of M_z left along $\mathbf{B}_0$ by the first tipping pulse. That pulse consisted of either one or two cycles of a sine or a cosine waveform applied on resonance for ^{1}H nuclei at 200 Hz. The corresponding field $B_0 = 4.7$ μT. Also shown are simulation results for both linearly and circularly polarized B_1 fields. In each case the amplitude of B_1 (which is varied) is normalized to the experimentally determined amplitude that produces a $\pi/2$ rotation.

The comparisons made in Fig. 5.19 clearly illustrate the inadequacy of the RWA for the experimental conditions considered here. That is, they demonstrate the role played by the counter-rotating component of the B_1 field in nuclear magnetization dynamics. The simulation results, presented here and corresponding to a linearly polarized B_1 field, are based on the assumption that the $\mathbf{B}_1$ field is uniform. Any inhomogeniety in $\mathbf{B}_1$ produces different rotation angles in different parts of the sample. Consequently the measured net rotation of $\mathbf{M}$ would be slightly different from that which is predicted by the simulation. Figure 5.20 shows data and simulations analogous to those in Fig. 5.19, for one-, two- and four-cycle sine waveforms at 200 Hz. Note in this case the absolute value of B_1 is given. From this plot one sees that significant deviations between the models (or between the data and predictions that rely on the RWA) begin to appear when $B_1 \simeq B_0 \simeq 5$ μT.
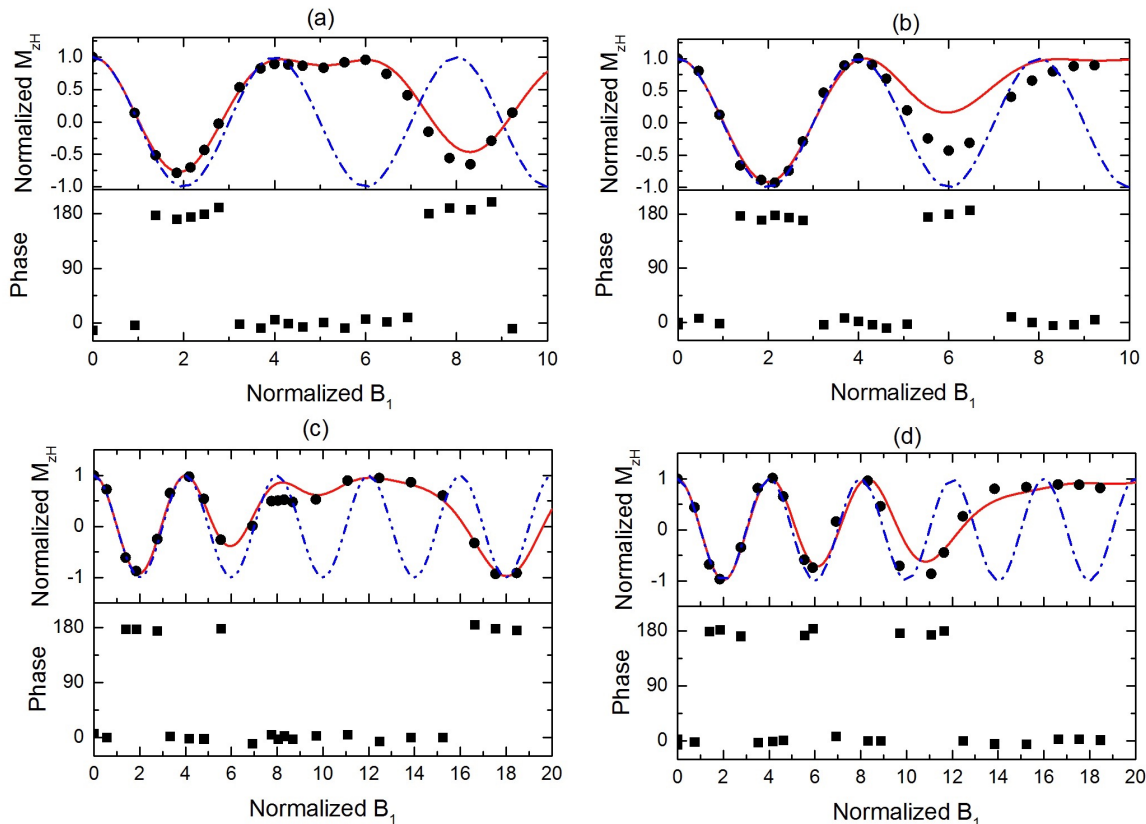
Figure 5.19: Illustration of the experimental B_1 field calibration: data (points) and simulation (curves) for residual ^{1}H nuclear magnetization M_{zH} left along $\mathbf{B}_0$ following a one (panels a and b) or two cycle (panels c and d) tipping pulse applied on resonance at 200 Hz. Results are shown for sine (panels a and c) and cosine waveforms (panels b and d). Calculations are shown for linearly polarized (solid lines) and circularly polarized (dash-dot lines) B_1 fields. Data acquired for ^{1}H nuclei on resonance at 200 Hz.

5.3.3 Conventional Tipping Pulses: Two Spin Species

A problem arises when two or more different spin species (with different gyromagnetic ratios) are present in a sample. In this case it is not possible to simultaneously generate a $\pi/2$ rotation for all nuclei using a conventional tipping pulse. Some fraction of the nuclear magnetization must be left parallel or anti-parallel to $\mathbf{B}_0$. This has implications for critical spin dressing experiments (CSD), because imperfections in the dressing field will tend to mix longitudinal and transverse components of the magnetization over time. This issue is addressed further in the next section, using composite tipping pulses. First, however, some of the implications of using conventional tipping pulses to set the initial conditions for a spin dressing experiment are examined in greater detail.

---

[17]A 12 V automotive battery (LC-RA1212P1), voltage regulator (LT 1962EMS8) and programmable current source (LT 3092EST) were used to drive the current for the gradient field $\mathbf{G}_y$. Pulsed gradients were then controlled by a fast solid state relay (CT137 60V - 200 mA).
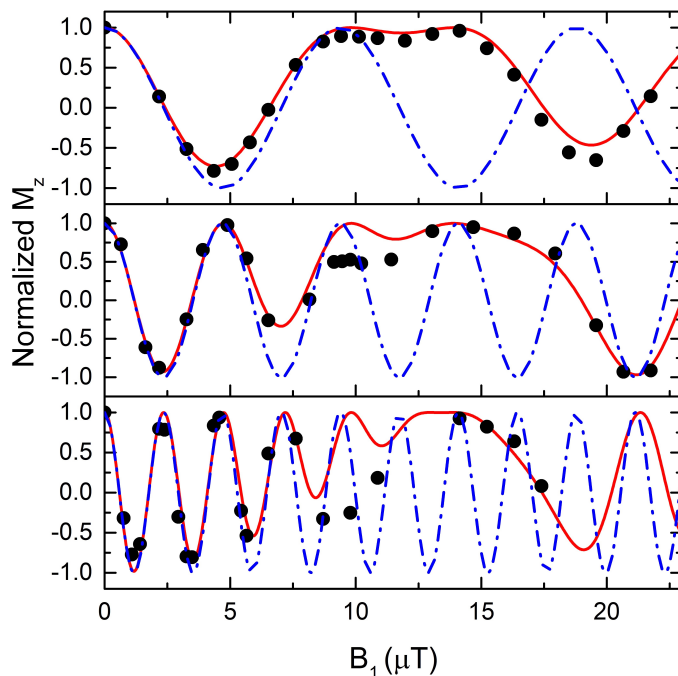
Figure 5.20: Fraction of initial ^{1}H nuclear magnetization left along $\mathbf{B}_0$ following a resonant tipping pulse consisting of one- (top), two- (middle), or four-cycles (bottom) of a 200 Hz sine waveform. When B_1 is comparable to B_0 model calculations based on the RWA (dash-dot line) fail. Much better agreement is observed between data (points) and simulations (solid line) when the full B_1 field is considered.

Consider two different spin species initially aligned with the static field B_0 and then subjected to a conventional tipping pulse. In the case of ^{1}H and ^{19}F, if the tipping pulse produces a $\pi/2$ rotation for ^{1}H it will leave a fraction of the ^{19}F magnetization $\mathbf{M}_F$ along $\mathbf{B}_0$ simply because $\gamma_F < \gamma_H$. If the RWA is employed, then the amplitude B_1^r of the right
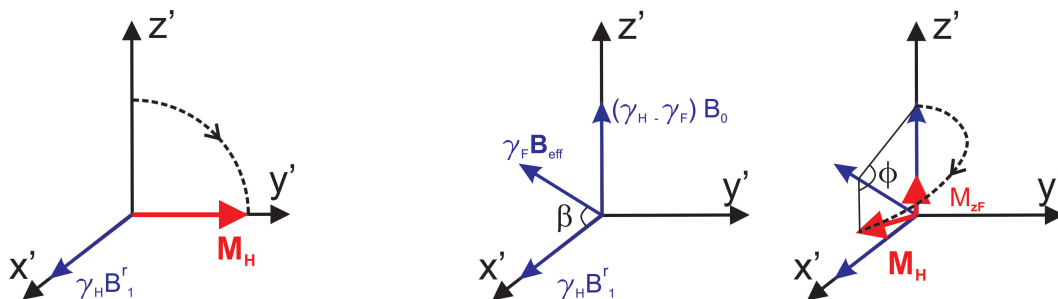
Figure 5.21: Magnetic fields experienced by ^{1}H (left) and ^{19}F (right) nuclei in a frame rotating at the ^{1}H Larmor frequency $\gamma_H B_0$, in the presence of a right hand rotating component of a circularly polarized tipping pulse B_1^r applied at the same frequency. The ^{19}F nuclei precess about an effective magnetic field $\mathbf{B}_{\text{eff}}$ that makes an angle β with respect to the x'-y' plane. When the tipping pulse produces a $\pi/2$ rotation for the ^{1}H nuclei it leaves a residual ^{19}F nuclear magnetization M_{zF} parallel to the static field B_0.

hand rotating component of a circularly polarized $\mathbf{B}_1$ field that produces a $\pi/2$ rotation for ^{1}H when applied on resonance is:

$$B_1^r = \frac{\pi}{2\gamma_H \Delta t} \tag{5.10}$$

where Δt is the pulse duration, which I will assume consists of an integer number N of periods of the hydrogen Larmor resonance frequency f_{LH}. If the B_1 field is linearly polarized, then its amplitude is $2B_1^r$. In the reference frame of the co-rotating component of $\mathbf{B}_1$, the fluorine nuclei see an effective magnetic field $\mathbf{B}_{eff}$ that has contributions from both $\mathbf{B}_0$ and $\mathbf{B}_1$ as shown in Fig. 5.21.

It can be shown that the angle β between $\mathbf{B}_{eff}$ and the equatorial plane satisfies [129]:

$$\tan\beta = 4N\frac{1-\alpha}{\alpha} \tag{5.11}$$

where $\alpha = \gamma_F/\gamma_H \sim 0.94$ is the ratio of the ^{19}F and ^{1}H gyromagnetic ratios. Moreover, the normalized residual magnetization M_{zF} of the ^{19}F nuclei left along $\mathbf{B}_0$ is given by:

$$M_{zF} = \sin^2\beta + \cos^2\beta \, \sin(\frac{\pi}{2} - \phi) \tag{5.12}$$

where ϕ is the angle by which $\mathbf{M}_F$ rotates around $\mathbf{B}_{eff}$:

$$\phi = \frac{\alpha\pi}{2\cos\beta} \tag{5.13}$$

$$= 2\pi\alpha N\sqrt{\frac{1}{16N^2} + \left(\frac{1-\alpha}{\alpha}\right)^2}. \tag{5.14}$$

Figure 5.22 shows examples of classical trajectories for $\mathbf{M}_H(t)$ and $\mathbf{M}_F(t)$ on the Bloch
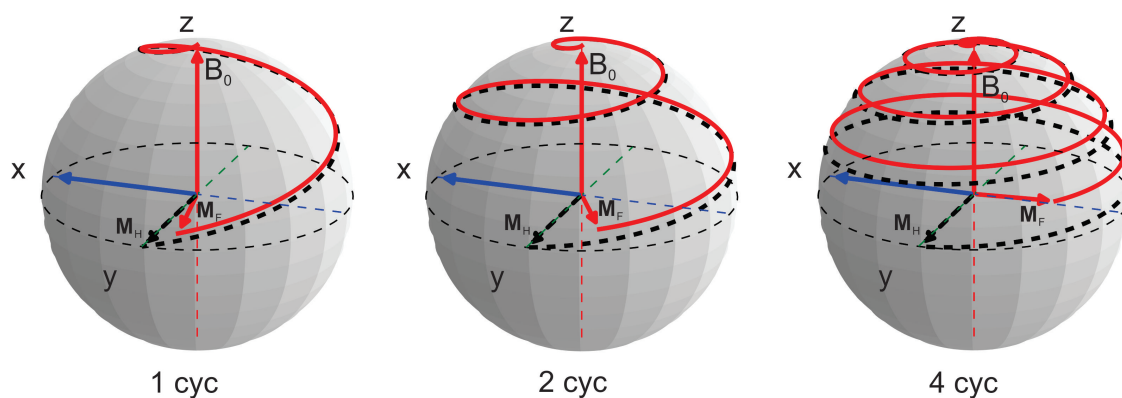
Figure 5.22: Classical trajectories of ^{1}H and ^{19}F nuclear magnetizations during the application of one- (left), two- (middle) and four-periods (right) of a circularly polarized magnetic field resonant with the ^{1}H nuclei at 200 Hz. In each cases the amplitude of B_1 is set to give a $\pi/2$ rotation for the ^{1}H nuclei.

	1 cyc	2 cyc	3 cyc	4 cyc	5 cyc	6 cyc	10 cyc
Circularly polarized	10.4 %	13.5%	18.7%	25.4%	33.4%	42.3%	77.5%
Linearly polarized $\sin(\omega t)$	3.8%	7.5%	12.8%	20.2%	28.7%	38.4%	75.9%
Linearly polarized $\cos(\omega t)$	15.3%	18.1%	23.1%	29.5%	37.0%	45%	78.7%

Table 5.6: Calculated residual ^{19}F nuclear magnetization, left along $\mathbf{B}_0$ when the ^{1}H nuclear magnetization is subjected to a $\pi/2$ rotation. Results for various waveforms and polarizations are shown. The duration of each pulse is given in terms of the number of cycles or periods of the 200 Hz B_1 waveform, which is applied at resonance for the ^{1}H nuclei. The results are obtained from a numerical solution of the Bloch equations.

sphere when they are subjected to circularly polarized B_1 fields at 200 Hz, as obtained from numerical integration of the Bloch equations. For a ^{1}H Larmor frequency $f_{LH} = 200$ Hz and a tipping pulse duration of two ^{1}H Larmor periods the residual ^{19}F magnetization aligned with $\mathbf{B}_0$ is 13.56% of the initial magnetization. The tipping pulse thus corresponds to a 82.3^o rotation for ^{19}F rather than $\pi/2$. This estimate ignores the contribution of the counter-rotating component of B_1. If the same computation is performed by direct numerical integration of the Bloch equations for infinite T_1 and T_2 the residual ^{19}F nuclear magnetization left along $\mathbf{B}_0$ is 8.4% for a sine waveform and 18.4% for a cosine waveform. Table 5.6 shows further simulation results for the normalized residual magnetization M_{zF} when the tipping pulse duration is N/f_{LH}. In each case the amplitude B_1 of the linearly polarized field produces a $\pi/2$ rotation for ^{1}H.

I measured M_{zH} and M_{zF}, in response to the application of linearly polarized tipping pulses using the method outlined in Sec. 5.3.1. The results are in good agreement with model calculations for sine and cosine waveforms. Figure 5.23 shows data acquired when 2 cycles of a linearly polarized tipping pulse was applied at frequency of 200 Hz, and the amplitude B_1 was set to produce a $\pi/2$ rotation for ^{1}H. The data in Fig. 5.23 were acquired in two experimental runs; one with deionized water and the other with HFB.[18] When $M_{zH} = 0$ I inferred 7 ± 2 % and 13 ± 2 % for M_{zF} when sine and cosine waveforms were employed, respectively. Note that the zero-crossings for M_{zH} and M_{zF} were obtained by fitting the experimental data with an empirical 4th-order polynomial function. The use of higher and lower order polynomial functions had little effect on the inferred residual M_{zF}. A sinusoidal fit function also yields very similar results.

5.3.3.1   Composite Tipping Pulse

Composite pulses, which are made up of continous conventional RF pulses, were invented by M. H. Levitt during the 1980s [130]. They have been used widely in NMR for population inversion [131], broadband spin excitation [132], compensation of RF pulse length errors

---

[18]This was done to increase SNR.

[133], nuclear quadrapole spectroscopy [134], quantum computing experiments to minimize systematic errors [135, 136, 137] and also in interferometry with ultra-cold atoms [138]. Their relevance to my experiments is that a composite pulse can be used to rotate both the
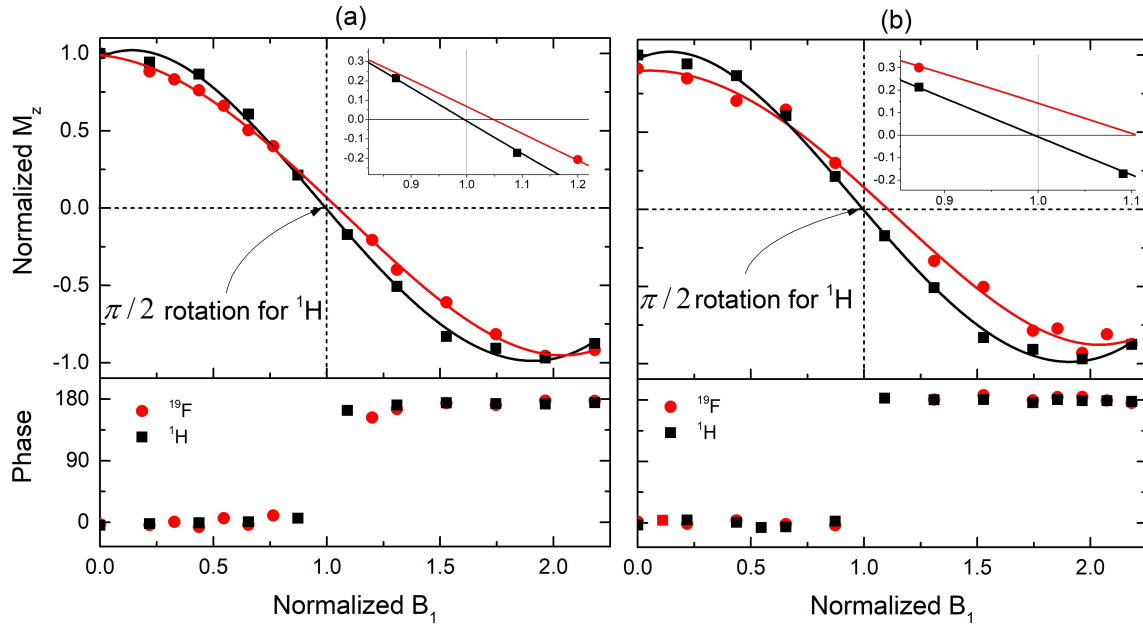
Figure 5.23: Experimental demonstration of the influence of linearly polarized tipping pulses on ^{1}H and ^{19}F nuclei, initially aligned with $\mathbf{B}_0$. Two periods of 200 Hz sine (left) and cosine (right) waveforms are applied on-resonance for the ^{1}H nuclei. Curves are empirical 4th order polynomial fit functions and are used to infer the fraction of the ^{19}F magnetization that is left along $\mathbf{B}_0$.
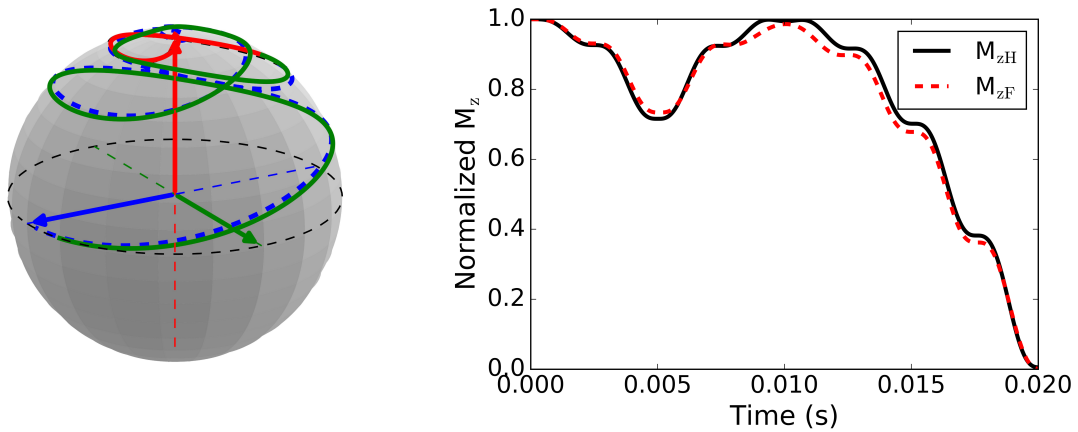
Figure 5.24: (Left) Classical trajectory of ^{1}H (solid line) and ^{19}F (dashed line) nuclear magnetization when a linearly polarized composite pulse consisting of one cycle of the waveform $\mathrm{B}_1 \sin(\omega t)$ and three cycles of the waveform $\mathrm{B}_1 \cos(\omega t + \theta)$ with $\theta = 175^o$ is applied at the ^{1}H Larmor frequency (200 Hz). The projections of $\mathbf{M}_\mathrm{H}$ and $\mathbf{M}_\mathrm{F}$ on $\mathbf{B}_0$ are also shown as a function of time.
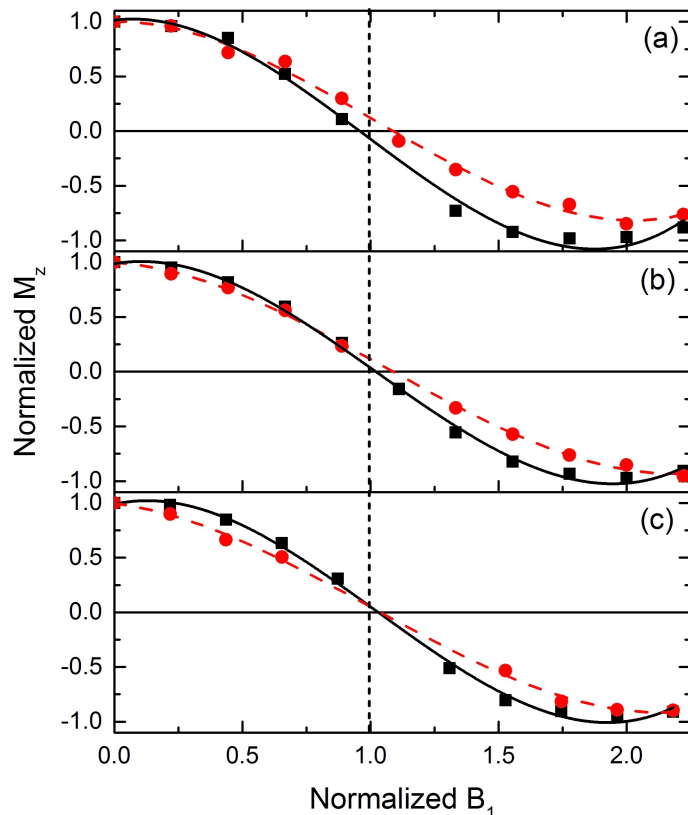
Figure 5.25: Experimental data demonstrating of the effect of the relative phase shift θ of the second tipping pulse in a composite pulse on the rotation of ^{1}H and ^{19}F nuclear spins. The composite pulse is made up of 1 and 3 cycles of on-resonance oscillations at 200 Hz. (a) $\theta = 158^o$; (b) $\theta = 178^o$ and (c) $\theta = 190^o$. Curves are empirical 3rd-order polynomial fit functions.

^{1}H and ^{19}F nuclear spins into the transverse plane.

There are three experimental parameters associated with conventional tipping pulses that can in principle be adjusted to generate $\pi/2$ rotations for two spin species. These parameters are (a) the duration of the tipping pulses, (b) the relative phase θ of pulses and (c) the frequency of pulses. We restrict solutions to a composite pulse that is made of two successive tipping pulses, in which the amplitude of the tipping pulse remains constant and in which there is no time delay between the pulses. We further restrict solutions to cases where the frequency of both pulses is on resonance for the ^{1}H nuclei and the duration of each pulse is an integral number of Larmor periods for the ^{1}H nuclei. All that remains then is the relative phase angle θ and the duration of each pulse. Still, this is sufficient to obtain the desired results. Table 5.7 shows a few examples of conditions that rotate both the ^{1}H and the ^{19}F nuclei into the transverse plane as obtained from numerical searches through the available phase space for a semi-classical model of spin precession. In this model nuclear magnetization of two spin species are initially along $B_0\hat{z}$ and a linearly polarized

N_1 (cycle)	N_2 (cycle)	B_1 duration (cycle)	B_1 (μT)	θ (degrees)	f (Hz)	f_{LH} (Hz)	M_{zH} (%)	M_{zF} (%)
1	0.264	1	2.349	307.5	200	200	-0.091	0.004
1	3.686	1	2.349	252.5	200	200	-0.140	-0.007
1	3.058	1	2.349	100.0	200	200	-0.160	-0.001
1	3.082	1	2.349	277.5	200	200	0.030	-0.14
1	2.076	1	2.349	22.5	200	200	0.083	-0.135
1	3.895	1	2.349	87.5	200	200	0.189	-0.091
1	1.268	2	1.174	325.0	200	200	-0.083	-0.076
1	2.944	2	1.174	175.0	200	200	-0.559	0.015
1	3.000	2	1.174	175.5	200	200	-1.401	-1.110
1	2.371	3	0.783	312.5	200	200	0.005	0.280
1	3.960	3	0.783	180.0	200	200	-0.250	0.046
1	3.557	4	0.587	295.0	200	200	0.293	-0.018
1	4.423	1	2.208	302.5	188	200	-0.079	-0.020
1	0.234	1	2.208	325.0	188	200	-0.078	-0.075
1	2.599	1	2.208	92.5	188	200	0.095	-0.066
1	2.139	1	2.208	67.5	188	200	-0.002	0.165
1	3.025	1	2.208	282.5	188	200	-0.315	0.016

Table 5.7: Examples of parameters, obtained from simulations of classical spin precession, for linearly polarized composite tipping pulses that simultaneously rotate ^{1}H and ^{19}F nuclear spins into the transverse plane. B_1 has a sine waveform and is linearly polarized. Note the resolution on θ is 2.5^o and that B_1 duration refers to the number of oscillation cycles at the tipping pulse frequency f.

$\mathbf{B}_1$ is applied along $\hat{x}$ direction. B_0 is 4.7 μT. Figure 5.24 shows classical trajectories of the nuclear magnetizations $\mathbf{M}_H$ and $\mathbf{M}_F$ for one of the examples listed in Table 5.7. Also shown is a plot of the two nuclear magnetizations as a function of time.

An experimental search for a composite pulse analogous to the one shown in Fig. 5.24 was conducted. Figure 5.25 shows data for M_z as a function of B_1, for three different phase angles θ. The desired effect (rotation of the spins of both species into the transverse plane) is observed at $\theta = 190^o$ rather than at 175° as was anticipated. The discrepancy may be due to inhomogeniety in $\mathbf{B}_1$ or the fact that $\mathbf{B}_1$ is not perfectly orthogonal to $\mathbf{B}_0$, because $\mathbf{B}_0$ includes contributions from background fields orthogonal to the sine-ϕ coil. However, the goal of putting $\mathbf{M}_H$ and $\mathbf{M}_F$ into the transverse plane, is achieved.

The composite tipping pulse described here will be used in future critical spin dressing experiments. In this thesis I only demonstrate critical spin dressing experiments that were initiated by conventional tipping pulses.

Chapter 6

Critical Spin Dressing Experiment

Critical spin dressing (CSD) has been proposed as an experimental technique that could enhance sensitivity in a planned search for the neutron electric dipole moment (nEDM) [28]. Despite this, CSD has not been demonstrated and experimentally evaluated. In this chapter I bring together the various experimental techniques described in Chs. 2-5 and perform a pulsed CSD experiment on ^{1}H and ^{19}F nuclei. To the best of my knowledge this represents the first experimental demonstration of CSD. I start with a method to analyse and interpret FID data acquired during pulsed CSD experiments. Next, I present experimental results demonstrating CSD. Results are presented both for conventional dressing field waveforms (in the sense that their use has been proposed and modelled) as well as what I will call unconventional waveforms. By this I simply mean that I have introduced innovations that may prove advantageous in future work. Finally I examine the influence of variations in the dressing field amplitude on CSD.

The data reported in this chapter were all acquired using a mixture of acetone (as a source of ^{1}H) and hexafluorobenzene (as a source of ^{19}F). Recall that the gyromagnetic ratio of ^{1}H is 6% larger than that of ^{19}F. This should be compared to the gyromagnetic ratio of ^{3}He which is 11% larger than the gyromagnetic ratio of the neutron. Hence the ^{1}H-^{19}F system provides a reasonable proxy to simulate and study aspects of the critical dressing problem that may be relevant to the n-^{3}He system.

Throughout this chapter I will compare experimental data for the CSD parameter $\eta^{'}$ with predictions based on theory and simulation, as described in Ch. 2. The simulations use a classical model of spin precession to predict modified gyromagnetic ratios $\gamma_{\mathrm{H}}^{'}$ and $\gamma_{\mathrm{F}}^{'}$ at any desired value of $y < 1$. The theoretical prediction is only valid for $y \ll 1$ and is based on the analytic expressions $\gamma_{\mathrm{H}}^{'} = \gamma_{\mathrm{H}} \, J_0(x_{\mathrm{H}})$ and $\gamma_{\mathrm{F}}^{'} = \alpha \gamma_{\mathrm{F}} \, J_0(\alpha x_{\mathrm{H}})$, where x_{H} is the dressing parameter x associated with ^{1}H nuclear spins and $\alpha = \gamma_{\mathrm{F}}/\gamma_{\mathrm{H}}$.
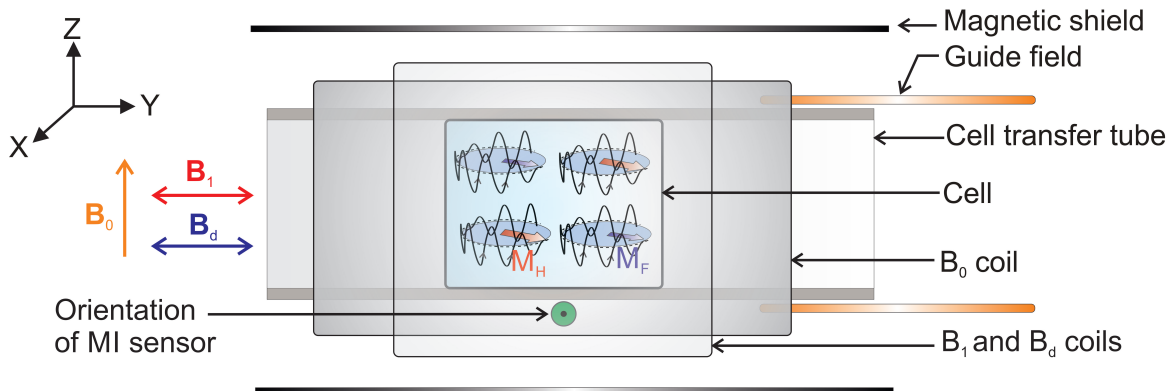
Figure 6.1: Approximate arrangement of components and fields during spin dressing experiments (Not to scale). See Fig. 5.1 for a more detailed depiction.

6.1 Overview the Experiment

A mixture of hexafluorobenzene (C_6F_6) and acetone (C_3H_6O) is pre-polarized in a 1.5 T field and then transported pneumatically into an experimental volume with μT-scale fields. A $\pi/2$ pulse is applied to initiate nuclear spin precession at ^{1}H Larmor frequencies f_{LH} of the order 200 Hz. The corresponding ^{19}F Larmor frequency is of the order 188 Hz. The ensuing oscillating magnetic field $\mathbf{B}_M$ associated with the precessing magnetization $\mathbf{M} = \mathbf{M}_H + \mathbf{M}_F$ is then directly monitored using magneto-impedance sensors arranged in a gradiometer configuration. Note that the tipping pulse used in all experiments presented in this chapter is a conventional tipping pulse based on a sine waveform.

To accomplish spin dressing, we apply an intense far off-resonant oscillating magnetic field $\mathbf{B}_d$ (the dressing field) at frequency f_d for a time Δt. This periodically drives $\mathbf{M}$ away from the equatorial plane of the Bloch sphere and reduces the net rate at which nuclear spin precession about the static field $\mathbf{B}_0$ occurs. Under critical dressing conditions both species precess at the same effective rate, and hence acquire the same modified gyromagnetic ratios $\gamma'_H = \gamma'_F$. The orientations of the various magnetic fields involved in the CSD experiment, and schematic (i.e. simplified) cartoons of nuclear spin trajectories on the Bloch sphere in response to the dressing field are shown in Fig. 6.1.

6.1.1 Data Analysis

The NMR data from which values of γ'_H and γ'_F are extracted typically consist of a superposition of two exponentially decaying sinusoids at the ^{1}H and ^{19}F NMR Larmor precession frequencies f_{LH} and f_{LF}. These frequencies are measured relative to a local oscillator that is used as the reference frequency f_{ref} for the phase sensitive detector (PSD). For most of the CSD experiments reported in this chapter I chose $f_{LH} = 200$ Hz (and hence $f_{LF} = 188$ Hz)

and $f_{\text{ref}} = 160$ Hz. Note that if $f_{\text{ref}} = f_{\text{LH}}$, the PSD output for the corresponding nucleus is an unmodulated exponentially decaying signal from which it is difficult to accurately extract phase information. By setting f_{ref} far enough away from f_L a reasonable modulation of FID signals is observed and extraction of phase (by fitting model equations to the data) is simplified. There is a trade off in this process between the accuracy to which phases can be extracted and the amplitude of the signals. The latter decreases as f_{ref} is displaced from f_{LH} because of the finite bandwidth of the PSD through which FID signals are passed.

Two FID signals are recorded in these experiments: one before and one after applying the dressing field B_d. As pointed out in Ch. 4, the total duration of the recorded FID signal, before application of the dressing pulse, plus the duration of the tipping pulse is chosen so that the dressing field always starts with a well-defined phase relationship with respect to the tipping pulse. Each FID is complex, with real and imaginary (or in-phase and quadrature) components as measured with respect to the local oscillator. In total there are four components to each CSD dataset that need to be modelled or fit by exponentially decaying sinusoids. An example of one such experimental recording is shown in Fig. 6.2. The model equation used to extract information from these data is:

$$f(t) = A_H \ e^{-t/T_{2H}^*} \ \cos(\omega_H t + \theta_H) \ + \ A_F \ e^{-t/T_{2F}^*} \ \cos(\omega_F t + \theta_F) \qquad (6.1)$$

where T_{2H}^* and T_{2F}^* are spin dephasing times, $\omega_H = 2\pi f_{\text{LH}}$ and $\omega_F = 2\pi f_{\text{LF}}$ are angular frequencies, θ_H and θ_F are initial phases, and A_H and A_F are initial signal amplitudes. Note that by "initial" I mean that all phases and amplitudes in these fit functions are extrapolated back to $t = 0$, even for the case of fits to data after the dressing field pulse.
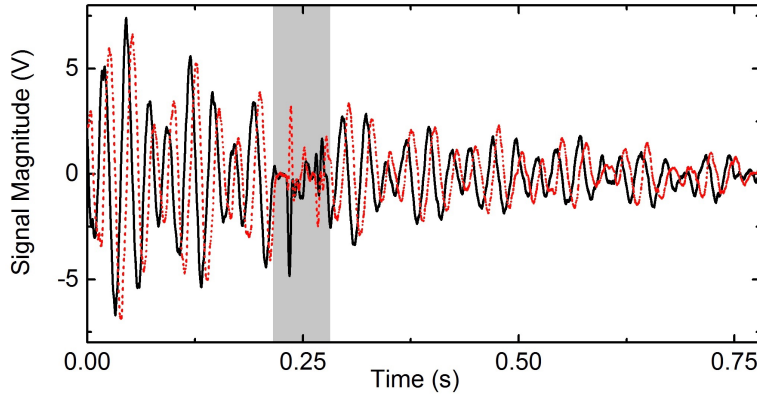
Figure 6.2: FID recording acquired from a mixture of hexafluorobenzene and acetone relative to a 160 Hz reference oscillator. The grey band indicates the period during which a 1 kHz/20 cycle duration dressing field characterized by (^{1}H) dressing parameters $x_H = 1.05$ and $y_H = 0.4$ is applied (and during which the Magneto-Impedance sensor response is saturated). The data were recorded at $f_{\text{LH}} = 200$ Hz, $f_F = 188$ Hz and with a PSD bandwidth of 125 Hz. The real (solid-line) and imaginary (short-dash line) components of the signal are both shown. Data like this are used to extract modified gyromagnetic ratios γ_H' and γ_F'.

For each recording consisting of two FIDs there are 32 fit parameters that need to be determined. However, only 14 of these parameters are independent: ω_F, ω_H, A_H, A_F, T_{2H}^*, T_{2F}^* and the 8 initial phases: $\theta_{H,Re,b}$, $\theta_{H,Im,b}$, $\theta_{H,Re,a}$, $\theta_{H,Im,a}$, $\theta_{F,Re,b}$, $\theta_{F,Im,b}$, $\theta_{F,Re,a}$ and $\theta_{F,Im,a}$. The indices b, a, Re and Im denote "before" and "after" the dressing field and the "real" and "imaginary" components of the FID signal, respectively.

The phases of the two components of the FID signals before and after the dressing field pulse are: $\theta_{H,b}$, $\theta_{H,a}$, $\theta_{F,b}$ and $\theta_{F,a}$, where:

$$\theta_{H,a} = \tan^{-1}(\cos(\theta_{H,Re,a})/\cos(\theta_{H,Im,a})) \tag{6.2}$$

$$\theta_{H,b} = \tan^{-1}(\cos(\theta_{H,Re,b})/\cos(\theta_{H,Im,b})) \tag{6.3}$$

$$\theta_{F,a} = \tan^{-1}(\cos(\theta_{F,Re,a})/\cos(\theta_{F,Im,a})) \tag{6.4}$$

$$\theta_{F,b} = \tan^{-1}(\cos(\theta_{F,Re,b})/\cos(\theta_{F,Im,b})). \tag{6.5}$$

The phase changes accumulated by the two species that can be directly attributed to the dressing field are:

$$\Delta\theta_H = \theta_{H,a} - \theta_{H,b} \tag{6.6}$$

$$= 2\pi y N\left(\frac{\gamma_H'}{\gamma_H} - 1\right) \tag{6.7}$$

and

$$\Delta\theta_F = \theta_{F,a} - \theta_{F,b} \tag{6.8}$$

$$= 2\pi y N\left(\frac{\gamma_F'}{\gamma_H} - \frac{\gamma_F}{\gamma_H}\right), \tag{6.9}$$

where $y = f_{LH}/f_d$, and the latter forms of the two equations make use of the dressing field conditions outlined in Sec. 4.2. Note that $\Delta\theta_H$ and $\Delta\theta_F$ do not include the phase accumulated due to normal Larmor precession, because all phases in the fit functions are referenced to time t = 0. The difference between the phase changes caused by the dressing field is then

$$\Delta\theta_{HF}(x,y) = \Delta\theta_H - \Delta\theta_F$$

$$= 2\pi y N\left[\left(\frac{\gamma_H' - \gamma_F'}{\gamma_H}\right) - \left(\frac{\gamma_H - \gamma_F}{\gamma_H}\right)\right]. \tag{6.10}$$

Let us call the first and second terms inside the square brackets of Eq. 6.10 $\eta'(x)$ and η, respectively. Note that η' is a function of the ^{1}H dressing parameter $x = x_H = \gamma_H B_d/\omega_d$
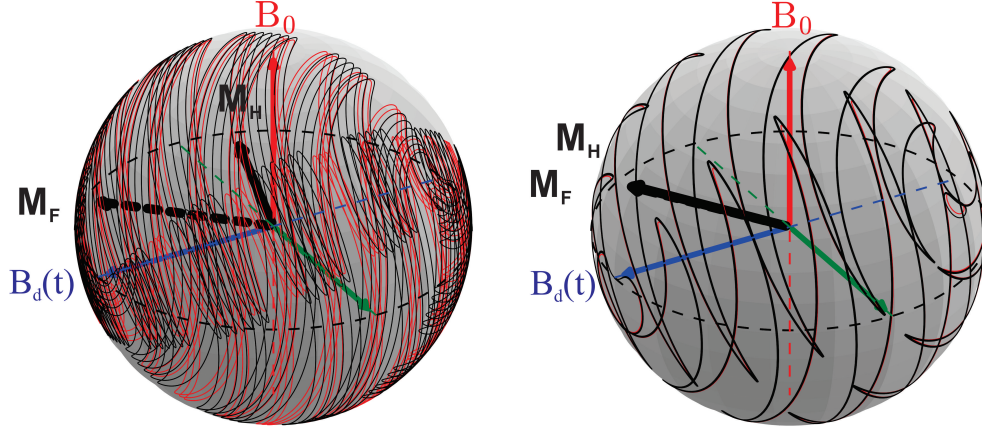
Figure 6.3: Semi-classical trajectories of ^{1}H (black) and ^{19}F (red) nuclear spins during dressing field pulses ($y_H = 0.1$; $\Delta t = 82.5$ ms; $f_{LH} = 100$ Hz; $f_d = 1$ kHz). Left: Dressing field amplitude detuned from critical conditions ($x_H = 1.000$; $x_F = 0.940$). Over time, the two trajectories diverge. Right: Critically dressed nuclear spin precession ($x_H = 1.286$; $x_F = 1.208$); the two trajectories never diverge. In both cases nuclear magnetizations are initially in phase before application of the dressing field $\mathbf{B}_d$.

and $y = y_H = \gamma_H B_0/\omega_d$.[1] Making use of Eq. 6.10, it can be written

$$\eta'(x, y) = \eta + \frac{\Delta\theta_{HF}(x, y)}{2\pi y N}. \tag{6.11}$$

In the absence of spin dressing (i.e. $x = 0$), $\Delta\theta_{HF}$ is zero because $\Delta\theta_H$ and $\Delta\theta_F$ are both individually equal to zero. Equivalently, $\Delta\theta_{HF}$ is zero because η' is equal to $\eta = 0.05923$. In general when a dressing field is applied, $\Delta\theta_{HF}$ is non-zero. In the special case where CSD conditions are generated, $\eta'(x, y)$ is zero. Thus η' is a useful parameter for characterizing CSD. Each time this function passes through zero as x and y are varied critical spin dressing conditions are obtained and the two species precess at the same average rate. In the experiments presented in this chapter I keep y fixed and vary x to reveal CSD.

Two sets of simulated semi-classical spin trajectories are shown in Fig. 6.3. In one case the dressing conditions are slightly detuned from CSD and the time average rates at which $\mathbf{M}_H$ and $\mathbf{M}_F$ precess about $\mathbf{B}_0$ are different. In the other case (CSD) the two nuclear magnetization vectors precess at the same time average rate.

6.1.2 Uncertainties

In this subsection I estimate the precision to which η' can be determined using my apparatus. In this estimate I ignore effects that an imperfect dressing field may have on η'. Such effects

---

[1]For the remainder of this chapter I will drop the subscripts on x_H and y_H, and simply refer to them as x and y.

	Average value	Standard Deviation
η	0.05930	$\pm$ 0.00008
$\Delta\theta_{\mathrm{H}}$	0°	$\pm$ 5°
$\Delta\theta_{\mathrm{F}}$	-6°	$\pm$ 8°
$\Delta\theta_{\mathrm{HF}}$	6°	$\pm$ 13°

Table 6.1: Means and standard deviations of parameters inferred from fits to 15 transients acquired without a dressing field ($x = 0$).

might be caused by asymmetry in the current circuit, geometry, homogeniety or alignment of $\mathbf{B}_{\mathrm{d}}$.

The various fit parameters such as the induced phase changes are influenced by the signal-to-noise ratio (SNR) of the data. The higher the SNR, the lower the fit uncertainty. To estimate a lower bound or minimum achievable uncertainty for $\eta^{'}$ I eliminated the dressing field pulse and recorded 15 FID signals. These signals were recorded at different times over a 2 hours period to account for drift that might occur in experimental parameters. Each transient was analysed using the fit function Eq. 6.1 to infer phases $\Delta\theta_{\mathrm{H}}$, $\Delta\theta_{\mathrm{F}}$ and $\Delta\theta_{\mathrm{HF}}$, as well as the parameter η specified in Eqs. 6.6 - 6.10. The average coefficient of determination R^2 which characterizes goodness of fit was 0.977. The means and standard deviations of the various parameters are listed in Table 6.1. The standard deviations can be used to calculate an uncertainty for $\eta^{'}$

$$\delta\eta^{'}(x,y) = \delta\eta + \frac{\delta\Delta\theta_{\mathrm{HF}}(x,y)}{2\pi y \mathrm{N}}.\tag{6.12}$$

For example, for a $\mathrm{N} = 20$ cycle-long dressing field pulse at $f_{\mathrm{d}} = 500$ Hz and with $f_{\mathrm{LH}} = 200$ Hz the estimated uncertainty in $\eta^{'}$, based on data from Table 6.1, is $\delta\eta^{'} = \pm 0.0046$ which in turn corresponds to a ± 0.96 Hz uncertainty in the inferred difference in modified ^{1}H and ^{19}F Larmor frequencies.

6.2 Observation of CSD: Conventional Waveform

Figure 6.4 summarizes the outcome of a series of ^{1}H and ^{19}F spin dressing experiments performed in the vicinity of critical dressing. Normalized apparent gyromagnetic ratios $\gamma^{'}/\gamma_{\mathrm{H}}$ and the parameter $\eta^{'}$ are plotted as a function of the dressing parameter x, for two different values of y. The parameter $\eta^{'}$ measures the deviation between normalized $\gamma^{'}_{\mathrm{H}}$ and $\gamma^{'}_{\mathrm{F}}$, and thus passes through zero at CSD. In detail, the dressing field pulses consisted of 20 complete cycles of a cosine waveform at $f_{\mathrm{d}} = 500$ Hz or $f_{\mathrm{d}} = 1$ kHz; hence they were either 40 ms or 20 ms long in duration. The static magnetic field was $B_0 = 4.69$ μT corresponding to $f_{\mathrm{LH}} = 200$ Hz, and ^{1}H dressing parameters $y_{\mathrm{H}} = 0.4$ and 0.2, respectively.[2] The time at

---

[2]The corresponding ^{19}F dressing parameters are $y_{\mathrm{F}} = 0.376$ and 0.188.
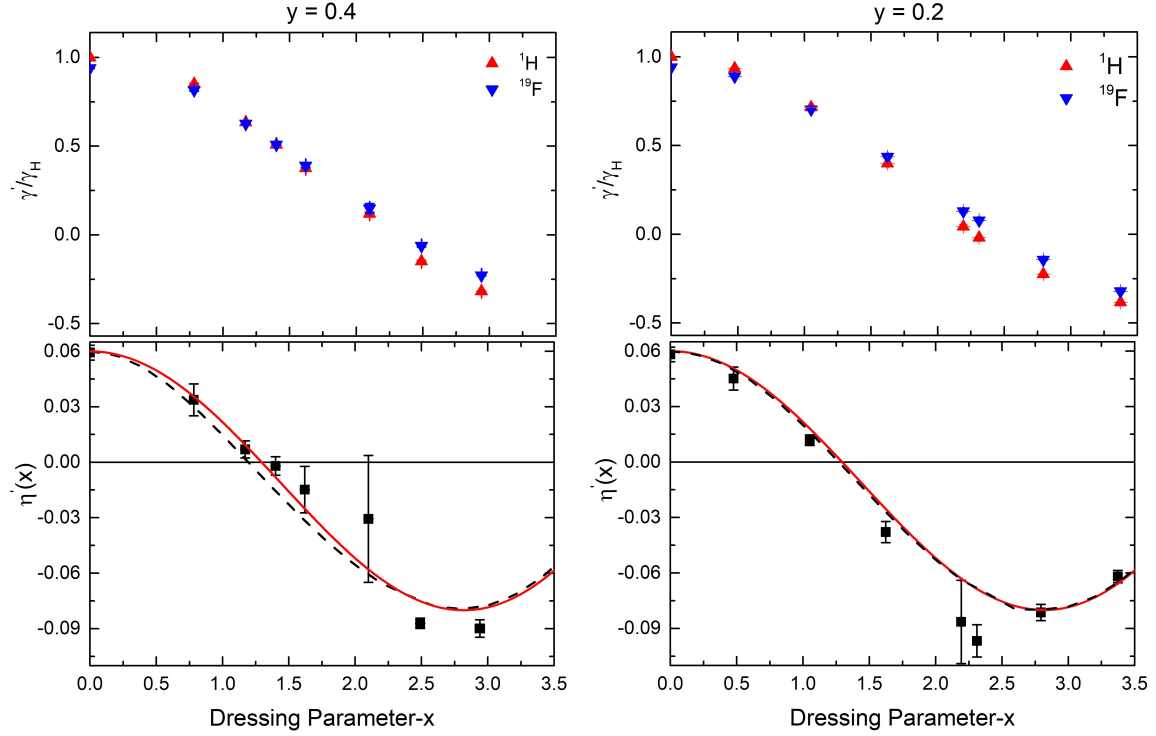
Figure 6.4: Outcomes of spin dressing experiments on ^{1}H and ^{19}F as characterized by normalized apparent gyromagnetic ratios γ'/γ_H and the parameter $\eta' = (\gamma'_H - \gamma'_F)/\gamma_H$. Experiments were performed in a static field $B_0 = 4.69 \ \mu T$, corresponding to a ^{1}H Larmor frequency $f_{LH} = 200$ Hz. A 20-cycle dressing field pulse was applied at frequencies $f_d = 500$ Hz (left) and $f_d = 1$ kHz (right) corresponding to dressing parameters $y_H = 0.4$ and $y_H = 0.2$, respectively. Also shown are curves representing expectations from theory (solid curve), see Eq. 6.15, and the simulation (dashed curve).

which the dressing field pulse is initiated is set to $t = 260$ ms,[3] which is equivalent to 52 and 48.9 ^{1}H and ^{19}F Larmor periods, respectively. In an ideal case this time would be an integer number of Larmor periods for both species. Thus the dressing field always starts with a fixed phase relationship with respect to the precessing magnetization. The experimental data displayed in Fig. 6.4 represent the averages of 5 and 7 repetitions for $y_H = 0.2$ and 0.4, respectively. The error bars represent the standard deviations of the observed distributions. Also shown in this figure are predictions for η' from theory and simulations. Recall from Sec. 2.2 that the quantum model predicts that in the regime $y \ll 1$, where the static field B_0 is much weaker than the dressing field B_d, the apparent gyromagnetic ratios of ^{1}H and

---

[3]$t = 0$ corresponds to the time at which the tipping pulse is initiated.

^{19}F and the corresponding values of $\eta^{'}$ become

$$\gamma_{\mathrm{H}}^{'} = \gamma_{\mathrm{H}} J_0(x_{\mathrm{H}}), \tag{6.13}$$

$$\gamma_{\mathrm{F}}^{'} = \gamma_{\mathrm{F}} J_0(x_{\mathrm{F}}), \tag{6.14}$$

$$\eta^{'} = J_0(x_{\mathrm{H}}) - \alpha J_0(\alpha x_{\mathrm{H}}) \tag{6.15}$$

where $\alpha = \gamma_{\mathrm{F}}/\gamma_{\mathrm{H}}$, $x_{\mathrm{H}} = \gamma_{\mathrm{H}} \mathrm{B_d}/\omega_{\mathrm{d}}$ and $x_{\mathrm{F}} = \gamma_{\mathrm{F}} \mathrm{B_d}/\omega_{\mathrm{d}}$. The simulation results shown in this figure were described in Sec. 2.1 and are based on a semi-classical model of spin precession.

The quality of data for $y_{\mathrm{H}} = 0.4$ is worse than that at $y_{\mathrm{H}} = 0.2$. I believe this is because of the generation of spin dressing echoes as discussed in Ch. 4. These are more likely to occur for $y \gtrsim 0.3$. This is illustrated in Fig. 6.5, which shows contours of simulated echo amplitudes as a function of x and y (see Sec. 4.3.2.3). In this phase space plot echoes happen more often in bright regions. Thus at $y = 0.4$, echoes are expected for $1 \lesssim x \lesssim 3$ but at $y = 0.2$ they are absent. The formation of echoes is not accounted for in the simple fit procedure outlined in Sec. 6.1.1, and so the spin precession phases extracted at $y = 0.4$ are more likely to be perturbed by this effect than those extracted at $y = 0.2$. This is consistent with the observation that better agreement with theory is observed at $y = 0.2$ than it is at $y = 0.4$ in Fig. 6.4.

At $y = 0.2$, the data agree with the simulation and theory except for outliers in the range $2 < x < 2.5$. In this range the modified gyromagnetic ratios $\gamma_{\mathrm{H}}^{'}$ and $\gamma_{\mathrm{F}}^{'}$ are both small. Hence the average precession rates about $\mathbf{B}_0$ are very low. Under these conditions, if $\mathbf{B}_0$ and $\mathbf{B}_{\mathrm{d}}$ are not orthogonal, an avoided crossing of energy levels is induced and the accumulated phases acquired by the ^{1}H and ^{19}F are influenced. This effect was discussed
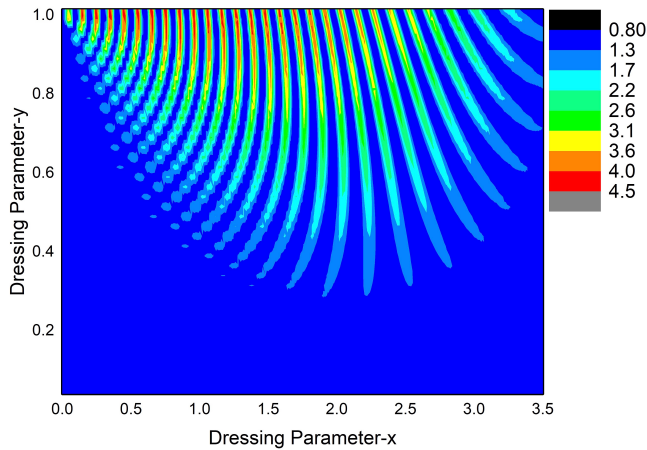
Figure 6.5: Contour plot of simulated echo amplitudes, as described in Sec. 4.3.2.3. Results shown for a 20 cycle cosine waveform dressing field applied at $f_{\mathrm{d}} = 500$ Hz. Echoes are less likely to occur in the blue regions.

in Sec. 2.4.1. It is not captured in the simulation results presented in Fig. 6.4 .

6.3   Observation of CSD: Unconventional Waveforms

The dressing field waveform employed in the previous section is not unique, although it is the only waveform that has been considered so far in the context of ^{3}He co-magnetometry for a
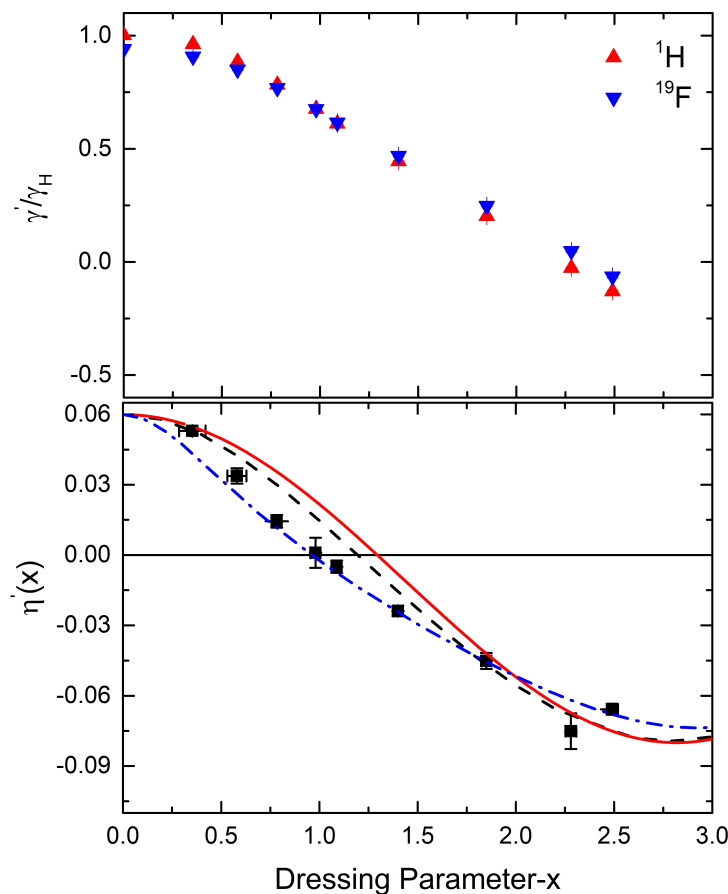
Figure 6.6: Outcomes of ^{1}H and ^{19}F spin dressing experiments as characterized by normalized apparent gyromagnetic ratios $\gamma^{'}/\gamma_H$ and the parameter $\eta^{'}$ defined in Eq. 6.11. Experiments were performed in a static field $B_0 = 4.69$ μT, corresponding to a ^{1}H Larmor frequency $f_{LH} = 200$ Hz. A 20-cycle dressing field pulse was applied at frequencies $f_d = 500$ Hz corresponding to dressing parameters $y_H = 0.4$. Unlike the analogous experiment summarized in Fig. 6.4 a phase-modulated dressing field waveform is employed. Also shown are curves representing expectations from theory (solid; $y \approx 0$; see Eq. 6.15; no phase modulation), a simulation without modulation (dashed, $y = 0.4$) and a simulation with modulation (dashed-dot, $y = 0.4$). Error bars represent standard deviations of observations for 4 repetitions.

neutron electric dipole moment search.[4] Here I show examples of spin dressing experiments in which the phase and the amplitude of the dressing field are modulated. I refer to these as unconventional waveforms although for at least one of the two examples there are good reasons to anticipate that it ought to be more robust than the conventional waveform. In the first example of an unconventional waveform the time dependence of $\mathbf{B}_d(t)$ is given by:

$$\mathbf{B}_d(t) \ = \ B_d \ \cos(2\pi f_d t \ + \ \phi) \ \hat{y} \tag{6.16}$$

where the phase ϕ is modulated between zero and π in alternate cycles. The motivation for this alternation is to minimize the accumulation of phase errors caused by potential asymmetries in the dressing field and thereby attempt to minimize potential undesired mixing of transverse and longitudinal components of the magnetization. Such schemes are common in NMR pulse sequences. When 20 cycles of this waveform are applied to ^{1}H and ^{19}F at $f_d = 500$ Hz in a field $B_0 = 4.7$ μT where the ^{1}H Larmor frequency is $f_{LH} = 200$ Hz, one finds that the first CSD point is located at $x_H = 0.98$ rather than $x_H = 1.29$ as was the case in Fig. 6.4. Figure 6.6 shows data for spin dressing experiments performed with this phase modulated dressing field. Also shown are predictions from the $y \ll 1$ theory (see Eq. 6.15) and the simulation. The $y \ll 1$ prediction from theory does not account for phase modulation and is simply shown for reference. Simulation results obtained from a semi-classical model of spin precession are shown with and without phase modulation. The experimental data and error bars represent the averages and standard deviations of 4 replicates of the experiment. Compared to data acquired without phase modulation (Fig. 6.4), the data in Fig. 6.6 exhibit less scatter and are more reproducible. It is informative to look at the phase space for spin dressing echo formation shown in Fig. 6.7, and to compare it to Fig. 6.5. At $y_H = 0.4$, the likelihood of echo formation, and consequently the likelihood of the phase measurement being perturbed, is much less when the phase-modulated waveform is employed.

As a second example of an unconventional dressing field waveform, data were acquired using an amplitude-modulated field:

$$\mathbf{B}_d(t) \ = \ B_d \ \cos(2\pi f_m t) \ \cos(2\pi f_d t \ + \ \phi) \ \hat{y}, \tag{6.17}$$

where the f_m is the modulation frequency. Additionally the phase of alternate cycles of the dressing field is modulated between 0 and π as in the previous example. The phase modulation is employed to minimize the accumulation of phase errors. In principle f_m could be set to any value, but in running various simulations I realized the limit $f_d \ll f_m$ might be of interest because the sensitivity of $\eta^{'}$ to variations in x_c (i.e. $d\eta^{'}/dx|_{x = x_c}$) seems to

---

[4]In the final stages of preparing my thesis I learned about simulations performed by E. Webb at Caltech, in which other dressing waveforms are considered [139]
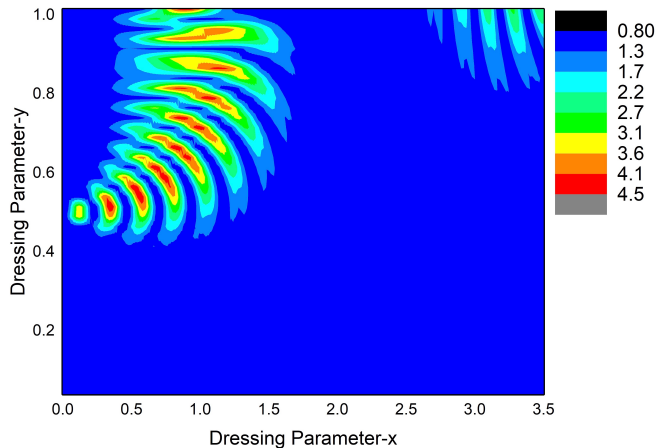
Figure 6.7: Contour plot of simulated echo amplitudes for the 500 Hz phase-modulated dressing field used to generate the data in Fig. 6.6. Echoes are less likely to occur in the blue regions.

be about $\sim 37\%$ smaller than it is without amplitude and phase modulation.[5] As one would expect in this limit the power spectrum of this waveform is dominated by contributions in the vicinity of f_{m}, not f_{d}. Clearly there is no longer a unique dressing parameter x in this case, but a reasonable estimate for the sake of comparison is to adopt the definition $x = \gamma_{\mathrm{H}} B_0 / 2\pi f_{\mathrm{m}}$.

Figure 6.8 shows data for η' as a function of x defined in this manner, for an experiment in which $f_{\mathrm{d}} = 500$ Hz, $f_{\mathrm{m}} = 5$ kHz and $f_{\mathrm{L}} = 200$ Hz. Also shown are predictions of the theory and simulation. In the case of the $y \ll 1$ theory η' is obtained from Eq. 6.15 when the standard dressing field waveform $B_{\mathrm{d}} \cos(2\pi f_{\mathrm{m}} t)\, \hat{y}$ is employed. In other words, no modulation is included, and the result is for reference only. In the case of the simulation, η' is obtained using a semi-classical model of spin precession in which the dressing field waveform in Eq. 6.17 is used. The CSD point is observed at $x_c = 1.71$ rather than $x_c = 1.29$ as expected from the $y \ll 1$ theory for a standard dressing field waveform. From this plot, it is indeed evident that the critical dressing condition is less sensitive to variations in x than it would be without amplitude modulation.

The example of CSD summarized in this section opens a window to searching for new dressing field waveforms that simultaneously minimize the accumulated errors and sensitivity of η' to variation in experimental parameters. Such efforts may help to increase the sensitivity of the planned nEDM experiment [28].
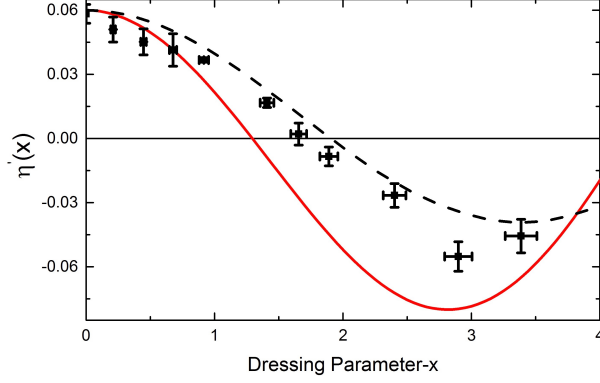
Figure 6.8: Outcomes of spin dressing experiments on ^{1}H and ^{19}F as characterized by the parameter $\eta^{'}$ defined in Eq. 6.11. Experiments were performed in a static field $B_0 = 4.69~\mu$T, corresponding to a ^{1}H Larmor frequency $f_{\mathrm{LH}} = 200$ Hz. An 8-cycle dressing field pulse was applied at frequency $f_{\mathrm{d}} = 500$ Hz corresponding to a dressing parameter $y_{\mathrm{H}} = 0.4$. Unlike the analogous experiment summarized in Fig. 6.4, a phase-and amplitude-modulated dressing field waveform is employed. The phase is periodically modulated between 0 and π and the amplitude is modulated at frequency $f_{\mathrm{m}} = 5$ kHz. Also shown are curves representing expectations from the $y \ll 1$ theory without modulation (solid, $y \approx 0$) and the simulation with modulation (dashed, $y = 0.4$).

6.4 Effect of Variations in x on CSD

From an experimental perspective, understanding the sensitivity of CSD conditions to variations in the dressing parameter x is important. Figure 6.9 shows the results of one such
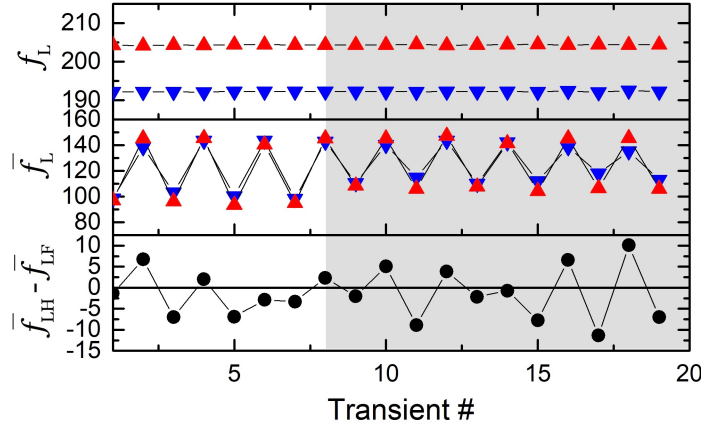
Figure 6.9: Effect of varying the spin dressing parameter x in the vicinity of critical dressing at $x_{\mathrm{c}} = 1.23$. The parameter y was fixed at 0.2 while x was alternated between 1.11 and 1.35 (white region) and 1.11 and 1.29 (grey region). In detail the dressing field consisted of 10 cycles of a waveform at $f_{\mathrm{d}} = 1$ kHz. Top panel: undressed Larmor frequencies (f_{L}). Middle panel: time-average Larmor frequencies ($\bar{f}_{\mathrm{L}}$). Bottom panel: the difference between the ^{1}H and ^{19}F time-average Larmor frequencies. This difference is nominally zero at the critical dressing point.

---

[5]The data in Figs. 6.4 (for $y = 0.2$), 6.6 and 6.8 yield values of 0.08, 0.06 and 0.05 for $d\eta^{'}/dx|_{x = x_c}$ respectively.

study, performed in the vicinity of critical dressing at $y = 0.2$ and $x = x_{\mathrm{H}} = 1.23$. To examine the effect of variations in x I fixed the parameter y by holding the static field $\mathrm{B_0}$ and the dressing frequency f_{d} constant and then alternated the amplitude $\mathrm{B_d}$ of the dressing field between the values 31.6 μT and 26 μT, corresponding to an alternation of x by ± 0.12 about the critical dressing point $x_{\mathrm{c}} = x_{\mathrm{H}} = 1.23$. Simultaneously I monitored the precession rates and phases of the undressed ^{1}H and ^{19}F nuclei before and after the dressing field pulse, and inferred their time-average precession rates, $\bar{f}_{\mathrm{LH}}$ and $\bar{f}_{\mathrm{LF}}$, during the dressing field pulse.

If x is fixed at x_c then $\gamma'_{\mathrm{H}} = \gamma'_{\mathrm{F}}$ and consequently $\bar{f}_{\mathrm{LH}} = \bar{f}_{\mathrm{LF}}$. However, when x is alternated about x_c,[6] $\bar{f}_{\mathrm{LH}} > \bar{f}_{\mathrm{LF}}$ for $x < x_c$ and $\bar{f}_{\mathrm{LH}} < \bar{f}_{\mathrm{LF}}$ for $x > x_c$. See Fig. 2.12-b. So, the sign of the difference $\bar{f}_{\mathrm{LH}} - \bar{f}_{\mathrm{LF}}$ should alternate as x alternates. This results in a modulation of $\bar{f}_{\mathrm{LH}} - \bar{f}_{\mathrm{LF}}$ that is evident in Fig. 6.9. These data also help to inform the accuracy, precision, and the reproducibility of $\bar{f}_{\mathrm{L}}$. For example, at $x = 1.11$ I measured $\bar{f}_{\mathrm{LH}}$ and $\bar{f}_{\mathrm{LF}}$ nine times over a four hour period and obtained $<\bar{f}_{\mathrm{LH}}> = 144.66 \pm 2.13$ Hz and $<\bar{f}_{\mathrm{LF}}> = 140.98 \pm 2.91$ Hz.[7]

Note that the dressing field pulse applied here is spectrally broad. For an N cycle-long dressing field pulse at frequency f_{d} the FWHM of the pulse is approximately $\Delta f_{\mathrm{d}} \simeq 1.2\, f_{\mathrm{d}}/$N. In this case $\Delta f_{\mathrm{d}} \simeq 120$ Hz. Consequently, the parameter

$$x = \frac{\gamma \mathrm{B_0}}{2\pi(f_{\mathrm{d}} \pm \frac{\Delta f_{\mathrm{d}}}{2})} \simeq x_0 \left(1 \mp \frac{\Delta f_{\mathrm{d}}}{2 f_{\mathrm{d}}}\right) \tag{6.18}$$

spans a range distributed about its central value $x_0 = \frac{\gamma \mathrm{B_d}}{\omega_{\mathrm{d}}}$ with a full width $\Delta x = x_0 1.2/$N, up to the first order of approximation. For a 10 cycle-long dressing field pulse this width is 12% of x_0. I believe that if one wants to control the state of the precessing ^{1}H-^{19}F system more accurately, longer dressing field pulses would need to be employed. This in turn will reduce the spectral width of x.

---

[6]More precisely, at the lowest critical dressing point, where the first crossing between $\gamma'_{\mathrm{H}}(x)/\gamma_{\mathrm{H}}$ and $\gamma'_{\mathrm{F}}(x)/\gamma_{\mathrm{H}}$ occurs.

[7]The uncertainties reported here represent the standard deviations.

Chapter 7

Conclusion

This thesis presents an experimental demonstration of the critical spin dressing (CSD) phenomenon for two spin species: hydrogen ^{1}H and fluorine ^{19}F. My work is motivated by a proposed search for the neutron electric dipole moment (nEDM) [28] using ultra-cold neutrons (UCN) and ^{3}He, which is planned to run at the Spallation Neutron Source (SNS) at Oak Ridge National Laboratory. Observation of a non-zero nEDM would represent evidence for CP symmetry violation and could shed light on the matter anti-matter asymmetry in the universe.

A crucial part of the SNS experiment, in one mode of operation, involves application of a strong far off-resonant oscillating magnetic field, called a dressing field. This dressing field can be used to modify and control the apparent Larmor precession rate of the UCN and ^{3}He in a static magnetic field. Under particular conditions, known as CSD, it should be possible to force UCN and ^{3}He to precess at the same effective rate. The central goal of my thesis was to generate the necessary conditions and to observe CSD experimentally. Rather than using UCN and ^{3}He which would require using sophisticated apparatus I used ^{1}H and ^{19}F nuclear spins, both of which are easy to incorporate into an appropriate ultra-low field NMR experiment. The combination of ^{1}H and ^{19}F is a reasonable proxy for experimental simulations of UCN and ^{3}He because the gyromagnetic ratios of the former differ by 6% while those of the latter differ by 11%. While there are close analogies between aspects of my experiment and the planned CSD experiment at the SNS in connection with the nEDM search, there are also differences. Perhaps one of the most important differences is that my experiment involves pulsed application of a dressing field while the SNS experiment will ultimately involve a continuous dressing field.

The spin dressing (SD) technique was developed during the 1960s and 1970s by C. Cohen-Tannoudji and S. Haroche [34]. They showed that the gyromagnetic ratio of a particle γ, and consequently its time average precession rate in a weak static field $\mathbf{B}_0$, can be modified when it is subjected to a strong off-resonant oscillating magnetic field $\mathbf{B}_d(t)$. The sign and magnitude of the modified gyromagnetic ratio γ' is a function of the intensity and frequency

of the dressing field. Theoretically it is possible, but prior to my work it had not yet been demonstrated, that a dressing field can force two spin species with different gyromagnetic ratios to precess about $\mathbf{B}_0$ at the same average precession rate. This is the concept of CSD. The frequency, f_d, and the amplitude, B_d, of the dressing field are described in terms of two dimensionless dressing parameters $x = \gamma B_d/2\pi f_d$ and $y = \gamma B_0/2\pi f_d$. Here x characterizes the intensity of the dressing field and y represents the ratio of the Larmor frequency to the dressing frequency. For the proposed search for the electric dipole moment of the neutron [28] CSD will be performed in the regime $y \ll 1$. In general, and from a technical point of view, to perform CSD in this regime, it is much easier to employ a weak magnetic field B_0, of order a few μT than it is to employ a strong field.

One challenge that is faced in the μT range of magnetic fields is that the thermal equilibrium nuclear magnetization and hence the signal-to-noise ratio (SNR) in a NMR experiment is small. Additionally the Larmor precession frequency and hence the time rate of change of the nuclear magnetization $\mathbf{M}$ is very low. As a result conventional inductive detection coils are a poor choice for attempting to detect NMR signals. To address these challenges I used remote NMR techniques [55] and Magneto-Impedance (MI) sensors. The use of MI sensors for detecting nuclear precession signals is a key element of my SD and CSD experiments. These sensors exhibit a noise density of $5 \text{ pT}/\sqrt{\text{Hz}}$ at 10 Hz, which is comparable to that of unshielded high-T_c Superconducting Quantum Interference Devices (SQUIDs). The most important advantage of MI sensors over SQUIDs or atomic magnetometers is that MI sensors operate at room temperature and do not require any sophisticated environmental or experimental conditions. This enabled me to design a very simple and robust NMR experiment to observe CSD phenomena.

I first evaluated the capabilities of MI sensors for the detection of NMR signals in a number of different ultra-low field (ULF) NMR experiments. I then used MI sensors to perform SD experiments on ^{1}H nuclei in water. The promising results obtained from these experiments convinced me to incorporate MI sensors into a CSD experiment.

When MI sensors are subjected to large magnetic fields, such as the dressing field in a SD experiment, they become saturated. Hence, I was not able to directly monitor the time average precession rate $\bar{f}_L$ of nuclear spins in SD or CSD experiments. I thus developed a simple method to infer $\bar{f}_L$ by examining the phase of precessing nuclear spins before and after application of a dressing field. Using this phase accumulation method I was able to demonstrate CSD for a conventional dressing field waveform, as was shown in Fig. 6.4. However, the quality of the data in that demonstration was not at all impressive. In a standard CSD experiment, as it is usually envisaged, the RF field (dressing field) is applied continuously. But this places heavy demands on the frequency, stability, and accuracy of applied fields. Typically, in NMR, one uses phase-cycling techniques to compensate for the accumulation of errors. A classic example is the use of phase alternation methods in the CPMG sequence [140] for observing spin echo trains. Motivated by this I alternated the

phase of applied dressing fields periodically between 0 and π and observed a significant improvement in the quality of CSD data, as was shown in Fig. 6.6.

Additionally, I used the apparatus I developed to investigate the role of initial conditions in CSD experiments as set by the $\pi/2$ pulse. Here I was interested in simultaneously putting the ^{1}H and ^{19}F nuclear magnetizations, $\mathbf{M}_H$ and $\mathbf{M}_F$, both of which are initially along $\mathbf{B}_0$, into the transverse plane before applying the dressing field. It is impossible to rotate both nuclear magnetizations by $\pi/2$ using conventional tipping pulses. However, it is possible to do this using composite tipping pulses. The composite tipping pulses I developed to simultaneously rotate $\mathbf{M}_H$ and $\mathbf{M}_F$ into the transverse plane comprise two conventional tipping pulses with the same amplitudes and frequencies, but with different durations and phases.

Below I briefly summarize the contents of this thesis, chapter by chapter.

Chapter 1 introduces the background and motivation to search for permanent electric dipole moments of particles. It then outlines a proposed search for the neutron electric dipole moment or nEDM [28] using the phenomenon of CSD. The phenomenon has not been demonstrated, despite the fact that it lies on the critical path for a planned nEDM experiment, in one mode of operation. This experiment is currently planned to come on-line at the Oak Ridge National Laboratory Spallation Neutron Source (SNS) in 2023. The motivation for my thesis was to develop the tools and apparatus to demonstrate and study CSD.

Chapter 2 reviews the theory needed to understand an ensemble of spin-1/2 particles interacting with a static magnetic field and an intense far off-resonant oscillating magnetic field. In this system one finds that the time average precession rate of the nuclear magnetization differs from the usual Larmor precession frequency. This precession can be described in terms of an apparent or modified gyromagnetic ratio $\gamma^{'}$. Two models are introduced (a semi-classical and a quantum model) and are used to calculate $\gamma^{'}$ in two different regimes characterized by the dimensionless parameter y. These models are eventually compared with experimental data for SD and CSD in Chapters 4 and 6. The semi-classical model is based on a simple determination of the time average precession rate of the nuclear magnetization $\mathbf{M}(\mathrm{t})$, obtained by numerical integration of the Bloch equations. The quantum model, which has been described previously [34, 48, 38] involves calculation of energy level differences in a system of interacting spins and photons. I show how the predictions of the two models are consistent when $y < 1$, but not when $y > 1$. This discrepancy is a consequence of a limitation in the method I used to extract the time-average precession rate from the semi-classical model of spin precession.

In the second part of Chapter 2, I describe the phenomenon of CSD in the regime $y < 1$ using both the quantum and semi-classical models. I focus on parameters that influence

CSD, including parameters such as the $\pi/2$ tipping pulse that sets the initial condition for a subsequent CSD experiment, as well as imperfections such as misalignment of the static and dressing fields.

Chapter 3 introduces the use of Magneto-Impedance (MI) sensors for detecting ultra-low field (ULF) NMR signals. MI sensors play a critical role in the apparatus I developed to monitor the average precession rates of dressed nuclear spins. Hence their suitability for detecting NMR signals was first evaluated before incorporating them into later SD and CSD experiments. The chapter begins with a description of the characteristics of MI sensors and then describes a series of NMR experiments I designed and performed to assess their capability for detecting longitudinal and transverse nuclear magnetizations. These experiments include Adiabatic Fast Passage (AFP), ULF NMR of spatially-modulated longitudinal nuclear magnetizations, and pulsed ULF NMR. This represents the first time that this kind of solid state magnetometer has been used for NMR. The same apparatus is used for all three of these experiments, with minor differences in applied magnetic fields and detection circuits. All three are classified as remote NMR experiments in which the sample is pre-polarized far away from the region of the apparatus in which signal detection occurs.

In the first experiment I imprinted an alternating longitudinal nuclear magnetization pattern on a stream of flowing water, in which the ^{1}H nuclei were first thermally pre-polarized in a 1.5 T magnetic field. The magnetization pattern was produced by turning an AFP field on and off at a modulation frequency f_m. When the AFP field is on, the ^{1}H nuclear magnetization $\mathbf{M}$ is adiabatically inverted and becomes anti-parallel to the local static field $\mathbf{B}_0$. And when the AFP field is off, $\mathbf{M}$ remains parallel to $\mathbf{B}_0$. The magnetic field $\mathrm{B_M}$ associated with this alternating magnetization pattern was then directly monitored using MI sensors placed close to the stream of flowing water. Data were acquired over the range 0.2 Hz $\leq$ f_m $\leq$ 30 Hz. When an equivalent noise bandwidth (ENBW) of 41.7 mHz was employed, a maximum SNR of order 80 was obtained with a modulation frequency f_m = 4 Hz.

In the second experiment, a steady flow of AFP-modulated water was subjected to a continuous on-resonant tipping field B_1 applied in a static magnetic field $\sim$20 μT. When B_1 is applied close to resonance, the orientation of the nuclear magnetization can be manipulated. This in turn influences the signal monitored by the MI sensors and results in a resonance profile. The width of the resonance depends on the average speed of the water flowing through the B_1 coil.

Finally in the third experiment, which was a pulsed ULF NMR experiment, the MI sensors were used to monitor the magnetic field associated with the transverse component (rather than the longitudinal component) of a precessing ^{1}H nuclear magnetization. The experiment was typically performed in a static magnetic field of 4.7 μT. When an ENBW of 41.6 Hz was employed a SNR of order 10 was achieved for a single shot measurement. The

MI sensors were also tested with a train of tipping pulses applied to periodically refocus the nuclear magnetization. The sensors recovered from saturation very quickly, on a time scale of a few ms, and spin echoes were successfully observed after each π pulse.

The promising results obtained from the experiments described in Chapter 3 suggest potential applications of MI sensors to ULF NMR spectroscopy. Their primary advantage over other types of magnetometers is the simplicity with which they can be incorporated into an apparatus.

Chapter 4 is dedicated to descriptions of pulsed SD experiments in which the modified gyromagnetic ratio γ' of ^{1}H nuclei of water is measured over a broad range of experimental parameters. The apparatus used to perform these experiments is the same as that described for the pulsed NMR experiments in Chapter 3, with the addition of an actively-shielded coil to produce an intense far off-resonant oscillating magnetic field $\mathbf{B}_d$ perpendicular to $\mathbf{B}_0$. Typical operating conditions for experiments performed in the regime $y < 1$ include $B_0 = 4.7$ μT (yielding a ^{1}H Larmor frequency of 200 Hz) and $B_d \lesssim 500$ μT applied at 500 Hz. A simple data analysis protocol for determining the phase accumulated by the precessing nuclear magnetization while the dressing field is applied is then used to infer γ'.

This apparatus was used to investigate spin dressing at $y = 0.4$ and $0 < x < 40$. This is much broader range of the parameter x than has been explored previously. The normalized modified ^{1}H gyromagnetic ratio ^{1}H observed in these experiments is consistent with the perturbation theory prediction $\gamma' = \gamma J_0(x)$ where $J_0(x)$ is the zeroth-order Bessel function. As y approaches 1 from below, minor deviations from the $y = 0$ behaviour (i.e. $J_0(x)$) were observed at small values of x, consistent with simulation results obtained using both the semi-classical model of spin precession and the quantum model described in Chapter 2.

In the regime $y > 1$, experimental data for γ'/γ for ^{1}H nuclei in water were consistent with predictions of the quantum model for small values of x, but not at large values of x. This is consistent with previous reports of SD [38] in which data for γ'/γ were only given at small values of x.

Chapter 4 also presents results for an unexpected revival of nuclear magnetization (or spin echo formation) in FID signals in response to the application of off-resonant dressing field pulses. This echo formation occurs more frequently in the regime $y > 1$ and less frequently in the regime $y < 1$. It strongly influences the interpretation of the accumulated phase of dressed nuclear spins and consequently influences determination of γ'/γ. A simple semi-classical model of spin precession was introduced in this chapter; it can predict echo formation as a function of the parameters x and y. This echo formation can also be explained in terms of a multi-photon absorption process [109]. In this picture an odd number of photons at far off-resonant frequencies can be absorbed by spin-1/2 particles. And, in

the presence of a static magnetic field gradient this results in echo formation.

Chapter 5 introduces a new apparatus that I developed to perform NMR experiments on multi-nuclear spin species. The apparatus does not rely on the flow of a liquid sample (water) through the polarization and measurement regions. Instead, it uses a pneumatic sample transfer system to transport a cell containing the sample, between a 1.5 T polarization station and the ULF NMR region. Once again MI sensors are used for signal detection to monitor NMR FID signals. The operation of the apparatus is illustrated for samples containing either one or two spin species.

The new apparatus is capable of monitoring ^{1}H Larmor precession over frequencies $f_L \geq 30$ Hz. Most of the NMR experiments I report are performed in the range $f_L = 100$ - 200 Hz. In this range samples comprising ^{1}H nuclei in deionized water thermally prepolarized to 1.5 T yield signals with SNR ~ 4.5 for single shot FID acquisitions with an ENBW of 83 Hz. After averaging 16 sequential FIDs the observed SNR is of order 18.5.

To investigate the simultaneous detection of ULF NMR signals from two spin species, a miscible mixture of hexafluorobenzene (source of ^{19}F nuclei) and acetone (source of ^{1}H nuclei) was employed. The FID signals obtained from this mixture at $B_0 = 4.7$ μT clearly involve two exponentially decaying sinusoids corresponding to two independently precessing nuclear magnetizations: $\mathbf{M}_H$ and $\mathbf{M}_F$, for ^{1}H and ^{19}F respectively. Fourier transforms of these signals reveal double peaks, corresponding to the two different nuclear precession frequencies.

When two nuclear spin species precess about a static magnetic field, one species can be used as a reference against which the precession of the other is monitored. This is the basis of co-magnetometery, which has applications to precision measurements in fundamental physics. In Chapter 5, co-magnetometery in a ^{1}H-^{19}F mixture is illustrated, and the average value of the ratio of the two gyromagnetic ratios was experimentally determined to be $\gamma_F/\gamma_H = 0.94070(9)$. This is consistent with the ratio $\gamma_F/\gamma_H = 0.94077(3)$ inferred from previous measurements [52].

Chapter 5 also discusses issues related to initial conditions in CSD experiments. In particular the initial conditions established by conventional tipping pulses are explored. The goal is to rotate the nuclear magnetizations of two spin species from an initial alignment parallel to $\mathbf{B}_0$, into the transverse plane of the Bloch sphere. This in turn should yield a well defined and clean initial condition for a subsequent CSD experiment. It is shown that under the conditions employed for my experiments, when the magnitude of the tipping pulse B_1 is larger than B_0, one can not ignore the counter-rotating component of $\mathbf{B}_1$. That is, the rotating wave approximation (RWA) breaks down. As a result the tipping angle does not vary sinusoidally as a function of the amplitude of the tipping pulse. Moreover one measures different rotation angles when different tipping pulse waveforms are applied. It is impossible to rotate the nuclear magnetizations of two spin species precisely by $\pi/2$

using only conventional tipping pulses whether the RWA is valid or not. A simple solution is to achieve rotation using composite tipping pulses. These are successive conventional tipping pulses with different frequencies, amplitudes, durations and relative phases. One example of a composite pulse was investigated for use as a tipping pulse for ^{1}H and ^{19}F and simultaneous $\pi/2$ rotations were observed with an accuracy of ~ 20 mrad.

Chapter 6 is devoted to critical spin dressing. It discusses the data analysis method used to infer modified gyromagnetic ratios of nuclear spins involved in CSD experiments. This method is an extension of the data analysis technique introduced in Chapter 4 and employed for SD experiments on ^{1}H nuclei in water. This method, and the apparatus described in Chapter 5, are then used to demonstrate CSD when a standard dressing field waveform is employed, as well as when modulated dressing field waveforms are employed. In the first case (standard waveform) the ^{1}H Larmor frequency was $f_{\mathrm{LH}} = 200$ Hz; 20-cycle dressing pulses were applied at frequencies $f_{\mathrm{d}} = 500$ Hz and 1 kHz corresponding to dressing parameters $y = 0.4$ and 0.2, respectively. It was observed that the quality of the data acquired at $y = 0.2$ was better than at $y = 0.4$. A simple approach to improving the quality of data in the latter case was then demonstrated. It involves periodically alternating the phase of the dressing field waveform between 0 and π. This is a very common thing to do in NMR experiments to suppress the accumulation of phase errors. These errors can be caused by factors such as asymmetries in geometry, current supply circuitry or the alignment of the oscillating field with respect to the static field. This initiative was successful and a big improvement in the quality of CSD data was observed. In another experiment performed at $f_{\mathrm{LH}} = 200$ Hz and $f_{\mathrm{d}} = 500$ Hz the phase and amplitude of the dressing field were simultaneously modulated. The phase was alternated between 0 and π and the amplitude was modulated at 5 kHz. This unconventional dressing field waveform suppressed sensitivity of the CSD conditions to variations in the parameter x by 37 %.

In summary, this thesis presents the first experimental demonstration of critical spin dressing. The demonstration is a pulsed CSD experiment in which ^{1}H and ^{19}F nuclear spins are forced to precess at the same time-averaged precession rate. It also describes the various experimental tools and analytical methods that I designed, developed and evaluated in order to carry out a demonstration of CSD.

In terms of experimental tools, I developed a simple and robust apparatus to monitor ULF NMR signals from multi-nuclear spin species. The most innovative part of this apparatus was the use of Magneto-Impedance sensors to monitor NMR signals. The capabilities of these sensors were evaluated in a series of NMR and SD experiments.

In terms of analytical tools, I used a technique that involved measuring the phase of nuclear precession signals before and after application of a dressing field pulse in order to infer the phase accumulated during the pulse. This enabled me to determine the average

precession rates of dressed spins even though the MI sensors were saturated while the dressing field was applied.

In terms of future directions, it is worth reiterating a number of suggestions that were made in the body of the thesis. These fall into three categories. First, this thesis has demonstrated the use of MI sensors for NMR, in the ultra-low field limit. One could imagine exploring similar applications of these sensors to experiments involving j-coupling spectroscopy, NMR relaxometry or diffusometry. It would be particularly interesting (and potentially advantageous) to integrate MI sensor technology with microfluidic chip technology in order to attempt to make progress in the field of solution NMR spectroscopy.

Second, the experiments I have reported in this thesis suggest that there is both a potential need and capability to explore and better understand nuclear magnetization dynamics in a dressed system with $y > 1$ and $x \simeq y$. As noted in Ch. 4 discrepancies between experimental observations and the predictions of the two simulation models (quantum and semi-classical) were observed in this regime. At the moment the origin and explanation for this inconsistency is unknown.

Third, with a demonstration of CSD having been accomplished it would be natural to upgrade the apparatus to improve the quality of data and further explore CSD. In this regard there are at least four specific lines of inquiry that could yield significant improvements.

First, I think it would be highly advantageous to develop methods that would permit the use of degassed samples. It has been demonstrated [52] that NMR relaxation times in excess of 10 s can be realized by degassing acetone and HFB. Long relaxation times would in turn allow one to perform dressing experiments over much longer time periods. Another improvement that could be addressed is to locate and eliminate a source of 60 cycle noise and associated 4th harmonics in my apparatus. This was the dominant source of noise during my CSD experiments. One might be able to boost the SNR in similar experiments by up to two orders of magnitude if this noise was removed. There would also be an advantage to demagnetizing the shields. This would allow one to perform CSD experiments at lower Larmor frequencies, and would eliminate the static field gradient that is believed to be caused by the innermost shield.

Second, it would almost certainly be useful to explore the effect of different initial $\pi/2$ tipping pulses on CSD. It would similarly be useful to explore the effects of variations of varying the magnetic fields $\mathbf{B}_0$ and $\mathbf{B}_{\text{d}}$ on CSD in greater detail. Note that to reveal the effects of these parameters a reasonably high SNR is desirable and so one would want to start by implementing the technical improvements listed above.

Third, as I demonstrated in Ch. 6, unconventional dressing waveforms can yield significant improvements in CSD experiments. In the final stages of preparing my thesis I learned about simulations in which other dressing waveforms have been considered [139]. It would

be both very interesting and potentially valuable to explore these proposed waveforms experimentally using the apparatus described in Ch. 5, as well as to investigate other possible dressing waveforms.

Fourth, one could attempt to adjust the relative orientation of the MI sensors and $\mathbf{B}_d$ in my apparatus so that the sensors are not saturated during application of dressing pulses. This might enable one to monitor the modified precession frequency of nuclear magnetic moments directly, and ultimately attempt to demonstrate continuous rather than pulsed CSD.

"Everything should be made as simple as possible,
but not simpler."
—Albert Einstein

Bibliography

[1] I. B. Khriplovich and S. K. Lamoreaux. CP violation without strangeness: electric dipole moments of particles, atoms, and molecules. Springer, 1997.

[2] E. M. Purcell and N. F. Ramsey. On the possibility of electric dipole moments for elementary particles and nuclei. *Physical Review*, **78**(6):807, 1950.

[3] J. H. Smith, E. M. Purcell, and N. F. Ramsey. Experimental limit to the electric dipole moment of the neutron. *Physical Review*, **108**(1):120, 1957.

[4] A. P. Serebrov, E. A. Kolomenskiy, A. N. Pirozhkov, I. A. Krasnoschekova, A. V. Vassiljev, A. O. Polyushkin, M. S. Lasakov, A. N. Murashkin, V. A. Solovey, A. K. Fomin, et al. New search for the neutron electric dipole moment with ultracold neutrons at ILL. *Physical Review C*, **92**(5):055501, 2015.

[5] A. D. Sakharov. Violation of CP invariance, c asymmetry, and baryon asymmetry of the universe. *JETP Letters.*, **5**:24–27, 1967.

[6] J. H. Christenson, J. W. Cronin, V. L. Fitch, and R. Turlay. Evidence for the 2 π decay of the K_2^0 meson. *Physical Review Letters*, **13**(4):138, 1964.

[7] B. Aubert, D. Boutigny, J. M. Gaillard, A. Hicheur, Y. Karyotakis, J. P. Lees, P. Robbe, V. Tisserand, A. Palano, G. P. Chen, et al. Observation of CP violation in the B^0 meson system. *Physical Review Letters*, **87**(9):091801, 2001.

[8] K. Abe, R. Abe, I. Adachi, B. S. Ahn, H. Aihara, M. Akatsu, G. Alimonti, K. Asai, M. Asai, Y. Asano, et al. Observation of large CP violation in the neutral B meson system. *Physical Review Letters*, **87**(9):091802, 2001.

[9] G. R. Farrar and M. E. Shaposhnikov. Baryon asymmetry of the universe in the standard model. *Physical Review D*, **50**(2):774, 1994.

[10] Y. Li, S. Profumo, and M. Ramsey-Musolf. A comprehensive analysis of electric dipole moment constraints on CP-violating phases in the MSSM. *Journal of High Energy Physics*, 2010(**8**):1–25, 2010.

[11] M. Pospelov and A. Ritz. Electric dipole moments as probes of new physics. *Annals of Physics*, **318**(1):119–169, 2005.

[12] J. Baron, W. C. Campbell, D. DeMille, J. M. Doyle, G. Gabrielse, Y. V. Gurevich, P. W. Hess, N. R. Hutzler, E. Kirilov, I. Kozyryev, et al. Order of magnitude smaller limit on the electric dipole moment of the electron. *Science*, **343**(6168):269–272, 2014.

[13] P. G. Harris, C. A. Baker, K. Green, P. Iaydjiev, S. Ivanov, D. J. R. May, J. M. Pendlebury, D. Shiers, K. F. Smith, M. Van der Grinten, et al. New experimental limit on the electric dipole moment of the neutron. *Physical Review Letters*, **82**(5):904, 1999.

[14] C. A. Baker, D. D. Doyle, P. Geltenbort, K. Green, M. G. D. Van der Grinten, P. G. Harris, P. Iaydjiev, S. N. Ivanov, D. J. R. May, J. M. Pendlebury, et al. Improved experimental limit on the electric dipole moment of the neutron. *Physical Review Letters*, **97**(13):131801, 2006.

[15] S. A. Murthy, D. Krause Jr, Z. L. Li, and L. R. Hunter. New limits on the electron electric dipole moment from cesium. *Physical Review Letters*, **63**(9):965, 1989.

[16] B. C. Regan, E. D. Commins, C. J. Schmidt, and D. DeMille. New limit on the electron electric dipole moment. *Physical Review Letters*, **88**(7):071805, 2002.

[17] B. Graner, Y. Chen, E. G. Lindahl, B. R. Heckel, et al. Reduced limit on the permanent electric dipole moment of ^{199}Hg. *Physical Review Letters*, **116**(16):161601, 2016.

[18] M. Bishof, R. H. Parker, K. G. Bailey, J. P. Greene, R. J. Holt, M. R. Kalita, W. Korsch, N. D. Lemke, Z. T. Lu, P. Mueller, et al. Improved limit on the ^{225}Ra electric dipole moment. *Physical Review C*, **94**(2):025501, 2016.

[19] R. H. Parker, M. R. Dietrich, M. R. Kalita, N. D. Lemke, K. G. Bailey, M. Bishof, J. P. Greene, R. J. Holt, W. Korsch, Z. T. Lu, et al. First measurement of the atomic electric dipole moment of ^{225}Ra. *Physical Review Letters*, **114**(23):233002, 2015.

[20] M. A. Rosenberry and T. E. Chupp. Atomic electric dipole moment measurement using spin exchange pumped masers of ^{129}Xe and ^{3}He. *Physical Review Letters*, **86**(1):22, 2001.

[21] J. J. Hudson, D. M. Kara, I. J. Smallman, B. E. Sauer, M. R. Tarbutt, and E. A. Hinds. Improved measurement of the shape of the electron. *Nature*, **473**(7348):493–496, 2011.

[22] I. B. Khriplovich and A. R. Zhitnitsky. What is the value of the neutron electric dipole moment in the Kobayashi-Maskawa model? *Physics Letters B*, **109**(6):490, 1982.

[23] M. E. Pospelov and I. B. Khriplovich. Electric dipole moment of the W boson and the electron in the Kobayashi-Maskawa model. *Soviet Journal of Nuclear Physics*, **53**:638–640, 1991.

[24] S. Ban, J. Dobaczewski, J. Engel, and A. Shukla. Fully self-consistent calculations of nuclear Schiff moments. *Physical Review C*, **82**(1):015501, 2010.

[25] X. G. He, B. H. J. McKellar, and S. Pakvasa. The neutron electric dipole moment. *International Journal of Modern Physics A*, **4**(19):5011–5046, 1989.

[26] I. I. Y. Bigi and N. G. Uraltsev. Effective gluon operators and the dipole moment of the neutron. *Sov. Phys. JETP*, **73**:198, 1991.

[27] Jonathan Engel, Michael J Ramsey-Musolf, and U Van Kolck. Electric dipole moments of nucleons, nuclei, and atoms: The Standard Model and beyond. *Progress in Particle and Nuclear Physics*, **71**:21–74, 2013.

[28] R. Golub and S. K. Lamoreaux. Neutron electric-dipole moment, ultracold neutrons and polarized ^{3}He. *Physics Reports*, **237**(1):1–62, 1994.

[29] T. M. Ito et al. Plans for a neutron edm experiment at SNS. *Journal of Physics: Conference Series*, **69**(1):012037, 2007.

[30] P. J. Mohr, D. B. Newell, and B. N. Taylor. CODATA recommended values of the fundamental physical constants: 2014. *Journal of Physical and Chemical Reference Data*, **45**(4):043102, 2016.

[31] J. L. Flowers, B. W. Petley, and M. G. Richards. A measurement of the nuclear magnetic moment of the helium-3 atom in terms of that of the proton. *Metrologia*, **30**(2):75, 1993.

[32] R. Schmid. New Search for the Neutron Electric Dipole Moment Using Ultracold Neutrons at the Spallation Neutron Source. PhD thesis, California Institute of Technology, 2014.

[33] nEDM Collaboration. A new search for the Neutron Electric Dipole Moment (funding pre-proposal submitted to the US Department of Energy) LA-UR 02-2331, March 2002.

[34] C. Cohen-Tannoudji and S. Haroche. Absorption et diffusion de photons optiques par un atome en interaction avec des photons de radiofréquence. *Journal de Physique*, **30**(2-3):153–168, 1969.

[35] E. Muskat, D. Dubbers, and O. Schärpf. Dressed neutrons. *Physical Review Letters*, **58**(20):2047, 1987.

[36] S. Eckel, S. K. Lamoreaux, M. E. Hayden, and T. M. Ito. Time-dependent spin dressing using a ^{3}He atomic beam. *Physical Review A*, **85**(3):032124, 2012.

[37] A. Esler, J. C. Peng, D. Chandler, D. Howell, S. K. Lamoreaux, C. Y. Liu, and J. R. Torgerson. Dressed spin of ^{3}He. *Physical Review C*, **76**(5):051302, 2007.

[38] P. H. Chu, A. M. Esler, J. C. Peng, D. H. Beck, D. E. Chandler, S. Clayton, B. Z. Hu, S. Y. Ngan, C. H. Sham, L. H. So, and others. Dressed spin of polarized ^{3}He in a cell. *Physical Review C*, **84**(2):022501, 2011.

[39] P. H. Chu. Neutron Electric Dipole Moment and Dressed Spin. PhD thesis, University of Illinois at Urbana-Champaign, 2012.

[40] G. K. Yagola, V. I. Zingerman, and V. N. Sepetyi. Determination of the precise value of the proton gyromagnetic ratio in strong magnetic fields. *Measurement Techniques*, **9**(7):914–917, 1966.

[41] R. K. Harris. Nuclear magnetic resonance spectroscopy. John Wiley and Sons Inc., 1986.

[42] D. R. Lide. CRC handbook of Chemistry and Physics, volume **85**. CRC press, 2004.

[43] G. D. Fuchs, V. V. Dobrovitski, D. M. Toyli, F. J. Heremans, and D. D. Awschalom. Gigahertz dynamics of a strongly driven single quantum spin. *Science*, **326**(5959):1520–1522, 2009.

[44] Y. J. Lin, K. Jiménez-García, and I. B. Spielman. Spin-orbit-coupled Bose-Einstein condensates. *Nature*, **471**(7336):83–86, 2011.

[45] N. Timoney, I. Baumgart, M. Johanning, A. F. Varón, M. B. Plenio, A. Retzker, and C. Wunderlich. Quantum gates and memory using microwave-dressed states. *Nature*, **476**(7359):185–188, 2011.

[46] D. A. Golter, T. K. Baldwin, and H. Wang. Protecting a solid-state spin from decoherence using dressed spin states. *Physical Review Letters*, **113**(23):237601, 2014.

[47] A. Abragam. The principles of nuclear magnetism. Oxford University Press, 1961.

[48] C. Cohen-Tannoudji. Atoms in electromagnetic fields, volume 1. World scientific, 1994.

[49] J. J. Sakurai. Advanced quantum mechanics. Pearson Education India, 1967.

[50] R. J. Glauber. Coherent and incoherent states of the radiation field. *Physical Review*, **131**(6):2766, 1963.

[51] N. Polonsky and C. Cohen-Tannoudji. Interprétation quantique de la modulation de fréquence. *Journal de Physique*, **26**(7):409–414, 1965.

[52] M. P. Ledbetter, S. Pustelny, D. Budker, M. V. Romalis, J. W. Blanchard, and A. Pines. Liquid-state nuclear spin comagnetometers. *Physical Review Letters*, **108**(24):243001, 2012.

[53] K. Mohri, T. Kohsawa, K. Kawashima, H. Yoshida, and L. Panina. Magneto-inductive effect (MI effect) in amorphous wires. *IEEE Transactions on Magnetics*, **28**(5):3150–3152, 1992.

[54] K. Mohri and Y. Honkura. Amorphous wire and CMOS IC based magneto-impedance sensors-Origin, topics, and future. *Sensor Letters*, **5**(1):267–270, 2007.

[55] M. P. Ledbetter, I. M. Savukov, D. Budker, V. Shah, S. Knappe, J. Kitching, D. J. Michalak, S. Xu, and A. Pines. Zero-field remote detection of NMR with a microfabricated atomic magnetometer. *Proceedings of the National Academy of Sciences*, **105**(7):2286–2290, 2008.

[56] I. K. Kominis, T. W. Kornack, J. C. Allred, and M. V. Romalis. A subfemtotesla multichannel atomic magnetometer. *Nature*, **422**(6932):596–599, 2003.

[57] A. N. Matlachov, P. L. Volegov, M. A. Espy, J. S. George, and R. H. Kraus. SQUID detected NMR in microtesla magnetic fields. *Journal of Magnetic Resonance*, **170**(1):1–7, 2004.

[58] M. C. D. Tayler, T. Theis, T. F. Sjolander, J. W. Blanchard, A. Kentner, S. Pustelny, A. Pines, and D. Budker. Invited Review Article: Instrumentation for nuclear magnetic resonance in zero and ultralow magnetic field. *Review of Scientific Instruments*, **88**(9):091101, 2017.

[59] Y. Pei, N. F. Yu, Q. Liu, and J. Liu. Theory and application of anisotropic magnetoresistive sensor. *Instrument Technique and Sensor*, **8**:012, 2004.

[60] F. Primdahl. The fluxgate magnetometer. *Journal of Physics E: Scientific Instruments*, **12**(4):241, 1979.

[61] D. F. He, M. Tachiki, and H. Itozaki. Highly sensitive anisotropic magnetoresistance magnetometer for Eddy-current nondestructive evaluation. *Review of Scientific Instruments*, **80**(3):036102, 2009.

[62] C. C. Lu, J. Huang, P. K. Chiu, S. L. Chiu, and J. T. Jeng. High-sensitivity low-noise miniature fluxgate magnetometers using a flip chip conceptual design. *Sensors*, **14**(8):13815–13829, 2014.

[63] J. Kubik and P. Ripka. Noise spectrum of pulse excited fluxgate sensor. *Sensors and Actuators A: Physical*, **132**(1):236–240, 2006.

[64] P. M. Drljača, P. Kejik, F. Vincent, D. Piguet, F. Gueissaz, and R. S. Popović. Single core fully integrated CMOS micro-fluxgate magnetometer. *Sensors and Actuators A: Physical*, **110**(1):236–241, 2004.

[65] B. David et al. The development of a High-T_c magnetocardiography system for unshielded environment. *IEEE Transactions of Superconductivity*, **7**(2), June 1997.

[66] L. G. C. Melo, D. Menard, A. Yelon, L. Ding, S. Saez, and C. Dolabdjian. Optimization of the magnetic noise and sensitivity of giant magnetoimpedance sensors. *Journal of Applied Physics*, **103**(3):033903, 2008.

[67] H. Hauser, J. Hochreiter, G. Stangl, R. Chabicovsky, M. Janiba, and K. Riedling. Anisotropic magnetoresistance effect field sensors. *Journal of magnetism and magnetic materials*, **215**:788–791, 2000.

[68] L. Panina and K. Mohri. Magneto-impedance effect in amorphous wires. *Applied Physics Letters*, 65(9):1189–1191, 1994.

[69] M. Ali. *Growth and study of magnetostrictive FeSiBC thin films for device applications.* PhD thesis, The University of Sheffield, 1999.

[70] M. Noda. Magneto-impedance effect in amorphous wires magnetized with asymmetrical current. *J. Magnetics Society of Japan*, **19**:485–488, 1995.

[71] I. Ismail, N. Nuryani, B. Purnama, D. Y. Kusuma, Q. Hidayah, O. R. Aji, R. S. Winanda, S. Inayati, N. Irsalinda, and I. T. R. Yanto. Critical diameter and magneto-impedance effect in electrodeposited $[Cu/Ni_{80}Fe_{20}]_3$ multilayer wire at low frequency. *AIP Conference Proceedings*, **1746**(1):020002, 2016.

[72] Y. Takemura, S. Masuda, K. Komatsu, T. Yamada, and K. Kakuno. Fundamental properties of magnetoelastic wave and magneto-impedance effect in FeSiB amorphous wires. In *Electronic Manufacturing Technology Symposium, 1995, Proceedings of 1995 Japan International, 18th IEEE/CPMT International*, pages 166–169. IEEE, 1995.

[73] S. Atalay and N. Bayri. Low field magnetoimpedance in FeSiB and CoSiB cosib amorphous wires. *Journal of Magnetism and Magnetic Materials*, **272**:1365–1367, 2004.

[74] C. Losin, C. Gomez-Polo, M. Knobel, and A. Grishin. Torsional dependence of second-harmonic amplitude of giant magnetoimpedance in FeCoSiB amorphous wire. *IEEE Transactions on Magnetics*, **38**(5):3087–3089, 2002.

[75] R. S. Beach and A. E. Berkowitz. Giant magnetic field dependent impedance of amorphous FeCoSiB wire. *Applied Physics Letters*, **64**(26):3652–3654, 1994.

[76] L. V. Panina, K. Mohri, K. Bushida, and M. Noda. Giant magneto-impedance and magneto-inductive effects in amorphous alloys. *Journal of Applied Physics*, **76**(10):6198–6203, 1994.

[77] L. Panina, K. Mohri, T. Uchiyama, M. Noda, and K. Bushida. Giant magneto-impedance in Co-rich amorphous wires and films. *IEEE Transactions on Magnetics*, **31**(2):1249–1260, 1995.

[78] L. Kraus. GMI modeling and material optimization. *Sensors and Actuators A: Physical*, **106**(1):187–194, 2003.

[79] H. Chiriac, M. Tibu, A. E. Moga, and D. D. Herea. Magnetic GMI sensor for detection of biomolecules. *Journal of Magnetism and Magnetic Materials*, **293**(1):671–676, 2005.

[80] D. J. Kim, D. G. Park, and J. H. Hong. Nondestructive evaluation of reactor pressure vessel steels using the giant magnetoimpedance sensor. *Journal of Applied Physics*, **91**(10):7421–7423, 2002.

[81] P. Ripka. Magnetic sensors and magnetometers. Artech House Publishers, 2001.

[82] M. H. Phan and H. X. Peng. Giant magnetoimpedance materials: Fundamentals and applications. *Progress in Materials Science*, **53**(2):323–420, 2008.

[83] C. P. Bidinosti, E. M. Chapple, and M. E. Hayden. The sphere in a uniform rf field-revisited. *Concepts in Magnetic Resonance Part B: Magnetic Resonance Engineering*, **31**(3):191–202, 2007.

[84] J. G. Powles. The adiabatic fast passage experiment in magnetic resonance. *Proceedings of the Physical Society*, **71**(3):497, 1958.

[85] F. M. White and I. Corfield. Viscous fluid flow. McGraw-Hill New York, 2006.

[86] C. P. Bidinosti, I. S. Kravchuk, and M. E. Hayden. Active shielding of cylindrical saddle-shaped coils: Application to wire-wound RF coils for very low field NMR and MRI. *Journal of Magnetic Resonance*, **177**(1):31–43, 2005.

[87] M. W. Reynolds. Computer code BIOTSAVART magnetic field calculator version 4.0.17 (Ripplon Software, Canada; http://www.ripplon.com). 1992.

[88] H. Y. Carr and E. M. Purcell. Effects of diffusion on free precession in nuclear magnetic resonance experiments. *Physical Review*, **94**(3):630, 1954.

[89] S. Meiboom and D. Gill. Modified spin-echo method for measuring nuclear relaxation times. *Review of Scientific Instruments*, **29**(8):688–691, 1958.

[90] J. L. Barnhart and R. N. Berk. Influence of paramagnetic ions and pH on proton NMR relaxation of biologic fluids. *Investigative Radiology*, **21**(2):132–136, 1986.

[91] T. Theis, J. W. Blanchard, M. C. Butler, M. P. Ledbetter, D. Budker, and A. Pines. Chemical analysis using J-coupling multiplets in zero-field NMR. *Chemical Physics Letters*, **580**:160–165, 2013.

[92] C. Charlier, S. N. Khan, T. Marquardsen, P. Pelupessy, V. Reiss, D. Sakellariou, G. Bodenhausen, F. Engelke, and F. Ferrage. Nanosecond time scale motions in proteins revealed by high-resolution NMR relaxometry. *Journal of the American Chemical Society*, **135**(49):18665–18672, 2013.

[93] P. Volegov, M. Flynn, R. Kraus, P. Magnelind, A. Matlashov, P. Nath, T. Owens, H. Sandin, I. Savukov, L. Schultz, et al. Magnetic resonance relaxometry at low and ultra low fields. In *17th International Conference on Biomagnetism Advances in Biomagnetism–Biomag2010*, pages 82–87. Springer, 2010.

[94] P. J. Ganssle, H. D. Shin, S. J. Seltzer, V. S. Bajaj, M. P. Ledbetter, D. Budker, S. Knappe, J. Kitching, and A. Pines. Ultra-low-field NMR relaxation and diffusion measurements using an optical magnetometer. *Angewandte Chemie International Edition*, **53**(37):9766–9770, 2014.

[95] E. Harel, C. Hilty, K. Koen, E. E. McDonnell, and A. Pines. Time-of-flight flow imaging of two-component flow inside a microfluidic chip. *Physical Review Letters*, **98**(1):017601, 2007.

[96] A. D. Stroock, S. K. W. Dertinger, A. Ajdari, I. Mezić, H. A. Stone, and G. M. Whitesides. Chaotic mixer for microchannels. *Science*, **295**(5555):647–651, 2002.

[97] D. J. Griffiths. Introduction to electrodynamics, 2005.

[98] E. L. Hahn. Spin echoes. *Physical Review*, **80**(4):580, 1950.

[99] A. E. Derome. Modern NMR techniques for chemistry research. Elsevier, 2013.

[100] E. O. Stejskal and J. D. Memory. High resolution NMR in the solid state: fundamentals of CP/MAS. Cambridge University Press, 1994.

[101] A. Schweiger and G. Jeschke. Principles of pulse electron paramagnetic resonance. Oxford University Press on Demand, 2001.

[102] S. I. Chu and D. A. Telnov. Beyond the floquet theorem: generalized floquet formalisms and quasienergy methods for atomic and molecular multiphoton processes in intense laser fields. *Physics Reports*, **390**(1):1–131, 2004.

[103] S. K. Son, S. Han, S. I. Chu, et al. Floquet formulation for the investigation of multiphoton quantum interference in a superconducting qubit driven by a strong ac field. *Physical Review A*, **79**(3):032301, 2009.

[104] H. Z. Jooya, K. Reihani, and S. I. Chu. A graph-theoretical representation of multiphoton resonance processes in superconducting quantum circuits. *Scientific Reports*, **6**:37544, 2016.

[105] H. K. Kelardeh, V. Apalkov, and M. I. Stockman. Graphene in ultrafast and superstrong laser fields. *Physical Review B*, **91**(4):045439, 2015.

[106] F. Fillion-Gourdeau, D. Gagnon, C. Lefebvre, and S. MacLean. Time-domain quantum interference in graphene. *Physical Review B*, **94**(12):125423, 2016.

[107] H. Hatanaka and N. Tabuchi. New line-narrowing effect in triple-quantum resonance in a two-level NMR system. *Journal of Magnetic Resonance*, **155**(119), 2002.

[108] Y. Zur, M. H. Levitt, and S. Vega. Multiphoton NMR spectroscopy on a spin system with I = 1/2. *The Journal of Chemical Physics*, **78**(9):5293–5310, 1983.

[109] I. Gromov and A. Schweiger. Multiphoton resonances in pulse EPR. *Journal of Magnetic Resonance*, **146**(1):110–121, 2000.

[110] J. H. Shirley. Solution of the schrödinger equation with a hamiltonian periodic in time. *Physical Review*, **138**(4B):B979, 1965.

[111] C. A. Michal, S. P. Hastings, and L. H. Lee. Two-photon Lee-Goldburg nuclear magnetic resonance: Simultaneous homonuclear decoupling and signal acquisition. *The Journal of Chemical Physics*, **128**(5):052301, 2008.

[112] C. A. Michal. Nuclear magnetic resonance noise spectroscopy using two-photon excitation. *The Journal of Chemical Physics*, **118**(8):3451–3454, 2003.

[113] D. Gagnon, F. Fillion-Gourdeau, J. Dumont, C. Lefebvre, and S. MacLean. Suppression of multiphoton resonances in driven quantum systems via pulse shape optimization. *Physical Review Letters*, **119**(5):053203, 2017.

[114] A. S. Kiryutin, A. N. Pravdivtsev, K. L. Ivanov, Y. A Grishin, H. M. Vieth, and A. V. Yurkovskaya. A fast field-cycling device for high-resolution NMR: Design and application to spin relaxation and hyperpolarization experiments. *Journal of Magnetic Resonance*, **263**:79–91, 2016.

[115] C. Y. Chou, M. Abdesselem, C. Bouzigues, M. Chu, A. Guiga, T. H. Huang, F. Ferrage, T. Gacoin, A. Alexandrou, and D. Sakellariou. Ultra-wide range field-dependent measurements of the relaxivity of $Gd_{1-x}Eu_xVO_4$ nanoparticle contrast agents using a mechanical sample-shuttling relaxometer. *Scientific Reports*, **7**, 2017.

[116] C. Charlier, S. N. Khan, T. Marquardsen, P. Pelupessy, V. Reiss, D. Sakellariou, G. Bodenhausen, F. Engelke, and F. Ferrage. Nanosecond time scale motions in proteins revealed by high-resolution NMR relaxometry. *Journal of the American Chemical Society*, **135**(49):18665–18672, 2013.

[117] J. Kauppinen and J. Partanen. Fourier transforms in spectroscopy. John Wiley & Sons, 2011.

[118] W. C. Griffith, M. D. Swallows, T. H. Loftus, M. V. Romalis, B. R. Heckel, and E. N. Fortson. Improved limit on the permanent electric dipole moment of Hg 199. *Physical Review Letters*, **102**(10):101601, 2009.

[119] T. W. Kornack, R. K. Ghosh, and M. V. Romalis. Nuclear spin gyroscope based on an atomic comagnetometer. *Physical Review Letters*, **95**(23):230801, 2005.

[120] B. J. Venema, P. K. Majumder, S. K. Lamoreaux, B. R. Heckel, and E. N. Fortson. Search for a coupling of the Earth's gravitational field to nuclear spins in atomic mercury. *Physical Review Letters*, **68**(2):135, 1992.

[121] D. Bear, R. E. Stoner, R. L. Walsworth, V. A. Kosteleckỳ, and C. D. Lane. Limit on Lorentz and *CPT* violation of the neutron using a two-species noble-gas maser. *Physical Review Letters*, **85**(24):5038, 2000.

[122] M. A. Bernstein, K. F. King, and X. J. Zhou. Handbook of MRI pulse sequences. Elsevier, 2004.

[123] J. A. Jones. Quantum computing with NMR. *Progress in Nuclear Magnetic Resonance Spectroscopy*, **59**(2):91–120, 2011.

[124] N. Linden, B. Hervé, R. J. Carbajo, and R. Freeman. Pulse sequences for NMR quantum computers: how to manipulate nuclear spins while freezing the motion of coupled neighbours. *Chemical Physics Letters*, **305**(1):28–34, 1999.

[125] A. Laucht, S. Simmons, R. Kalra, G. Tosi, J. P. Dehollain, J. T. Muhonen, S. Freer, F. E. Hudson, K. M. Itoh, D. N. Jamieson, et al. Breaking the rotating wave approximation for a strongly driven dressed single-electron spin. *Physical Review B*, **94**(16):161302, 2016.

[126] F. Bloch and A. Siegert. Magnetic resonance for nonrotating fields. *Physical Review*, **57**(6):522, 1940.

[127] P. Forn-Díaz, J. Lisenfeld, D. Marcos, J. J. García-Ripoll, E. Solano, C. J. P. M. Harmans, and J. E. Mooij. Observation of the bloch-siegert shift in a qubit-oscillator system in the ultrastrong coupling regime. *Physical Review Letters*, **105**(23):237001, 2010.

[128] A. P. Saiko, G. G. Fedoruk, and S. A. Markevich. Multiphoton transitions in a spin system driven by strong bichromatic field. *Journal of Experimental and Theoretical Physics*, **105**(5):893–899, 2007.

[129] M. E. Hayden and P. J. Nacher. History and physical principles of MRI. In Luca SABA, editor, *Magnetic Resonance Imaging Handbook*, volume 1. CRC press, 2016.

[130] M. H. Levitt. Composite pulses. *Progress in Nuclear Magnetic Resonance Spectroscopy*, **18**(2):61–122, 1986.

[131] M. H. Levitt and R. Freeman. NMR population inversion using a composite pulse. *Journal of Magnetic Resonance (1969)*, **33**(2):473–476, 1979.

[132] R. Tycko, H. M. Cho, E. Schneider, and A. Pines. Composite pulses without phase distortion. *Journal of Magnetic Resonance (1969)*, **61**(1):90–101, 1985.

[133] M. H. Levitt and R. Freeman. Compensation for pulse imperfections in NMR spin-echo experiments. *Journal of Magnetic Resonance (1969)*, **43**(1):65–80, 1981.

[134] G. Y. Li, Y. Jiang, and X. W. Wu. Composite pulse excitation for spin-1 pure nuclear quadrupole resonance spectroscopy in powders. *Chemical Physics Letters*, **202**(1-2):82–86, 1993.

[135] H. K. Cummins and J. A. Jones. Use of composite rotations to correct systematic errors in NMR quantum computation. *New Journal of Physics*, **2**(1):6, 2000.

[136] H. K. Cummins, G. Llewellyn, and J. A. Jones. Tackling systematic errors in quantum logic gates with composite rotations. *Physical Review A*, **67**(4):042308, 2003.

[137] W. G. Alway and J. A. Jones. Arbitrary precision composite pulses for NMR quantum computing. *Journal of Magnetic Resonance*, **189**(1):114–120, 2007.

[138] J. M. McGuirk. High precision absolute gravity gradiometry with atom interferometry. PhD thesis, Stanford University, 2001.

[139] Bradley Filippone. Private communication.

[140] E. Fukushima and S. B. W. Roeder. Experimental pulse NMR: a nuts and bolts approach. Addison-Wesley Reading, MA, 1981.